THERMAL CONVECTION IN SLENDER LATERALLY-HEATED CAVITIES

by

PING WANG

Thesis submitted for the degree of
Doctor of Philosophy

Department of Mathematics
City University
London

October 1992

To my parents

Acknowledgements

I am very grateful to my supervisor, Professor P.G. Daniels, without whose patience, encouragement and thoughtful and constructive advice I could not have completed this research . I am deeply indebted to Professor J.C. Patterson for many valuable comments, and suggestions. I also benefited from stimulating discussions with Dr. N.G.Wright and Mr J. Snell. Finally, I would like to take this opportunity to express my appreciation to the Committee of Vice-Chancellors and Principals of the Universities of the United Kingdom and to the Department of Mathematics of City University for financial support over three years, which assured the completion of this thesis.

Abstract

Two-dimensional convective flows in shallow and tall cavities with adiabatic or conducting horizontal boundaries and driven by differential heating of the two vertical end walls, are studied numerically over a range of Rayleigh numbers and Prandtl numbers . As the Rayleigh number increases, nonlinearity first affects the flow structure in the turning regions near the ends of the cavity. These 'end-zone problems' have been investigated by a combined computational and analytical approach. Numerical solutions are found using a DuFort-Frankel-Multigrid method, and appear to be in good agreement with theoretical predictions of a boundary-layer structure at high values of the Rayleigh number. For time-dependent shallow cavity flows, new theoretical solutions and numerical solutions are obtained by both analytical and computational methods.

A numerical scheme for finding thermal convective flows in a finite laterally heated cavity is described in detail in Chapter 2. The end-zone problems for tall cavities with conducting and adiabatic horizontal boundaries are considered in Chapters 3 and 4 respectively. For shallow cavities, the end-zone problems for these two thermal boundary conditions are considered in Chapters 5 and 6. Finally, time-dependent shallow cavity flows for insulated horizontal boundaries are investigated using both analytical and computational methods in Chapter 7.

Contents

List of Tables

List of Figures

Chapter 1

Introduction

1.1 Background

Convective motions driven by lateral temperature gradients in slender cavities are important in many areas of interest in industry and in nature. Applications include the temperature control of circuit board components under natural convection in the electronics industry, heating and ventilation control in building design and construction, cooling systems for nuclear reactors in the nuclear industry, flows and heat transfer associated with all stages of the power generation process, solar-energy collectors in the power industry and atmospheric and fluvial dispersion in the environment.

Due to the wide range of applications, studies of natural convection flow and heat transfer have been vigorously pursued for many years. A typical model of convection driven by a lateral thermal gradient consists of a two dimensional rectangular cavity with the two vertical end walls held at different constant temperatures . In order to determine the flow structure and heat transfer across cavities with different physical properties, numerous analytical, experimental and computational techniques have been used .

Experimental investigations of cavity flows driven by lateral heating have been reported by Elder (1965), Rossby (1965), Imberger (1974), and more recently by Patterson and Imberger (1980), Ostrach (1981),Patterson (1984), Simpkins and Chen (1986), Armfield (1989) and Patterson (1989). In general, these flows consist of a main circulation in which fluid rises at the hot wall, sinks at the cold wall, and travels laterally across the intervening core region. The governing equations for two dimensional motion within a cavity which represent the conservation of mass, momentum and energy are the continuity equation

$$\frac{\partial u^*}{\partial x^*} + \frac{\partial w^*}{\partial z^*} = 0, \tag{1.1.1}$$

the x^*-momentum equation

$$\frac{\partial u^*}{\partial t^*} + u^*\frac{\partial u^*}{\partial x^*} + w^*\frac{\partial u^*}{\partial z^*} = -\frac{1}{\rho_0}\frac{\partial p^*}{\partial x^*} + \nu\nabla^2 u^*, \tag{1.1.2}$$

the z^*-momentum equation

$$\frac{\partial w^*}{\partial t^*} + u^*\frac{\partial w^*}{\partial x^*} + w^*\frac{\partial w^*}{\partial z^*} = -\frac{1}{\rho_0}\frac{\partial p^*}{\partial z^*} + \nu\nabla^2 w^* + g\beta(T^* - T_0), \tag{1.1.3}$$

and the energy equation

$$\frac{\partial T^*}{\partial t^*} + u^*\frac{\partial T^*}{\partial x^*} + w^*\frac{\partial T^*}{\partial z^*} = \kappa\nabla^2 T^*, \tag{1.1.4}$$

where (x^*, z^*) are Cartesian co-ordinates, x^* in the direction along the lower horizontal boundary and z^* in the vertical direction with the origin at the bottom of the cold wall ($x^* = 0$). u^* and w^* are the velocity components in the directions x^* and z^* respectively and T^* is the temperature with $T^* = T_0$ on the cold wall; p^* is the pressure and ν, κ and g are the density, kinematic viscosity, thermal diffusivity and acceleration due to gravity (see Figure 1.1). It is assumed that the fluid density is given by

$$\rho^* = \rho_0(1 - \beta(T^* - T_0)) \tag{1.1.5}$$

where ρ_0 is the density at $T^* = T_0$ and β is the coefficient of thermal expansion. In line with the Oberbeck-Boussinesq approximation the variation of density with temperature is assumed only to affect the buoyancy term in (1.1.3).

By appropriate re-scaling of the variables, elimination of the pressure and introduction of a stream function ψ , the basic equations may be reduced to the non-dimensional form

$$\sigma^{-1}\left(\frac{\partial\omega}{\partial t}+J(\omega,\psi)\right)=\nabla^2\omega+R\frac{\partial T}{\partial x} \tag{1.1.6}$$

$$\nabla^2\psi=-\omega \tag{1.1.7}$$

$$\frac{\partial T}{\partial t}+J(T,\psi)=\nabla^2 T \tag{1.1.8}$$

where

$$\sigma=\frac{\nu}{\kappa} \tag{1.1.9}$$

is the Prandtl number and

$$R=\frac{g\beta\triangle T h^3}{\kappa\nu} \tag{1.1.10}$$

is the Rayleigh number based on the cavity height h and the temperature difference $\triangle T$ between the two vertical walls. Details are given in Section 2.2 below. Here the vorticity is defined by

$$\omega=\frac{\partial w}{\partial x}-\frac{\partial u}{\partial z} \tag{1.1.11}$$

with the two Jacobians given by

$$J(\omega,\psi)=\frac{\partial\omega}{\partial x}\frac{\partial\psi}{\partial z}-\frac{\partial\omega}{\partial z}\frac{\partial\psi}{\partial x},\quad J(T,\psi)=\frac{\partial T}{\partial x}\frac{\partial\psi}{\partial z}-\frac{\partial T}{\partial z}\frac{\partial\psi}{\partial x}. \tag{1.1.12}$$

The rigid walls are impermeable and at constant temperature so that

$$\psi=\frac{\partial\psi}{\partial x}=0,\quad x=0,\,L \tag{1.1.13}$$

and

$$T=0,\quad x=0;\quad T=1,\quad x=L \tag{1.1.14}$$

where

$$L=\frac{l}{h} \tag{1.1.15}$$

is the aspect ratio of the cavity, l being the cavity length. In the insulating case, the boundary conditions on the horizontal walls are

$$\frac{\partial T}{\partial z} = 0 \quad \text{on } z = 0,\ 1 \tag{1.1.16}$$

and in the conducting case

$$T = \frac{x}{L} \quad \text{on } z = 0,\ 1. \tag{1.1.17}$$

Thus, in the Boussinesq approximation, the flow structure is dependent on three non-dimensional parameters: a Rayleigh number R based on the height of the cavity and the temperature difference across the end walls, the Prandtl number σ of the fluid, and the aspect ratio L (length/height).

For cavities of different aspect ratio, Rayleigh number and Prandtl number, extensive numerical results have been obtained by researchers during the past twenty-five years. Elder (1966) obtained a numerical solution for a rectangular enclosure. Quon (1972) carried out finite difference computations for convection in a square cavity for a variety of dynamical boundary conditions, Rayleigh numbers and Prandtl numbers. Cormack, Leal and Seinfeld (1974) obtained numerical solutions in shallow cavities for a variety of Rayleigh numbers while de Vahl Davis and Mallinson (1975) studied the stability and transition of tall- cavity flows numerically. Comparisons of numerical results with experiment for natural convection in an air-filled cavity were made by Jones (1976) and de Vahl Davis and Jones (1983) described a comparative numerical study of convection flows in a square cavity .More detailed numerical studies of cavity flows have been carried out by de Vahl Davis (1968), Vest and Arpaci (1969), Seki (1978), Bejan and Tien (1978) and Lee (1981), while Shiralkar, Gadgil and Tien (1981) investigated numerically the high Rayleigh number regime. For tall slot flows numerical results have been obtained by Lee and Korpela (1983). Drummond and Korpela (1987) have also discussed numerical results for a shallow cavity with a variety of Rayleigh numbers and Prandtl numbers and further numerical studies have been carried out by Haldenwang and Labrosse (1986) , Gaskell and Wright (1987) and Winters (1988).

Theoretical studies concerning the various flow regimes in square and moderate aspect ratio cavities have been carried out by several researchers. The heat transfer in rectangular geometries was studied by Batchelor (1954) in the context of problems related to cavities used in building insulation. He examined different flow regimes which arise depending on the values of R and L. For small values of R, heat transfer was found to be predominantly by conduction.For tall cavities ($L \rightarrow 0$) this results in a linear temperature distribution between the two vertical walls with a cubic vertical velocity profile and no transverse flow except near the two ends. The fully developed vertical flow between infinite, parallel, vertical, isothermal plates was also studied by Ostrach (1952). Batchelor (1954) also proposed a possible solution structure for large Rayleigh numbers ($R \rightarrow \infty$ with L finite) but this was later corrected by Gill (1966) who derived an approximate solution for the heat transfer across the cavity by utilizing boundary layer techniques. The latter solution which consists of vertical boundary layers that entrain and detrain fluid from a convectively-dominated, vertically-stratified core,was restricted to infinite Prandtl numbers. Many aspects of the high Rayleigh number structure, including its form for finite Prandtl numbers and the structure of boundary layers near the horizontal walls (Blythe, Daniels and Simpkins 1983) remain undetermined.

For a shallow cavity ($L \rightarrow \infty$) and Rayleigh numbers $R \ll L$ the flow is again dominated by conduction and consists of a Hadley cell driven by the constant horizontal temperature gradient set up between the end walls. Cormack, Leal and Imberger (1974) predicted that the flow consists of two distinct parts: a parallel flow in the core region which extends for most of the length of the cavity and a second, non-parallel flow near the ends. Non-linear convective effects first become significant at the ends of the cavity where the flow is turned when $R_1 = \frac{R}{L} = O(1)$. Hart (1972) found that for small σ the Hadley cell is susceptible to a variety of instabilities. For Rayleigh numbers greater than some critical value $R_1 = R_{1c}(\sigma)$ the parallel core flow is destroyed and replaced by stationary multiple cells (Daniels, Blythe and Simpkins 1987). These transverse rolls are actually an integral part of

the steady-state solution in the cavity, unlike the longitudinal and time-dependent instabilities which also exist. Their existence was confirmed by numerical simulations of the end-zone flow at low Prandtl numbers by Hart (1983). During recent years, new work has focused on the nonlinear end-zone structure in cases where the multiple-cell instability is avoided. Then, as the Rayleigh number increases, the extent of the end-zones increases and as $R_1 \rightarrow \infty$ a complicated asymptotic structure develops. Certain key features of this structure were established by Daniels, Blythe and Simpkins (1987a) for the case where the horizotal walls of the cavity are perfectly insulated. In the end zone near the cold wall the structure involves the formation of a thermally- driven vertical boundary layer at the wall which entrains fluid and conveys it to the bottom corner of cavity where it is expelled into the core in the form of a horizontal wall jet studied by Daniels and Gargaro (1992a). As the jet diffuses there is a second stage of evolution where both buoyancy and the effect of an inviscid recirculation in the main part of the end zone come into play (Daniels and Gargaro 1992b). The limiting boundary-layer structures that develop are of fundamental importance because an understanding of these is needed before being able to proceed to the next regime where $R \gg L$. For the case where the horizontal walls of the cavity are perfectly conducting, certain properties of the end-zone solution for $R_1 = O(1)$ have been discussed by Gargaro (1991) but here little analytical progress has been made in identifying the limiting structure of the solution as $R_1 \rightarrow \infty$. Both of the above problems are typical of a wide class of 'end-zone' problems where full solutions of the governing equations and boundary conditions require a numerical approach. The main aim of the present work is to develop a computational method of solution for such problems and to obtain results which can be compared with asymptotic predictions. A combined numerical and analytical approach of this type is essential in identifying the correct solution at large Rayleigh numbers.

The shallow cavity end zone problem with adiabatic or conducting boundaries on the top and bottom requires the solution of the full nonlinear Oberbeck-Boussinesq

system (1.1.6)-(1.1.8), with R replaced by R_1, in a semi-infinite domain $x \geq 0$, $0 \leq z \leq 1$. Assuming the cold end wall to be located as $x = 0$, the relevant boundary conditions on the three rigid walls of the end zone can be expressed in non-dimensional form as

$$\psi = \frac{\partial \psi}{\partial z} = 0, \quad z = 0, 1 \tag{1.1.18}$$

$$\psi = \frac{\partial \psi}{\partial x} = 0, \quad x = 0 \tag{1.1.19}$$

$$\frac{\partial T}{\partial z} = 0 \quad z = 0, 1 \quad \text{insulating case,} \tag{1.1.20}$$

$$T = x \quad z = 0, 1 \quad , \quad \text{conducting case.} \tag{1.1.21}$$

where , for a steady-state solution, matching with the core flow requires

$$\left.\begin{aligned} \psi &\rightarrow R_1 F(z) \\ T &\sim x + c + R_1 G(z) \end{aligned}\right\} \quad (x \rightarrow \infty) \tag{1.1.22}$$

where

$$F(z) = \frac{1}{24} z^2 (1 - z)^2 \tag{1.1.23}$$

and for the conducting case $c = 0$ and

$$G(z) = \frac{1}{120} z^5 - \frac{1}{48} z^4 + \frac{1}{72} z^3 - \frac{1}{720} z \tag{1.1.24}$$

and for the insulating case c is an unknown constant and

$$G(z) = \frac{1}{120} z^5 - \frac{1}{48} z^4 + \frac{1}{72} z^3 - \frac{1}{1440}. \tag{1.1.25}$$

For a steady-state solution, separate consideration of the flow near the hot end wall can be avoided by appealing to the centrosymmetry of the flow (Gill 1966). One advantage associated with the end-zone problem is that it involves only two parameters R_1 and σ, as opposed to the full cavity problem which also involves the aspect ratio. The outer boundary condition (1.1.22) in the semi-infinite domain is a novel feature of the numerical problem previously investigated in detail by Daniels, Blythe and Simpkins (1987) using an eigenvalue analysis.

For sufficiently small aspect ratio ($L \rightarrow 0$), equivalent to a tall cavity, the flow is dominated by conduction and a linear temperature field drives a vertical two-way

flow which must be turned at each end of the cavity . The resulting system of equations is linear if $A \ll 1$, where A is the Rayleigh number based on the cavity width, and the domain can be subdivided into a core and two end regions in a similar way to the structure for a shallow cavity first proposed by Cormack, Leal and Imberger (1974). The flow in the end zones becomes nonlinear when $A = O(1)$ and the relevant end-zone problem and certain features of its solution have been set out by Daniels (1985). Again the flow is subject to instability either of a time-dependent type or in the form of stationary convection forced throughout the slot when the Rayleigh number reaches a critical value $A_c(\sigma)$. Unlike the shallow cavity, multi-cellular convection is possible for any finite Prandtl number, although at infinite Prandtl number $A_c \rightarrow \infty$ and instability is avoided. In that case it is possible to follow the evolution of the flow into the so-called 'convective' regime first identified experimentally by Elder (1965). This evolution is discussed by Daniels (1985) and at infinite Prandtl number the core flow of the convective regime where $A = O(L^{-1})$ can be modelled by a vertical boundary-layer system. Solutions of this are described by Daniels (1987) and lead to a criterion for stationary instability of the convective flow at a critical value of AL, consistent with Elder's experimental observations of the onset of stationary multi-cell convection in high Prandtl number oils. Further theoretical work has discussed possible horizontal boundary-layer structures (Daniels 1987a) and has identified a position of minimum heat transfer (Daniels 1990), again at a critical value of AL.

As stated earlier, at finite Prandtl numbers, multi-cell convection occurs in the conductive regime when $A \geq A_c(\sigma)$, values of $A_c(\sigma)$ having been obtained by Vest and Arpaci (1969) for a range of Prandtl numbers. Critical values of A for the onset of time-dependent instability have been discussed by Korpela, Gozum and Baxi (1973) and there are also related stability analyses incorporating the convective regime by Birikh (1972) , Gill and Kirkham (1970), Mizushima and Gotoh (1983) and Bergholz (1978). Hart (1971) has analysed flow stability in slots inclined at various angles to the vertical both theoretically and experimentally and has also

computed the energy distribution of perturbation quantities to determine the source of instability.

Although there is much numerical work describing full numerical simulations of vertical slot flow, such as that by Lee and Korpela (1983), the nonlinear problem discussed by Daniels (1985) in which the full Oberbeck-Boussinesq equations must be solved subject to matching with the conductive core solution has not previously been studied numerically. For the bottom end zone and in suitable non-dimensional variables, the problem is to solve the equations (1.1.6)-(1.1.8), in which R is replaced by A, in a semi-infinite domain $0 \leq x \leq 1$, $z \geq 0$ subject to boundary conditions on the three rigid walls of the cavity given by

$$\psi = \frac{\partial \psi}{\partial z} = 0, \quad z = 0, \tag{1.1.26}$$

$$\psi = \frac{\partial \psi}{\partial x} = 0 \quad x = 0,\ 1, \tag{1.1.27}$$

$$T = 0, \quad x = 0, \tag{1.1.28}$$

$$T = 1, \quad x = 1, \tag{1.1.29}$$

with

$$\frac{\partial T}{\partial z} = 0, \quad (z = 0), \tag{1.1.30}$$

for the case of an adiabatic lower wall or

$$T = x \quad , \quad z = 0, \tag{1.1.31}$$

for the case of a conducting lower wall, and subject to matching with the core solution

$$\left.\begin{aligned} \psi &\to AF(x) \\ T &\to x \end{aligned}\right\} \quad (z \to \infty), \tag{1.1.32}$$

where

$$F(x) = \frac{x^2}{24}(1-x)^2.$$

Again the end zone problem involves just two non-dimensional parameters, the Rayleigh number, A, and the Prandtl number, σ. In general a numerical solution is necessary.

With the development of computer science and numerical analysis , a number of very powerful numerical methods have been devised for solving fluid dynamical problems and indeed the whole development of numerical methods for approximating differential equations has always been strongly influenced and motivated by their application to the equations of fluid dynamics. Not only the work of Von Neumann (1950) but also that of Courant (1928), Richardson (1927), Southwell (1940, 1956) and many more recent contributors bears ample testimony to this fact. Increasingly, however, there has been a trend towards the development of methods specifically for fluid dynamics, and the most widely used methods are those based on either finite differences or finite elements . The relevant aspects of numerical analysis involved in such methods are discussed by Froberg (1969), Keller (1970), Dahlquist, Bjorck and Anderson (1974), Ames (1977) , Smith (1978) and Froberg (1985). An introduction to computational fluid mechanics is given by Chow (1979) and Roache (1976) in relation to finite difference methods, and by Gullagher, Oden, Taylor and Zienkiewicz (1975) and Chung (1978) in relation to finite element methods. More recent developments of numerical methods for fluid dynamics have been discussed by Morton and Baines (1982). Boundary layer computations are described by Patankar and Spalding (1970) and Bradshaw, Cebeci and Whitelay (1981). An early detailed account of a finite difference computer program for calculating recirculatory two-dimensional flows is given by Gosman , Pun, Runchal, Spalding and Wolfshtein (1969) and some useful notes on methods of computational convection may be found in Patankar (1980).

With the development of the finite element method, numerical results for natural convection in a rectangular cavity have been obtained by a number of researchers using this effective technique. Upson, Gresho and Lee (1980), used the finite element method with Newton-Raphson iteration to model the convective flow in a square cavity and the same method was also used by Winters (1983,1988). Finite element methods, originally developed for structural analysis, are being used increasingly in fluid mechanics and convection. Although more accurate for a given discretization,

they are also more elaborate than finite difference methods, and are particularly suited to problems involving irregular geometry. Finite difference methods require relatively little algebra to set up for a problem with regular boundaries, and these methods are widely used in convection. In general, finite difference and finite element methods are still widely used and for both methods the accuracy of solutions can be improved by using finer grids. Here an efficient finite difference method is used for solving the end-zone convection problems discussed earlier.

1.2 Research Plan

Although this thesis focuses on the solution of the various end-zone problems by numerical techniques , some new analysis is also presented for the structure of time-dependent flows in shallow cavities. Numerical codes based on the DuFort-Frankel method and a multigrid algorithm have been designed and have led to successful attacks on these problems. Numerical results applicable to both shallow and tall cavities with different boundary conditions have been obtained and compared, where appropriate, with theoretical predictions and the results of experiments.

Chapter 2 describes an efficient numerical scheme for thermal convection in a laterally heated cavity and the DuFort-Frankel-Multigrid method is set out in detail. Numerical results for square cavity flow with insulated horizontal boundaries are presented, which show good agreement with results given by previous investigators. Theoretical predictions of the corner structure are also obtained, which show consistency with the computational solution. Finally a comprison is made with numerical results obtained by use of the Harwell Flow3D code.

Chapters 3 and 4 focus on thermal convection in a tall laterally heated cavity with both conducting and adiabatic horizontal boundaries . Numerical results for the relevant end-zone problems are obtained for a range of Rayleigh numbers from $A = 500$ to $A = 70000$ and for different Prandtl numbers. The flow patterns

show that the parallel flow in the core region is destroyed at $A_c \approx 7880\sigma$, in good agreement with the analysis carried out by Daniels (1985) and with the stability analysis of Vest and Arpaci (1969), Korpela, Gozum and Baxi (1973) and Bergholz (1978).

Chapters 5 and 6 are concerned with thermal convection in a shallow laterally heated cavity with conducting and insulating horizontal boundaries respectively. Numerical solutions of the end-zone problems are found over a range of Rayleigh numbers $R = 100 \sim 20000$ and Prandtl numbers $\sigma = 0.05 \sim 6.983$. In the insulated case, a comparison is made with theoretical predictions for the boundary-layer structure at high values of the Rayleigh number. The numerical computation of the parameter c in (1.1.22) is compared with theoretical predictions of c for low Rayleigh numbers by Cormack Leal and Imberger (1974) and for high Rayleigh numbers by Daniels, Blythe and Simpkins (1987a). For low Prandtl numbers $\sigma \leq 0.12$, the parallel core flow is destroyed at Rayleigh numbers $R_1 > R_{1c}(\sigma)$, and here the numerical results are compared with the analysis of Hart (1971) .

Chapter 7 contains new theoretical and numerical solutions for time-dependent thermally-driven shallow cavity flows with insulated boundaries. During recent years, much work has been done on steady state flow in shallow cavities and more work on related time dependent flows needs to be considered. Patterson and Imberger (1980) carried out one of the first investigations of the transient flow in a rectangular cavity ,in which a theoretical and computational investigation identified many of the important length, time and velocity scales of the flow. This allowed a classification of the possible flows into regimes determined by the parameters of the flow, the Rayleigh number, Prandtl number and aspect ratio. A number of features of the flow were identified, and in particular the approach to steady state was oscillatory under certain conditions. Ivey (1984) carried out a series of experiments designed to test for the existence of the osillatory behaviour , and evidence of oscillations was found . Schladow,Patterson and Street (1989) performed more detailed numerical simulations of the Ivey experiment. Their results showed the oscillatory

behaviour in the net Nusselt number, and supported the conclusions of Patterson and Imberger (1980). The first experimental evidence that confirmed the presence of the oscillatory behaviour and many other aspects of the time-dependent flow was due to Patterson and Armfield (1990). In contrast, there has been comparatively little work on the time-evolution of flows in shallow cavities where $L \gg 1$. The present study investigates such time dependent flows theoretically and numerically for different initial conditions. The numerical work makes use of the DuFort-Frankel Multigrid code and for certain initial configurations the end-zone equations must be solved subject to

$$\left.\begin{aligned} \psi &\to R_1 \tilde{F}(z,t) \\ T &\sim x + R_1 \tilde{G}(z,t) \end{aligned}\right\} \quad (x \to \infty) \tag{1.2.1}$$

in place of (1.1.22). Here $\tilde{F}(z,t)$ and $\tilde{G}(z,t)$ are functions of z and t determined by an analytical solution of the main core region. Attention is focused on a family of initial configurations for which the fluid is static and for which there exists a linear temperature distribution along the length of the cavity. In gereral, two main stages of evolution are identified, an initial stage $t = O(1)$ where the main core flow adjusts to the thermal forcing and a second, much longer stage $t = O(L^2)$ where the motion generated within each end zone acts to modify the thermal balance across the core. A final steady state is achieved consistent with the computations carried out in Chapter 6.

Chapter 2

Thermal Convection in a Laterally Heated Cavity

2.1 Introduction

In this chapter a numerical method for solving the cavity convection problem is presented which allows the flow structure and heat transfer across the cavity to be determined for given values of the aspect ratio, Prandtl number and Rayleigh number. The numerical algorithm is based on a finite difference representation of the governing equations and boundary conditions which adequately models the flow in a finite cavity. Numerical results are presented which show good agreement with previous work. Comparisons are made of the numerical solution with theoretical predictions of the flow near the corners of the cavity.

Section 2.2 describes a mathematical formulation for two-dimensional cavity flow with insulated boundaries or conducting boundaries. The governing equations are dominated by three important parameters , the Rayleigh number R, Prandtl number σ, and aspect ratio L. Section 2.3 describes a fast and efficient numerical method of solution based on a Dufort-Frankel-Multigrid algorithm. The overall scheme of computation is given and, in Section 2.4, numerical results are presented for a square

cavity with insulated boundaries . Comparison is made with analytical predictions of the behaviour near each corner and with results obtained by alternative methods. The accuracy and convergence of the scheme is also discussed.

2.2 Formulation

A closed rectangular cavity of length l and height h is considered in which two-dimensional motions are generated by maintaining the vertical end walls at different fixed temperatures T_0 and $T_0 + \Delta T$. The appropriate governing equations, subject to the Boussinesq approximation, are given in (1.1.1)-(1.1.4) and consist of the continuity equation

$$\frac{\partial u^*}{\partial x^*} + \frac{\partial w^*}{\partial z^*} = 0, \tag{2.2.1}$$

the Navier-Stokes equations,

$$\frac{\partial u^*}{\partial t^*} + u^*\frac{\partial u^*}{\partial x^*} + w^*\frac{\partial u^*}{\partial z^*} = -\frac{1}{\rho_0}\frac{\partial p^*}{\partial x^*} + \nu\nabla^2 u^*, \tag{2.2.2}$$

$$\frac{\partial w^*}{\partial t^*} + u^*\frac{\partial w^*}{\partial x^*} + w^*\frac{\partial w^*}{\partial z^*} = -\frac{1}{\rho_0}\frac{\partial p^*}{\partial z^*} + \nu\nabla^2 w^* + g\beta(T^* - T_0), \tag{2.2.3}$$

and the heat equation

$$\frac{\partial T^*}{\partial t^*} + u^*\frac{\partial T^*}{\partial x^*} + w^*\frac{\partial T^*}{\partial z^*} = \kappa\nabla^2 T^*. \tag{2.2.4}$$

The boundary conditions on the cavity walls are

$$u^* = w^* = 0 \quad \text{on all boundaries}, \tag{2.2.5}$$

with

$$\frac{\partial T^*}{\partial z^*} = 0 \quad \text{on} \quad z^* = 0, h, \tag{2.2.6}$$

for insulated horizontal boundaries and

$$T^* = T_0 + \Delta T x^*/l \quad \text{on} \quad z^* = 0, h, \tag{2.2.7}$$

for conducting horizontal boundaries. On the vertical walls

$$T^* = T_0 \quad \text{on} \quad x^* = 0, \quad T^* = T_0 + \Delta T \quad \text{on} \quad x^* = l. \tag{2.2.8}$$

Here T^* is the temperature, p^* is the pressure, u^* and w^* are the horizontal and vertical velocity components and (x^*, z^*) are Cartesian co-ordinates such that the acceleration due to gravity, g, is in the negative z^* direction. ρ_0 is the density at temperature T_0 and ν, κ and β are the kinematic viscosity, thermal diffusivity and coefficient of thermal expansion respectively, assumed to be constant.

By introducing the transformations

$$x^* = hx, \quad z^* = hz, \quad u^* = \frac{\kappa}{h}u, \quad w^* = \frac{\kappa}{h}w, \quad T^* = T_0 + \Delta TT, \quad t^* = \frac{h^2}{\kappa}t \tag{2.2.9}$$

and by defining a stream function ψ such that

$$u = \frac{\partial \psi}{\partial z}, \quad w = -\frac{\partial \psi}{\partial x} \tag{2.2.10}$$

the basic equations may be written in non-dimensional form as

$$\sigma^{-1}\left(\frac{\partial \omega}{\partial t} + J(\omega, \psi)\right) = \nabla^2 \omega + R\frac{\partial T}{\partial x}, \tag{2.2.11}$$

$$\nabla^2 \psi = -\omega, \tag{2.2.12}$$

$$\frac{\partial T}{\partial t} + J(T, \psi) = \nabla^2 T, \tag{2.2.13}$$

where

$$\sigma = \frac{\nu}{\kappa} \tag{2.2.14}$$

is the Prandtl number and

$$R = \frac{g\beta \Delta T h^3}{\kappa \nu} \tag{2.2.15}$$

is the Rayleigh number. Here the pressure has been eliminated and

$$\omega = \frac{\partial w}{\partial x} - \frac{\partial u}{\partial z} \tag{2.2.16}$$

is the vorticity, with the two Jacobians given by

$$J(\omega,\psi)=\frac{\partial\omega}{\partial x}\frac{\partial\psi}{\partial z}-\frac{\partial\omega}{\partial z}\frac{\partial\psi}{\partial x},\quad J(T,\psi)=\frac{\partial T}{\partial x}\frac{\partial\psi}{\partial z}-\frac{\partial T}{\partial z}\frac{\partial\psi}{\partial x}. \tag{2.2.17}$$

The boundary conditions on the cavity walls are

$$\psi=\frac{\partial\psi}{\partial x}=0,\quad x=0,\,L;\quad \psi=\frac{\partial\psi}{\partial z}=0,\quad z=0,\,1 \tag{2.2.18}$$

$$T=0,\quad x=0;\quad T=1,\quad x=L \tag{2.2.19}$$

with

$$\frac{\partial T}{\partial z}=0\quad \text{on}\ \ z=0,\,1 \tag{2.2.20}$$

for insulated walls, or

$$T=\frac{x}{L}\quad \text{on}\ \ z=0,\,1 \tag{2.2.21}$$

for conducting walls, where

$$L=\frac{l}{h} \tag{2.2.22}$$

is the aspect ratio of the cavity. Figure 2.1 shows the flow domain.

2.3 Numerical Scheme

In order to solve the system (2.2.11)–(2.2.22) numerically, a finite difference method is considered. For evolution equations, Crank-Nicholson (Crank and Nicholson 1947) and Peaceman-Rachford (Peaceman and Rachford 1955) methods have been used extensively. The P-R method is an alternating direction implicit (ADI) method. Both methods have their advantages and disadvantages. They are unconditionally stable, so that a large time step can be used, but on the other hand, at each time step, a big discretized system of equations has to be solved either by a direct method such as Gaussian elimination or by an indirect (or iterative) method, such as Successive Over-Relaxation (Smith 1978). Thus, significant computational time is needed to solve the discretized systems at each time step. In recent years, another method called the Dufort-Frankel method, as outlined by Roache (1972), has

been used frequently. Like the Crank-Nicholson and Peaceman-Rachford methods, it has second-order accuracy but since it is an explicit method, it must meet the Courant condition to achieve numerical stability. Although the size of the time step is restricted by this condition, it is still a very effective and fast method.

For elliptic equations, a five-point scheme can be adopted in which centred differences are used to approximate the original partial differential equation. The resulting equations are solved by using an iteration which is accelerated by a Multilevel method (Brandt 1977). This method has been seen to give fast convergence.

Here the Dufort-Frankel method is used to solve the evolution equations (2.2.12), (2.2.14), and the Multilevel method to solve the Poisson equation (2.2.13). Although the primary interest here is the steady-state solution for which other numerical iterative methods might be adopted, the time evolution of the flow will be studied in Chapter 7 and the proposed method has the advantage of being applicable there also.

For the given domain $0 \leq x \leq L$, $0 \leq z \leq 1$ we use Δx, Δz as the space steps and Δt as the time step, as shown in Figures 2.2 and 2.3. We now consider the finite difference algorithm for each equation.

2.3.1 Energy Equation

For the energy equation and boundary conditions

$$\left.\begin{aligned} &\frac{\partial T}{\partial t} + J(T, \psi) = \nabla^2 T \\ &T = 0,\ x = 0; \quad T = 1,\ x = L \\ &\frac{\partial T}{\partial z} = 0,\ z = 0,\ 1; \quad \text{or } T = \frac{x}{L},\ z = 0,\ 1 \end{aligned}\right\} \tag{2.3.1}$$

the Dufort-Frankel method is used with

$$t = k\Delta t \quad (k = 0, 1, 2, \cdots),$$

$$x = i\Delta x \quad (i = 0, 1, 2, \cdots, N_x),$$

$$z = j\Delta z \quad (j = 0, 1, 2, \cdots, N_z).$$

We denote

$$T(x, z, t) = T^k_{i,j}, \quad \psi(x, z, t) = \psi^k_{i,j}$$

and use

$$\frac{\partial T^k_{i,j}}{\partial t} \approx \frac{(T^{k+1}_{i,j} - T^{k-1}_{i,j})}{2\Delta t}$$

and

$$\nabla^2 T^k_{i,j} \approx \frac{T^k_{i+1,j} + T^k_{i-1,j} - T^{k+1}_{i,j} - T^{k-1}_{i,j}}{(\Delta x)^2} + \frac{T^k_{i,j+1} + T^k_{i,j-1} - T^{k+1}_{i,j} - T^{k-1}_{i,j}}{(\Delta z)^2}.$$

Substitution of these approximation operators into (2.3.1) yields

$$\begin{aligned} \frac{T^{k+1}_{i,j} - T^{k-1}_{i,j}}{2\Delta t} + J(T^k_{i,j}, \psi^k_{i,j}) &= \frac{(T^k_{i+1,j} + T^k_{i-1,j} - T^{k+1}_{i,j} - T^{k-1}_{i,j})}{(\Delta x)^2} \\ &\quad + \frac{(T^k_{i,j+1} + T^k_{i,j-1} - T^{k+1}_{i,j} - T^{k-1}_{i,j})}{(\Delta z)^2} \end{aligned} \tag{2.3.2}$$

and rearrangement of (2.3.2) gives an explicit equation for $T^{k+1}_{i,j}$:

$$T^{k+1}_{i,j} = \frac{\frac{\Delta t(T^k_{i+1,j} + T^k_{i-1,j})}{(\Delta x)^2} + \frac{\Delta t(T^k_{i,j+1} + T^k_{i,j-1})}{(\Delta z)^2} - \Delta t J(T^k_{i,j}, \psi^k_{i,j}) + x_1 T^{k-1}_{i,j}}{x_2}, \tag{2.3.3}$$

where

$$x_1 = \frac{1}{2} - \frac{\Delta t}{(\Delta x)^2} - \frac{\Delta t}{(\Delta z)^2},$$

$$x_2 = \frac{1}{2} + \frac{\Delta t}{(\Delta x)^2} + \frac{\Delta t}{(\Delta z)^2}.$$

For the nonlinear term $J(T, \psi)$, Arakawa's (1966) scheme is used. The Jacobian

$$J(T, \psi) = \frac{\partial T}{\partial x}\frac{\partial \psi}{\partial z} - \frac{\partial T}{\partial z}\frac{\partial \psi}{\partial x}$$

can be rewritten in several ways as follows:

$$\begin{aligned} J(T,\psi) &= J_1 = -\hat{j}\cdot(\Delta\times(T\Delta\psi)), \\ J(T,\psi) &= J_2 = -\hat{j}\cdot(\Delta T\times\Delta\psi), \\ J(T,\psi) &= J_3 = \hat{j}\cdot(\Delta\times(\psi\Delta T)), \end{aligned}$$

where $\Delta = \hat{i}\frac{\partial}{\partial x}+\hat{k}\frac{\partial}{\partial z}$ is the 2-D gradient operator, and $\hat{i}$, $\hat{j}$, $\hat{k}$ are unit vectors. These expressions are the same in the differential form, but are different in finite difference form. Arakawa's method is to set

$$J(T,\,\psi) = \frac{J_1+J_2+J_3}{3},$$

where

$$\begin{aligned} J_1 &= -\hat{j}\cdot(\Delta\times(T\Delta\psi)) \\ &= \frac{\partial(T\frac{\partial\psi}{\partial z})}{\partial x}-\frac{\partial(T\frac{\partial\psi}{\partial x})}{\partial z} \\ &\approx \frac{1}{4\Delta x\Delta z}[T_{i+1,j}(\psi_{i+1,j+1}+\psi_{i+1,j-1})-T_{i-1,j}(\psi_{i-1,j+1}-\psi_{i-1,j-1}) \\ &\quad -T_{i,j+1}(\psi_{i+1,j+1}-\psi_{i-1,j+1})+T_{i,j-1}(\psi_{i+1,j-1}-\psi_{i-1,j-1})], \\ J_2 &= -\hat{j}\cdot(\Delta T\times\Delta\psi) \\ &= \frac{\partial T}{\partial x}\frac{\partial\psi}{\partial z}-\frac{\partial T}{\partial z}\frac{\partial\psi}{\partial x} \\ &\approx \frac{1}{4\Delta x\Delta z}[(T_{i+1,j}-T_{i-1,j})(\psi_{i,j+1}-\psi_{i,j-1})-(T_{i,j+1}-T_{i,j-1})(\psi_{i+1,j}-\psi_{i-1,j})], \\ J_3 &= \hat{j}\cdot(\Delta\times(\psi\Delta T)) \end{aligned}$$

$$= -\frac{\partial(\psi\frac{\partial T}{\partial z})}{\partial x} + \frac{\partial(\psi\frac{\partial T}{\partial x})}{\partial z}$$

$$\approx -\frac{1}{4\Delta x\Delta z}[\psi_{i+1,j}(T_{i+1,j+1} - T_{i+1,j-1}) - \psi_{i-1,j}(T_{i-1,j+1} - T_{i-1,j-1})$$

$$-\psi_{i,j+1}(T_{i+1,j+1} - T_{i-1,j+1}) + \psi_{i,j-1}(T_{i+1,j-1} - T_{i-1,j-1})].$$

Thus, finally, the Jacobian can be expressed as

$$\begin{aligned} J(T_{i,j},\psi_{i,j}) = \frac{1}{12\Delta x\Delta z}\{&(T_{i+1,j} - T_{i-1,j})(\psi_{i,j+1} - \psi_{i,j-1}) \\ &-(T_{i,j+1} - T_{i,j-1})(\psi_{i+1,j} - \psi_{i-1,j}) \\ &+T_{i+1,j}(\psi_{i+1,j+1} - \psi_{i+1,j-1}) - T_{i-1,j}(\psi_{i-1,j+1} - \psi_{i-1,j-1}) \\ &-T_{i,j+1}(\psi_{i+1,j+1} - \psi_{i-1,j+1}) + T_{i,j-1}(\psi_{i+1,j-1} - \psi_{i-1,j-1}) \\ &-\psi_{i+1,j}(T_{i+1,j+1} - T_{i+1,j-1}) + \psi_{i-1,j}(T_{i-1,j+1} - T_{i-1,j-1}) \\ &+\psi_{i,j+1}(T_{i+1,j+1} - T_{i-1,j+1}) - \psi_{i,j-1}(T_{i+1,j-1} - T_{i-1,j-1})\}. \end{aligned} \tag{2.3.4}$$

There are several different ways to approximate the boundary conditions for T. Here we give two different formulae which are conditionally stable and explicit. On the vertical walls we simply have

$$T_{0,j} = 0, \qquad T_{N_x,j} = 1, \qquad 0 \le j \le N_z.$$

For insulated horizontal boundaries we must satisfy

$$\left.\frac{\partial T}{\partial z}\right|_{z=0,1} = 0.$$

Using central differences, we have

$$\frac{1}{\Delta z}\left(T^k_{i,j+1} - T^k_{i,j-1}\right) = 0$$

so that

$$T^k_{i,j+1} = T^k_{i,j-1} \quad \text{for} \quad j = 0 \quad \text{and} \quad j = N_z. \tag{2.3.5}$$

In order to obtain expressions for T along the horizontal boundaries, we note that the energy equation has the form

$$\frac{\partial T}{\partial t} = \frac{\partial^2 T}{\partial x^2} + \frac{\partial^2 T}{\partial z^2} \text{ on } z = 0 \text{ and } z = 1 \tag{2.3.6}$$

and use the Dufort-Frankel scheme with

$$\frac{\partial}{\partial t} T^k_{i,j} \approx \frac{1}{2\Delta t}\left(T^{k+1}_{i,j} - T^{k-1}_{i,j}\right)$$

and

$$\begin{aligned} \nabla^2(T^k_{i,j}) \approx\ & \frac{1}{(\Delta x)^2}[T^k_{i+1,j} + T^k_{i-1,j} - T^{k+1}_{i,j} - T^{k-1}_{i,j}] \\ & + \frac{1}{(\Delta z)^2}[T^k_{i,j+1} + T^k_{i,j-1} - T^{k+1}_{i,j} - T^{k-1}_{i,j}]. \end{aligned}$$

Substituting these operators into (2.3.6) and using (2.3.5) we have second-order accurate formulae

$$T^{k+1}_{i,0} = \frac{\frac{\Delta t}{(\Delta x)^2}[T^k_{i+1,0} + T^k_{i-1,0}] + \frac{\Delta t}{(\Delta z)^2} 2T^k_{i,1} + x_1 T^{k-1}_{i,0}}{x_2}, \tag{2.3.7}$$

$$T^{k+1}_{i,N_z} = \frac{\frac{\Delta t}{(\Delta x)^2}[T^k_{i+1,N_z} + T^k_{i-1,N_z}] + \frac{\Delta t}{(\Delta z)^2} 2T^k_{i,N_z-1} + x_1 T^{k-1}_{i,N_z}}{x_2}, \tag{2.3.8}$$

$$i = 1, 2, ..., N_x - 1,$$

for the determination of the boundary values of the temperature.

An alternative method of obtaining boundary values of T is to set

$$\frac{\partial}{\partial t} T^k_{i,j} \approx \frac{T^{k+1}_{i,j} - T^k_{i,j}}{\Delta t},$$

$$\nabla^2(T^k_{i,j}) \approx \frac{1}{(\Delta x)^2}[T^k_{i+1,j} - 2T^k_{i,j} + T^k_{i-1,j}] + \frac{1}{(\Delta z)^2}[T^k_{i,j+1} - 2T^k_{i,j} + T^k_{i,j-1}].$$

Substituting these expressions into the energy equation and using (2.3.5), we obtain an explicit scheme which is conditionally stable and has first order accuracy:

$$T^{k+1}_{i,0} = \frac{\Delta t}{(\Delta x)^2}(T^k_{i+1,0} - 2T^k_{i,0} + T^k_{i-1,0}) + \frac{\Delta t}{(\Delta z)^2}(2T^k_{i,1} - 2T^k_{i,0}) + T^k_{i,0}, \qquad (2.3.9)$$

$$i = 1, 2, ..., N_x - 1,$$

$$T^{k+1}_{i,N_z} = \frac{\Delta t}{(\Delta x)^2}(T^k_{i+1,N_z} - 2T^k_{i,N_z} + T^k_{i-1,N_z}) + \frac{\Delta t}{(\Delta z)^2}(2T^k_{i,N_z-1} - 2T^k_{i,N_z}) + T^k_{i,N_z}, \qquad (2.3.10)$$

$$i = 1, 2, ..., N_x - 1.$$

In the conducting case, we simply have

$$T^{k+1}_{i,0} = i\Delta x/L, \quad T^{k+1}_{i,N_z} = i\Delta x/L, \quad 0 \le i \le N_x. \qquad (2.3.11)$$

From (2.3.3), (2.3.4) and either (2.3.7)-(2.3.8) or (2.3.9)-(2.3.10) we can obtain the numerical solution for the temperature in the whole region for the case of insulated walls; in the conduction case we use (2.3.3), (2.3.4) and (2.3.11). However, we should observe that the above schemes are three-layer schemes $(k+1, k, k-1)$, that is the computational procedure needs to use the values of the solution at two previous time levels. Therefore in order to use the schemes, the solutions for two initial time levels must be obtained first. The above schemes can then be used to obtain the values at the next time level, and so on. Usually the initial conditions in the flow field will determine the values at the first time level and the problem therefore reduces to obtaining the values at the second time level. The following method is adopted.

Set

$$\frac{\partial}{\partial t}T^2_{i,j} \approx \frac{T^2_{i,j} - T^1_{i,j}}{\Delta t},$$

$$\nabla^2(T^2_{i,j}) \approx \frac{T^2_{i+1,j} - 2T^2_{i,j} + T^2_{i-1,j}}{(\Delta x)^2} + \frac{T^2_{i,j+1} - 2T^2_{i,j} + T^2_{i,j-1}}{(\Delta z)^2}$$

and substitute these approximations into equation (2.3.1), giving

$$\frac{T^2_{i,j} - T^1_{i,j}}{\Delta t} + J(T^1_{i,j}, \psi^1_{i,j}) = \frac{T^2_{i+1,j} - 2T^2_{i,j} + T^2_{i-1,j}}{(\Delta x)^2} + \frac{T^2_{i,j+1} - 2T^2_{i,j} + T^2_{i,j-1}}{(\Delta z)^2}.$$

Thus

$$T^2_{i,j} = \frac{\frac{\Delta t}{(\Delta x)^2}(T^2_{i+1,j} + T^2_{i-1,j}) + \frac{\Delta t}{(\Delta z)^2}(T^2_{i,j+1} + T^2_{i,j-1}) - \Delta t J(T^1_{i,j}, \psi^1_{i,j}) + T^1_{i,j}}{x_3} \quad (2.3.12)$$

$$i = 1, 2, ..., N_x - 1, \quad j = 1, 2, ..., N_z - 1.$$

where

$$x_3 = 1 + \frac{2\Delta t}{(\Delta x)^2} + \frac{2\Delta t}{(\Delta z)^2}.$$

In the insulating case we can obtain the boundary values of T from

$$T^2_{i,0} = \frac{\frac{\Delta t}{(\Delta x)^2}(T^2_{i+1,0} - T^2_{i-1,0}) + \frac{\Delta t}{(\Delta z)^2}2T^2_{i,1} + T^1_{i,0}}{x_3}, \quad (2.3.13)$$

$$T^2_{i,N_z} = \frac{\frac{\Delta t}{(\Delta x)^2}(T^2_{i+1,N_z} - T^2_{i-1,N_z}) + \frac{\Delta t}{(\Delta z)^2}2T^2_{i,N_z-1} + T^1_{i,N_z}}{x_3},$$

$$i = 1, 2, ..., N_x - 1. \quad (2.3.14)$$

The above schemes (2.3.12) and (2.3.13)- (2.3.14) are unconditionally stable and have first-order accuracy in time and second-order accuracy in space. Since these schemes are implicit, Successive Over-Relaxation is used to solve the system of linear equations for T:

$$\tilde{T}^{2(m)}_{i,j} = \frac{\frac{\Delta t}{(\Delta x)^2}(T^{2(m-1)}_{i+1,j} + T^{2(m)}_{i-1,j}) + \frac{\Delta t}{(\Delta z)^2}(T^{2(m-1)}_{i,j+1} + T^{2(m)}_{i,j-1}) - \Delta t J(T^1_{i,j}, \psi^1_{i,j}) + T^1_{i,j}}{x_3},$$

(2.3.15)

$$\tilde{T}^{2(m)}_{i,0} = \frac{\frac{\Delta t}{(\Delta x)^2}(T^{2(m-1)}_{i+1,0} - T^{2(m)}_{i-1,0}) + \frac{\Delta t}{(\Delta z)^2} 2T^{2(m-1)}_{i,1} + T^{1}_{i,0}}{x_3}, \tag{2.3.16}$$

$$\tilde{T}^{2(m)}_{i,N_z} = \frac{\frac{\Delta t}{(\Delta x)^2}(T^{2(m-1)}_{i+1,N_z} - T^{2(m)}_{i-1,N_z}) + \frac{\Delta t}{(\Delta z)^2} 2T^{2(m)}_{i,N_z-1} + T^{1}_{i,N_z}}{x_3}, \tag{2.3.17}$$

$$T^{2(m)}_{i,j} = \lambda \tilde{T}^{2(m)}_{i,j} + (1-\lambda) T^{2(m-1)}_{i,j}, \tag{2.3.18}$$

$$T^{2(m)}_{i,0} = \lambda \tilde{T}^{2(m)}_{i,0} + (1-\lambda) T^{2(m-1)}_{i,0}, \tag{2.3.19}$$

$$T^{2(m)}_{i,N_z} = \lambda \tilde{T}^{2(m)}_{i,N_z} + (1-\lambda) T^{2(m-1)}_{i,N_z}, \tag{2.3.20}$$

$$i = 1, 2, ..., N_x - 1, \qquad j = 1, 2, ..., N_z - 1.$$

Here λ is the relaxation parameter whose optimum value was found to be about 1.2; m is the iteration index of the SOR and the iteration continues until

$$\max_{i,j} |T^{2(m+1)}_{i,j} - T^{2(m)}_{i,j}| < \epsilon_0,$$

where ϵ_0 is a very small positive number usually taken to be 10^{-6}.

Initial conditions determine the solution at the first time level, and then in the insulating case (2.3.12)-(2.3.20) the solution at the second time-level and thereafter (2.3.3), (2.3.4) and either (2.3.7)-(2.3.8) or (2.3.9)- (2.3.10) are used to obtain the solution for T at further time levels. The convergence criterion and numerical stability of the whole procedure will be discussed later.

2.3.2 Vorticity Equation

For the vorticity equation

$$\sigma^{-1}\left(\frac{\partial \omega}{\partial t} + J(\omega, \psi)\right) = \nabla^2 \omega + R\frac{\partial T}{\partial x}, \tag{2.3.21}$$

we use the same method as for the energy equation with

$$x = i\Delta x \qquad (i = 0, 1, 2, ..., N_x),$$
$$z = j\Delta z \qquad (j = 0, 1, 2, ..., N_z),$$
$$t = k\Delta t \qquad (k = 0, 1, 2, ...),$$

$$\omega(x,z,t) = \omega^k_{i,j}, \quad T(x,z,t) = T^k_{i,j}, \quad \psi(x,z,t) = \psi^k_{i,j},$$

$$\frac{\partial}{\partial t}(\omega^k_{i,j}) \approx \frac{1}{2\Delta t}(\omega^{k+1}_{i,j}, -\omega^{k-1}_{i,j}),$$

$$\nabla^2(\omega^k_{i,j}) \approx \frac{1}{(\Delta x)^2}[\omega^k_{i+1,j} + \omega^k_{i-1,j} - \omega^{k+1}_{i,j} - \omega^{k-1}_{i,j}]$$

$$+\frac{1}{(\Delta z)^2}[\omega^k_{i,j+1} + \omega^k_{i,j-1} - \omega^{k+1}_{i,j} - \omega^{k-1}_{i,j}],$$

and

$$\frac{\partial}{\partial x}(T^k_{i,j}) \approx \frac{1}{2\Delta x}(T^k_{i+1,j} - T^k_{i-1,j}).$$

Thus

$$\omega^{k+1}_{i,j} = \frac{\frac{\Delta t}{(\Delta x)^2}(\omega^k_{i+1,j} + \omega^k_{i-1,j}) + \frac{\Delta t}{(\Delta z)^2}(\omega^k_{i,j+1} + \omega^k_{i,j-1}) - \Delta t\sigma^{-1}J(\omega^k_{i,j}, \psi^k_{i,j})}{\bar{x}_2},$$

$$+\frac{\frac{\Delta t}{2\Delta x}R(T^k_{i+1,j} - T^k_{i-1,j}) + \bar{x}_1\omega^{k-1}_{i,j}}{\bar{x}_2} \tag{2.3.22}$$

where

$$\bar{x}_1 = \frac{1}{2\sigma} - \frac{\Delta t}{(\Delta x)^2} - \frac{\Delta t}{(\Delta z)^2},$$

$$\bar{x}_2 = \frac{1}{2\sigma} + \frac{\Delta t}{(\Delta x)^2} + \frac{\Delta t}{(\Delta z)^2}.$$

For the nonlinear term, we use Arakawa's scheme (1966)

$$
\begin{aligned}
J(\omega_{i,j},\psi_{i,j}) \;=\; & \frac{1}{12\Delta x\Delta z}\{(\omega_{i+1,j}-\omega_{i-1,j})(\psi_{i,j+1}-\psi_{i,j-1}) - \\
& (\omega_{i,j+1}-\omega_{i,j-1})(\psi_{i+1,j}-\psi_{i-1,j}) + \\
& \omega_{i+1,j}(\psi_{i+1,j+1}-\psi_{i+1,j-1}) - \omega_{i-1,j}(\psi_{i-1,j+1}-\psi_{i-1,j-1}) - \\
& \omega_{i,j+1}(\psi_{i+1,j+1}-\psi_{i-1,j+1}) + \omega_{i,j-1}(\psi_{i+1,j-1}-\psi_{i-1,j-1}) - \\
& \psi_{i+1,j}(\omega_{i+1,j+1}-\omega_{i+1,j-1}) + \psi_{i-1,j}(\omega_{i-1,j+1}-\omega_{i-1,j-1}) + \\
& \psi_{i,j+1}(\omega_{i+1,j+1}-\omega_{i-1,j+1}) - \psi_{i,j-1}(\omega_{i+1,j-1}-\omega_{i-1,j-1})\}\,.
\end{aligned}
\tag{2.3.23}
$$

Boundary values of the vorticity are obtained from a Taylor series expansion as follows. For points near $x = 0$, we have

$$
\psi(\Delta x,z) = \psi_{1,j} \approx \psi_{0,j} + \Delta x\frac{\partial\psi}{\partial x}\bigg|_{x=0} + \frac{(\Delta x)^2}{2!}\frac{\partial^2\psi}{\partial x^2}\bigg|_{x=0} + \frac{(\Delta x)^3}{3!}\frac{\partial^3\psi}{\partial x^3}\bigg|_{x=0}, \tag{2.3.24}
$$

$$
\psi(2\Delta x,z) = \psi_{2,j} \approx \psi_{0,j} + 2\Delta x\frac{\partial\psi}{\partial x}\bigg|_{x=0} + \frac{(2\Delta x)^2}{2!}\frac{\partial^2\psi}{\partial x^2}\bigg|_{x=0} + \frac{(2\Delta x)^3}{3!}\frac{\partial^3\psi}{\partial x^3}\bigg|_{x=0} \tag{2.3.25}
$$

and from the boundary conditions for ψ we know that

$$
\psi_{0,j} = \frac{\partial\psi}{\partial x}|_{x=0} = 0.
$$

Multiplying (2.3.24) by 8 and subtracting it from (2.3.25), we obtain

$$
\psi_{2,j} - \psi_{1,j} = -2(\Delta x)^2\,\frac{\partial^2\psi}{\partial x^2}\bigg|_{x=0}. \tag{2.3.26}
$$

In addition, we know that on the wall $x = 0$

$$
-\,\omega_{0,j} = \frac{\partial^2\psi}{\partial x^2}\bigg|_{x=0}, \tag{2.3.27}
$$

so that from (2.3.26)

$$
-\,\omega_{0,j} = \frac{1}{2(\Delta x)^2}(8\psi_{1,j} - \psi_{2,j}), \qquad j = 0,1,2,...,N_z. \tag{2.3.28}
$$

Similarly, we can obtain discretized forms for the other surfaces:

$$-\omega_{N_x,j} = \frac{1}{2(\Delta x)^2}(8\psi_{N_x-1,j} - \psi_{N_x-2,j}), \quad j = 0,1,2,...,N_z, \tag{2.3.29}$$

$$-\omega_{i,0} = \frac{1}{2(\Delta x)^2}(8\psi_{i,1} - \psi_{i,2}), \quad i = 0,1,2,...,N_x, \tag{2.3.30}$$

$$-\omega_{i,N_z} = \frac{1}{2(\Delta x)^2}(8\psi_{i,N_z-1} - \psi_{i,N_z-2}), \quad i = 0,1,2,...,N_x. \tag{2.3.31}$$

An alternative form of the vorticity boundary conditions is obtained as follows. A central difference approximation of (2.3.27) gives

$$\omega_{0,j} = -\frac{\psi_{1,j} - 2\psi_{0,j} + \psi_{-1,j}}{(\Delta x)^2}$$

but since $\frac{\partial \psi}{\partial x}|_{x=0} = 0$, we have $\psi_{1,j} = \psi_{-1,j}$ and therefore

$$\omega_{0,j} = -\frac{2\psi_{1,j} - 2\psi_{0,j}}{(\Delta x)^2} = -\frac{2\psi_{1,j}}{(\Delta x)^2}, \qquad j = 0,1,2,...,N_z. \tag{2.3.32}$$

Similarly

$$\omega_{i,0} = -\frac{2\psi_{i,1}}{(\Delta z)^2}, \qquad i = 0,1,2,...,N_x, \tag{2.3.33}$$

$$\omega_{N_x,j} = -\frac{2\psi_{N_x-1,j}}{(\Delta x)^2}, \qquad j = 0,1,2,...,N_z, \tag{2.3.34}$$

$$\omega_{i,N_z} = -\frac{2\psi_{i,N_z-1}}{(\Delta z)^2}, \qquad i = 0,1,2,...,N_x. \tag{2.3.35}$$

The two methods mentioned here have both been used successfully in the past (Drummond 1987). We mainly use formulae (2.3.28) — (2.3.31) which are second-order accurate, although the first-order formulae (2.3.32) — (2.3.35) are more stable and we can choose either method according to requirements.

The scheme (2.3.22) is a three-layer scheme $(k+1, k, k-1)$, and as with the energy equation another method is needed to obtain the second time-level values. The following scheme is used.

In the equation

$$\sigma^{-1}\left(\frac{\partial \omega}{\partial t}+J(\omega,\psi)\right)=\nabla^2\omega+R\frac{\partial T}{\partial x},$$

we set

$$\frac{\partial}{\partial t}(\omega^2_{i,j})=\frac{\omega^2_{i,j}-\omega^1_{i,j}}{\Delta t},\quad \frac{\partial T^2_{i,j}}{\partial x}=\frac{1}{2\Delta x}(T^2_{i+1,j}-T^2_{i-1,j})$$

$$\nabla^2\omega^2_{i,j}=\frac{1}{(\Delta x)^2}\{\omega^2_{i+1,j}-2\omega^2_{i,j}+\omega^2_{i-1,j}\}+\frac{1}{(\Delta z)^2}\{\omega^2_{i,j+1}-2\omega^2_{i,j}+\omega^2_{i,j-1}\},$$

to obtain

$$\frac{\sigma^{-1}}{\Delta t}(\omega^2_{i,j}-\omega^1_{i,j})+\sigma^{-1}J(\omega^1_{i,j},\psi^1_{i,j})=\frac{1}{(\Delta x)^2}\{\omega^2_{i+1,j}-2\omega^2_{i,j}+\omega^2_{i-1,j}\}$$

$$+\frac{1}{(\Delta z)^2}\{\omega^2_{i,j+1}-2\omega^2_{i,j}+\omega^2_{i,j-1}\}+\frac{R}{2\Delta x}(T^2_{i+1,j}-T^2_{i-1,j}).$$

Rearranging the above form, we have

$$\omega^2_{i,j}=\frac{\frac{\Delta t}{(\Delta x)^2}(\omega^2_{i+1,j}+\omega^2_{i-1,j})+\frac{\Delta t}{(\Delta z)^2}(\omega^2_{i,j+1}+\omega^2_{i,j-1})}{\bar{x}}$$
$$+\frac{\frac{\Delta tR}{2\Delta x}(T^2_{i+1,j}-T^2_{i-1,j})+\sigma^{-1}\omega^1_{i,j}-\frac{\Delta t}{\sigma}J(\omega^1_{i,j},\psi^1_{i,j})}{\bar{x}} \qquad (2.3.36)$$

where

$$\bar{x}=\frac{1}{\sigma}+\frac{2\Delta t}{(\Delta x)^2}+\frac{2\Delta t}{(\Delta z)^2}.$$

The above formula (2.3.36) provides an unconditionally stable, implicit scheme and has first-order accuracy in time and second-order accuracy in space. We use Successive Under-Relaxation (SUR) to solve the linear system (2.3.36) to obtain the numerical solution for ω at interior points; the boundary schemes described previously are still applicable. The under-relaxation takes the form

$$\tilde{\omega}_{i,j}^{2(m)} = \frac{\frac{\Delta t}{(\Delta x)^2}\left(\omega_{i+1,j}^{2(m-1)} + \omega_{i-1,j}^{2(m)}\right) + \frac{\Delta t}{(\Delta z)^2}\left(\omega_{i,j+1}^{2(m-1)} + \omega_{i,j-1}^{2(m)}\right)}{\bar{x}}$$

$$+\frac{\frac{\Delta t R}{2\Delta x}\left(T_{i+1,j}^2 - T_{i-1,j}^2\right) + \sigma^{-1}\omega_{i,j}^1 - \frac{\Delta t}{\sigma}J\left(\omega_{i,j}^1, \psi_{i,j}^1\right)}{\bar{x}} \qquad (2.3.37)$$

$$\omega_{i,j}^{2(m)} = \lambda\tilde{\omega}_{i,j}^{2(m)} + (1-\lambda)\omega_{i,j}^{2(m-1)} \qquad (2.3.38)$$

$$i = 1, 2, ..., N_x - 1, \quad j = 1, 2, ..., N_z - 1.$$

Here λ is the relaxation parameter; the optimum parameter was found to be about 0.6; m is the iteration index of the SUR and the iteration continues until

$$\max_{i,j} |\omega_{i,j}^{2(m+1)} - \omega_{i,j}^{2(m)}| < \epsilon_0,$$

where ϵ_0 is a very small positive number usually taken to be 10^{-6}.

The whole computation procedure for ω is similar to that for T. Initial conditions determine the solution at the first time level, then (2.3.36) and (2.3.38) the solution at the second time level and thereafter (2.3.22) and (2.3.23) are used to obtain the interior solution for ω at further time levels. The boundary values are obtained either from (2.3.28) — (2.3.31) or from (2.3.32) — (2.3.35). The convergence criterion and numerical stability of the whole procedure will be discussed later.

2.3.3 Poisson Equation

The stream function ψ satisfies

$$\frac{\partial^2\psi}{\partial x^2} + \frac{\partial^2\psi}{\partial z^2} = -\omega, \qquad (2.3.39)$$

$$\psi = \frac{\partial\psi}{\partial x} = 0, \quad x = 0, L; \quad \psi = \frac{\partial\psi}{\partial z} = 0, \quad z = 0, 1 \qquad (2.3.40)$$

and we use a Multigrid method to obtain the numerical solution.This is based on the five-point scheme and Successive Over-Relaxation, both widely used for this kind of

elliptic equation. The main idea is to use the solution on a coarse grid to revise the required solution on a fine grid. It has been proved theoretically and practically that the Multigrid method has more advantages than other methods, as it has a better rate of convergence. Here we do not give a full theoretical analysis of the algorithm, which is described in detail by Brandt (1977).

A central difference approximation is used to discretize the original equation, giving

$$\psi_{i,j} = \frac{(\Delta z)^2(\psi_{i+1,j} + \psi_{i-1,j}) + (\Delta x)^2(\psi_{i,j+1} + \psi_{i,j-1}) + \omega_{i,j}(\Delta x)^2(\Delta z)^2}{2(\Delta x)^2 + 2(\Delta z)^2} \quad (2.3.41)$$

and then we use Successive Over-Relaxation to solve the above system of linear equations for $\psi_{i,j}$:

$$\psi_{i,j}^{(m)} = \psi_{i,j}^{(m-1)} + \frac{\lambda}{2(\Delta x)^2 + 2(\Delta z)^2}\left[(\Delta z)^2(\psi_{i+1,j}^{(m-1)} + \psi_{i-1,j}^{(m)}) + (\Delta x)^2(\psi_{i,j+1}^{(m-1)} + \psi_{i,j-1}^{(m)}) + \omega_{i,j}(\Delta x)^2(\Delta z)^2\right] - \lambda\psi_{i,j}^{(m-1)}, \quad (2.3.42)$$

where m is the iteration index and λ is the relaxation parameter. The optimum value of this parameter was found to be about 1.7. The full Multigrid algorithm is summarized in Figure 2.4.

The main features of the scheme are described as follows. A suitable mesh size $\Delta x, \Delta z$ and relaxation parameter λ are chosen and (2.3.41), (2.3.42) used to obtain an approximate value of $\psi_{i,j}$. The convergence criterion I (see Figure 2.4) is a very strong and strict one, typically

$$\|\nabla^2\psi^n + \omega\| < \epsilon,$$

where ϵ is a very small positive number and n is the grid index. However, in the actual computation we use $\max_{i,j} |\psi_{i,j}^{n(m+1)} - \psi_{i,j}^{n(m)}| < \epsilon_0$ instead of the above condition, where ϵ_0 was usually taken as 10^{-6} and m is the iteration index on the grid n. The convergence criterion II (see Figure 2.4) is a weaker criterion than I, usually taken as

$$\frac{\text{The final norm of the residue}}{\text{The penultimate norm of the residue}} \geq \eta$$

where η is a positive constant, usually in the range $0.6 \leq \eta < 1$.

For the coarse grid $n-1$, we take $\bar{\Delta}x = 2\Delta x, \bar{\Delta}z = 2\Delta z$ and define $D^n_{i,j} = \nabla^2\psi^n + \omega$ for the fine grid, where

$$D^n_{i,j} = \frac{\psi^n_{i+1,j} - 2\psi^n_{i,j} + \psi^n_{i-1,j}}{(\Delta x)^2} + \frac{\psi^n_{i,j+1} - 2\psi^n_{i,j} + \psi^n_{i,j-1}}{(\Delta z)^2} + \omega_{i,j}.$$

Using a linear interpolation, we have $D^{n-1} = I^{n-1}_n D^n$ in the coarse grid,where I^{n-1}_n denotes the change of value from the points on the fine grid to the corresponding points on the coarse grid. We set $D^n = \nabla^2\psi^n + \omega$, and $D^{n-1} = I^{n-1}_n D^n = \sum_i \rho_i D^n(x + ih)$ where h is the spatial step. Usually, we take $\rho_0 = 1; \rho_i = 0$ if $i \neq 0$. Now, we can solve the remainder equations $\nabla^2\bar{\psi}^{n-1} = D^{n-1}$in the coarse grid. Using (2.3.42), we have

$$\bar{\psi}^{(m)}_{i,j} = \bar{\psi}^{(m-1)}_{i,j} + \lambda\left[\frac{(\Delta z)^2(\bar{\psi}^{(m-1)}_{i+1,j} + \bar{\psi}^{(m)}_{i-1,j}) + (\Delta x)^2(\bar{\psi}^{(m-1)}_{i,j+1} + \bar{\psi}^{(m)}_{i,j-1})}{2(\Delta x)^2 + 2(\Delta z)^2} - \frac{D_{i,j}(\Delta x)^2(\Delta z)^2}{2(\Delta x)^2 + 2(\Delta z)^2}\right] + \lambda\bar{\psi}^{(m-1)}_{i,j}$$

where λ and m are as previously defined.

In order to obtain the value of $\bar{\psi}$ in the fine grid, we use I^n_{n-1} to denote a linear interpolation from the grid $n-1$ to the grid n. In the two dimensional space, we can take

$$\begin{aligned}
\bar{\psi}^n_{i,j} &= \bar{\psi}^{n-1}_{i,j}, \quad i,j \text{ even} \\
&= \frac{1}{2}(\bar{\psi}^{n-1}_{i,j-1} + \bar{\psi}^{n-1}_{i,j+1}), \quad \text{i even;} \quad j \text{ odd ;} \\
&= \frac{1}{2}(\bar{\psi}^{n-1}_{i-1,j} + \bar{\psi}^{n-1}_{i+1,j}), \quad \text{i odd;} \quad j \text{ even ;} \\
&= \frac{1}{4}(\bar{\psi}^{n-1}_{i+1,j+1} + \bar{\psi}^{n-1}_{i-1,j+1} + \bar{\psi}^{n-1}_{i+1,j-1} + \bar{\psi}^{n-1}_{i-1,j-1}), \quad i,j \quad \text{odd,}
\end{aligned}$$

where $\bar{\psi}^n$ is the value of the remainder for the fine grid, and $\bar{\psi}^{n-1}$ for the coarse

grid. Then, we use $\bar{\psi}^n$ to correct the value in the fine grid. The whole procedure is repeated until criterion I is satisfied and then the computation is stopped.

2.3.4 Velocity Field

This is given by

$$u = \frac{\partial \psi}{\partial z}, \quad w = -\frac{\partial \psi}{\partial x} \tag{2.3.43}$$

and use of a central-difference approximation gives

$$u_{i,j} = \frac{\psi_{i,j+1} - \psi_{i,j-1}}{2\Delta z}, \quad w_{i,j} = -\frac{\psi_{i+1,j} - \psi_{i-1,j}}{2\Delta x} \tag{2.3.44}$$

at interior points $i = 1, 2, ..., N_x - 1, \quad j = 1, 2, ..., N_z - 1$. On the boundary, we simply have

$$u_{i,j} = w_{i,j} = 0, \quad i = 0, N_x; \quad j = 0, N_z.$$

2.3.5 The Overall Scheme of Computation

This is shown in Figure 2.5. The main components of the scheme for the insulating case are summarised as follows.

(a). Begin by setting initial conditions throughout the flow domain, for example $T = x/L$ and $u = w = \psi = \omega = 0$.

(b). Calculate the new temperature T at each grid point at the second time level using equations (2.3.12)-(2.3.20). The iteration is terminated when the following condition is satisfied:

$$\max_{i,j} |T_{i,j}^{2(m+1)} - T_{i,j}^{2(m)}| < \epsilon_0,$$

where m is the iteration index in the SOR scheme and ϵ_0 is usually taken to be 10^{-6}.

(c). Calculate the new vorticity ω at each interior grid point at the second time level using equations (2.3.36)-(2.3.38). The iteration is terminated when the following condition is satisfied:

$$\max_{i,j} |\omega_{i,j}^{2(m+1)} - \omega_{i,j}^{2(m)}| < \epsilon_0,$$

where m is the iteration index in the SOR scheme and ϵ_0 is usually taken to be 10^{-6}.

(d). Calculate the stream function at all interior grid points using equations (2.3.41) (2.3.42) and the Multi-grid algorithm. The iteration is terminated when the following condition is satisfied

$$\max_{i,j} |\psi_{i,j}^{m+1} - \psi_{i,j}^{m}| < \epsilon_0,$$

where m is the iteration index in the SOR scheme and ϵ_0 is usually taken to be 10^{-6}.

(e). Calculate the vorticity at the walls using (2.3.28) —(2.3.31).

(f). Calculate the velocities at each interior grid point using (2.3.44).

(g). Calculate the time steps required for numerical stability of equations (2.3.3), (2.3.8) and (2.3.22), i.e. for the first step:

$$\Delta t \leq 0.95 \left[\frac{2}{(\Delta x)^2} + \frac{2}{(\Delta z)^2} \right]^{-1}$$

and for the remaining time steps

$$\Delta t \leq 0.95 \left[0.75 \left(\frac{|u_{i,j}|}{\Delta x} + \frac{|w_{i,j}|}{\Delta z} \right) \right]^{-1} \quad \text{for } \sigma < 1,$$

$$\Delta t \leq 0.95 \left[0.75\sigma \left(\frac{|u_{i,j}|}{\Delta x} + \frac{|w_{i,j}|}{\Delta z} \right) \right]^{-1} \quad \text{for } \sigma \geq 1,$$

which is a modified form of the Courant condition (Drummond 1981).

(h). Calculate the temperature T at the next time step in the whole region using (2.3.3), (2.3.4) and (2.3.7)-(2.3.8).

(i). Calculate the vorticity ω at the next time step for the interior points using (2.3.22).

(j). Calculate the stream function as in Step (d).

(k). Calculate the vorticity at the walls using (2.3.28) — (2.3.31), as in Step (e).

(l). Calculate the velocities as in Step (f).

(m). Periodically the convergence of the solution is checked. The computation is stopped when the following conditions are satisfied, corresponding to the attainment of a steady-state solution:

$$\max_{i,j} |T_{i,j}^{k+1} - T_{i,j}^{k}| < \epsilon_1,$$

$$\max_{i,j} |\omega_{i,j}^{k+1} - \omega_{i,j}^{k}| < \epsilon_2,$$

where k is the time level index and ϵ_1 and ϵ_2 are usually taken to be 10^{-6}. Otherwise the procedure is repeated from Step (g).

2.4 Results and Discussion

2.4.1 Results

The algorithm discussed in Section 2.3 was used to investigate the solution in a square cavity (L=1) with insulated upper and lower boundaries for $\sigma = 0.733$ and $R = 14660$ (see Figure 2.6). Results of the computations are displayed in contour plots of the stream function, temperature and vorticity, shown in Figure 2.7. The structure of the temperature indicates that strong horizontal temperature gradients

are maintained in the lower hot and upper cold corners of the cavity. Since buoyancy forces are proportional to the horizontal temperature gradient, these regions produce vigorous convection up the hot wall and down the cold wall, and the rising and sinking fluid particles complete a single-cell circulation in the cavity. Figures 2.8-2.10 show profiles of the solution in the central (or core) region of the cavity.

In Figure 2.8, the horizontal component of the fluid velocity at the core mid-section is shown as a function of vertical distance. Figures 2.9 and 2.10 indicate that the fluid temperature in the central region varies roughly linearly with depth and is independent of lateral position, in line with a boundary-layer model of the flow at high Rayleigh numbers proposed by Gill (1966).

2.4.2 Corner Structure

A useful comparison with the numerical results is provided by a theoretical analysis of the flow structure in the corners of the cavity, where the vorticity field has a quite complex form (Figure 2.11).

Equations (2.2.12) — (2.2.14) can be written in the steady-state form

$$\nabla^4\psi = R\frac{\partial T}{\partial x} + \frac{1}{\sigma}\frac{\partial(\nabla^2\psi,\psi)}{\partial(x,z)}, \tag{2.4.1}$$

$$\nabla^2 T = \frac{\partial(T,\psi)}{\partial(x,z)}, \quad \omega = -\nabla^2\psi, \tag{2.4.2}$$

with boundary conditions

$$\psi = \frac{\partial\psi}{\partial x} = 0, \quad x = 0, L, \quad \psi = \frac{\partial\psi}{\partial z} = 0, \quad z = 0, 1, \tag{2.4.3}$$

$$T = 0, \quad x = 0; \quad T = 1, \quad X = L, \tag{2.4.4}$$

$$\frac{\partial T}{\partial z} = 0, \quad z = 0, 1. \tag{2.4.5}$$

In the corner $(x, z) = (0, 0)$, assume Taylor series expansions

$$\begin{aligned}\psi = a &+ bx + cz \\ &+ dx^2 + exz + fz^2 \\ &+ gx^3 + hx^2z + kxz^2 + lz^3 \\ &+ mx^4 + nx^3z + px^2z^2 + qxz^3 + rz^4 + \cdots,\end{aligned}$$

$$\begin{aligned}T = A &+ Bx + Cz \\ &+ Dx^2 + Exz + Fz^2 + \cdots.\end{aligned}$$

From the boundary conditions

$$a + cz + fz^2 + lz^3 + rz^4 = 0,$$

$$a + bx + dx^2 + gx^3 + mx^4 = 0,$$

$$c + ex + hx^2 + nx^3 = 0,$$

$$b + ez + kz^2 + qz^3 = 0,$$

$$A + Cz + Fz^2 = 0,$$

$$C + Ex = 0.$$

It is easily established that the only non-zero constants are p, B and D, i.e.

$$\left.\begin{aligned}\psi &\sim px^2z^2 \\ T &\sim Bx + Dx^2\end{aligned}\right\} (x,z) \to (0,0).$$

Also

$$\omega = -\nabla^2\psi \sim -2px^2 - 2pz^2 = -2p(x^2 + z^2)$$

and in (2.4.1) and (2.4.2) we therefore have

$$\left.\begin{aligned}&\nabla^4\psi = -\nabla^2\omega \sim 8p \\ &RT_x \sim RB \\ &\tfrac{\partial(\omega,\psi)}{\partial(x,z)} \sim \omega_x\psi_z - \omega_z\psi_x \to 0\end{aligned}\right\} (x,z) \to (0,0)$$

and

$$\left.\begin{array}{rcl} \nabla^2 T & \sim & 2D \\ \frac{\partial(T,\psi)}{\partial(x,z)} & \sim & T_x\psi_z - T_z\psi_x \to 0 \end{array}\right\} (x,z) \to (0.0)$$

Hence a balance in these equations requires $D = 0$ and $8p = RB$ so that as $(x,z) \to (0,0)$ we expect

$$T \sim Bx, \tag{2.4.6}$$

$$\psi \sim \frac{RB}{8}x^2z^2, \tag{2.4.7}$$

$$\omega \sim -\frac{RB}{4}(x^2+z^2), \tag{2.4.8}$$

where B is a constant.

Similarly for the corner $(x,z) = (L,0)$, we have

$$T \sim 1 + \bar{B}(x-L) \tag{2.4.9}$$

$$\psi \sim \frac{R\bar{B}}{8}(x-L)^2z^2 \tag{2.4.10}$$

$$\omega \sim -\frac{R\bar{B}}{4}((x-L)^2+z^2) \tag{2.4.11}$$

as $(x,z) \to (L,0)$ where $\bar{B}$ is a constant.

The results of Figure 2.7 are in good qualitative agreement with the above theoretical approximations for the temperature and stream function, but for the vorticity a more detailed picture of the corner region is required in order to observe the radial dependence (2.4.8). Figure 2.11 shows the vorticity contours near the corners in more detail, indicating good qualitative agreement with the prediction of the theory. A quantitative comparison based on the value of the constant B for the corner $(x,z) = (0,0)$ in Figures 2.12 and 2.13 also shows good agreement but indicates that the vorticity field attains the required form very close to the corner (see also Table 2.1). Given the discrepancies caused by both the truncation error in the theoretical result (2.4.8) and the truncation error of the numerical scheme, the above comparison seems reasonable.

2.4.3 Accuracy and Convergence

In order to test the accuracy and convergence of the numerical algorithm, four different grids were used for the computations: $11 \times 11, 21 \times 21, 31 \times 31$ and 41×41. Figures 2.14, 2.15 and 2.16 show the contoured fields for each grid. With more grid points, the accuracy of the computation improves, but the convergence rate slows down. Table 2.2 shows more information about how the grid size affects the accuracy and convergence of the computation. A comparison of results from computations on 11×11 and 21×21 grids shows that the stream function is changed by about 6% and the vorticity by about 8% for the denser grid, with the computation time increasing by 33%. There is very little difference between the results for the 31×31 grid and the 41×41 grid, with less than a 0.4% change in the value of the stream function maximum at the centre of the cavity.

2.4.4 Comparison of Results with Previous Work

Results for a square cavity at $\sigma = 0.733$ and $R = 14660$ have been obtained by several other workers and are partially listed in Table 2.3. The maximum value of the stream function at the centre of the cavity is used to make the comparison and it is evident that the results obtained in the present study compare well with those of other workers.

Cormack, Leal and Seinfeld (1974) used the two-step, alternating direction, implicit method (A.D.I.) developed by Peaceman and Rachford (1955) to approximate the original equations. This A.D.I technique has the advantage over explicit methods that it is numerically more stable and hence allows the use of a large time step Δt. It has the disadvantage, however, that each iteration requires more computational time than does a method with an explicit technique. Drummond (1981) used the Dufort-Frankel method, and other finite difference methods have been widely used aswell by a number of investigators, such as the second upwind differencing

scheme of Kublbeck , Merker and Straub (1980).

Finally, in order to have an additional check on the present numerical code, the Harwell Flow3D code was used to compute the convective flow in a square cavity with $R = 14660$ and $\sigma = 0.733$. The profiles of temperature on the top wall obtained by the two codes are illustrated in Figure 2.17, and are in excellent agreement.

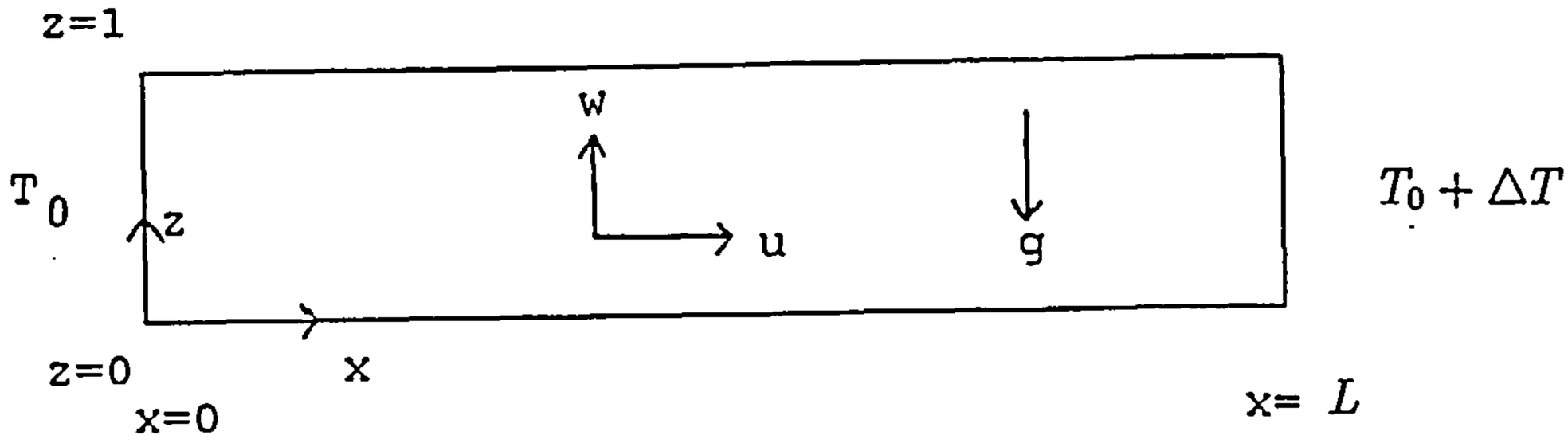

Figure 2.1: Non-dimensional formulation of the physical system.

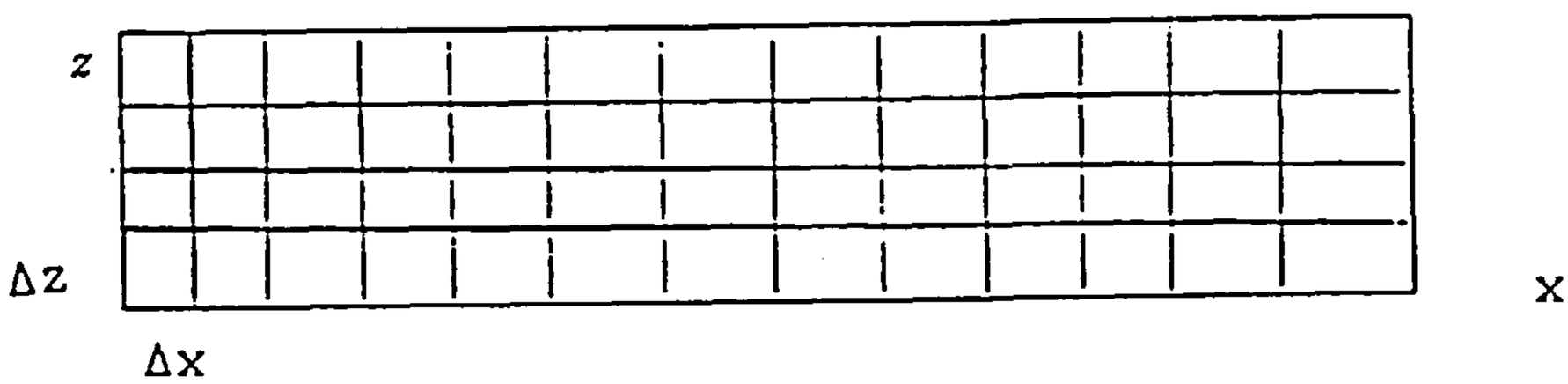

Figure 2.2: The discretized domain of the cavity

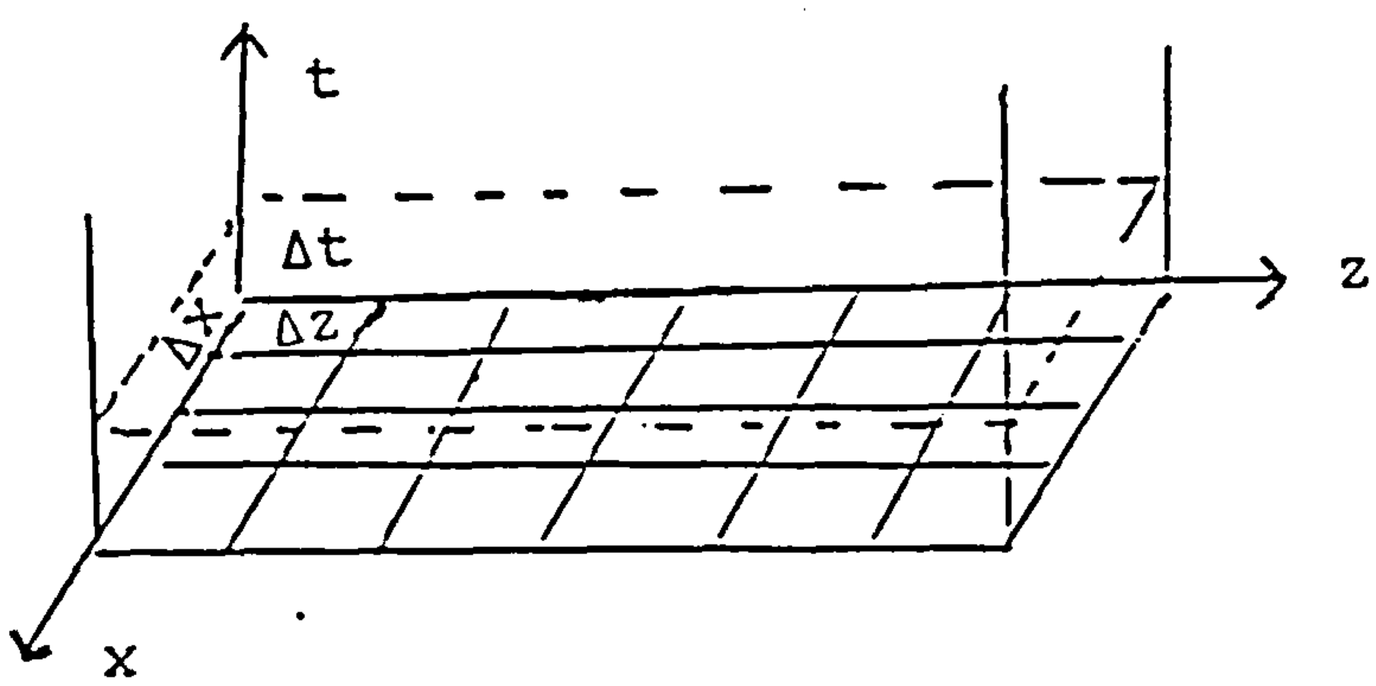

Figure 2.3: Discretized domain containing the time parameter t.

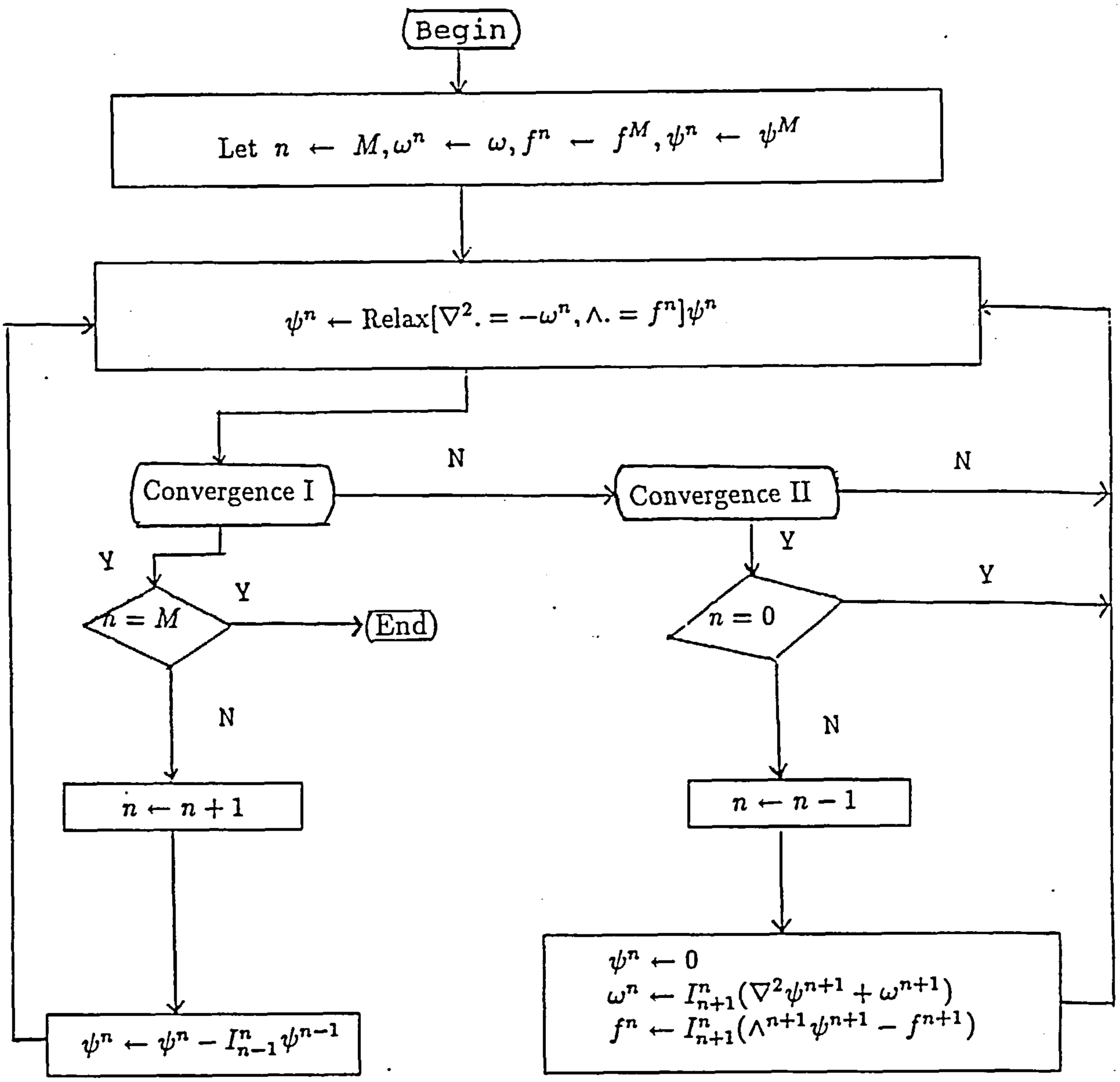

Figure 2.4: The block diagram of the Multigrid method for solving the equation $\nabla^2\psi = -\omega$ with $\wedge\psi = f$ on the boundaries.

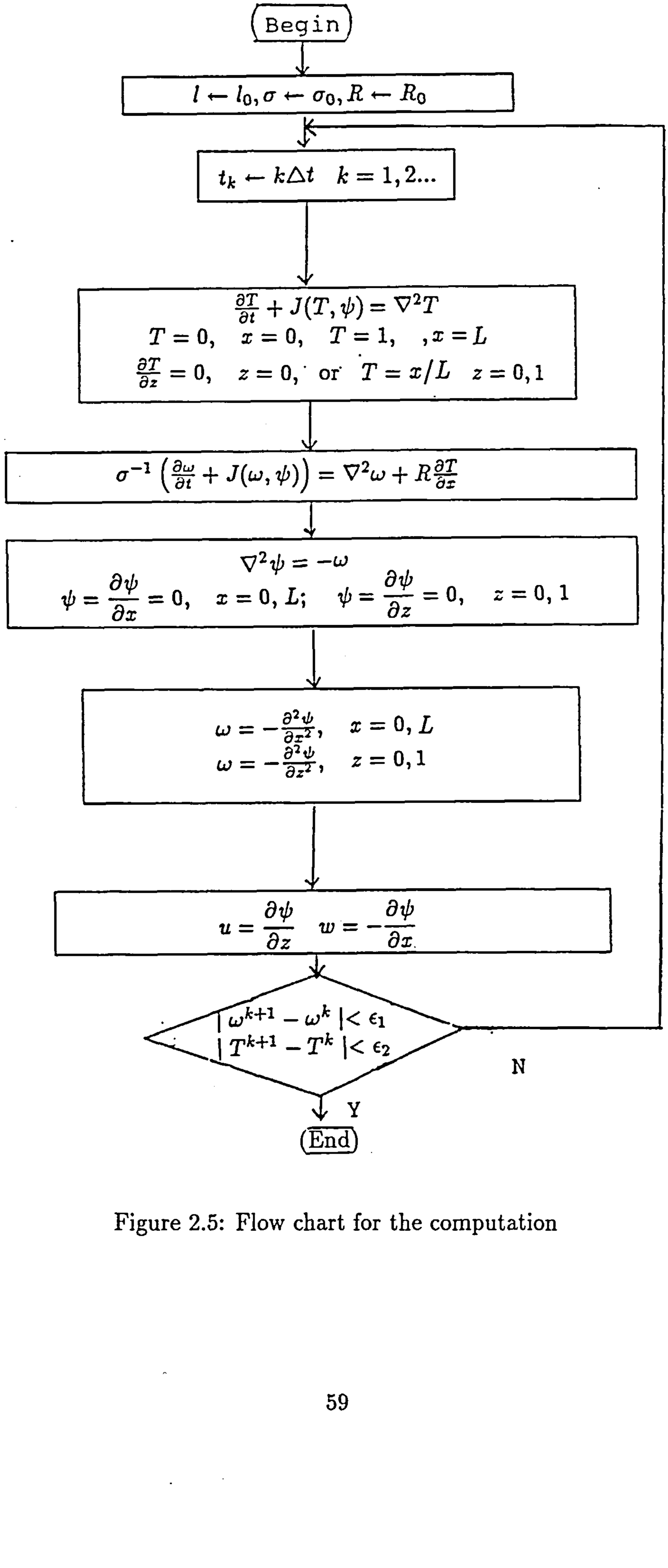

Figure 2.5: Flow chart for the computation

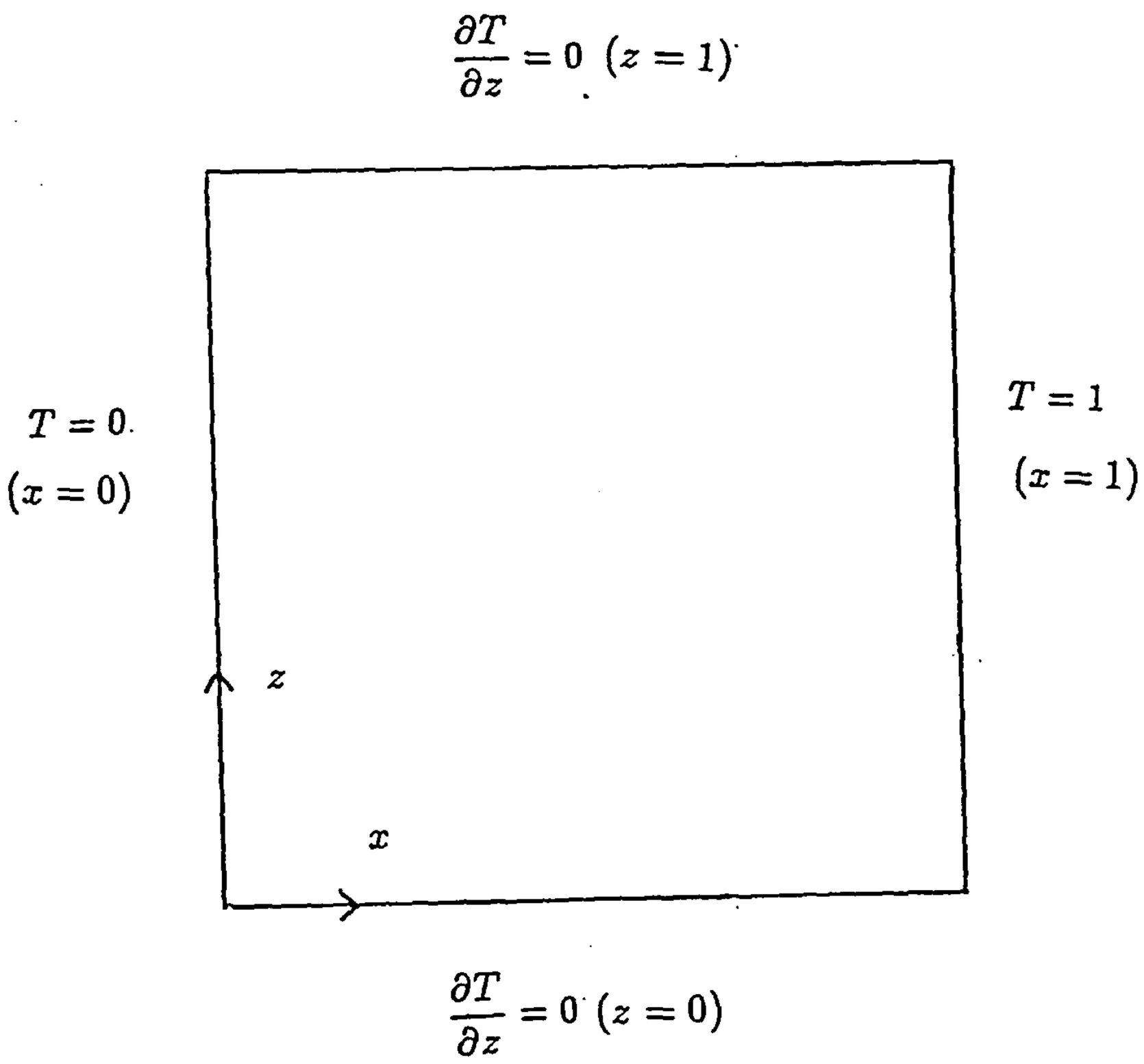

Figure 2.6: Computational domain for the results shown in Figures 2.7-2.16.

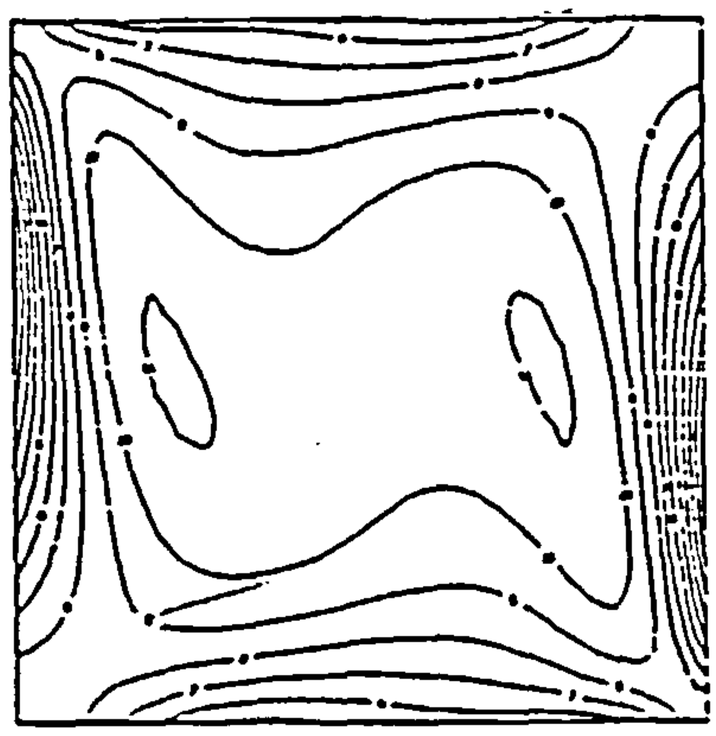

(a)

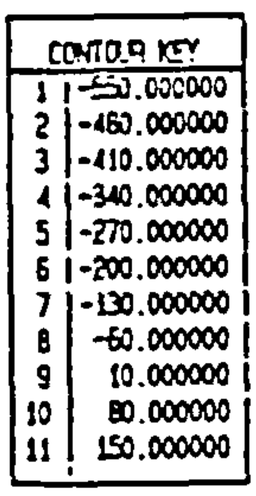

CONTOUR KEY	
1	-550.000000
2	-460.000000
3	-410.000000
4	-340.000000
5	-270.000000
6	-200.000000
7	-130.000000
8	-60.000000
9	10.000000
10	80.000000
11	150.000000

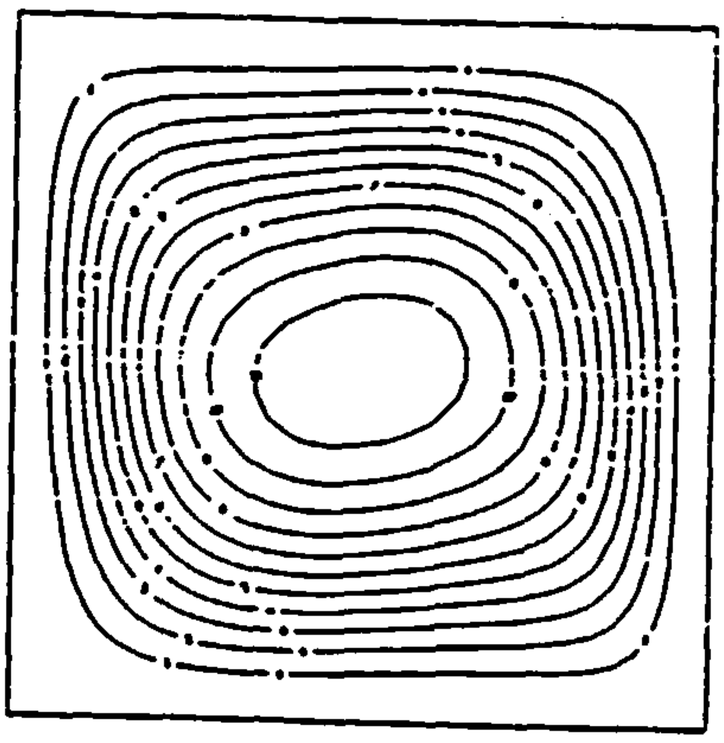

(b)

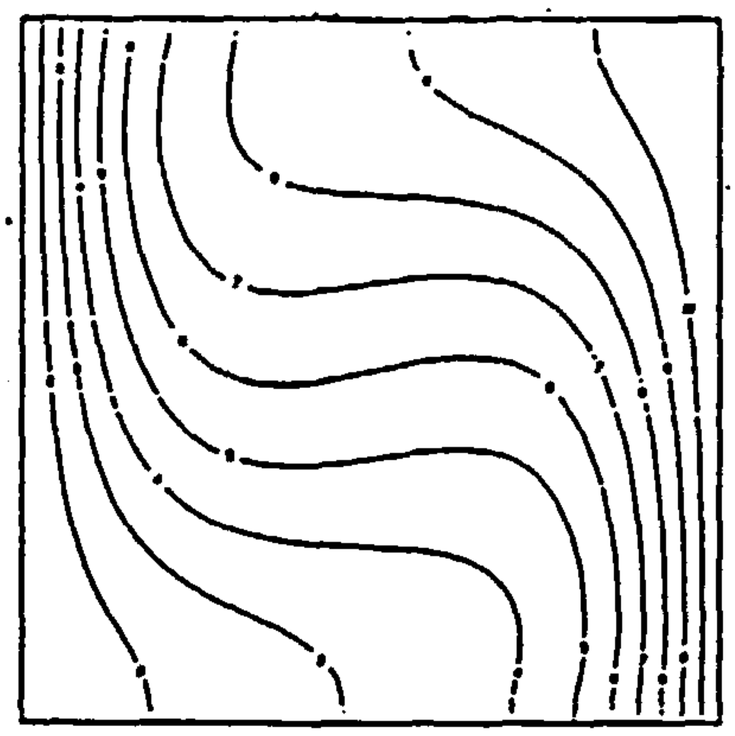

CONTOUR KEY	
1	0.000000
2	0.100000
3	0.200000
4	0.300000
5	0.400000
6	0.500000
7	0.600000
8	0.700000
9	0.800000
10	0.900000
11	1.000000

(c)

Figure 2.7: Results for $\sigma = 0.733$, $R = 14660$ using a 31×31 grid showing (a) vorticity contours, (b) streamlines, (c) isotherms.

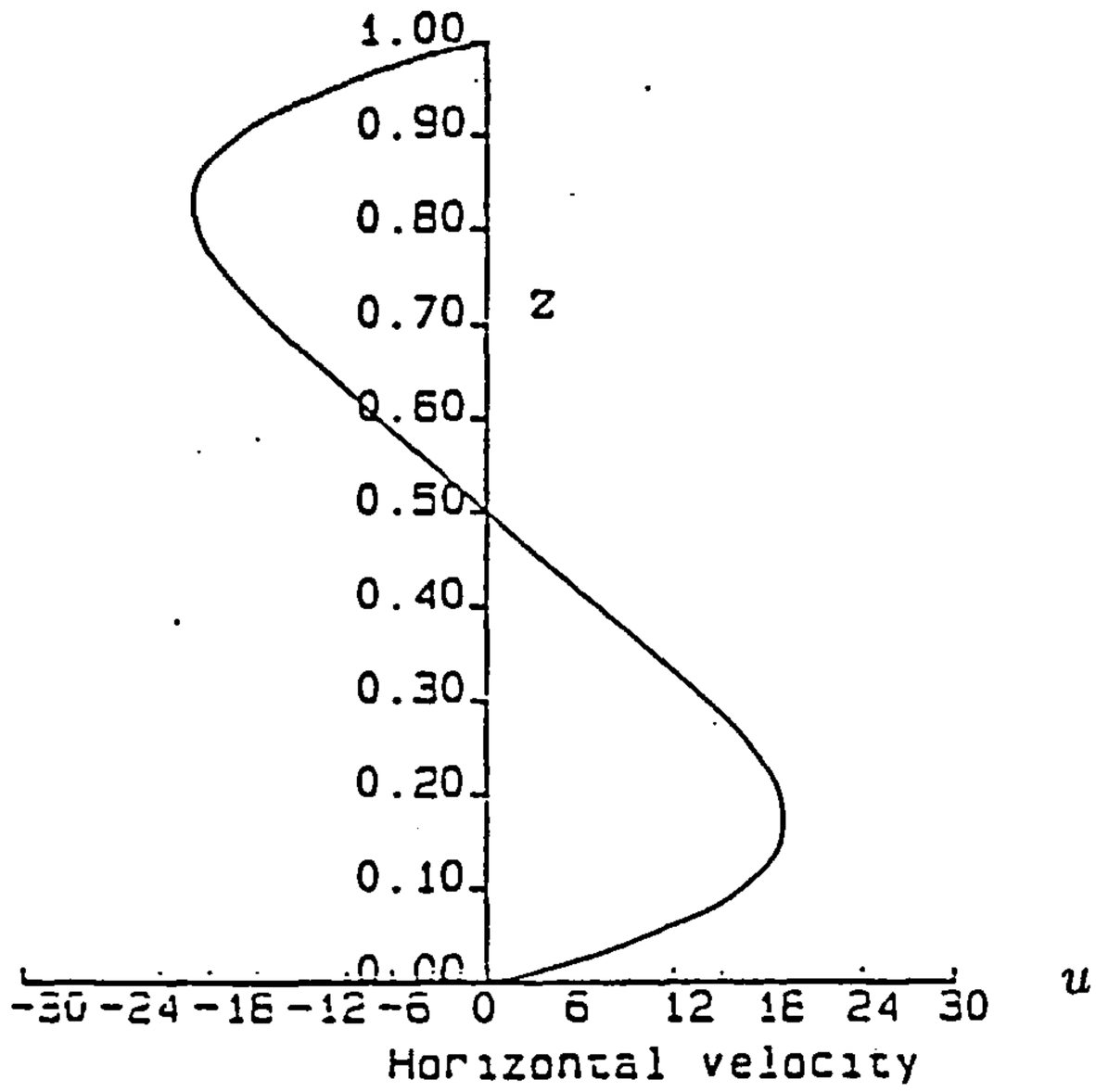

Figure 2.8: Profile of horizontal velocity at $x = 0.5$ for $\sigma = 0.733$, $R = 14660$ and a 41×41 grid.

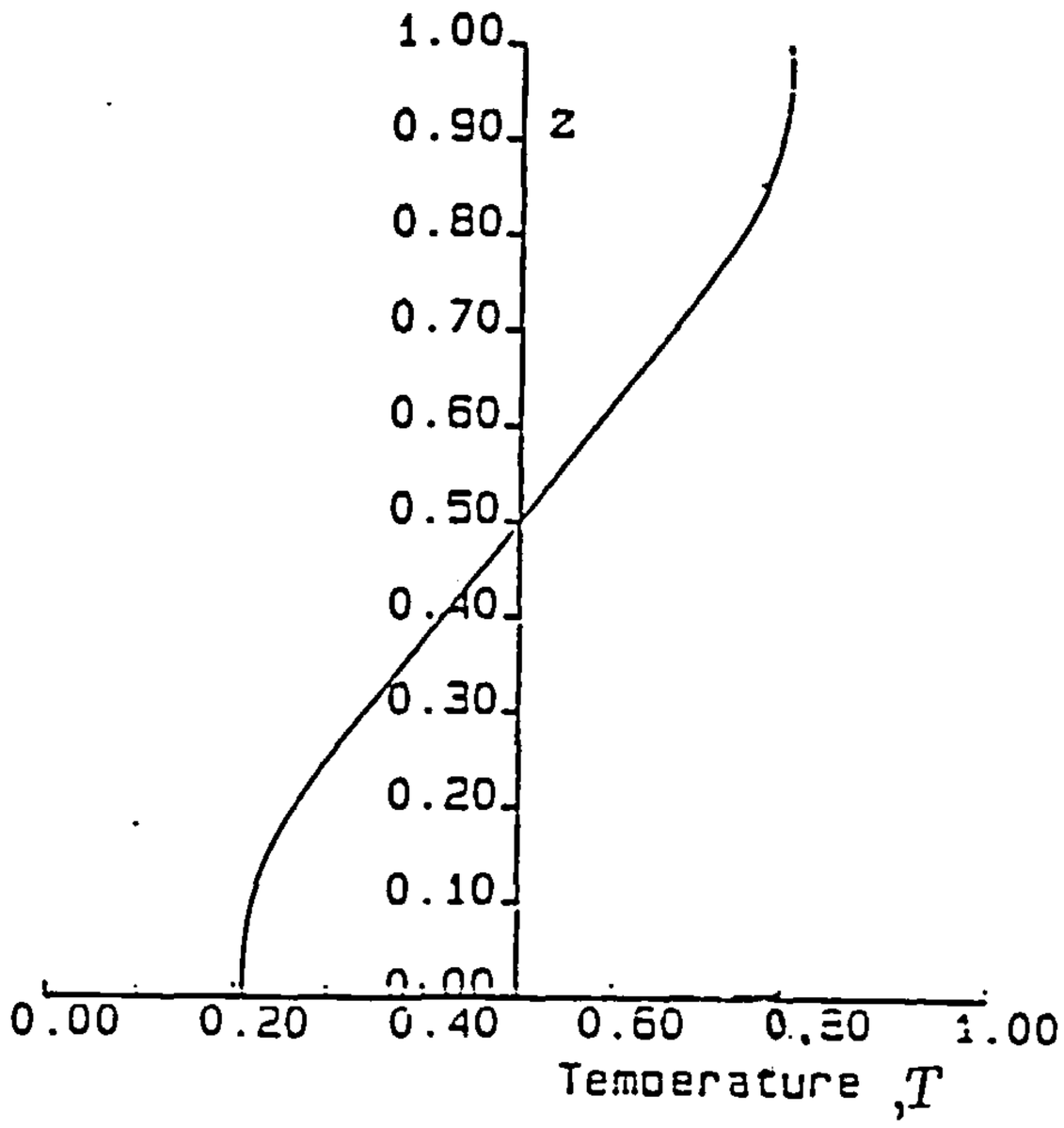

Figure 2.9: Profile of temperature at $x = 0.5$ for $\sigma = 0.733$, $R = 14660$ and a 41×41 grid.

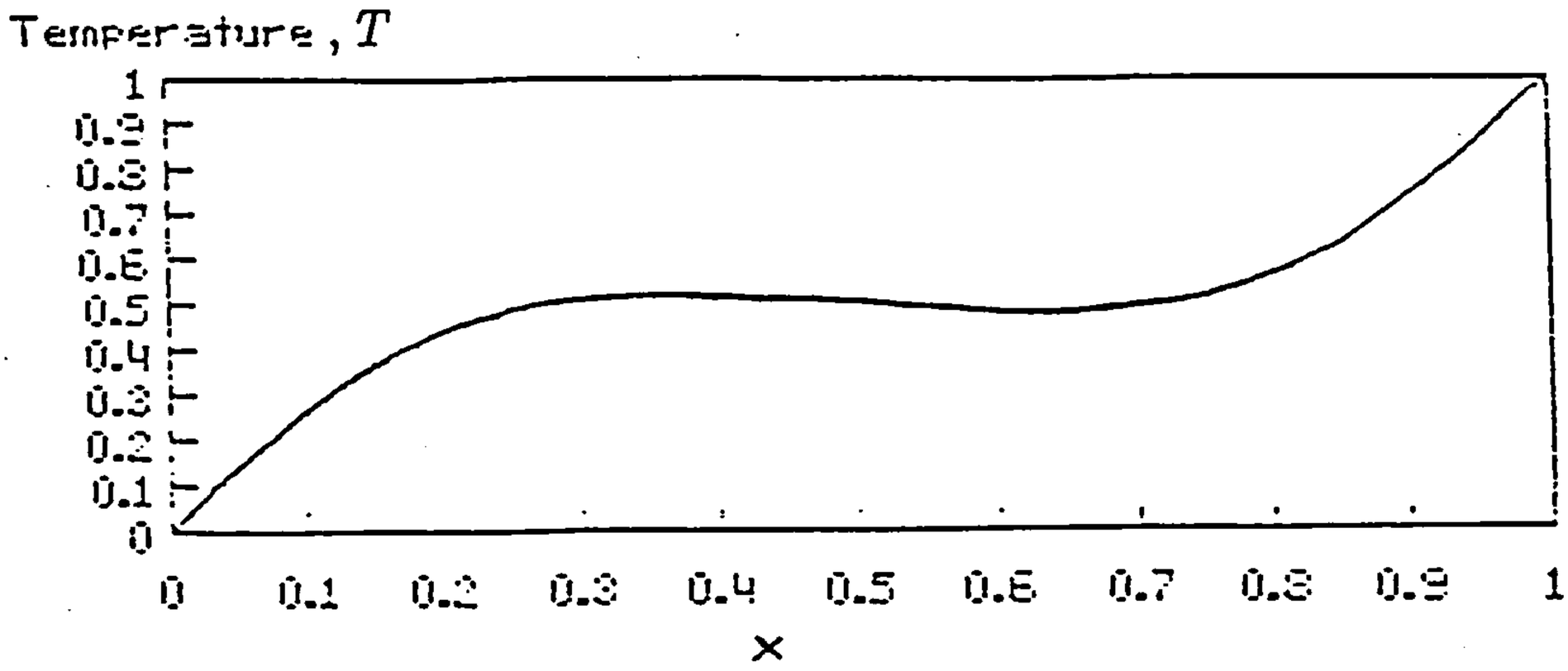

Figure 2.10: Temperature profile at $z = 0.5$ for $\sigma = 0.733$, $R = 14660$ and a 41×41 grid.

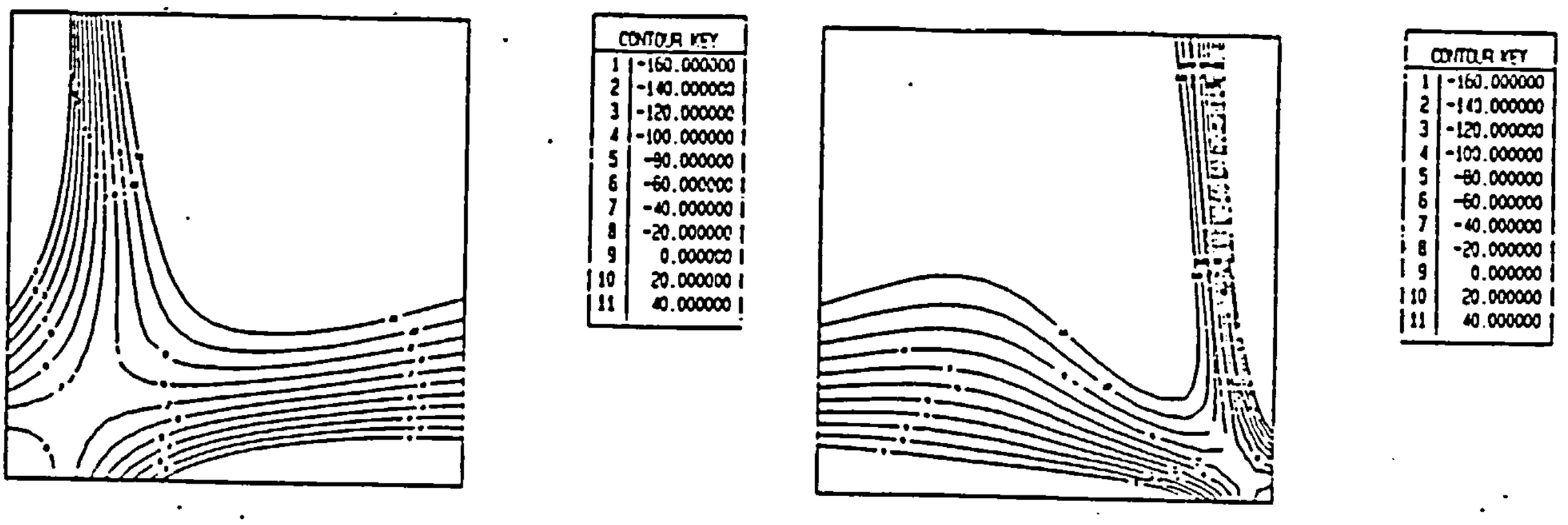

Figure 2.11: Vorticity contours near the corners with $\sigma = 0.733$, $R = 14660$ and a 41×41 grid: (a) bottom cold corner ($0 \leq x \leq 0.5, 0 \leq z \leq 0.5$), (b) bottom hot corner ($0.5 \leq x \leq 1.0, 0 \leq z \leq 0.5$).

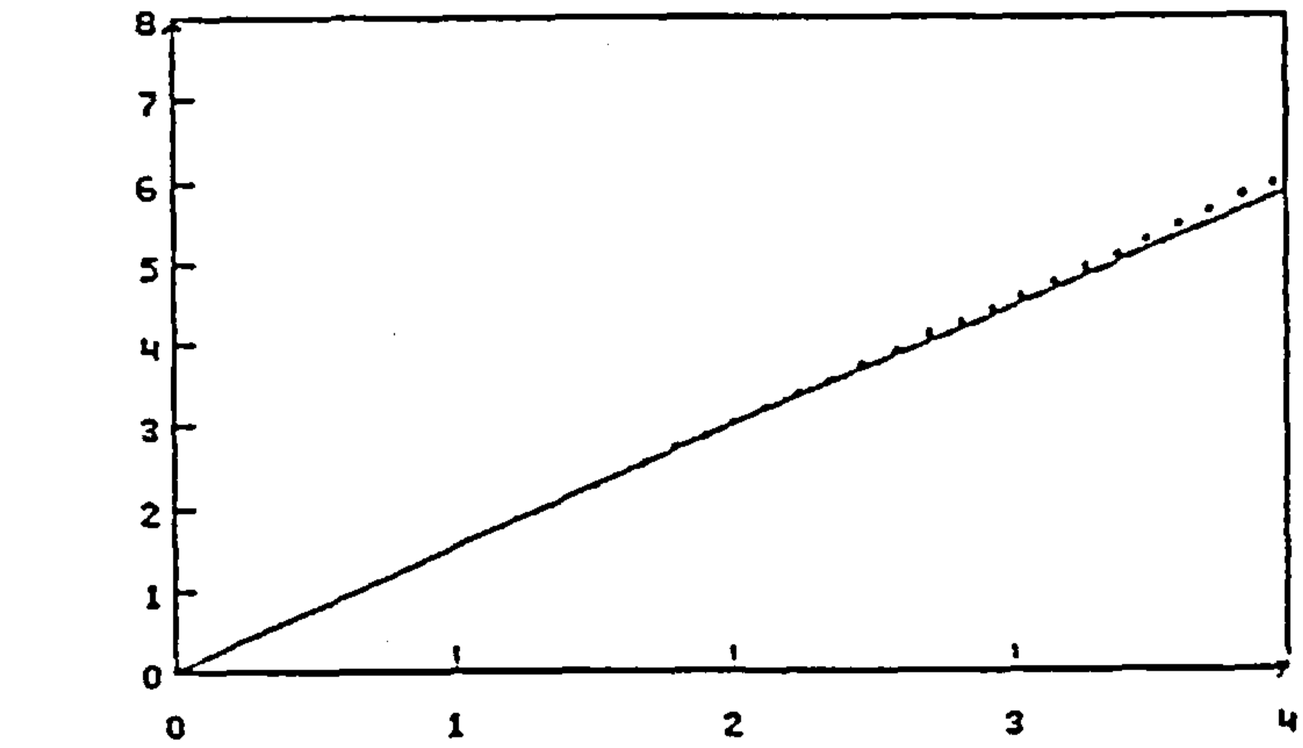

Figure 2.12: Profile of temperature on $z = 0$ near the bottom cold corner.

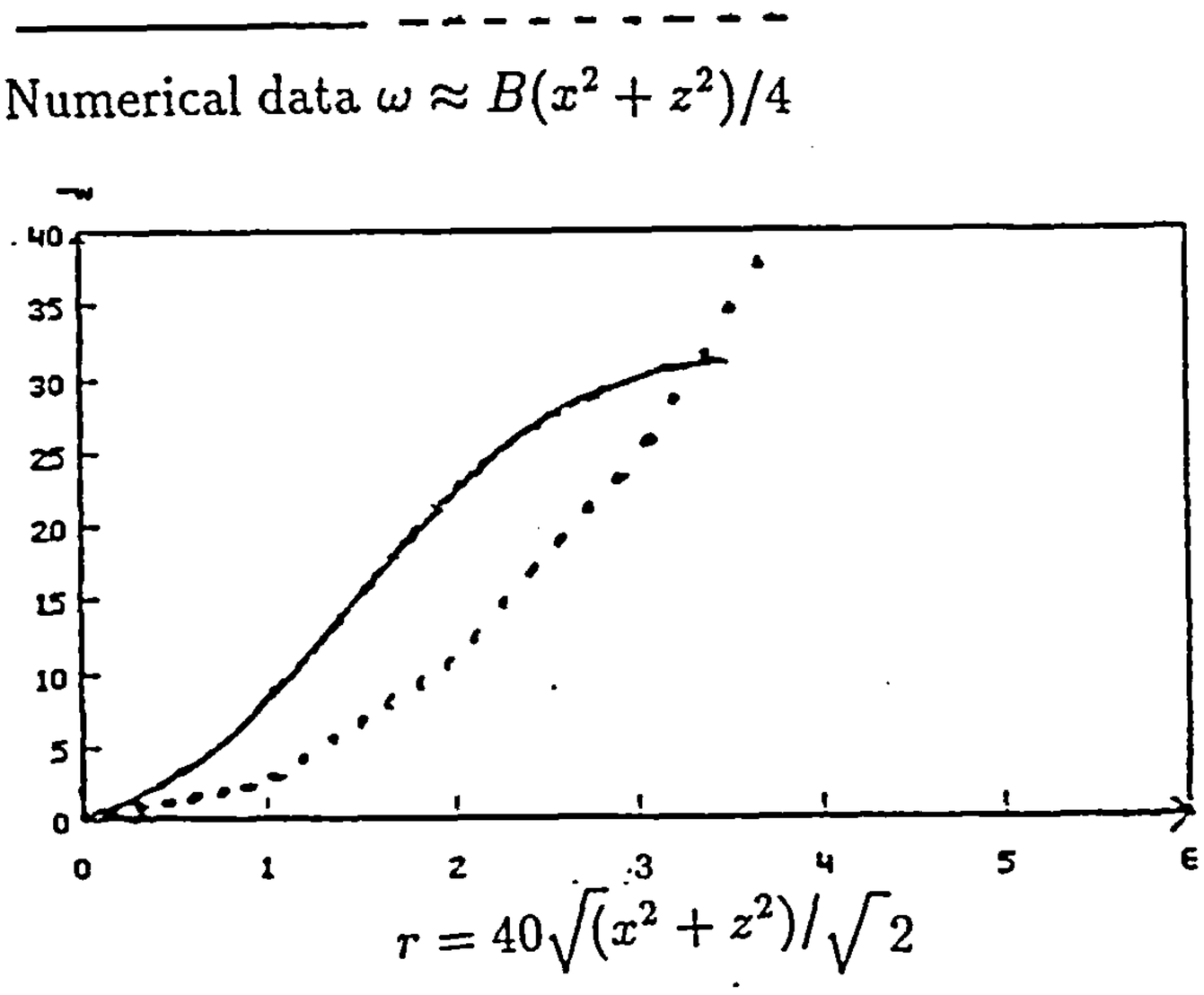

Figure 2.13: Profile of vorticity on the line $x = z$ near the bottom cold corner.

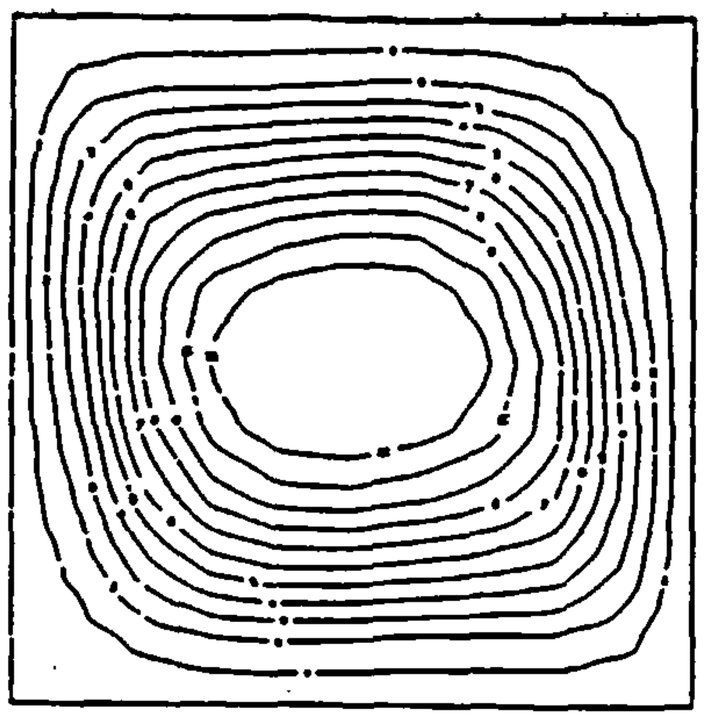

(a)

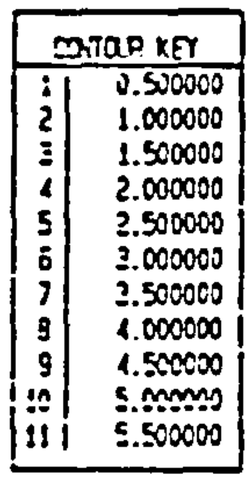

CONTOUR KEY	
1	0.500000
2	1.000000
3	1.500000
4	2.000000
5	2.500000
6	3.000000
7	3.500000
8	4.000000
9	4.500000
10	5.000000
11	5.500000

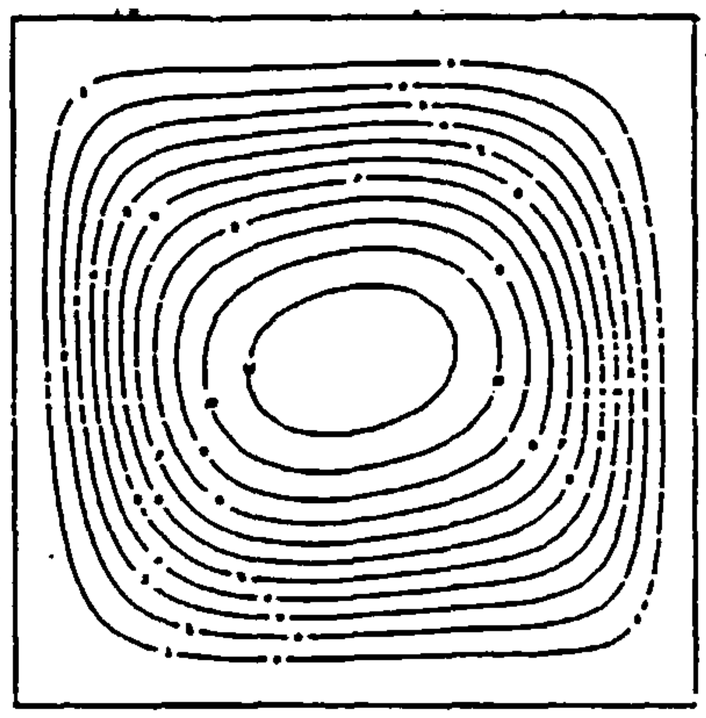

(c)

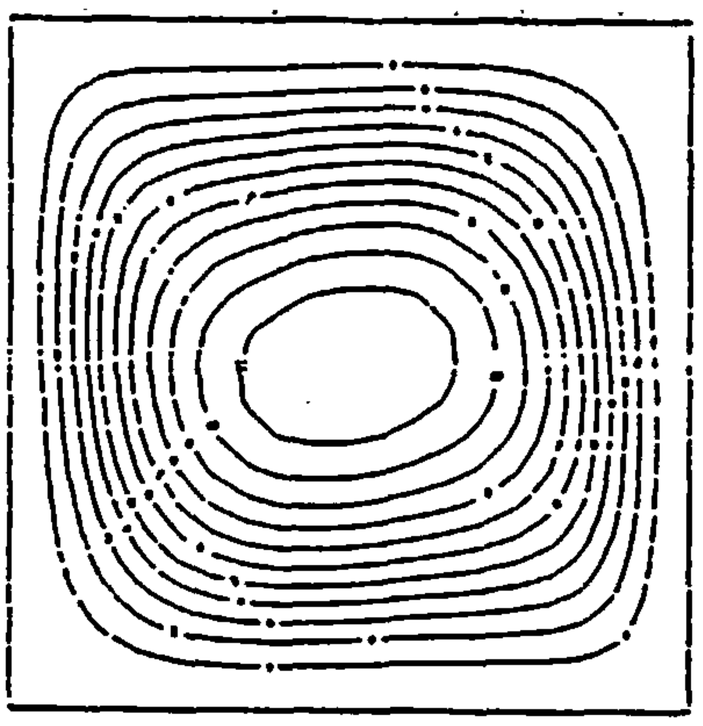

(b)

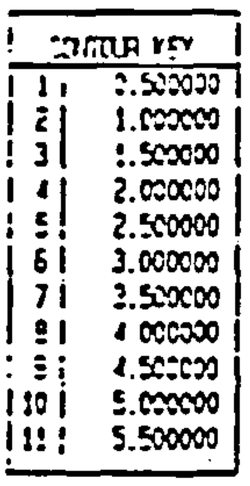

CONTOUR KEY	
1	0.500000
2	1.000000
3	1.500000
4	2.000000
5	2.500000
6	3.000000
7	3.500000
8	4.000000
9	4.500000
10	5.000000
11	5.500000

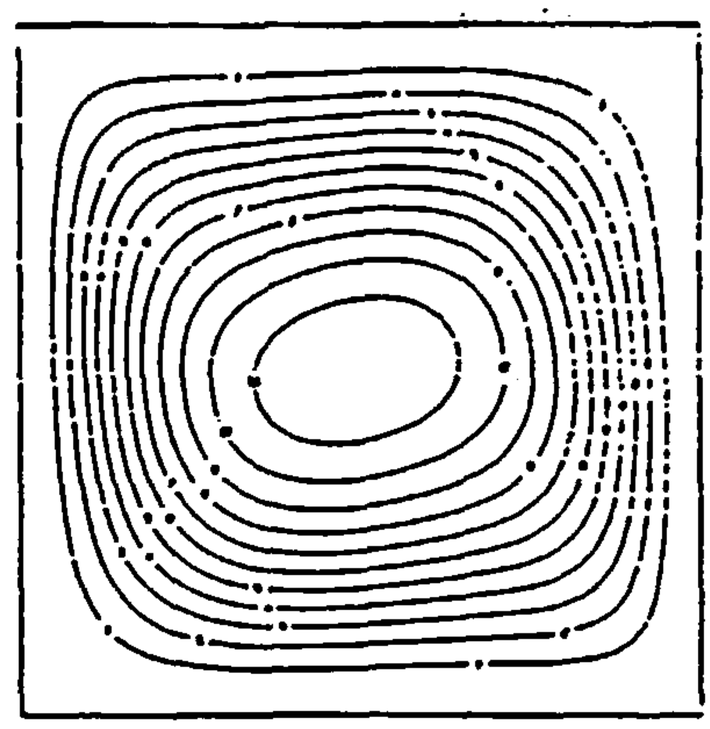

(d)

Figure 2.14: Streamlines for $\sigma = 0.733$, $R = 14660$ and different grids (a) 11×11, (b) 21×21, (c) 31×31, (d) 41×41.

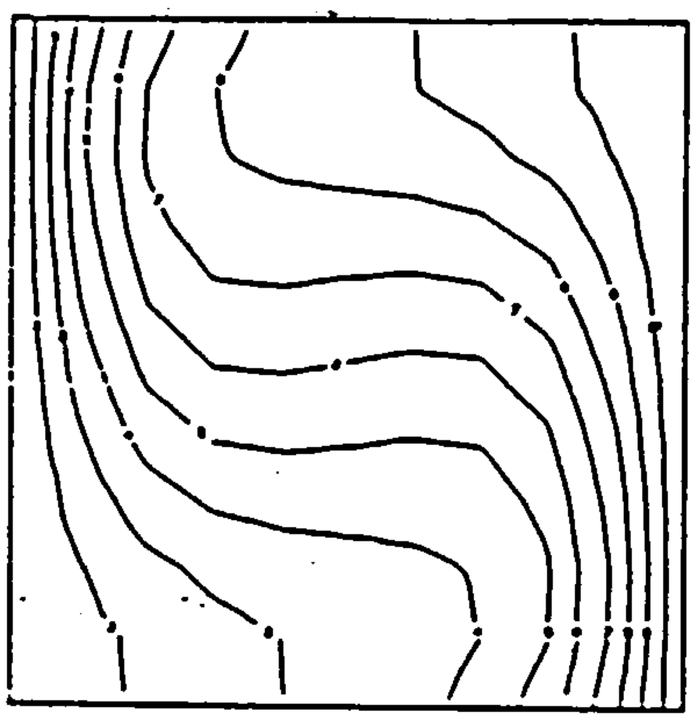

CONTOUR KEY	
1	0.000000
2	0.100000
3	0.200000
4	0.300000
5	0.400000
6	0.500000
7	0.600000
8	0.700000
9	0.800000
10	0.900000
11	1.000000

(a)

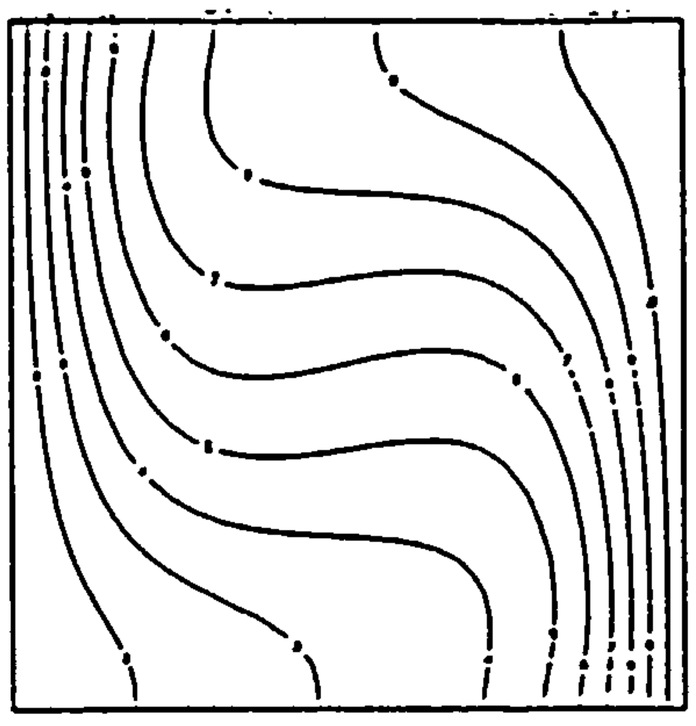

CONTOUR KEY	
1	0.000000
2	0.100000
3	0.200000
4	0.300000
5	0.400000
6	0.500000
7	0.600000
8	0.700000
9	0.800000
10	0.900000
11	1.000000

(c)

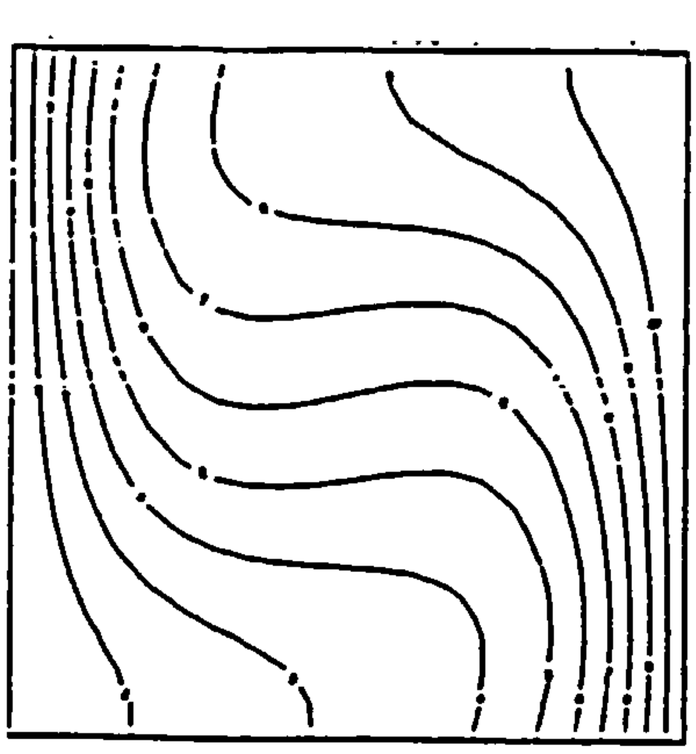

CONTOUR KEY	
1	0.000000
2	0.100000
3	0.200000
4	0.300000
5	0.400000
6	0.500000
7	0.600000
8	0.700000
9	0.800000
10	0.900000
11	1.000000

(b)

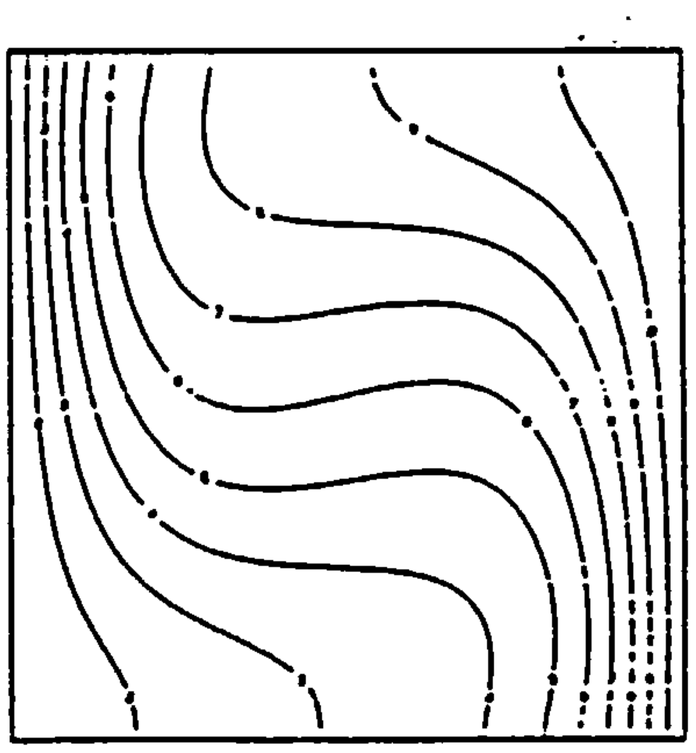

CONTOUR KEY	
1	0.000000
2	0.100000
3	0.200000
4	0.300000
5	0.400000
6	0.500000
7	0.600000
8	0.700000
9	0.800000
10	0.900000
11	1.000000

(d)

Figure 2.15: Isotherms for $\sigma = 0.733$, $R = 14660$ and different grids (a) 11×11, (b) 21×21, (c) 31×31, (d) 41×41.

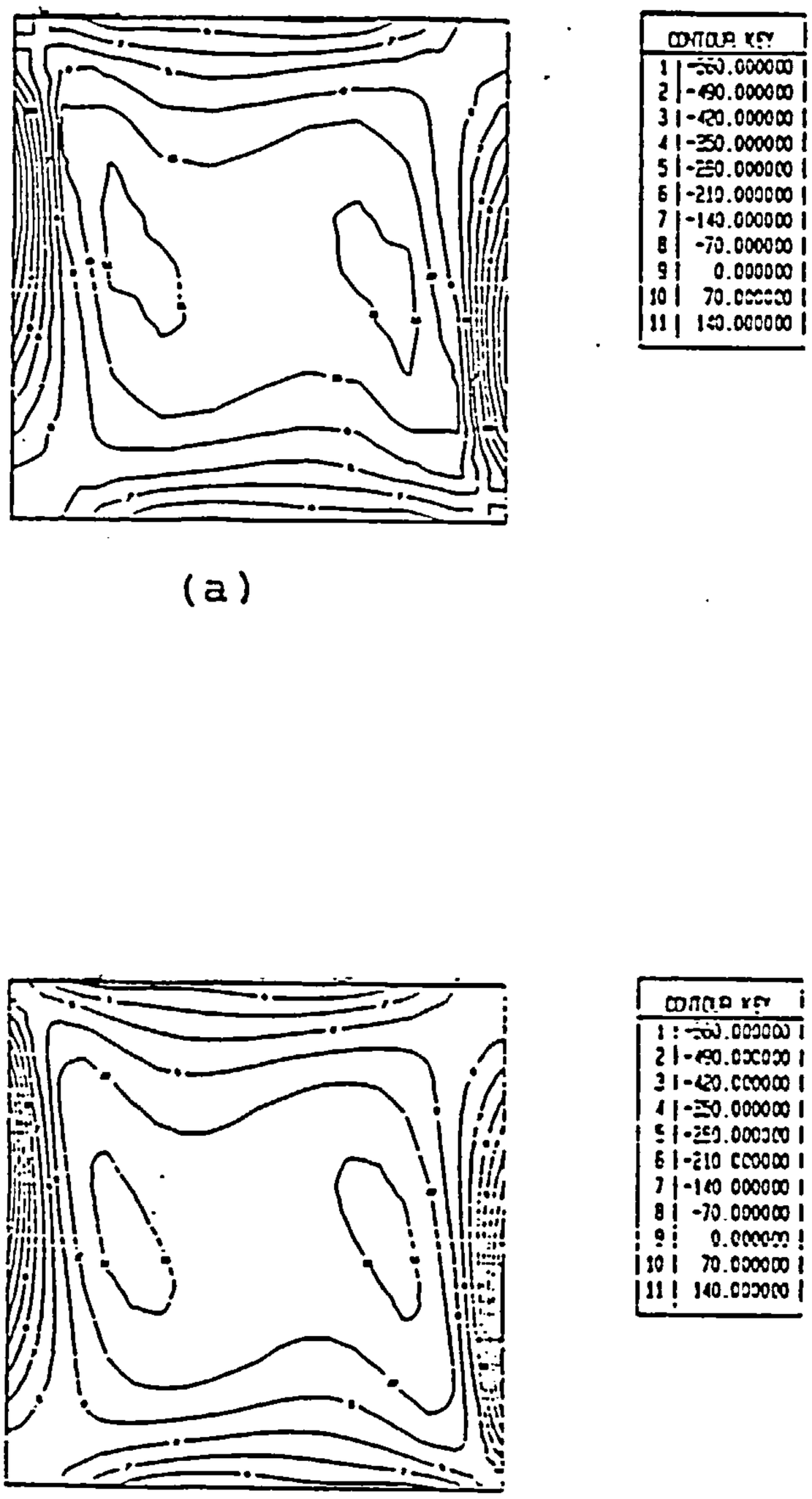

Figure 2.16: Vorticity contours for $\sigma = 0.733$, $R = 14660$ and different grids (a) 11×11, (b) 21 × 21, (c) 31 × 31, (d) 41 × 41.

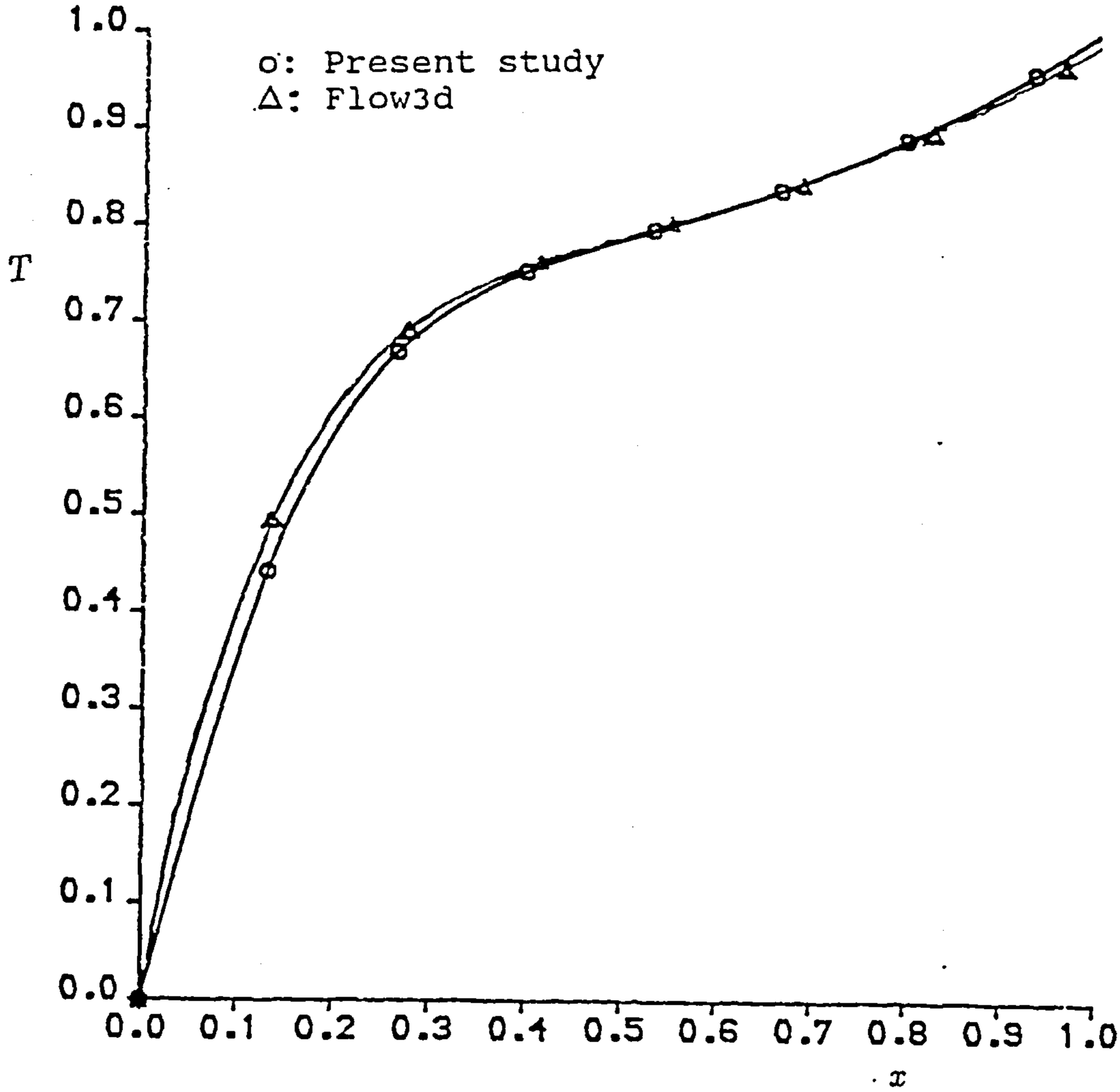

Figure 2.17: Temperature on the top wall as given by the present study and by FLOW3D for a square cavity with $\sigma = 0.733$, $R = 14660$. The grid size in each case is 41×41. The FLOW3D code is based on a finite volume method (Hybrid).

Position	Temperature	Vorticity	T/x	$4\omega/(r \times r \times R)$	Discrepancy
$r^2 = 1/800$ $x = z = 1/40$	0.01528	-10.00467	0.61116	2.18381	1.57
$r^2 = 1/1600$ $x = 1/40, z = 0$	0.01517	-7.496098	0.6068	1.0914	0.49

Table 2.1: Numerical data near the bottom cold corner.

Grid size	Total time steps	Rate of increase of time step	A	B	C	D
11×11	142		6.3512		107.6772	
21×21	211	33%	5.9592	6%	99.1966	8%
31×31	358	42%	5.9003	1%	97.6774	2%
41×41	437	18%	5.8811	0.3%	97.1338	0.6%

Table 2.2: Influence of computational grid on A: Maximum value of stream function, B: The changing rate of stream function, C: Maximum value of vorticity, D: The changing rate of vorticity.

Researchers	Grid size	Maximum value of streamfunction
Cormack, Leal and Seinfeld (1974)	21×21	3.92
Kublbeck, Merker and Straub (1980)	21×21	4.277
Drummond (1981)	17×17	4.26
	33×33	4.063
Present study	11×11	4.332
	21×21	4.064
	31×31	4.024
	41×41	4.011

Table 2.3: Comparison of results with previous work. Here the parameters are R=14660.0, $\sigma = 0.733$, and the maximum values are scaled by $10^{-4}/R$.

Chapter 3

Thermal Convection in a Tall Laterally Heated Cavity with Conducting Boundaries

3.1 Introduction

In this chapter, two-dimensional flows driven by horizontal temperature gradients in a tall cavity with conducting boundaries at the top and bottom are considered. The theoretical description of the flow in a vertical slot, based on the Boussinesq approximation, began with the analysis of the conductive regime by Batchelor (1954). The transfer of heat across the cavity by pure conduction leads to a horizontally stratified vertical core flow with a cubic velocity profile corresponding to upward motion in the hotter half of the slot and downward motion in the cooler half. It has been shown (Vest and Arpaci 1969, Korpela, Gozum and Baxi 1973, Bergholz 1978) that the flow is unstable to travelling waves for fluids of Prandtl number $\sigma > 12.7$ and to stationary cells for $\sigma < 12.7$. The critical value of the Rayleigh number for

stationary instability in the form of transverse rolls is

$$A_c \sim 7.8 \times 10^3 \sigma.$$

Here A is the Rayleigh number based on cavity width and this result is valid for almost the entire range of Prandtl numbers $\sigma > 0$ (Vest and Arpaci 1969). This result is of crucial significance in the description of the base flow in the vertical slot, for when $A > A_c$ the conductive core solution will be destroyed by an imperfect bifurcation associated with the penetration of cells from the end zones of the slot (Daniels 1985). However, for $A < A_c$, the structure of the flow in the limit as $L \rightarrow 0$ has two main regions: a parallel flow in the core region, and nonlinear convective flow near the ends of the slot where the flow must be turned. The end-zone problem first formulated by Daniels (1985) contains two parameters, A and σ, instead of the three-parameter problem considered in numerical simulations of the full slot flow by , for example, Lee and Korpela (1983) and Drummond (1985). Daniels discussed various analytical features of the end-zone problem. In particular, it was argued that the break-down of the conductive regime is associated with the inward penetration of nonlinear convective effects from the end zones. At finite and small Prandtl numbers this takes the form of an imperfect bifurcation at the critical value of the Rayleigh number,A_c, leading to the establishment of a multiple-roll state throughout the slot. For infinite Prandtl number there is a more gradual penetration in which the vertical extent of the end zones expands as $A \rightarrow \infty$, the end zones eventually filling the entire slot when $A = O(L^{-1})$, and leading to the so-called convective regime studied using boundary-layer techniques by Daniels (1987). For the conductive regime where $A = O(1)$ relatively little is known of the detailed flow structure in the end regions, where the full Oberbeck-Boussinesq equations apply. The cavity is assumed to have thermally conducting horizontal boundaries and the centro-symmetry of the overall flow (Gill 1966) implies that the solution for only one of the end regions needs to be considered.

Here, complete numerical solutions of the nonlinear end zone problem are obtained for Rayleigh numbers, A, ranging from 500 to 9000 and for a Prandtl number

$\sigma = 0.733$ equivalent to that of air.

Section 3.2 describes the mathematical formulation of the tall cavity flow, and the core solution in the limit as $L \to 0$ is given in Secton 3.3. The end-zone problem is also formulated and in Section 3.4 an efficient numerical scheme of solution is outlined, based on that developed for the rectangular cavity in Chapter 2. The numerical results and a comparison with theory are given in Section 3.5.

3.2 Formulation

The slot is defined by the region $0 \leq x^* \leq l$, $0 \leq z^* \leq h$, with the vertical sidewalls $x^* = 0$ and $x^* = l$ maintained at constant temperatures T_0 and $T_0 + \Delta T$, respectively. Non-dimensional variables of temperature, velocity, length and time are defined by

$$T^* = T_0 + \Delta T \bar{T}(x, z, t), \tag{3.2.1}$$

$$(u^*, w^*) = \frac{\kappa(\bar{u}, \bar{w})}{l}, \tag{3.2.2}$$

$$(x^*, z^*) = l(x, z), \tag{3.2.3}$$

$$t^* = \frac{l^2}{\kappa} t, \tag{3.2.4}$$

where κ is the thermal diffusivity.

By introducing a stream function $\bar{\psi}$ such that

$$\bar{u} = \frac{\partial \bar{\psi}}{\partial z}, \quad \bar{w} = -\frac{\partial \bar{\psi}}{\partial x},$$

the governing equations, subject to the Boussinesq approximation, can be written in non-dimensional form as

$$\sigma^{-1}\left(\frac{\partial \bar{\omega}}{\partial t} + J(\bar{\omega}, \bar{\psi})\right) = \nabla^2 \bar{\omega} + A \frac{\partial \bar{T}}{\partial x}, \tag{3.2.5}$$

$$\nabla^2 \bar{\psi} = -\bar{\omega}, \tag{3.2.6}$$

$$\frac{\partial \bar{T}}{\partial t} + J(\bar{T}, \bar{\psi}) = \nabla^2 \bar{T}, \tag{3.2.7}$$

where the Prandtl number σ and the Rayleigh number A are defined by

$$\sigma = \frac{\nu}{\kappa}, \quad A = \frac{g\beta \triangle T l^3}{\kappa \nu}. \tag{3.2.8}$$

Here ν is the kinematic viscosity, β is the coefficient of thermal expansion, and g is the acceleration due to gravity. It should be noted that the non-dimensionalisation used in this chapter is based on the cavity width rather than the cavity height used in Chapter 2.

The boundary conditions on the vertical sidewalls are

$$\bar{\psi} = \frac{\partial \bar{\psi}}{\partial x} = 0 \quad \text{on} \quad x = 0, 1, \tag{3.2.9}$$

$$\bar{T} = 0 \quad \text{on} \quad x = 0, \tag{3.2.10}$$

$$\bar{T} = 1 \quad \text{on} \quad x = 1. \tag{3.2.11}$$

The horizontal surfaces are assumed to be conducting so that

$$\bar{\psi} = \frac{\partial \bar{\psi}}{\partial z} = 0 \quad \text{on} \quad z = 0, H, \tag{3.2.12}$$

$$\bar{T} = x \quad \text{on} \quad z = 0, H, \tag{3.2.13}$$

where $H = h/l$ is the vertical aspect ratio of the slot. As noted by Gill (1966) the above equations and boundary conditions allow solutions which possess the centrosymmetry properties:

$$\left.\begin{aligned} \bar{\psi}(x, z, t) &= \bar{\psi}(1-x, H-z, t), \\ \bar{T}(x, z, t) &= 1 - \bar{T}(1-x, H-z, t) \\ \bar{\omega}(x, z, t) &= \bar{\omega}(1-x, H-z, t) \end{aligned}\right\} \tag{3.2.14}$$

so that in general for the steady-state solution only half of the flow domain needs to be considered; the motion is controlled by the three parameters σ,A and H.

3.3 Core Solution and End-Zone Structure

The flow in the slot is characterised by several different regimes which are identified by the relative sizes of the Rayleigh number A and the aspect ratio H, the latter being assumed large. The regime of interest here is that where A is $O(1)$ when the steady-state core flow throughout most of the slot is the conductive solution

$$\bar{T} = T_c(x), \quad \bar{\psi} = AF(x), \quad (0 < z < H), \tag{3.3.1}$$

where

$$T_c(x) = x \quad , \quad F(x) = \frac{x^2}{24}(1-x)^2. \tag{3.3.2}$$

This solution, originally given by Batchelor (1954), is actually an exact solution of the full equations (3.2.5)-(3.2.7) representing an anti-symmetric vertical motion with fluid ascending in the hotter half of the slot ($x > \frac{1}{2}$) and descending in the cooler half ($x < \frac{1}{2}$). Near the ends of the slot the fluid must be turned and the solution (3.3.1) is clearly invalid. Since the overall motion can be assumed centro-symmetric only the solution at the lower end of the slot needs to be considered, and it is clear that if A is of $O(1)$, the motion in an end zone defined by $0 \leq x \leq 1$, $0 \leq z \leq \infty$ will be governed by the steady-state version of the full nonlinear Boussinesq equations (3.2.5)-(3.2.7). It is convenient computationally to consider the time-dependent equations, so the local solution in the end zone is written

$$\left.\begin{aligned} \bar{T} &= T(x,z,t) + \cdots \\ \bar{\psi} &= \psi(x,z,t) + \cdots \\ \bar{\omega} &= \omega(x,z,t) + \cdots \end{aligned}\right\}, \quad (H \to \infty), \tag{3.3.3}$$

and then T, ψ and ω satisfy

$$\sigma^{-1}\left(\frac{\partial \omega}{\partial t} + J(\omega, \psi)\right) = \nabla^2 \omega + A\frac{\partial T}{\partial x}, \tag{3.3.4}$$

$$\nabla^2 \psi = -\omega, \tag{3.3.5}$$

$$\frac{\partial T}{\partial t} + J(T, \psi) = \nabla^2 T. \tag{3.3.6}$$

The boundary conditions on the rigid, thermally conducting cavity walls are

$$\psi = \frac{\partial \psi}{\partial z} = 0, \quad z = 0, \tag{3.3.7}$$

$$\psi = \frac{\partial \psi}{\partial x} = 0, \quad x = 0,\ 1, \tag{3.3.8}$$

$$T = 0, \quad x = 0; \quad T = 1, \quad x = 1, \tag{3.3.9}$$

$$T = x \quad , z = 0, \tag{3.3.10}$$

while as $z \to \infty$ it is required that

$$T \to T_c(x), \quad \psi \to AF(x), \quad (z \to \infty) \tag{3.3.11}$$

in order that the solution matches smoothly with that in the core. It is seen that the end-zone problem (3.3.4)-(3.3.11) is controlled by two parameters, the Rayleigh number A and the Prandtl number σ and that for general values of these parameters in the range $A \geq 0, \quad \sigma \geq 0$ a numerical solution is required. This is discussed in the next section.

3.4 Numerical Scheme for the End-Zone Problem

The numerical scheme developed in Chapter 2 for the finite cavity can be adapted to solve the end-zone problem as the governing equations are the same and the boundary conditions just require modification to cater for the outer form (3.3.11) at $z = \infty$. This is handled by a finite truncation of z so that the condition

$$T = T_c(x), \quad \psi = AF(x), \tag{3.4.1}$$

is applied in the computational domain at $z = z_\infty < \infty$. It is then necessary to ensure that z_∞ is chosen sufficiently large that the computed solution does indeed approximate the actual solution of (3.3.4)-(3.3.11).

The thermal boundary conditions can be stated in discretized form as

$$T_{i,0} = i\Delta x, \quad T_{i,N_z} = i\Delta x, \quad (i = 0, 1, 2, ..., N_x) \tag{3.4.2}$$

$$T_{0,j} = 0, \quad T_{N_x,j} = 1, \quad (j = 0, 1, 2, ..., N_z) \tag{3.4.3}$$

for all time levels where $N_z = z_\infty/\Delta z$, $N_x = \frac{1}{\Delta x}$ and Δx and Δz are the space steps.

For the vorticity, the boundary conditions derived in Chapter 2 are used on the finite cavity walls and for the outer condition

$$\omega_{i,N_z} = -AF''(i\Delta x), \quad (i = 0, 1, 2, ..., N_x) \tag{3.4.4}$$

is used at all time levels.

Finally , for the stream function , ψ, conditions (3.3.7), (3.3.8) and (3.4.1) give

$$\psi_{0,j} = 0, \quad \psi_{N_x,j} = 0, \quad (j = 0, 1, 2, ..., N_z) \tag{3.4.5}$$

$$\psi_{i,0} = 0, \quad \psi_{i,N_z} = AF(i\Delta x), \quad (i = 0, 1, 2, ..., N_x) \tag{3.4.6}$$

at all time levels.

Some guidance on the choice of the outer boundary z_∞ is provided by results of an eigenvalue analysis of the outer condition (3.3.11) by Daniels (1985). This shows that the outer forms $T_c = x$ and $AF(x)$ are approached generally through a behaviour of the form

$$T \sim x + O(e^{-\alpha z}), \quad \psi \sim A\{F(x) + O(e^{-\alpha z})\} \tag{3.4.7}$$

as $z \to \infty$ where, for $A < A_c$, the leading eigenvalue α has positive real part and varies from the value π at $A = 0$ to zero as $A \to \infty$, with

$$\alpha \sim 2.58 \times 10^3 A^{-1} \quad (A \to \infty)$$

(Daniels 1985). This latter result indicates an e-folding decay length for the end zone of $z \sim 3.88 \times 10^{-4} A$ so that for large values of A, the outer boundary of the computational domain must be increased accordingly.

In order to determine the heat transfer along the cold, hot and bottom walls of the cavity, the local heat fluxes are considered in dimensionless form:

$$Nu_{loc} = \frac{\partial T}{\partial x}|_{x=0} \quad ,$$

$$Nu_{loc} = \frac{\partial T}{\partial x}|_{x=1} \quad ,$$

$$Nu_{loc} = \frac{\partial T}{\partial z}|_{z=0} \quad .$$

Numerically these are approximated by Taylor series expansions. On the cold wall

$$\frac{\partial T}{\partial x}\,|_{x=0} = \frac{18T_{1,j} - 9T_{2,j} + 2T_{3,j} - 11T_{0,j}}{6\Delta x}, \quad (j = 0, 1, 2, ..., N_z) \tag{3.4.8}$$

where $T_{0,j} = 0$; on the hot wall

$$\frac{\partial T}{\partial x}\,|_{x=1} = -\frac{18T_{N_x-1,j} - 9T_{N_x-2,j} + 2T_{N_x-3,j} - 11T_{0,j}}{6\Delta x}, \quad (j = 0, 1, 2, ..., N_z), \tag{3.4.9}$$

where $T_{N_x,j} = 1$; on the bottom wall

$$\frac{\partial T}{\partial z}\,|_{z=0} = \frac{18T_{i,1} - 9T_{i,2} + 2T_{i,3} - 11T_{i,0)}}{6\Delta z}, \quad (i = 0, 1, 2, ..., N_x), \tag{3.4.10}$$

where $T_{i,0} = i\Delta x$.

Average heat fluxes for each wall may then be defined as

$$\alpha = \int_0^\infty (\frac{\partial T}{\partial x}|_{x=0} - 1)dz \quad , \quad x = 0, \tag{3.4.11}$$

$$\beta = \int_0^\infty (\frac{\partial T}{\partial x}|_{x=1} - 1)dz \quad , \quad x = 1, \tag{3.4.12}$$

$$\gamma = \int_0^1 \frac{\partial T}{\partial z}|_{z=0} dx, \quad z = 0. \tag{3.4.13}$$

where α and β represent contributions relative to a state of pure conduction. Integration of the energy equation (3.3.6) for steady-state motion in the end zone and use of the boundary conditions (3.3.8) gives

$$\int_0^\infty (\frac{\partial T}{\partial x}|_{x=1} - 1)dz - \int_0^\infty (\frac{\partial T}{\partial x}|_{x=0} - 1)dz + \int_0^1 \frac{\partial T}{\partial z}|_{z=\infty} dx - \int_0^1 \frac{\partial T}{\partial z}|_{z=0} dx = A \int_0^1 F(x) \frac{dT_c}{dx} dx \tag{3.4.14}$$

and using (3.3.11) yields

$$\beta - \alpha - \gamma = \frac{A}{720}. \tag{3.4.15}$$

This relation can be used as a check on the accuracy of the computation. Simpson's rule is used to calculate the integrals (3.4.11)- (3.4.13).

The following initial conditions are used to start the computation:

$$\left.\begin{aligned} T &= x \\ \psi &= 0 \\ \omega = u &= w = 0 \end{aligned}\right\} (0 \leq x \leq 1), \quad (0 \leq z < z_\infty) \tag{3.4.16}$$

$$\left.\begin{aligned} T &= x \\ \psi &= AF(x) \\ \omega &= -AF''(x) \\ u &= w = 0 \end{aligned}\right\} (0 \leq x \leq 1), \quad (z = z_\infty) \tag{3.4.17}$$

and the overall scheme of computation is the same as that set out in Chapter 2 for the finite cavity.

3.5 Numerical Results and Discussion

Numerical results were obtained for a Prandtl number $\sigma = 0.733$ equivalent to that of air and for a range of Rayleigh numbers $500 \leq A \leq 9000$. For low Rayleigh numbers a 30×90 grid was used with an outer boundary $z_\infty = 3$, while for higher Rayleigh numbers, $(A \geq 3000)$, a 25×175 grid was used with an outer boundary $z_\infty = 7$. In the numerical solution for low Rayleigh numbers it is relatively easy to achieve good accuracy and fast convergence to the steady state solution. At higher Rayleigh numbers accuracy is affected mainly by the formation of boundary layer structures near the walls and although accuracy can be improved by use of a finer grid, the smaller time step needed to maintain stability affects the rate of convergence. In general it is necessary to make a compromise in the choice of grid size and more sophisticated numerical techniques would be needed to treat the boundary layer structures which arise at very high Rayleigh numbers.

Contours of the steady state stream function, vorticity and temperature for different Rayleigh numbers are given in Figures 3.1-3.5. These contours indicate that at low Rayleigh numbers ($A = 500$), the core solution is valid throughout most of the cavity except in roughly square areas near the ends where the flow turns direction. As the Rayleigh number increases, the nonlinearity of the end-zone flow gradually spreads vertically, and non-parallel flow occurs over an extended range of z, typically $0 < z < 4$ when $A = 5000$ (Figure 3.3). At high Rayleigh numbers ($A > 5000$) the temperature field shows evidence of the development of a boundary-layer structure at the lower corner near the hot wall, which acts as a strong source of vorticity. Since buoyancy forces are proportional to the horizontal temperature gradient, this region produces vigorous convection up the hot wall, with most of the temperature variation occurring near the wall. Across the base region of the cavity, the isotherms are deflected towards the hot wall, indicating a tendency to align with the flow, characteristic of domination by convection in this part of the flow.

Figure 3.4 shows that when $A = 7000$ a multiple-cell structure begins to appear in the streamline field which at $A = 9000$ has developed to the stage where the outer boundary condition can no longer be applied consistently. These results are in good agreement with linear stability theory based on the breakdown of the parallel core flow. Small disturbances $\tilde{T}$ and $\tilde{\psi}$ of arbitrary two-dimensional form are superimposed upon the basic state in the following manner:

$$T = x + \tilde{T} \quad \psi = A(F + \tilde{\psi}).$$

The general solution of the linearised stability equations can then be written as a superposition of Fourier modes which for stationary convection take the form

$$(\tilde{\psi}(x,z), \tilde{T}(x,z)) = (\phi(x), \theta(x))exp(i\alpha z) \tag{3.5.1}$$

where α is the vertical wave number. Thus

$$T = x + \theta(x)exp(i\alpha z), \tag{3.5.2}$$

$$\psi = A(F + \phi(x))exp(i\alpha z), \tag{3.5.3}$$

where, from (3.3.4)-(3.3.6), θ and ϕ satisfy

$$\theta'' - \alpha^2\theta = -i\alpha A F'\phi \tag{3.5.4}$$

$$\phi'''' - 2\alpha^2\phi'' + \alpha^4\phi = \theta' - \frac{i\alpha A}{\sigma}\{(-\alpha^2 F' - F''')\phi + F'\phi''\}. \tag{3.5.5}$$

From (3.3.8)-(3.3.9) the appropriate boundary conditions are

$$\theta = \phi = \phi' = 0 \quad \text{on} \quad x = 0, 1. \tag{3.5.6}$$

The system (3.5.3)-(3.5.5) has been previously considered by Vest and Arpaci (1969), Hart (1970), Korpela, Gozum and Baxi (1973), Bergholz(1978) and more recently by Daniels (1985). Real values of the wave number, corresponding to multi-cellular convection, occur for Rayleigh numbers $A > A_c(\sigma)$ where

$$A_c \approx 7880\sigma$$

and the corresponding critical value of the wavenumber is

$$\alpha_c \approx 2.8.$$

As explained by Daniels (1985), the multi-cellular motion is actually forced to occur as part of the steady state solution in the end zone, as the eigenvalue corresponding to α_c is one of the infinite family of eigenvalues generated by the need for the end-zone solution to adjust from the parallel core flow to the boundary conditions (3.3.7)-(3.3.10).

The present numerical study includes two cases for which multi-cellular flow should be present, given that $A_c = 5776$ when $\sigma = 0.733$. These are the cases $A = 7000$ and $A = 9000$ where secondary vortices are indeed observed in the computation (Figures 3.4, 3.5). The wavelength just discernible in Figure 3.5, $z \approx 2.5$ is reasonably consistent with the critical wavelength $2\pi/\alpha_c = 2.24$ predicted by the linear stability analysis.

Figures 3.6-3.8 illustrate the local Nusselt numbers with $\sigma = 0.733$ for different Rayleigh numbers on the cold, hot and bottom walls of the cavity. On the bottom

wall, the position of the maximum value of Nu moves from $x \approx 0.5$ at $A = 500$ to $x \approx 0.68$ at $A = 9000$, and on the hot and cold walls, the local Nusselt number curves change sharply near the bottom of the cavity, reaching their maximum and minimum values at around $x = 0.5$ before approaching their limiting core values (if $A < A_c$) on a longer scale in z which increases as A increases, consistent with the result (3.4.15). For $A > A_c$, the solutions show the emergence of oscillatory behaviour associated with multi-cell convection and the outer boundary condition is no longer approached smoothly.

The results shown in Figures 3.6-3.8 were found to be in good agreement with the integral property (3.4.15) of the end zone system, and as A increases the transfer of heat through the end zone is seen to be dominated largely by the increased inward transfer, relative to the conductive state, through both the bottom wall and the hot sidewall. On the cold sidewall the outward transfer of heat is reduced relative to that of the conductive state. As the fluid passes through the end zone the gain in heat relative to the conductive state increases as A increases, generating a more vigorous upward motion near the hot sidewall.

Figures 3.9-3.10 show the skin friction on each sidewall, indicating the rapid adjustment near the bottom of the hot wall and a much longer scale of adjustment with increasing Rayleigh number as the flow approaches the bottom of the cold wall. There is no evidence of separation near the corner. The two curves for $A = 7000$ and $A = 9000$ show strong oscillations as expected from the stability analysis.

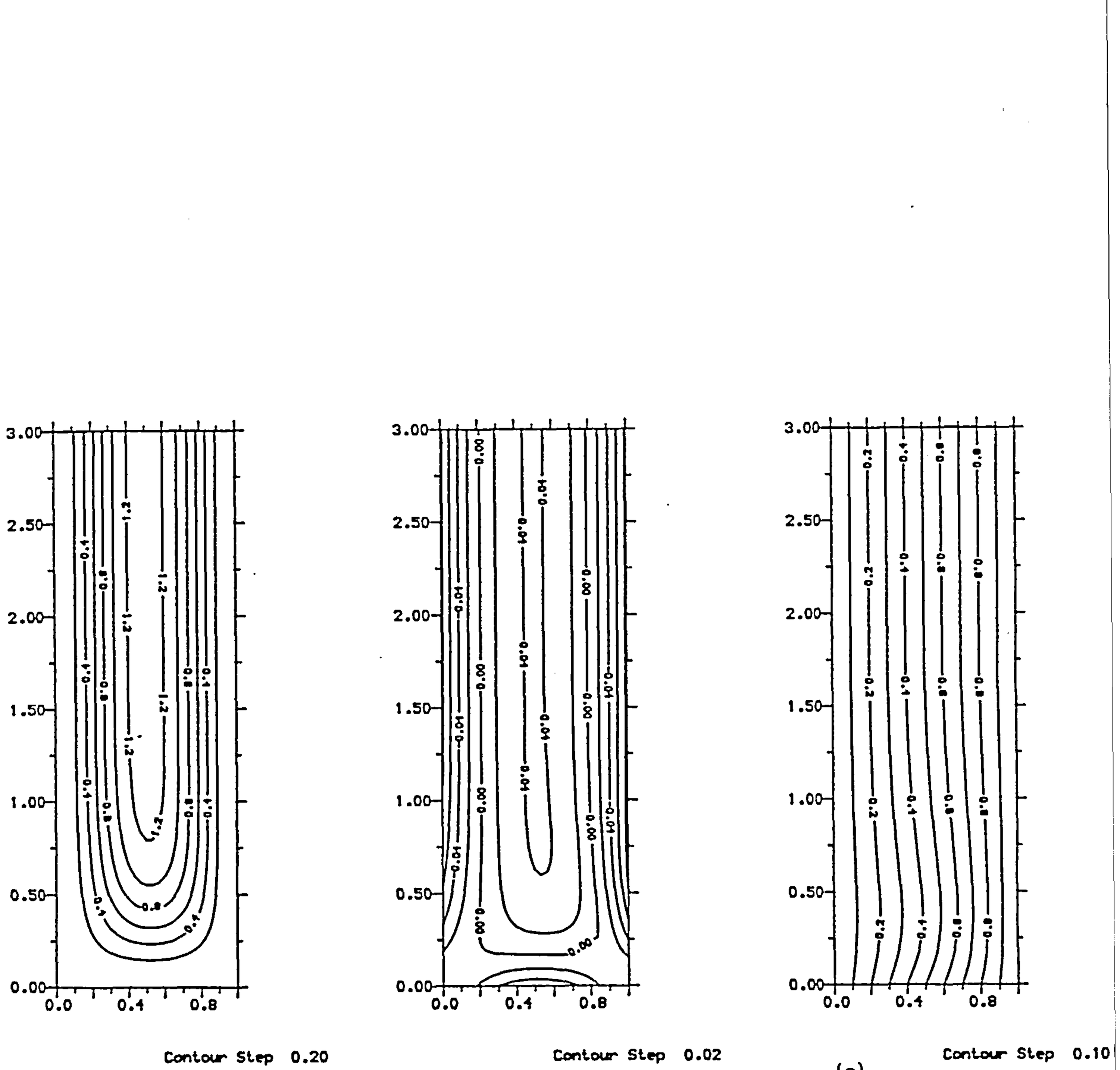

Figure 3.1: Contours of the steady-state solution for (a) stream function , (b) vorticity, (c) temperature, for $\sigma = 0.733$ and $A = 500$, using a 30×90 computational grid with $z_\infty = 3$.

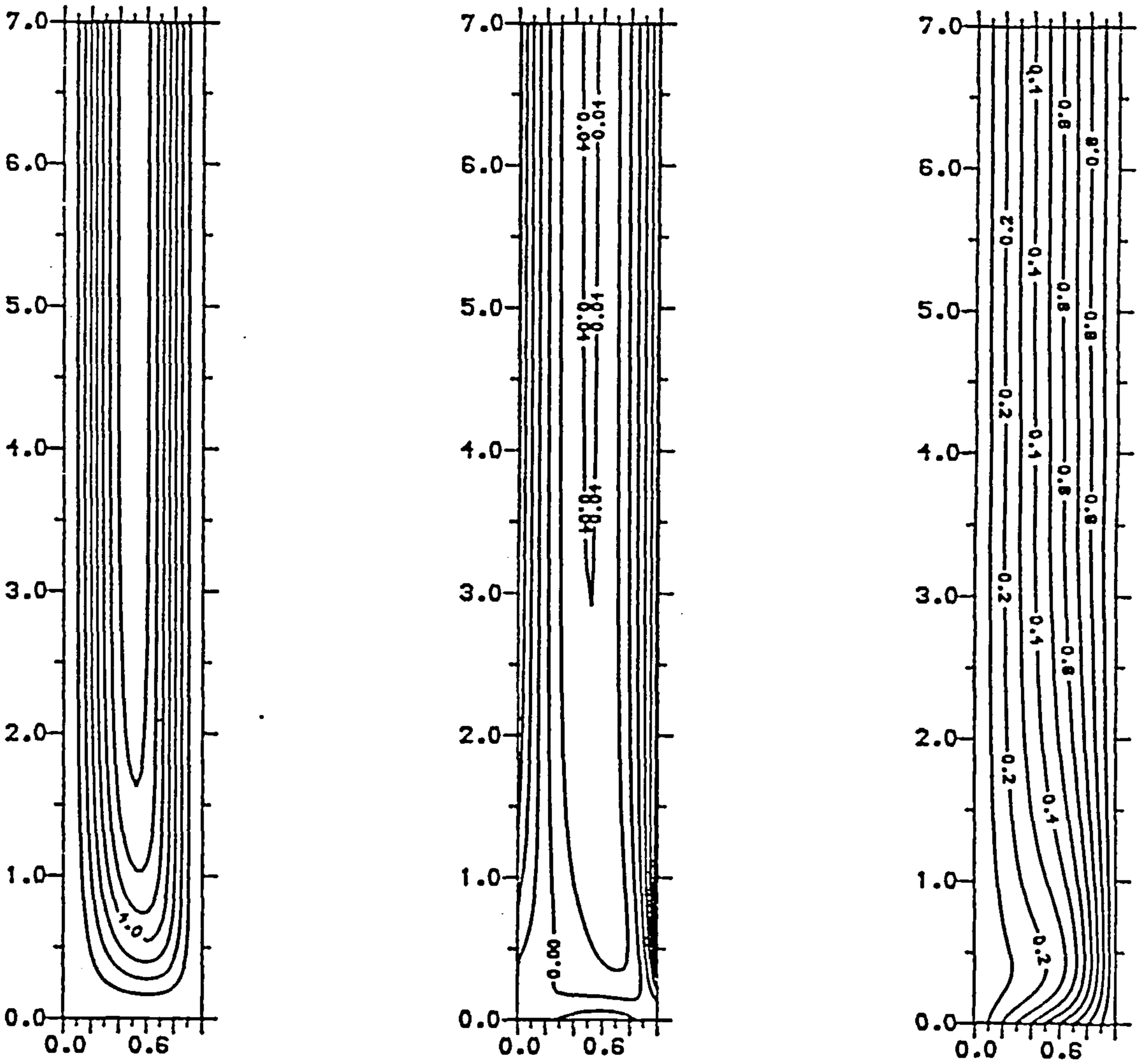

Figure 3.2: Contours of the steady-state solution for (a) stream function , (b) vorticity, (c) temperature, for $\sigma = 0.733$ and $A = 3000$, using a 25×175 computational grid with $z_\infty = 7$.

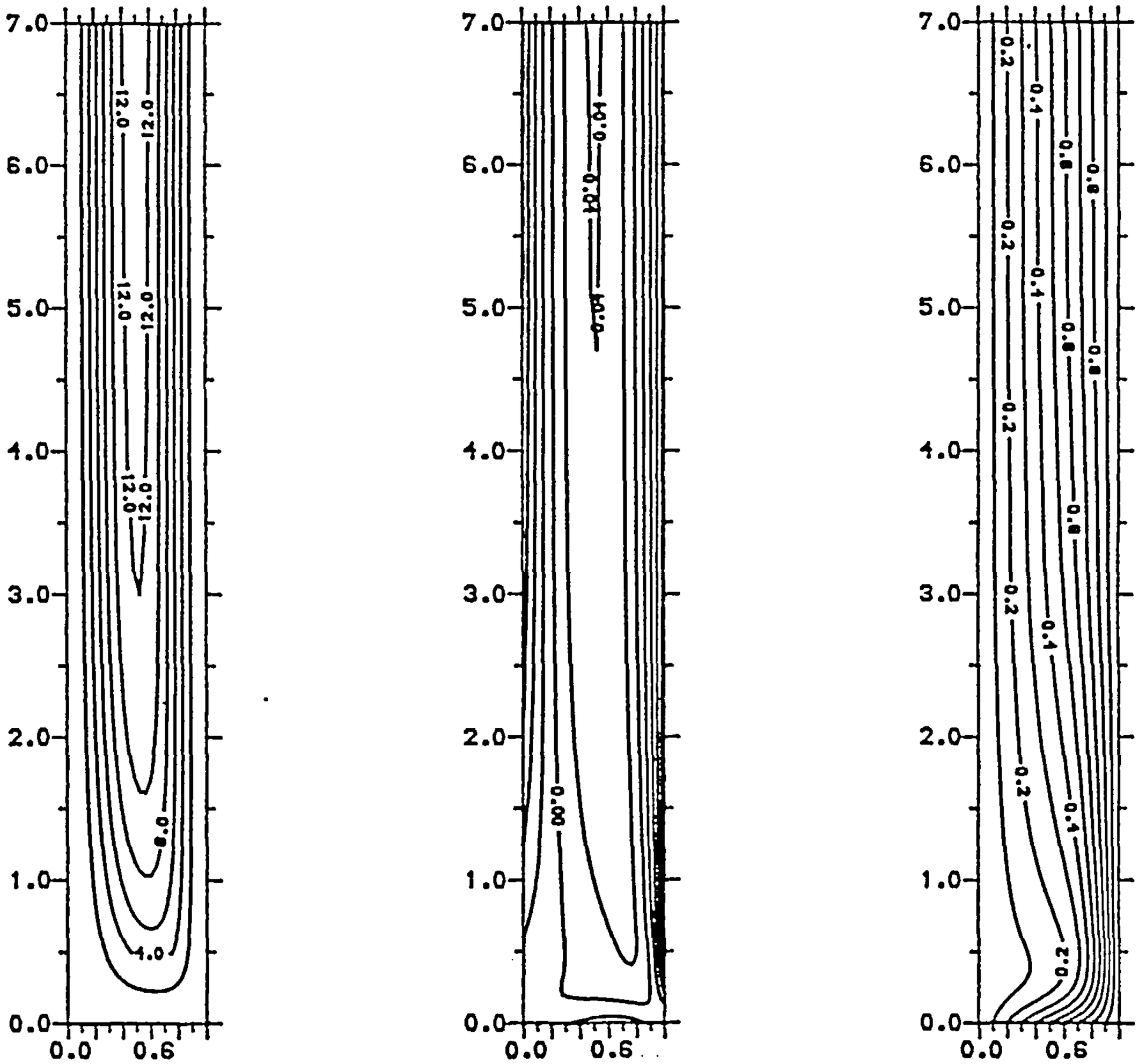

(a) (b) (c)

Figure 3.3: Contours of the steady-state solution for (a) stream function , (b) vorticity, (c) temperature, for $\sigma = 0.733$ and $A = 5000$, using a 25×175 computational grid with $z_\infty = 7$.

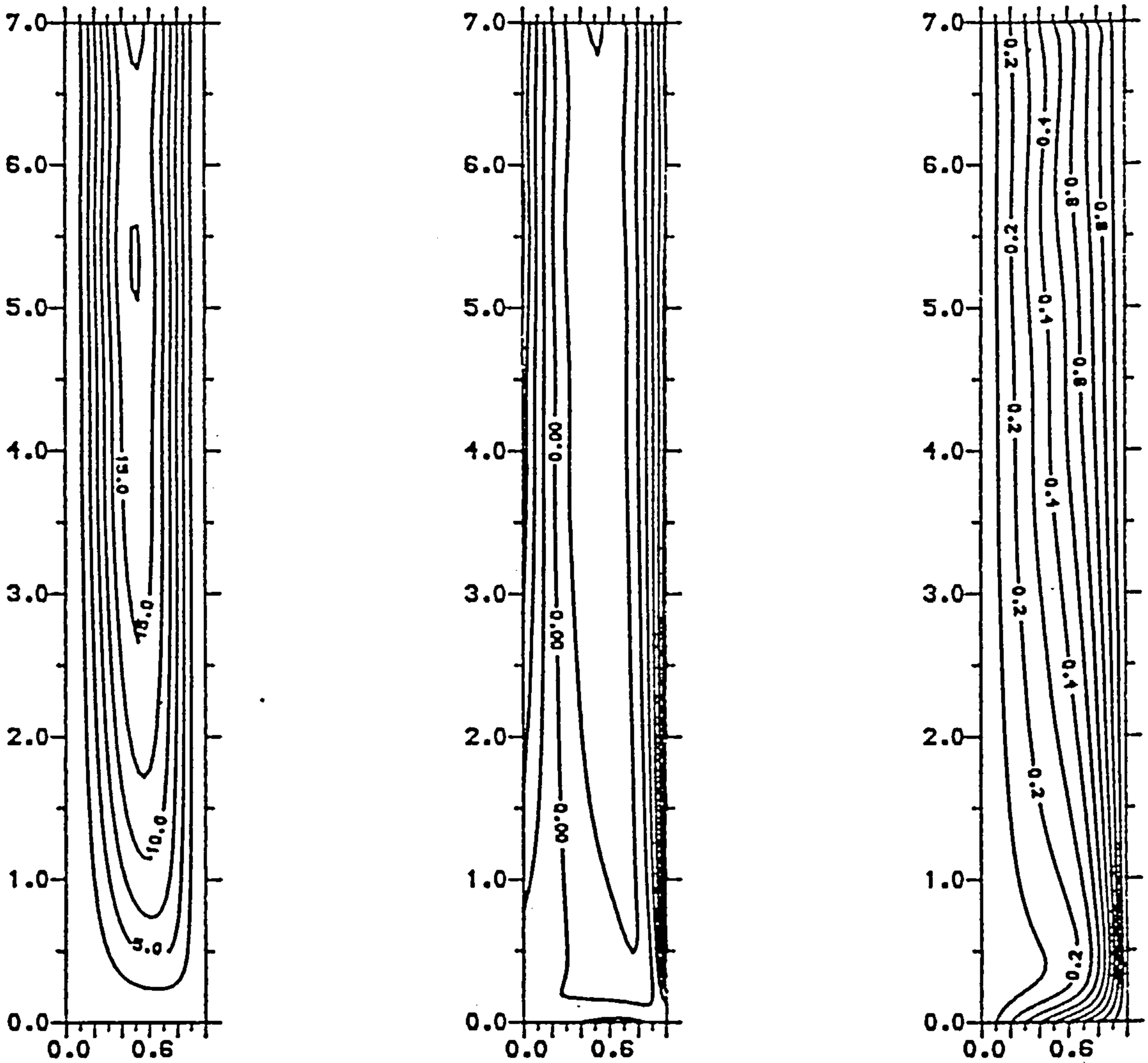

Figure 3.4: Contours of the steady-state solution for (a) stream function , (b) vorticity, (c) temperature, for $\sigma = 0.733$ and $A = 7000$, using a 25×175 computational grid with $z_\infty = 7$.

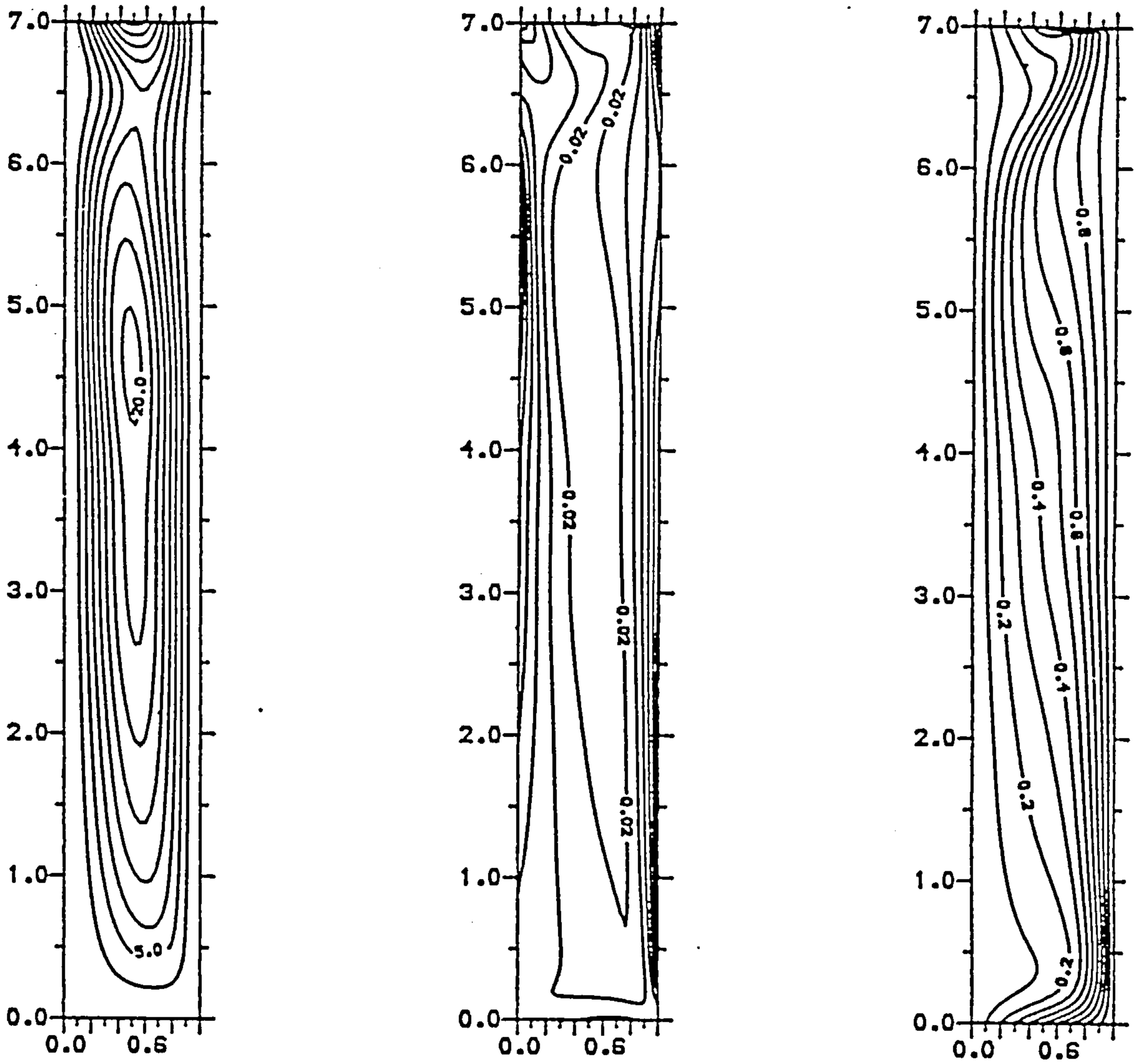

Figure 3.5: Contours of the steady-state solution for (a) stream function , (b) vorticity, (c) temperature, for $\sigma = 0.733$ and $A = 9000$, using a 25×175 computational grid with $z_\infty = 7$.

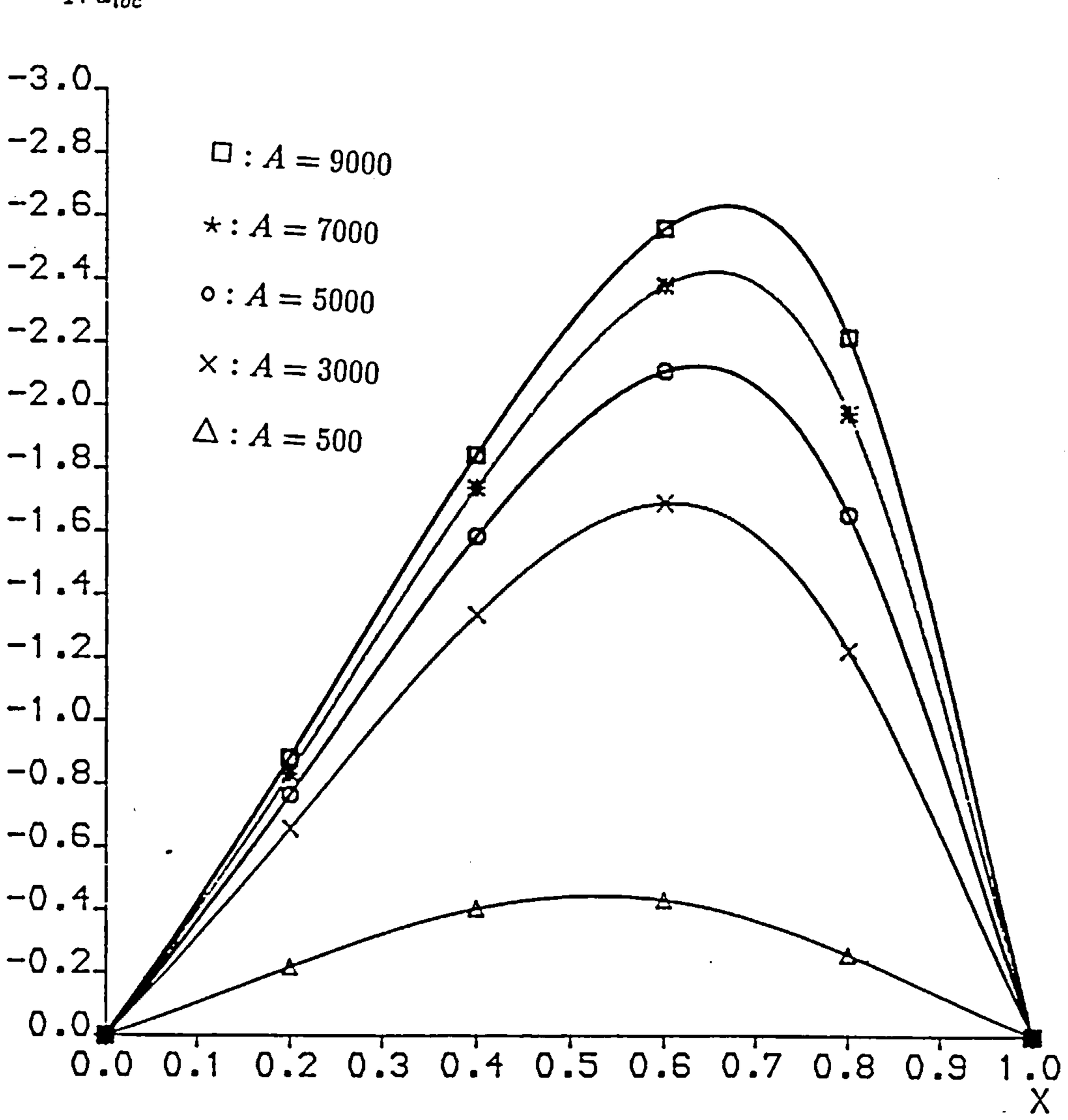

Figure 3.6: The local Nusselt number with $\sigma = 0.733$ for different Rayleigh numbers on the bottom wall for the conducting case.

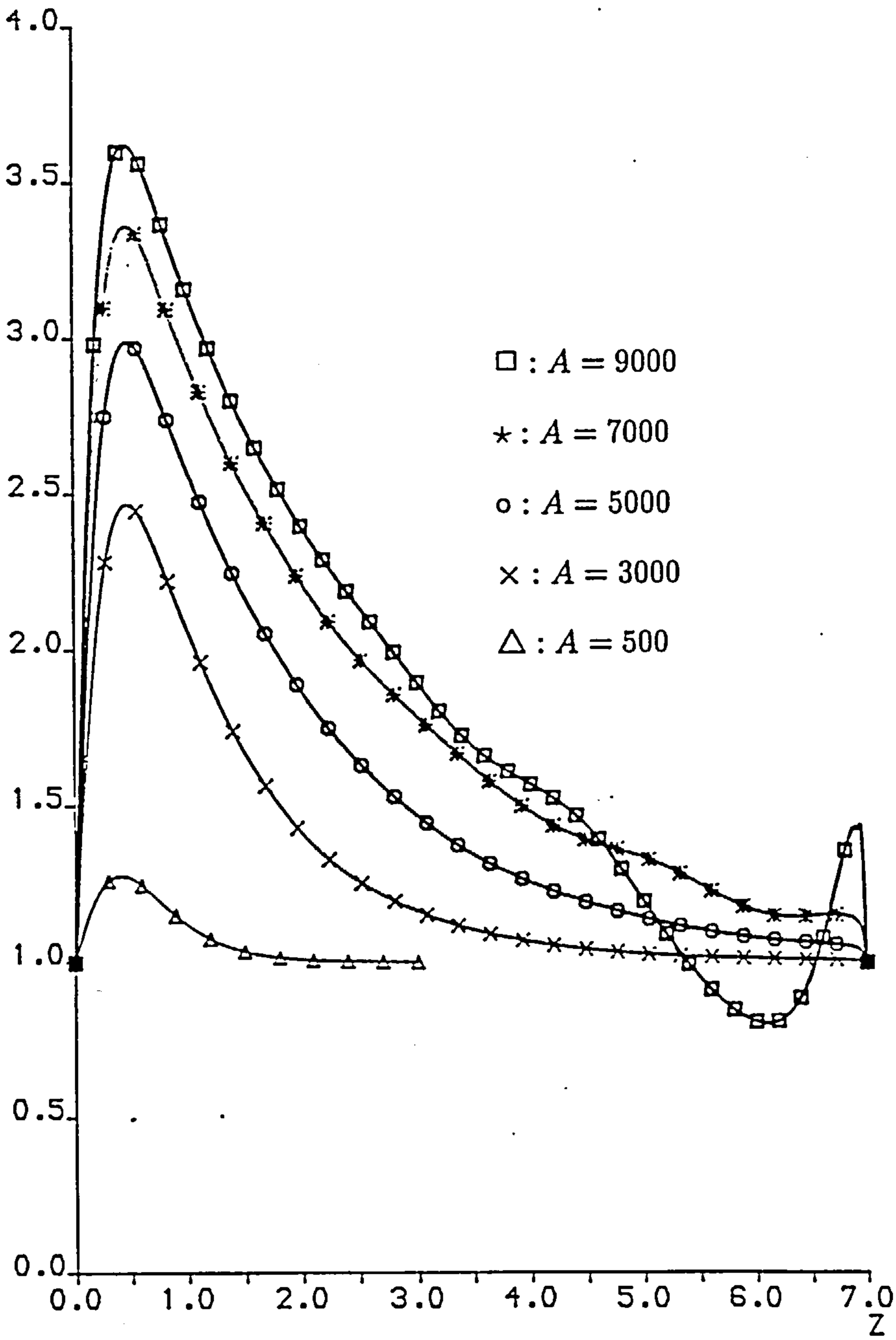

Figure 3.7: The local Nusselt number with $\sigma = 0.733$ for different Rayleigh numbers on the hot wall for the conducting case.

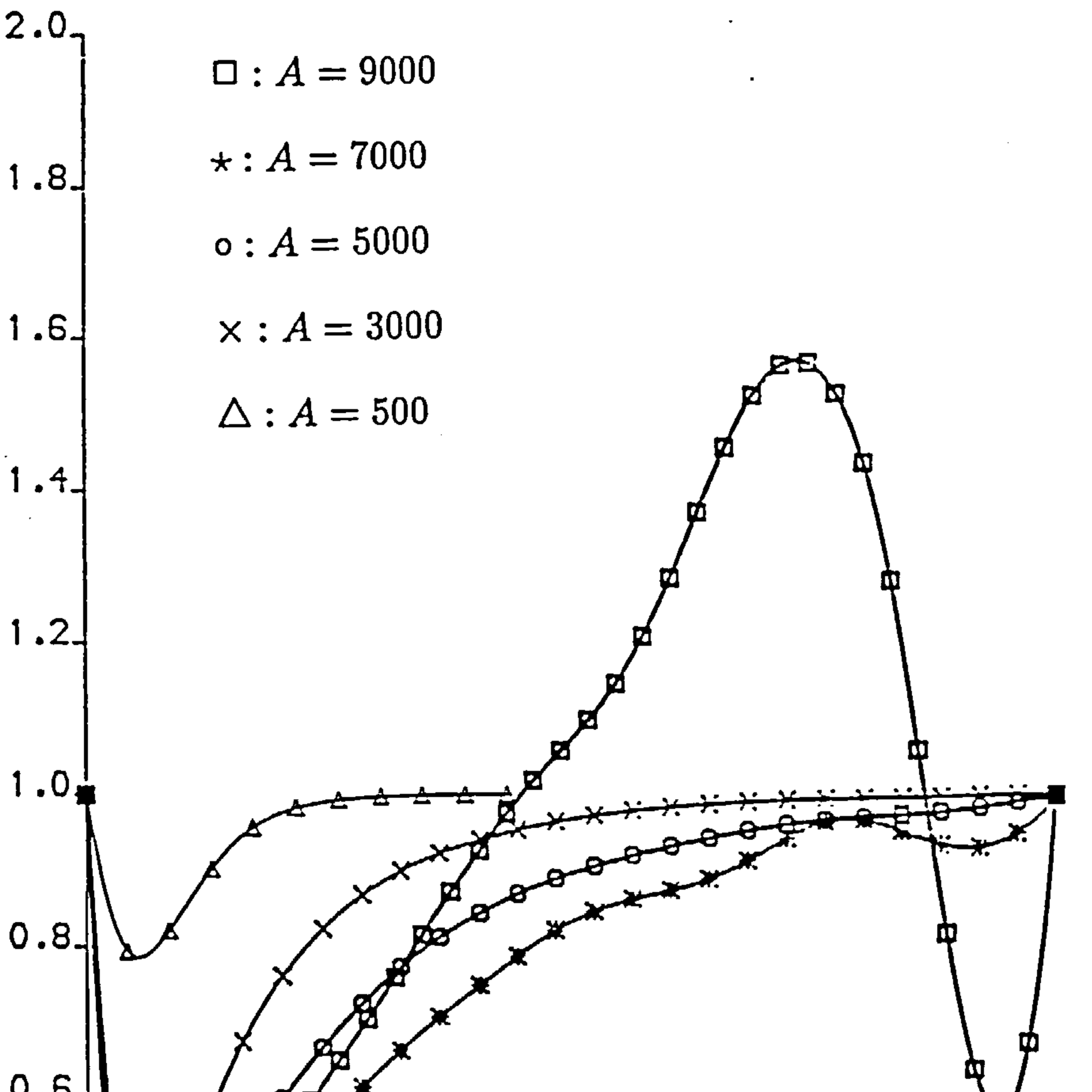

Figure 3.8: The local Nusselt number with $\sigma = 0.733$ for different Rayleigh numbers on the cold wall for the conducting case.

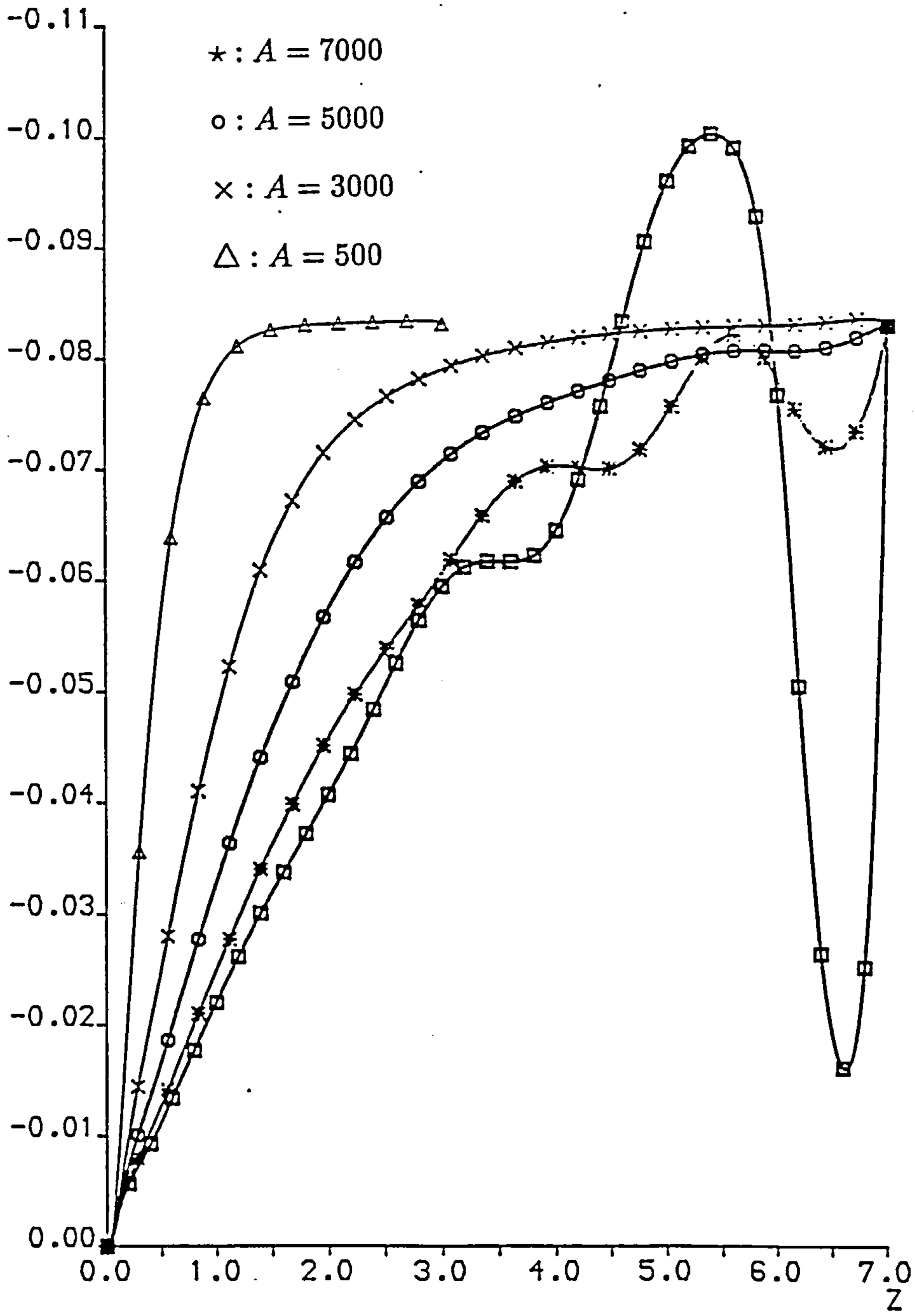

Figure 3.9: The skin friction $\partial w/\partial x \mid_{x=0}$ with $\sigma = 0.733$ for different Rayleigh numbers on the cold wall for the conducting case, which is given by vorticity function $\omega \mid_{x=0}$.

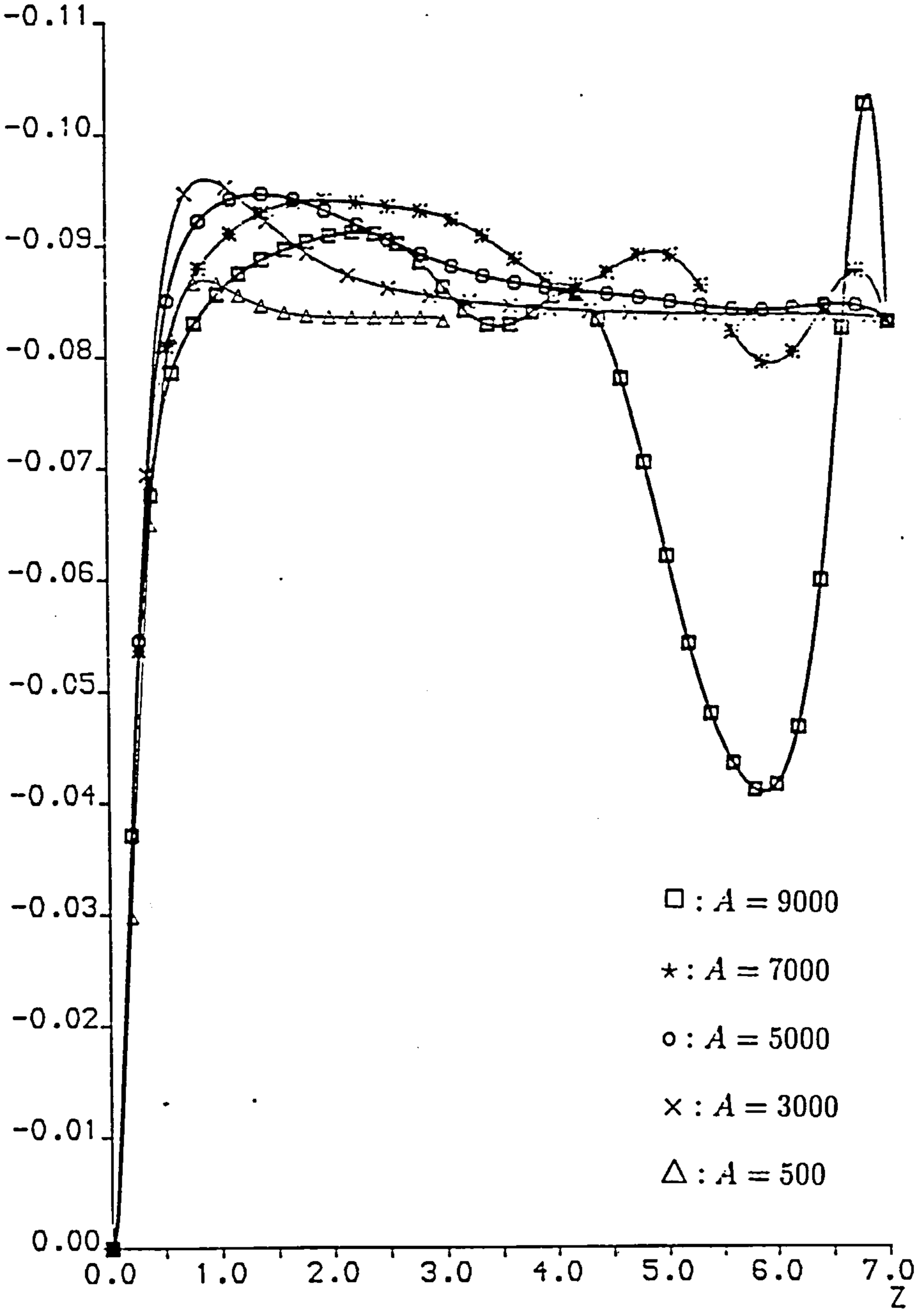

Figure 3.10: The skin friction with $\sigma = 0.733$ for different Rayleigh numbers on the hot wall for the conducting case.

Chapter 4

Thermal Convection in a Tall Laterally Heated Cavity with Adiabatic Boundaries

4.1 Introduction

In this chapter, two-dimensional flows in narrow, laterally heated vertical slots with adiabatic upper and lower boundaries are considered. Since this problem is very similar to the one discussed in Chapter 3 many of the features are the same, including both the structure of the core solution and the analysis of its stability. Thus the critical value of the Rayleigh number for stationary instability in the form of transverse rolls is

$$A_c \approx 7.8 \times 10^3 \sigma.$$

The effects of the new horizontal boundary conditions are felt only within the end zones of the cavity and in this chapter , the numerical solution of the end-zone problem is discussed in detail.

In Section 4.2, the overall flow structure is described briefly and the end-zone

problem is stated . Properties of the solution are discussed including the heat transfer and in Section 4.3 a numerical scheme similar to that used in the conducting case is described. Numerical results are obtained for a wide range of Rayleigh numbers, up to 70000, and for Prandtl numbers corresponding to air ($\sigma = 0.733$) and water ($\sigma = 6.983$). Contributions to the heat transfer from within the end zone allow the overall Nusselt number to be calculated and compared with results obtained by other workers using either full numerical simulations of the cavity flow or experimental methods. The results of the computations are also compared with the linear stability analysis of the core flow. The results for air are described in Section 4.4 and for water in Section 4.5.

4.2 Core Solution and End-Zone Structure

As in Chapter 3, the governing equations, subject to the Boussinesq approximation, can be written in the non-dimensional form (3.2.5)-(3.2.7) and the boundary conditions on the sidewalls in the form (3.2.9)-(3.2.11). The horizontal surfaces are now assumed to be insulated so that in addition

$$\bar{\psi} = \frac{\partial \bar{\psi}}{\partial z} = 0 \quad \text{on} \quad z = 0, H \quad , \tag{4.2.1}$$

$$\frac{\partial \bar{T}}{\partial z} = 0 \quad \text{on} \quad z = 0, H \quad , \tag{4.2.2}$$

where $H = h/l$ is the vertical aspect ratio of the slot. The steady-state solution of the above equations and boundary conditions can still be assumed centrosymmetric (Gill 1966), so that only half of the flow domain needs to be considered.

When the vertical aspect ratio H is large, and A is order one, the exact steady-state conductive core solution of (3.2.5)–(3.2.7) is

$$\bar{T} = T_c(x), \quad \bar{\psi} = AF(x) \tag{4.2.3}$$

where $T_c(x) = x$ and $F(x) = \frac{x^2}{24}(1-x)^2$. In the end-zone at the bottom of the slot

$$\bar{T} = T(x,z,t) + \cdots, \quad \bar{\psi} = \psi(x,z,t) + \cdots, \quad (H \to \infty)$$

and the end-zone problem is to solve

$$\sigma^{-1}(\frac{\partial \omega}{\partial t} + J(\omega, \psi)) = \nabla^2 \omega + A\frac{\partial T}{\partial x}, \tag{4.2.4}$$

$$\nabla^2 \psi = -\omega, \tag{4.2.5}$$

$$\frac{\partial T}{\partial t} + J(T, \psi) = \nabla^2 T, \tag{4.2.6}$$

subject to

$$\psi = \frac{\partial \psi}{\partial z} = 0, \quad z = 0, \tag{4.2.7}$$

$$\psi = \frac{\partial \psi}{\partial x} = 0, \quad x = 0, 1, \tag{4.2.8}$$

$$T = 0, \quad x = 0; \quad T = 1, \quad x = 1, \tag{4.2.9}$$

$$\frac{\partial T}{\partial z} = 0, \quad z = 0, \tag{4.2.10}$$

$$T \to T_c(x), \quad \psi \to AF(x) \quad (z \to \infty). \tag{4.2.11}$$

In general this system must be solved by a numerical method which is discussed in the next section; only minor modification is required to the scheme outlined in Chapter 3.

The local Nusselt numbers for the cold and hot walls may be defined by

$$Nu_{loc} = \frac{\partial T}{\partial x}|_{x=0} dz \quad , \tag{4.2.12}$$

$$Nu_{loc} = \frac{\partial T}{\partial x}|_{x=1} dz \tag{4.2.13}$$

and then the average heat flux for each wall of the end zone, relative to a state of pure conduction, is represented by

$$\alpha = \int_0^\infty (\frac{\partial T}{\partial x}|_{x=0} - 1) dz \quad , \quad x = 0, \tag{4.2.14}$$

$$\beta = \int_0^\infty (\frac{\partial T}{\partial x}|_{x=1} - 1) dz \quad , \quad x = 1. \tag{4.2.15}$$

Integration of the energy equation (4.2.6) for steady-state motion in the end zone and use of the boundary conditions (4.2.8) and (4.2.10) gives

$$\int_0^\infty (\frac{\partial T}{\partial x}|_{x=1} - 1) dz - \int_0^\infty (\frac{\partial T}{\partial x}|_{x=0} - 1) dz = A \int_0^1 F(x) \frac{dT_c}{dx} dx \tag{4.2.16}$$

from which it follows that

$$\beta - \alpha = \frac{A}{720} \quad . \tag{4.2.17}$$

This relation can be used as a check on the accuracy of the computational solution.

In addition, the values of α and β, together with the centrosymmety of the flow, can be used to provide the overall Nusselt number for the cold wall of the cavity

$$Nu = \int_0^H \frac{\partial T}{\partial x}|_{x=0} dz. \tag{4.2.18}$$

This integral comprises three parts, arising from the main core contribution, where (4.2.3) applies, together with the convective corrections arising from each end zone. Thus

$$Nu = \int_0^\infty (\frac{\partial \bar{T}}{\partial x}|_{x=0} - 1)dz + \int_0^H dz + \int_{H-\infty}^H (\frac{\partial \bar{T}}{\partial x}|_{x=0} - 1)dz$$

but for a centrosymmetric steady-state solution the third integral evaluated within the upper end-zone can be replaced by an integral over the hot wall of the lower end zone. Thus

$$\begin{aligned} Nu &\sim \int_0^\infty (\frac{\partial T}{\partial x}|_{x=0} - 1)dz + \int_0^H dz + \int_0^\infty (\frac{\partial T}{\partial x}|_{x=1} - 1)dz, \quad (H \to \infty), \\ &\sim H + \alpha + \beta \quad , \quad (H \to \infty). \end{aligned} \tag{4.2.19}$$

4.3 Numerical Scheme for the End-Zone Problem

The system (4.2.4)-(4.2.11) was solved numerically on the computational domain $0 \leq x \leq 1, 0 \leq z \leq z_\infty$ using the method outlined in Chapter 3. Various grid sizes and outer boundaries were used to find solutions for a range of Rayleigh numbers. As in the conducting case, the extent of the end zone increases with increasing Rayleigh number, requiring a larger outer boundary to be used. This increases the amount of computational work for a given spatial step size. Coarser computational grids can be used but there must be sufficient grid points to cover thin boundary layers which

develop near the hot wall at large Rayleigh numbers. Because the solution structure involves both short and long scales for large Rayleigh numbers the computational requirements become severe. One effective way to save computational time is to use the numerical results for a low Rayleigh number computation as the initial state to compute the solution for a higher Rayleigh number, provided the same grid size is used. This saved alot of computational time. The numerical scheme has second-order accuracy both in space and time. The final steady state was usually achieved by requiring $\max_{i,j} |T_{i,j}^{k+1} - T_{i,j}^{k}| < 10^{-6}$ and $\max_{i,j} |\omega_{i,j}^{k+1} - \omega_{i,j}^{k}| < 10^{-6}$ where k is the time index.

The numerical scheme described in Chapter 3 is used , except that the boundary condition on the bottom wall is replaced by (4.2.11). Thus for the stream function and vorticity

$$\psi_{i,0} = 0 \quad , i = 0, 1, \cdots, N_x, \tag{4.3.1}$$

$$-\omega_{i,0} = \frac{1}{2(\Delta z)^2}(8\psi_{i,1} - \psi_{i,2}), \quad i = 1, 2, \cdots, N_x, \tag{4.3.2}$$

for all time levels, while the approximation for the temperature is the same as that introduced in Section 2.3 For example, when the time level index $k = 2$,

$$T_{i,0}^{2} = \frac{\frac{\Delta t}{(\Delta x)^2}(T_{i+1,0}^{2} - T_{i-1,0}^{2}) + \frac{\Delta t}{(\Delta z)^2} 2T_{i,1}^{2} + T_{i,0}^{1}}{\tilde{x}}, \; i = 1, 2, \cdots, N_x - 1 \tag{4.3.3}$$

where $\tilde{x} = 1 + \frac{2\Delta t}{(\Delta x)^2} + \frac{2\Delta t}{(\Delta z)^2}$.

In order to solve (4.3.3), Successive Over-Relaxation (SOR) is used:

$$\tilde{T}_{i,0}^{2(m)} = \frac{\frac{\Delta t}{(\Delta x)^2}(T_{i+1,0}^{2(m-1)} - T_{i-1,0}^{2(m)}) + \frac{\Delta t}{(\Delta z)^2} 2T_{i,1}^{2(m-1)} + T_{i,0}^{1}}{\tilde{x}} \tag{4.3.4}$$

$$T_{i,0}^{2(m)} = \lambda \tilde{T}_{i,0}^{2(m)} + (1 - \lambda) T_{i,0}^{2(m-1)}, \tag{4.3.5}$$

$$i = 1, 2, \cdots, N_x - 1$$

where λ is the relaxation parameter and m is the iteration index of the SOR. The

iteration continues until

$$\max_i |T_{i,0}^{2(m+1)} - T_{i,0}^{2(m)}| < \epsilon_0 \quad ,$$

where ϵ_0 is a very small positive number, usually taken to be 10^{-6}. When $k > 2$

$$T_{i,0}^{k+1} = \frac{\frac{\Delta t}{(\Delta x)^2}(T_{i+1,0}^k - T_{i-1,0}^k) + \frac{\Delta t}{(\Delta z)^2} 2T_{i,1}^k + x_1 T_{i,0}^{k-1}}{x_2}, \; i = 1, 2, \cdots, N_x - 1, \quad (4.3.6)$$

where

$$x_1 = \frac{1}{2} - \frac{\Delta t}{(\Delta x)^2} - \frac{\Delta t}{(\Delta z)^2}, \quad x_2 = \frac{1}{2} + \frac{\Delta t}{(\Delta x)^2} + \frac{\Delta t}{(\Delta z)^2}.$$

The initial conditions are taken to be the same as those adopted in Chapter 3, (3.4.16)–(3.4.17), and the overall flow chart for the computation is the same as that described for the finite cavity. The numerical results are discussed in the next two sections.

4.4 Numerical Results for Air

Numerical results were obtained for air ($\sigma = 0.733$) for a wide range of Rayleigh numbers, equivalent to the range for the conducting case considered in Chapter 3. The grid sizes and the outer boundaries were the same as those described in the previous chapter, and the accuracy and convergence of the solutions followed a very similar pattern to that of the computations for the conducting case. The steady-state flow patterns are illustrated in Figures 4.1–4.5 by contours of stream function, vorticity and temperature for Rayleigh numbers ranging from 500 to 9000. As expected, the transition from conductive flow at low Rayleigh number to convective flow at high Rayleigh number is similar to that observed in the case of conducting boundaries, except near the base where the isotherms are free to shift towards the hot wall, convected by the turning motion of the fluid. The streamlines show that at $A = 500$, the flow pattern is nearly symmetric, but at higher Rayleigh numbers there is asymmetry caused by the accentuated upward motion near the hot wall,

associated with the formation of a thermal boundary layer there. The vorticity fields also show that strong horizontal vorticity gradients are set up near the hot wall resulting in vigorous convection there. When A reaches the critical Rayleigh number $A_c \approx 7880\sigma$ (see Figures 4.4–4.5), the parallel flow approaching the core is replaced by multicellular convection, as in the computations of Chapter 3. The end zone solution can no longer be treated in isolation, the outer boundary condition (4.2.3) is inconsistent, and a multiple-cell structure occurs in the whole slot. These features are consistent with the linear stability analysis discussed in the previous chapter.

Figures 4.6–4.7 show the skin friction on the hot and cold walls respectively, and in particular the rapid rise in skin friction at the bottom of the hot wall where it overshoots its asymptotic value for large z. For $A > A_c$, the results clearly demonstrate the appearance of spatial oscillations and the form of these is in reasonable agreement with the linear stability theory, which predicts a wavelength $2\pi/\alpha_c \approx 2.24$ for air. Figure 4.8 shows the skin friction on the bottom wall , indicating how asymmetry develops as the Rayleigh number increases. This behaviour is consistent with the change of the flow pattern observed in Figures 4.1–4.5, the skin friction maximum shifting considerably towards the hot wall.

The local Nusselt numbers are plotted in Figures 4.9 –4.10. On the cold wall, the local Nusselt number increases in the z direction, and decreases as A increases. This indicates that a region with a very weak horizontal temperature gradient then exists near the corner of the cold wall. Thus the heat transfer in this region is relatively small. On the hot wall, there are strong horizontal temperature gradients and the heat transfer reaches a maximum value near the bottom of the wall and then decreases along the z direction. Figure 4.10 also shows that the local Nusselt number for the hot wall increases with A, as more heat is transferred into the upward-moving fluid. Most of this heat is then conveyed, via the core, to the end zone at the top of the cavity, where it leaves through the cold wall. This process is represented by the steady-state integral of the energy equation $\beta - \alpha = A/720$ obtained in (4.2.17),

the right-hand side being a measure of the heat flux conveyed through the core region. This result was used to test the accuracy of the numerical computations, as shown in Table 4.2. This shows good consistency and for higher Rayleigh numbers the discrepancy increases as it becomes more difficult to adequately resolve the solution.

Figure 4.11 shows the temperature on the bottom wall, and indicates the transition from the linear conductive form when A is small to an asymmetric form when A is large. The latter demonstrates how most of the thermal adjustment occurs near the hot wall at the base of the cavity, consistent with the formation of a vertical boundary layer region there as $A \to \infty$. The overall Nusselt number Nu is obtained by using (4.2.13) and the numerical results which are listed in Table 4.1. The results show good agreement with previous numerical calculations for the whole cavity by Lee and Korpela (1983) and Raithby and Wong (1981), and also compare well with the experiments of ElSherbiny, Raithby and Hollands (1981). It should be noted that the numerical results of the end-zone computation for one pair of the parameters A and σ can be used to provide approximations to the Nusselt number for all aspect ratios H provided H is sufficiently large for the conductive regime to apply in the core. This is a significant advantage of the asymptotic methods adopted here.

4.5 Numerical Results for Water

Numerical results were obtained for water ($\sigma = 6.983$) for a wide range of Rayleigh numbers varying from 500 to 70000. The outer boundaries used in the computations varied from 3 to 60, and various grid sizes were used according to the value of the Rayleigh number.Unlike the case of air , much higher Rayleigh numbers were considered here, so that much larger outer boundaries were needed and grid sizes ranged from 30×90, 25×175 and 18×280 to 12×600. Most of the computations for high Rayleigh numbers were based on the use of solutions for lower Rayleigh number as the initial states, thereby reducing the computational time needed.

Contours of stream function, vorticity and temperature, including some detailed results for the fields near the bottom wall are presented in Figures 4.12 –4.23 for Rayleigh numbers $500 \leq A \leq 50000$, which are below the critical Rayleigh number for stationary transverse rolls

$$A_c \approx 7880\sigma = 55049$$

predicted by linear stability theory. These graphs provide detailed information about the flow structure of water in the end regions of the cavity; because instability is delayed to much higher Rayleigh numbers when the Prandtl number is large, the nonlinear development of the flow can be followed much further than for the case of air.

The results show how , as the Rayleigh number increases, the region of nonparallel flow near the base of the cavity spreads upwards so that for $A = 3000$ (Figure 4.13), parallel flow exists only for $z \geq 4$. Similarly, the isotherms show a significant deflection from the vertical over the region $0 \leq z \leq 4$, and are roughly parallel for $z \geq 4$. For $A = 14000$ (Figure 4.15) the isotherms near the lower corner are compressed towards the hot wall leading to an almost isothermal region over most of the base. The 0.1 isotherm indicates a shape similar to that of the streamline at the same location in the left half of the cavity, suggesting that except near the hot wall, most of the flow near the base of the cavity is dominated by convection. For $A = 30000$ (Figures 4.16-4.18), where the outer boundary is taken at $z_\infty = 30$, a detailed picture of the flow near the base (Figure 4.17) shows a similar behaviour for the 0.05 isotherm, which follows the streamline pattern before being deflected sharply to the bottom boundary in the region $z \leq 0.4$. Near the hot wall, the region $0.8 < x < 1$, $0 \leq z \leq 2$ shows tightly-packed isotherms indicating strong horizontal temperature gradients and the formation of a vertical thermal boundary layer. The local heat transfer into the system is a maximum near the base of the hot wall. The vorticity field (Figure 4.18) shows a complex structure near the lower, hot corner and a region of maximum vorticity near the hot wall associated with the vertical boundary layer. Further computations for $A = 40000$ (Figures 4.19-4.22)

and $A = 50000$ (Figure 4.23) show a similar behaviour.

For $A = 60000$ (Figure 4.24) the parallel flow region at the outermost part of the end zone becomes susceptible to minor oscillations, consistent with a critical Rayleigh number $A_c \approx 55000$. These are shown in close-up in Figure 4.25. The critical wavenumber predicted by linear stability theory is $\alpha \approx 2.8$ (Vest and Arpaci 1969, Bergholz 1978), equivalent to a wavelength $z = 2\pi/\alpha \approx 2.24$ between the centres of neighbouring, co-rotating cells. This compares well with a value of about 2.1 obtained by measurement in Figure 4.25. At even higher Rayleigh number, $A = 70000$ (Figures 4.26, 4.27) the multiple cell structure becomes clearly established along the centre-line of the parallel flow region.

Figures 4.28–4.32 show the profiles of skin friction on the cold, hot and bottom walls of the cavity for different Rayleigh numbers . On the cold wall, the curves gradually change from zero to a maximum value along the z direction , but on the hot wall, they change dramatically near the bottom wall at large values of the Rayleigh number. This corresponds to the formation of the vertical boundary layer; the hot corner provides a strong source of vorticity and is termed the 'starting corner' by McIntyre(1968) in his study of thermal convection in a rotating annulus. Figure 4.32 shows the skin friction on the bottom wall for different Rayleigh numbers . The maximum value at low Rayleigh number is approximately at the centre of the slot , but gradually moves towards the hot wall as A increases. This is because at high Rayleigh numbers, the flow is accelerated near the lower, hot corner by the presence of the vertical boundary-layer on the hot wall.

The local Nusselt numbers on the cold and hot walls are plotted in Figures 4.33–4.34 for different Rayleigh numbers. Obviously, the heat transfer is dominated by conduction at low Rayleigh numbers where $Nu_{loc} \approx 1$ and for higher Rayleigh numbers the main contribution relative to the conductive state occurs close to the bottom of the hot wall. On the cold wall the heat transfer out of the end zone is reduced relative to the conductive value as the Rayleigh number increases. Heat

entering the system through the hot wall is converted mostly into the vertical transfer $A/720$ and is conveyed to the upper end zone via the parallel flow in the core.

Figure 4.35 shows the temperature on the bottom wall .At low Rayleigh number ($A = 500$) the profile is approximately linear and as A increases the major variation shifts to the neighbourhood of the hot wall, with most of the base of the cavity then at the temperature of the cold wall. This is consistent with the large Rayleigh number structure at infinite Prandtl number proposed by Daniels (1985, 1987) and described in Section 4.2. The numerical computations described here are broadly consistent with the main features of this structure, including the existence of an outer zone of vertical extent $O(A)$, which allows adjustment to the parallel core flow, and a thin horizontal layer of height $O(A^{-1/4})$ which is dominated by convection and feeds fluid into the base of a vertical boundary layer on the hot wall. The Prandtl number of the computations is, in fact, large but finite so as A increases the end zone problem no longer has a consistent solution when A exceeds $A_c \approx 55000$. The multiple cells which then appear are consistent with the wavelength predicted by stability analysis.

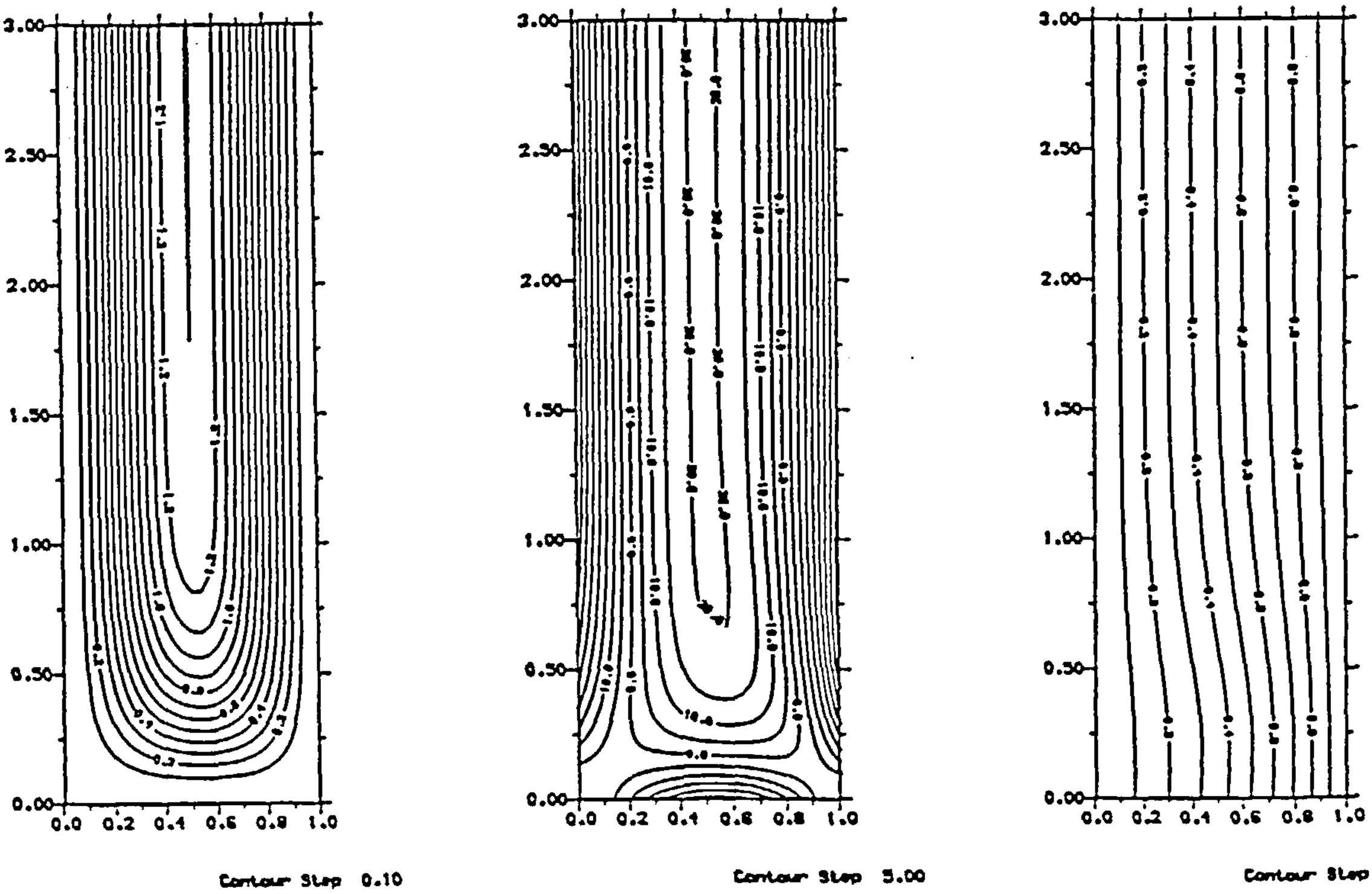

Figure 4.1: Contours of the steady-state solution for (a) stream function , (b) vorticity, (c) temperature, for $\sigma = 0.733$ and $A = 500$, using a 30×90 computational grid with $z_\infty = 3$.

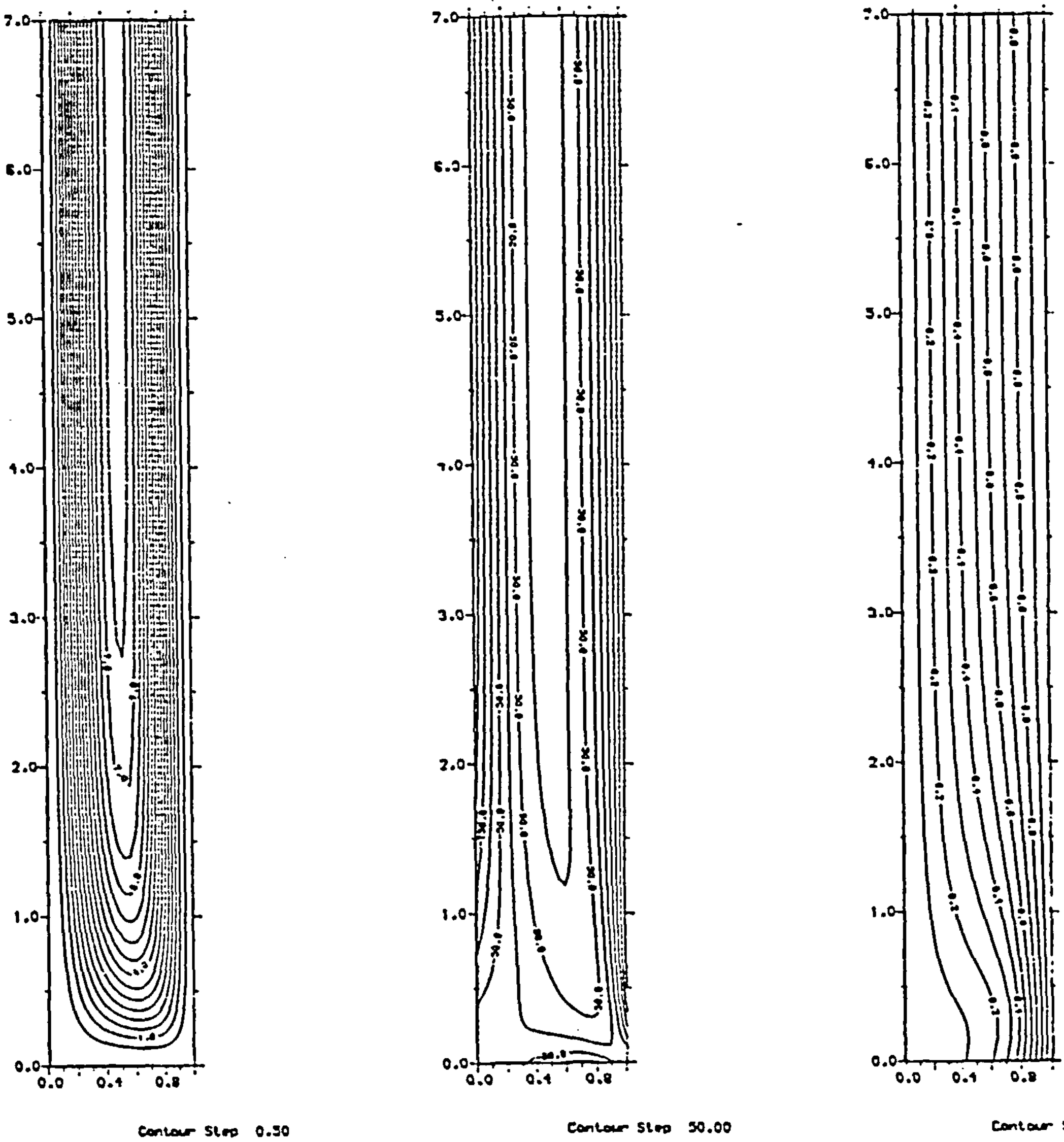

(a) (b) (c)

Figure 4.2: Contours of the steady-state solution for (a) stream function , (b) vorticity, (c) temperature, for $\sigma = 0.733$ and $A = 3000$, using a 25×175 computational grid with $z_\infty = 7$.

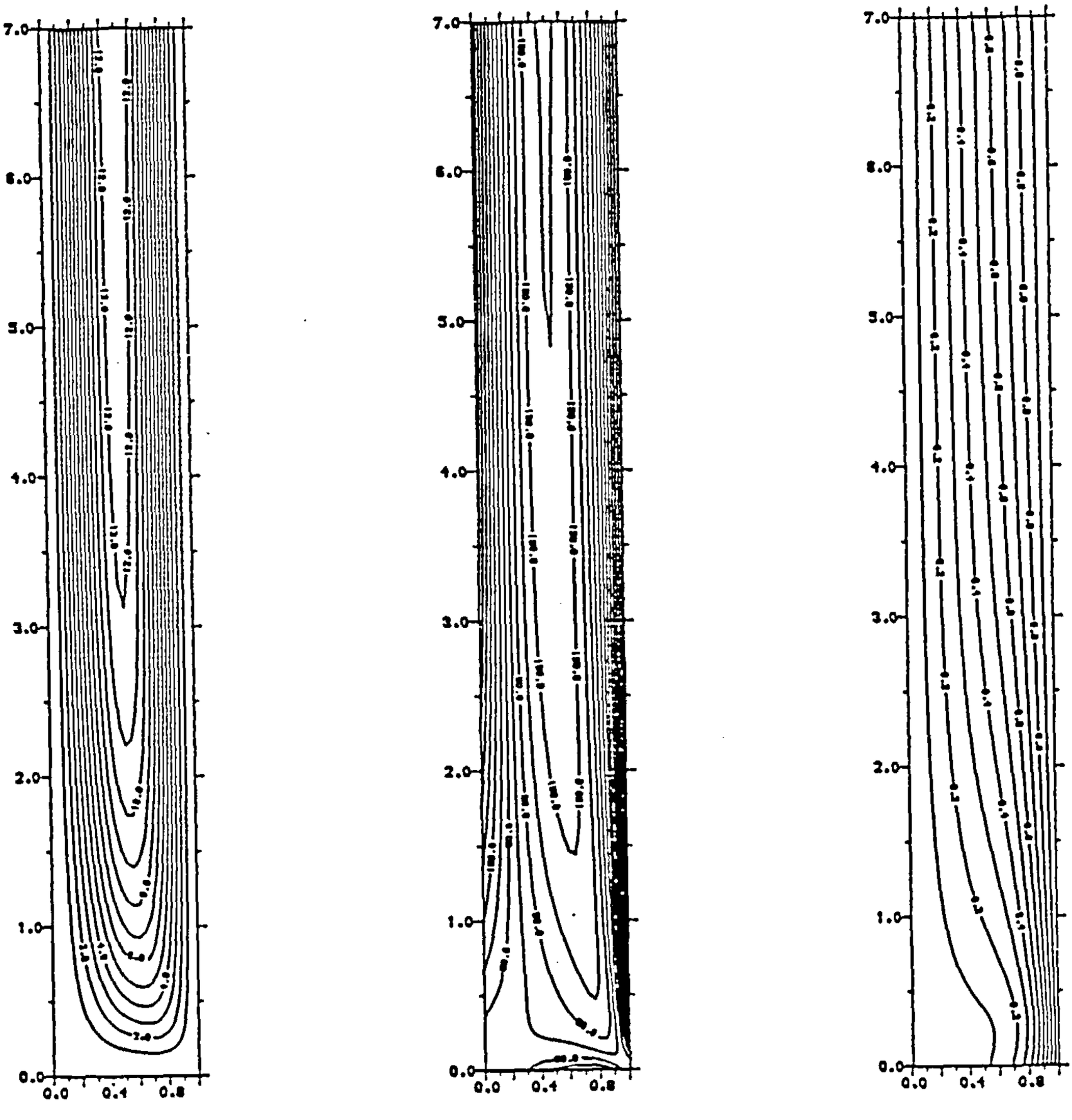

Figure 4.3: Contours of the steady-state solution for (a) stream function , (b) vorticity, (c) temperature, for $\sigma = 0.733$ and $A = 5000$, using a 25×175 computational grid with $z_\infty = 7$.

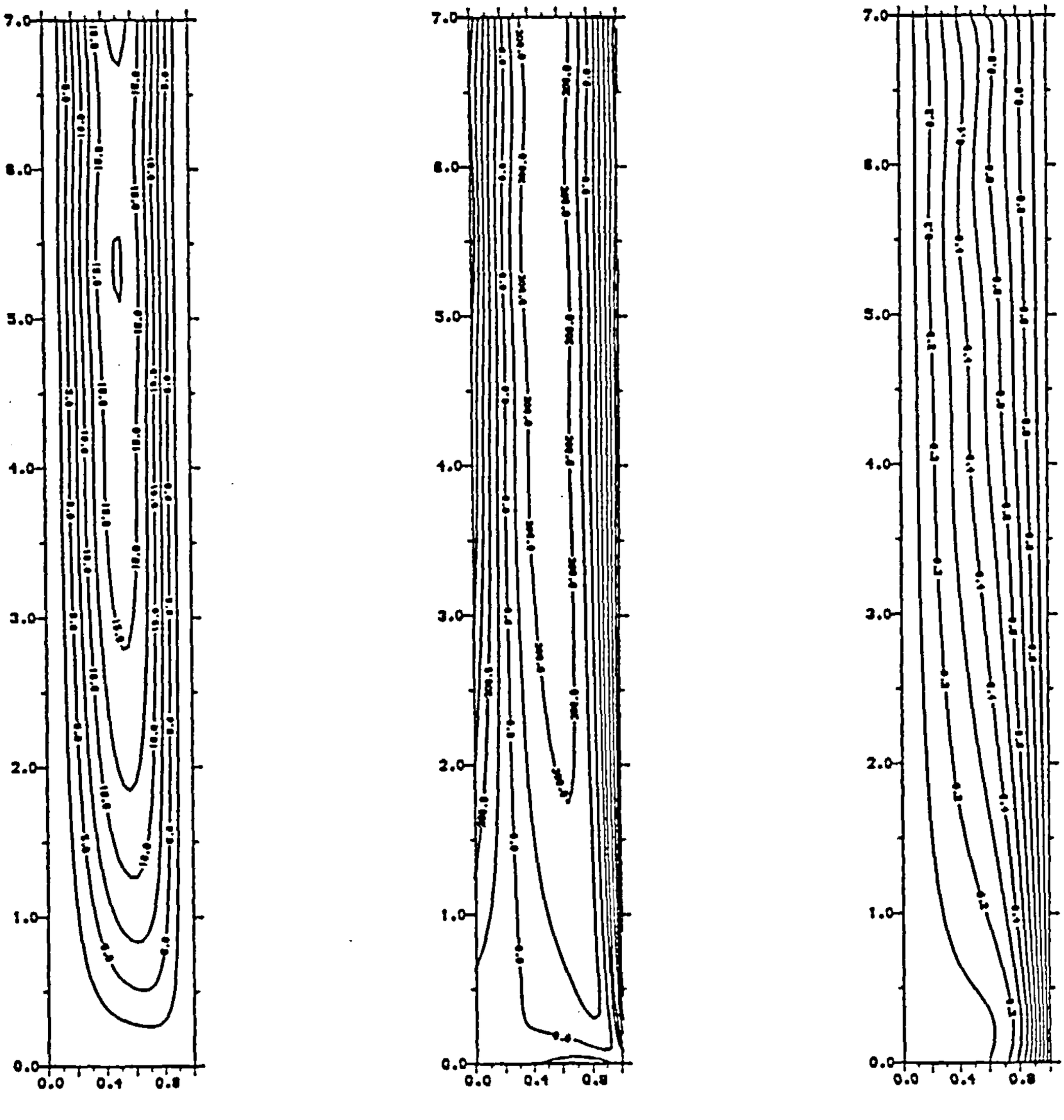

Figure 4.4: Contours of the steady-state solution for (a) stream function , (b) vorticity, (c) temperature, for $\sigma = 0.733$ and $A = 7000$, using a 25×175 computational grid with $z_\infty = 7$.

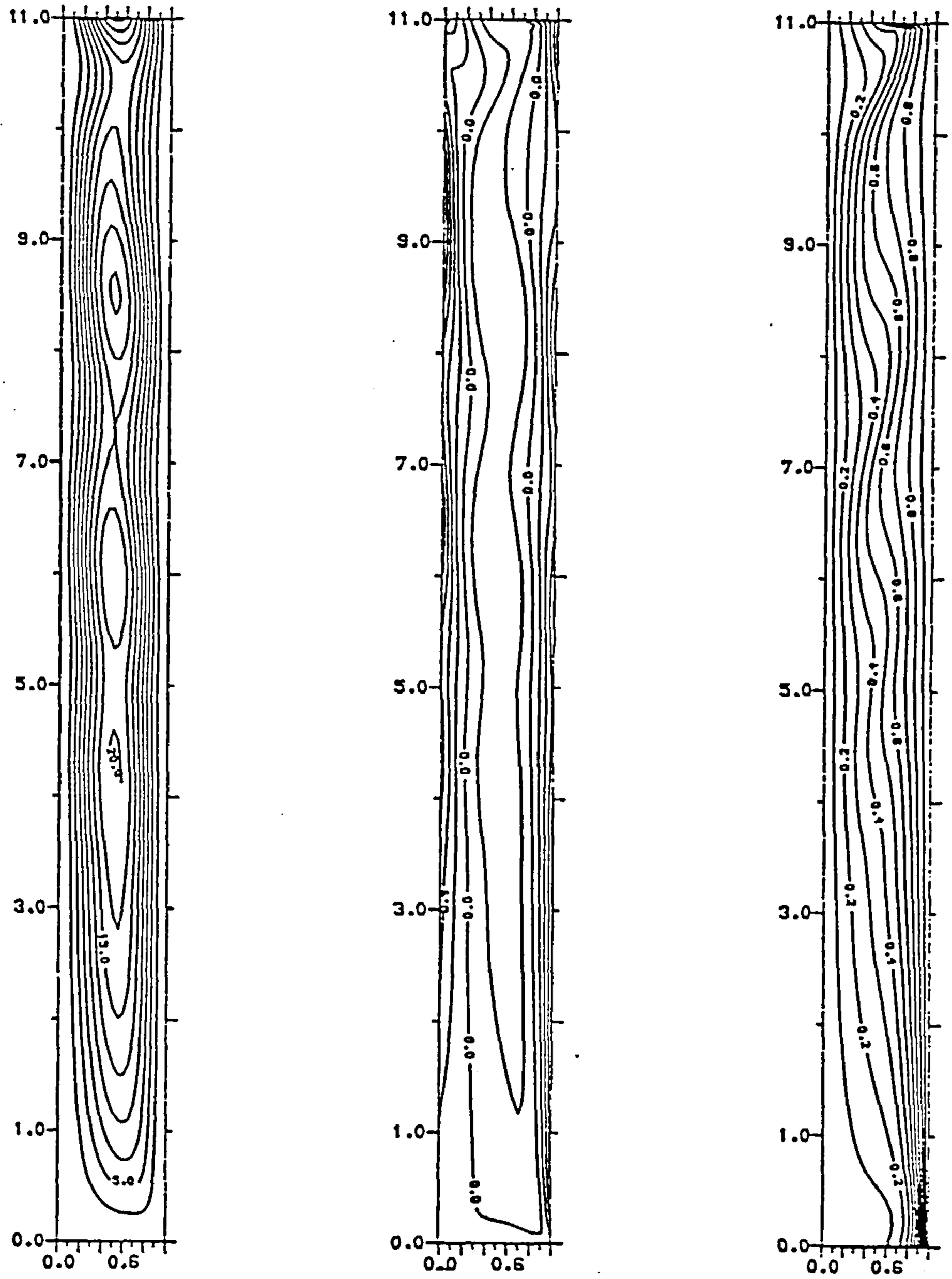

Figure 4.5: Contours of the steady-state solution for (a) stream function , (b) vorticity, (c) temperature, for $\sigma = 0.733$ and $A = 9000$, using a 25×175 computational grid with $z_\infty = 11$.

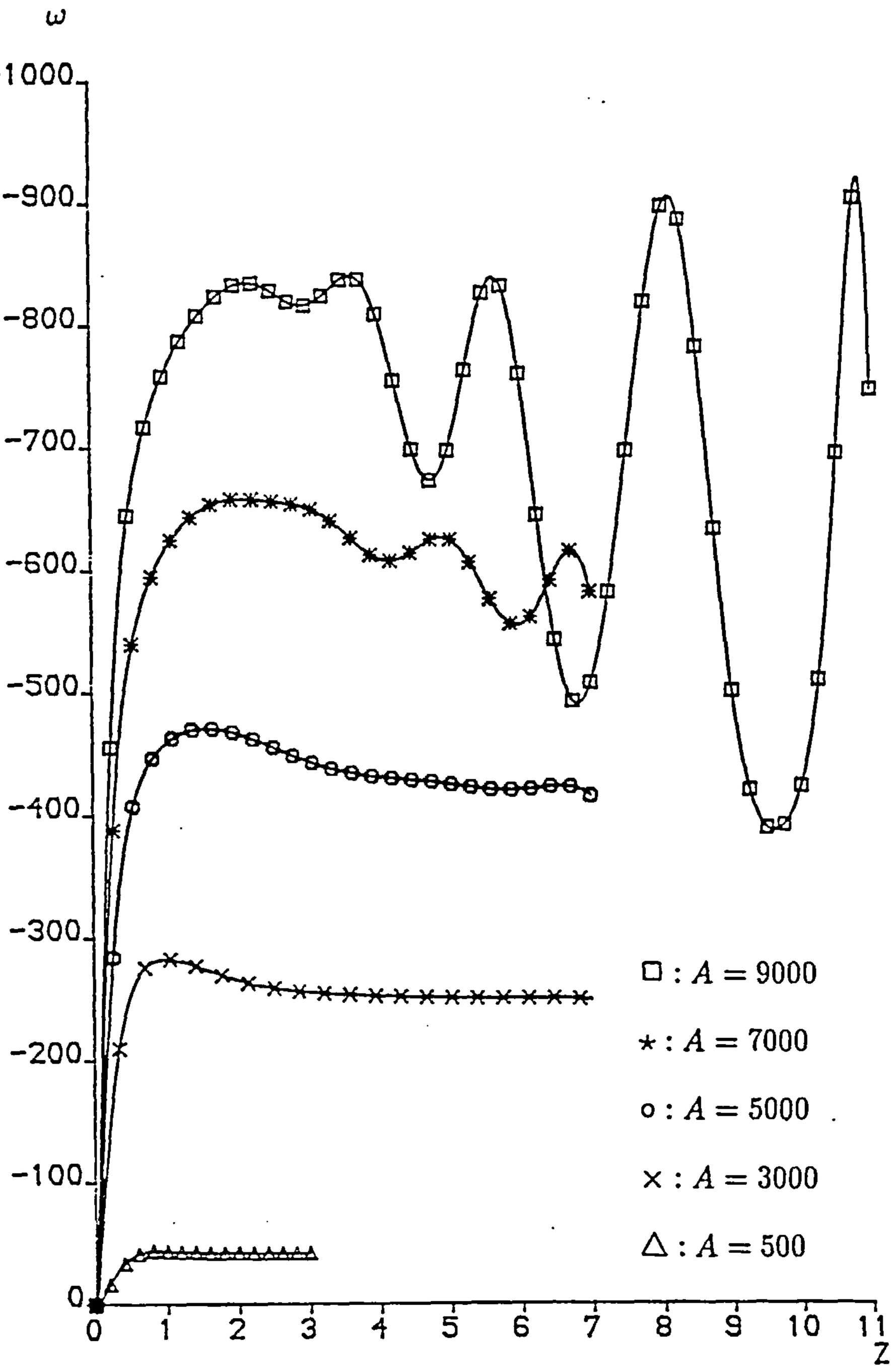

Figure 4.6: The skin friction with $\sigma = 0.733$ for different Rayleigh numbers on the hot wall for the insulating case.

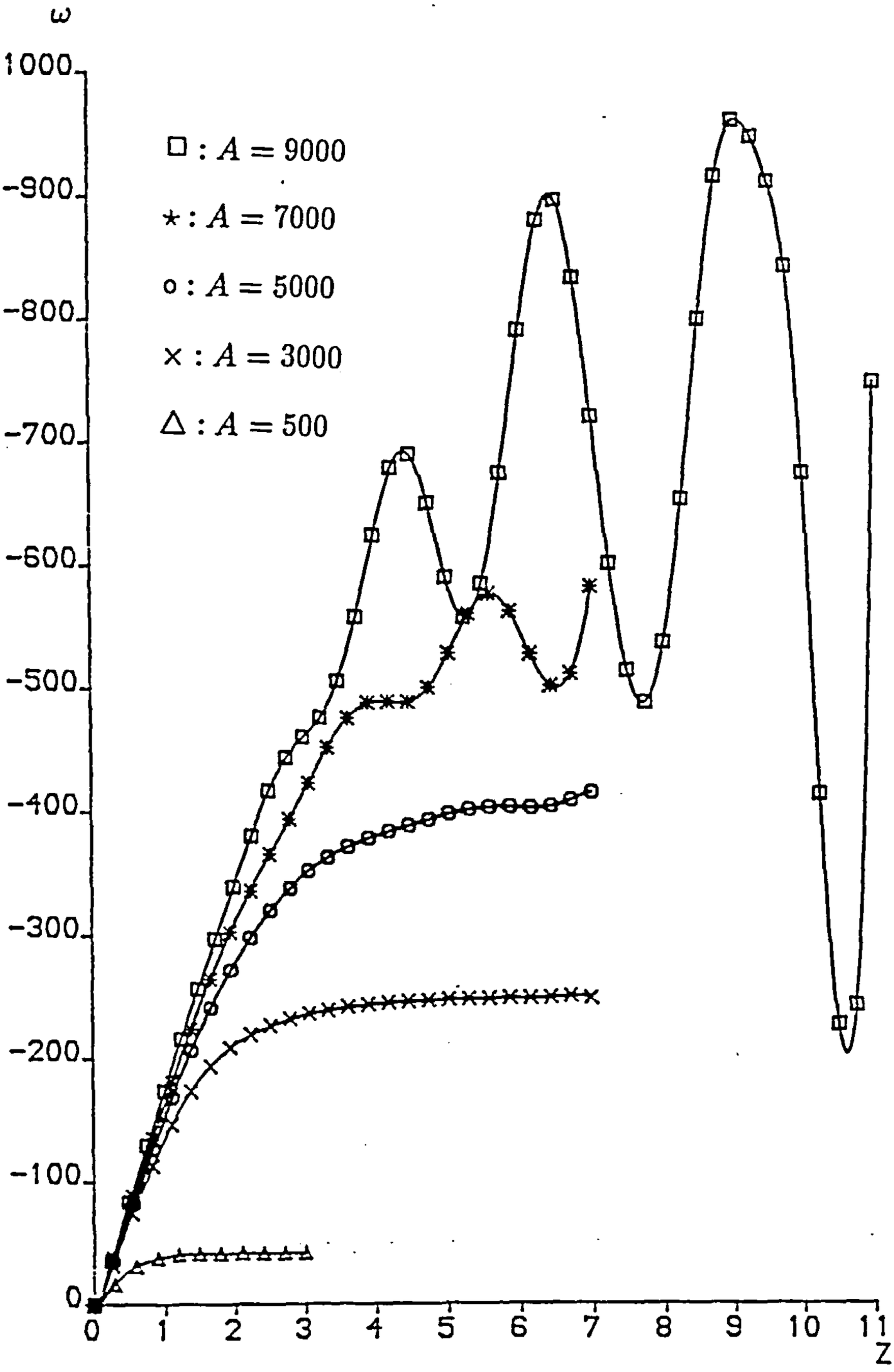

Figure 4.7: The skin friction with $\sigma = 0.733$ for different Rayleigh numbers on the cold wall for the insulating case.

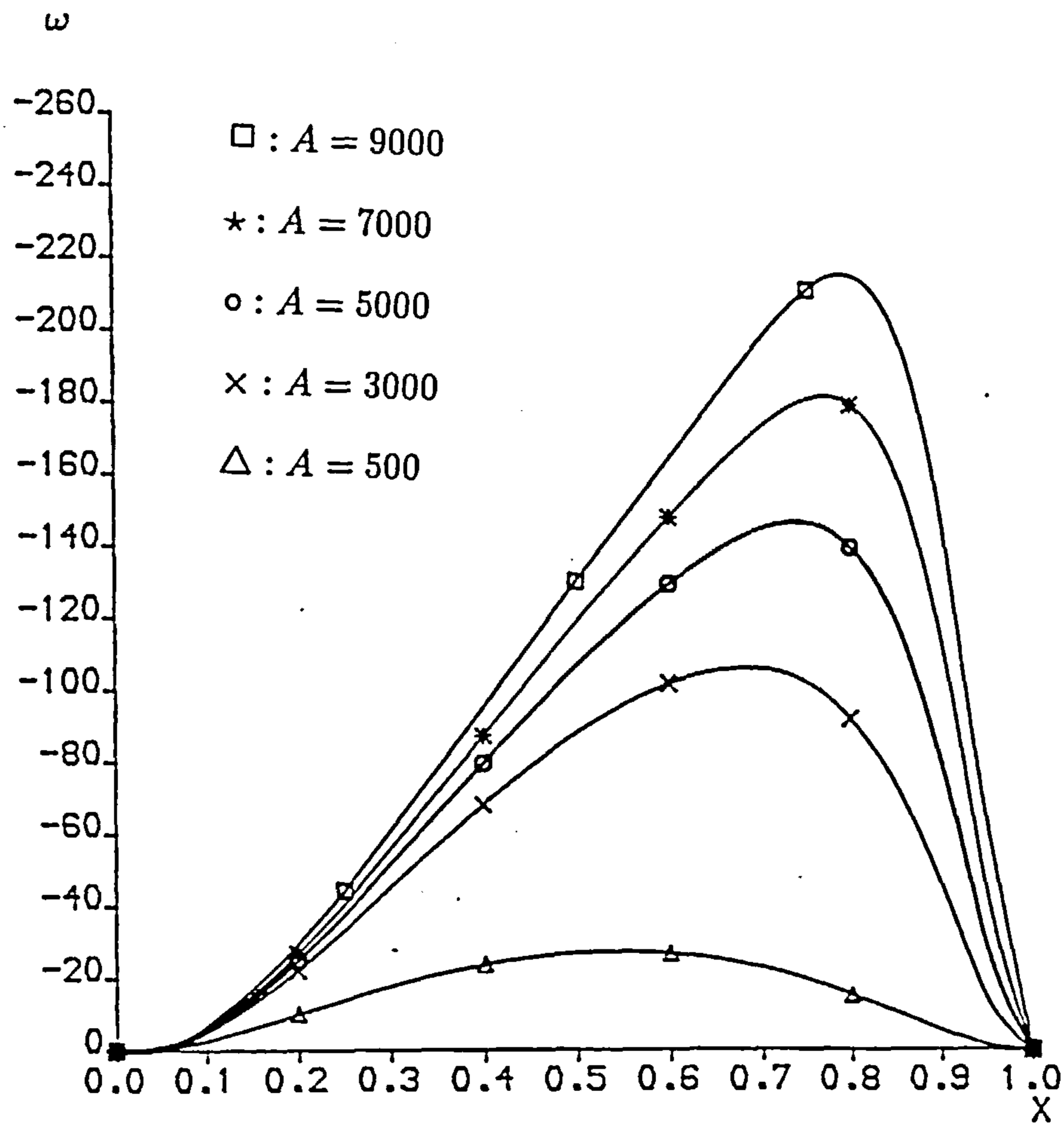

Figure 4.8: The skin friction with $\sigma = 0.733$ for different Rayleigh numbers on the bottom wall for the insulating case.

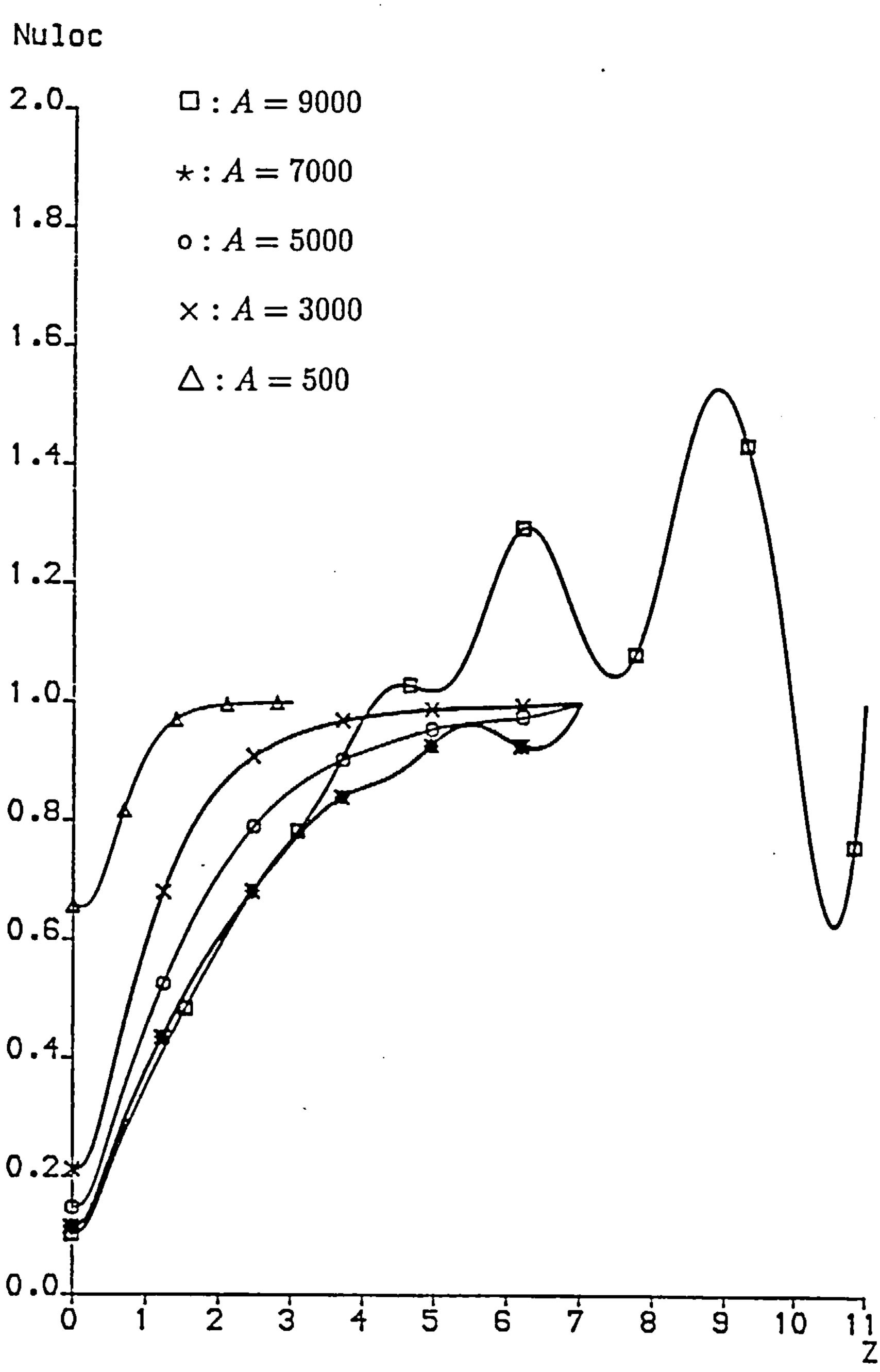

Figure 4.9: The local Nusselt number with $\sigma = 0.733$ for different Rayleigh numbers on the cold wall for the insulating case.

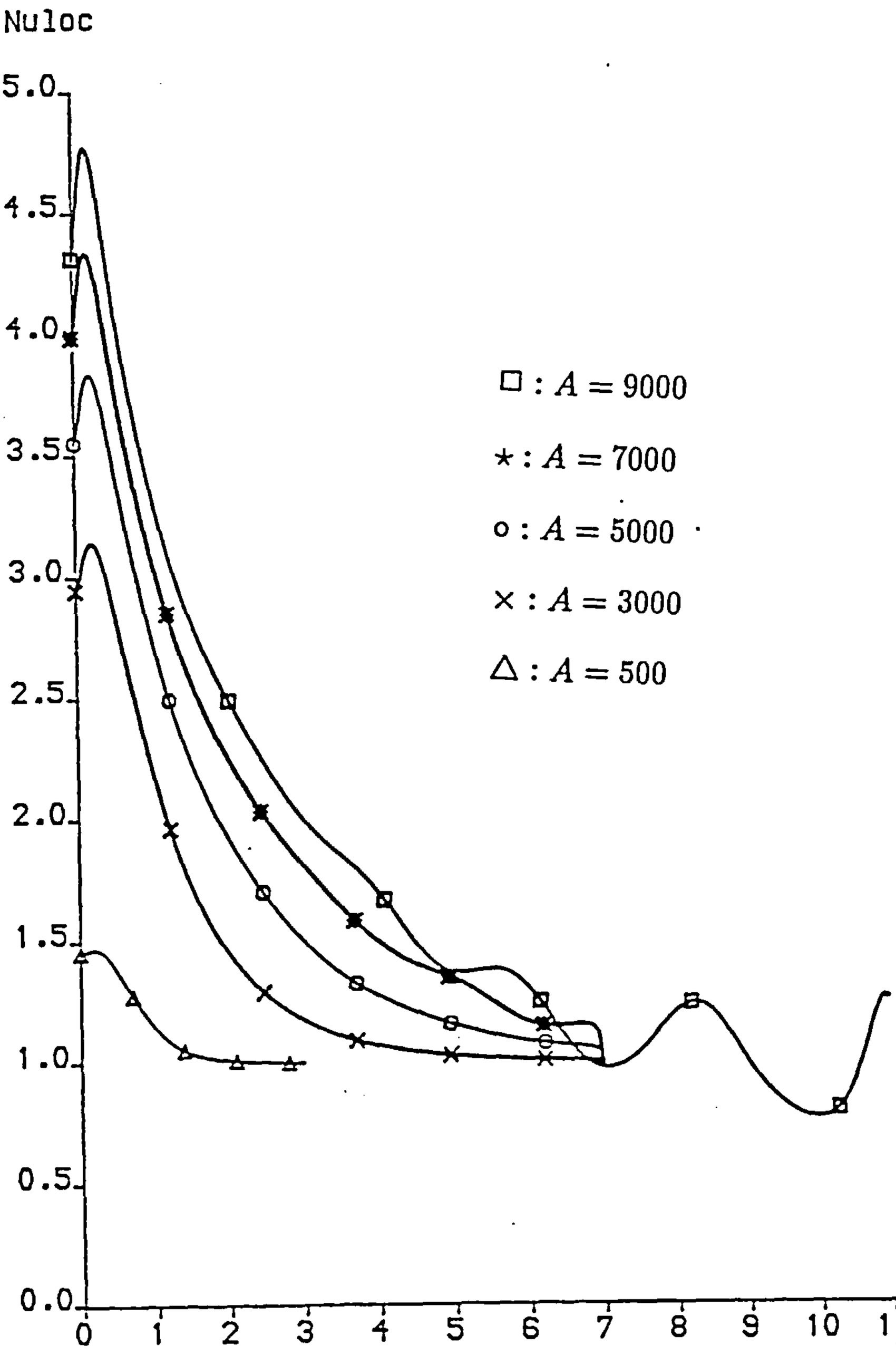

Figure 4.10: The local Nusselt number with $\sigma = 0.733$ for different Rayleigh numbers on the hot wall for the insulating case.

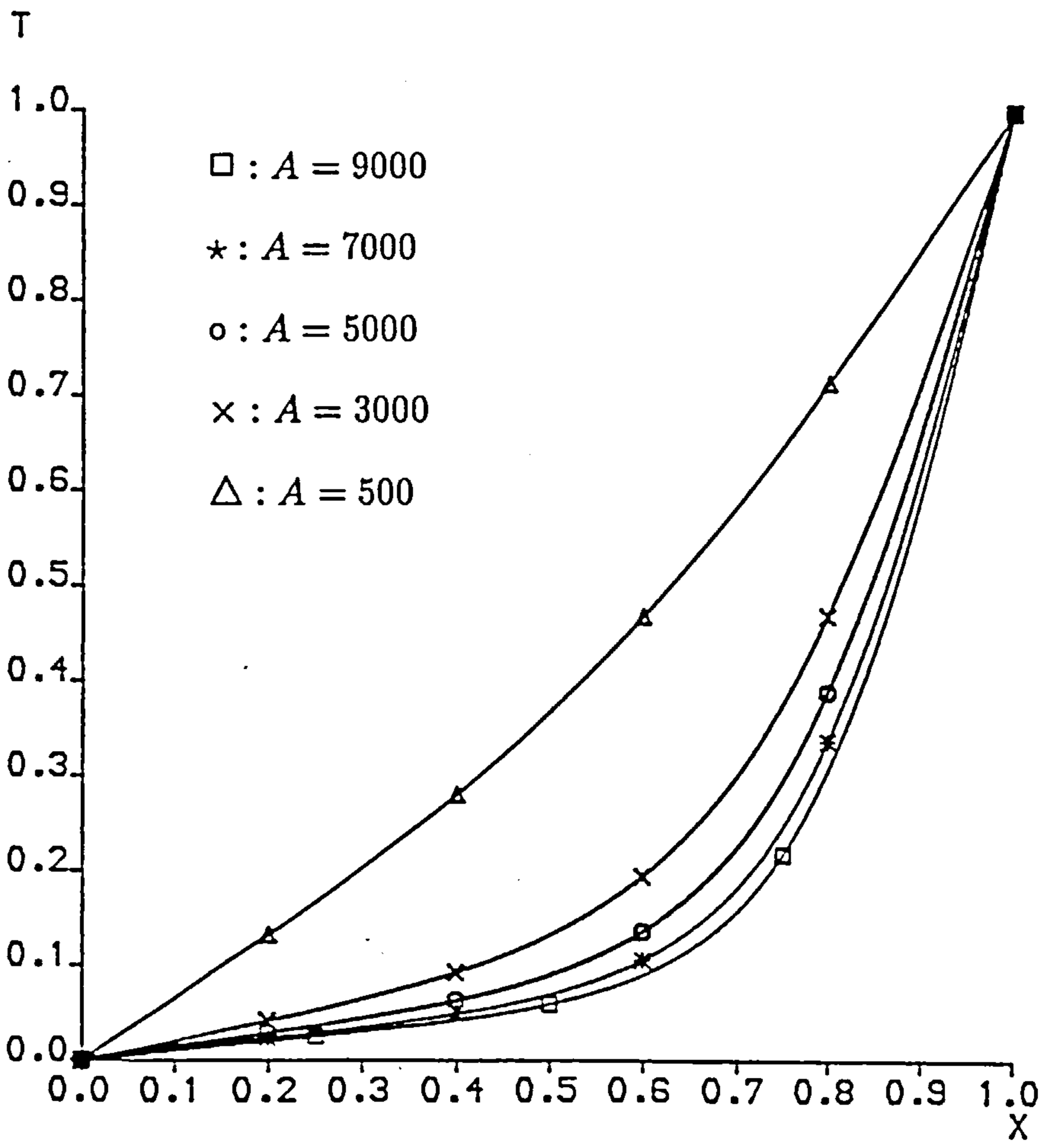

Figure 4.11: The temperature with $\sigma = 0.733$ for different Rayleigh numbers on the bottom wall for the insulating case.

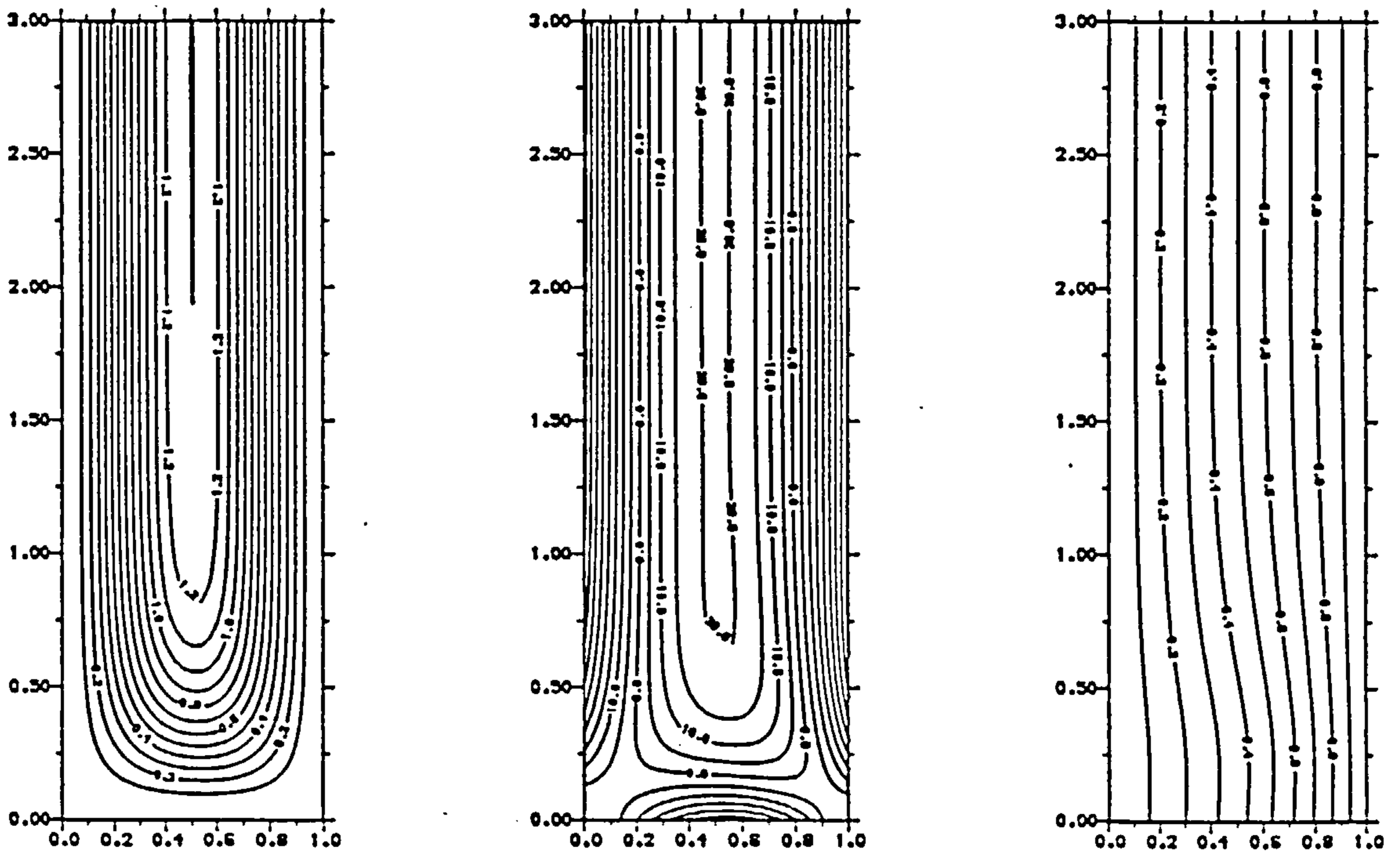

Figure 4.12: Contours of the steady-state solution for (a) stream function , (b) vorticity, (c) temperature, for $\sigma = 6.983$ and $A = 500$, using a 30×90 computational grid with $z_\infty = 3$.

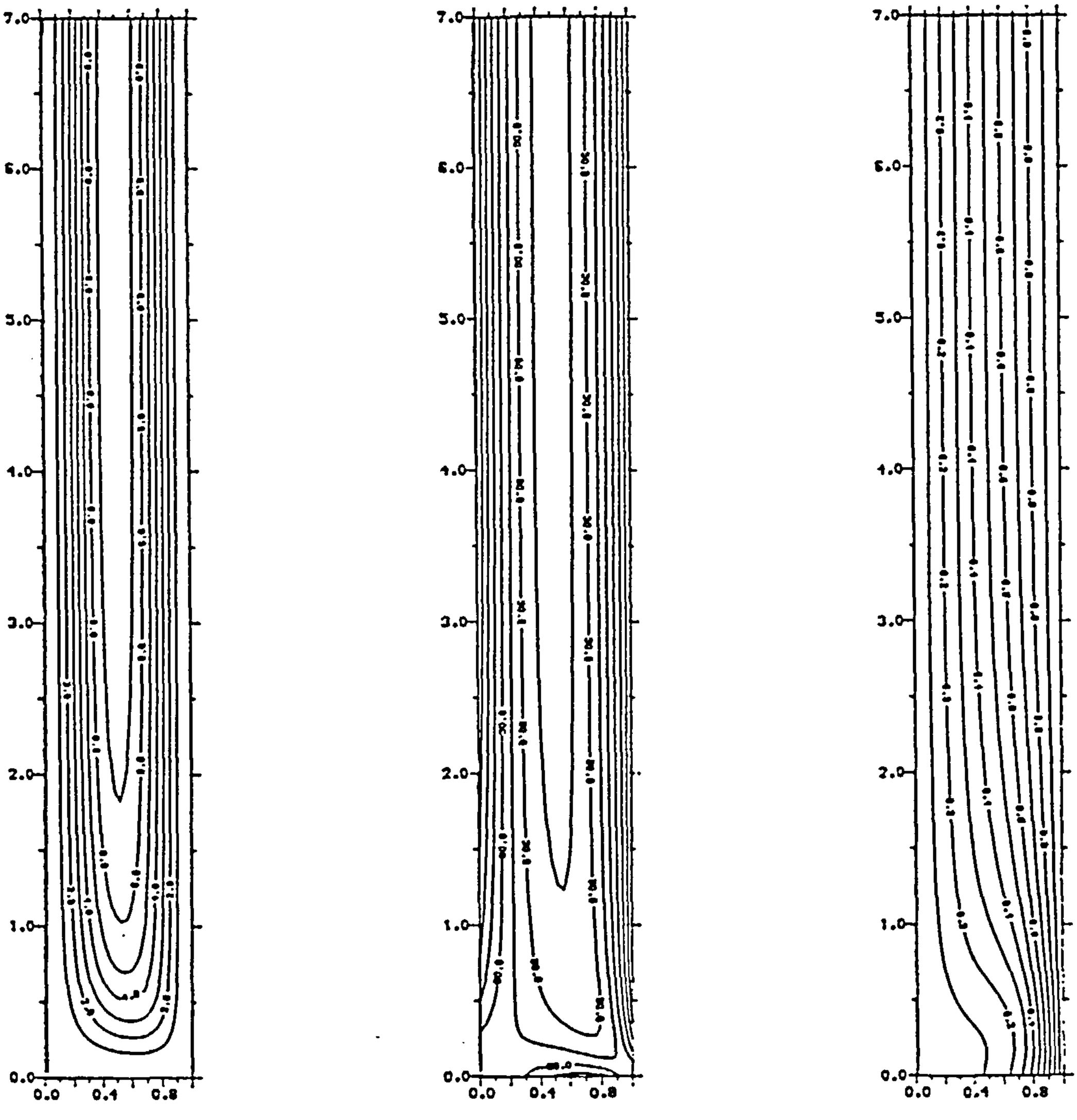

Figure 4.13: Contours of the steady-state solution for (a) stream function , (b) vorticity, (c) temperature, for $\sigma = 6.983$ and $A = 3000$, using a 25×175 computational grid with $z_\infty = 7$.

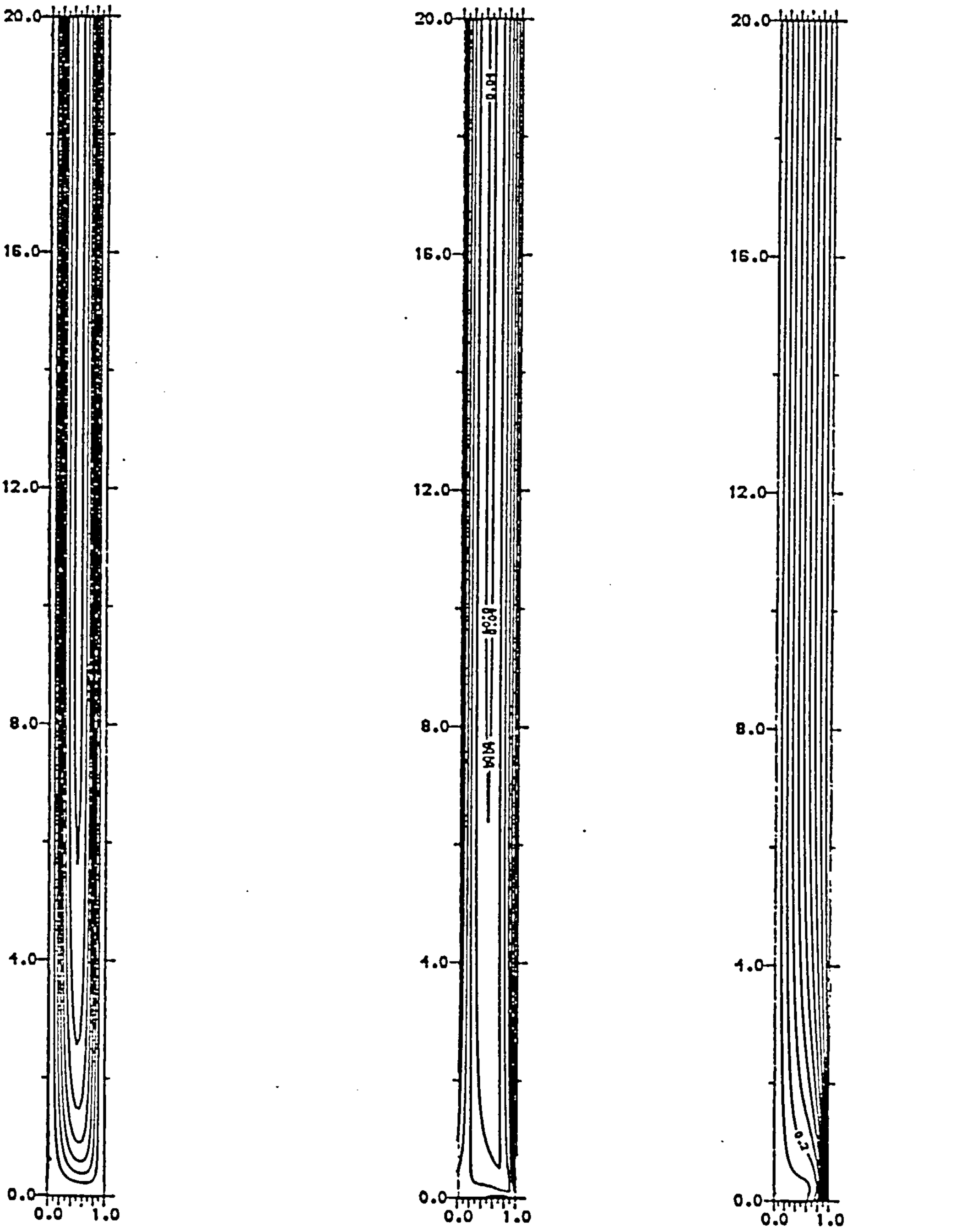

Figure 4.14: Contours of the steady-state solution for (a) stream function , (b) vorticity, (c) temperature, for $\sigma = 6.983$ and $A = 7000$, using a 18×280 computational grid with $z_\infty = 20$.

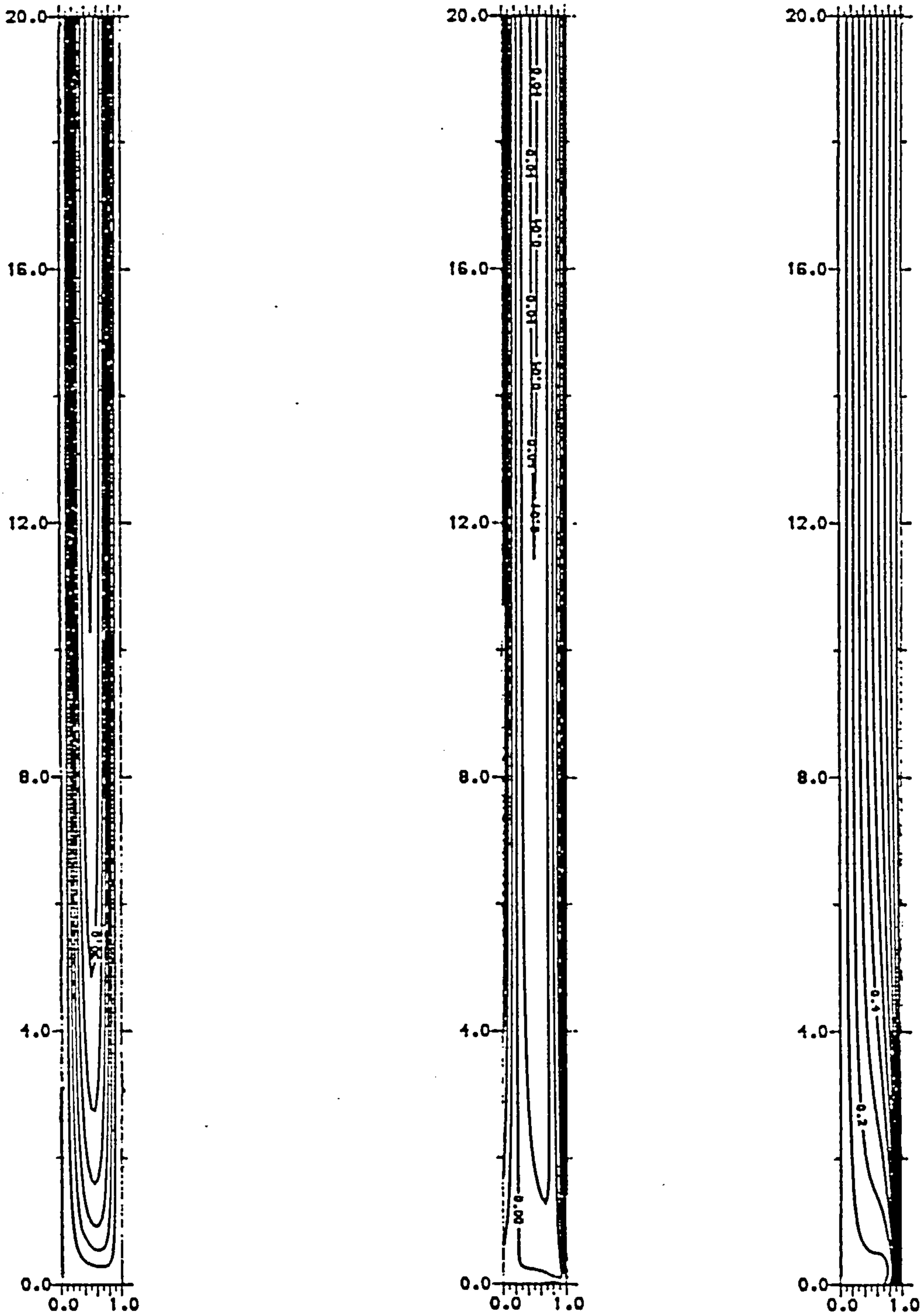

Figure 4.15: Contours of the steady-state solution for (a) stream function , (b) vorticity, (c) temperature, for $\sigma = 6.983$ and $A = 14000$, using a 18×280 computational grid with $z_\infty = 20$.

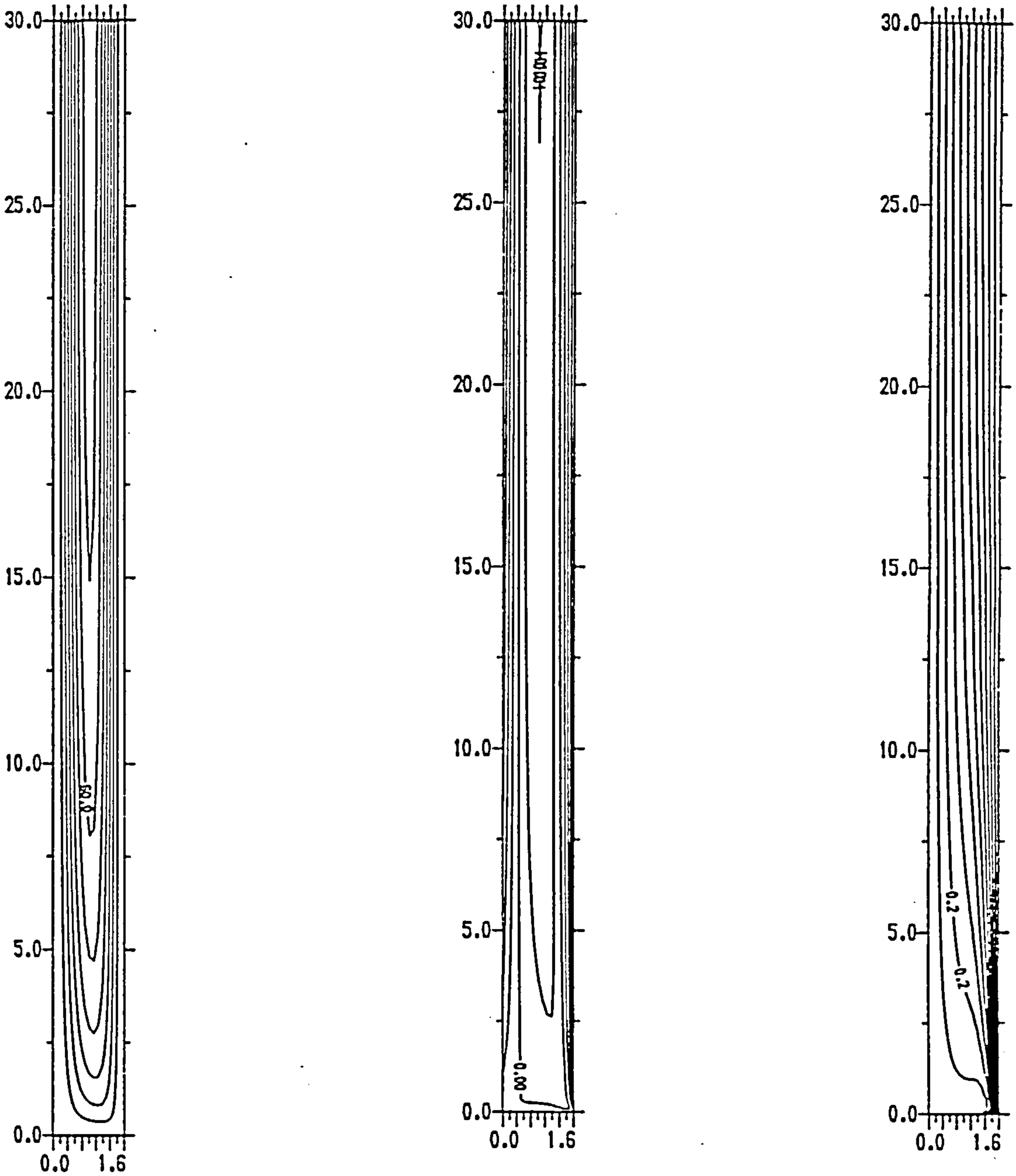

Figure 4.16: Contours of the steady-state solution for (a) stream function , (b) vorticity, (c) temperature, for $\sigma = 6.983$ and $A = 30000$, using a 16×360 computational grid with $z_\infty = 30$.

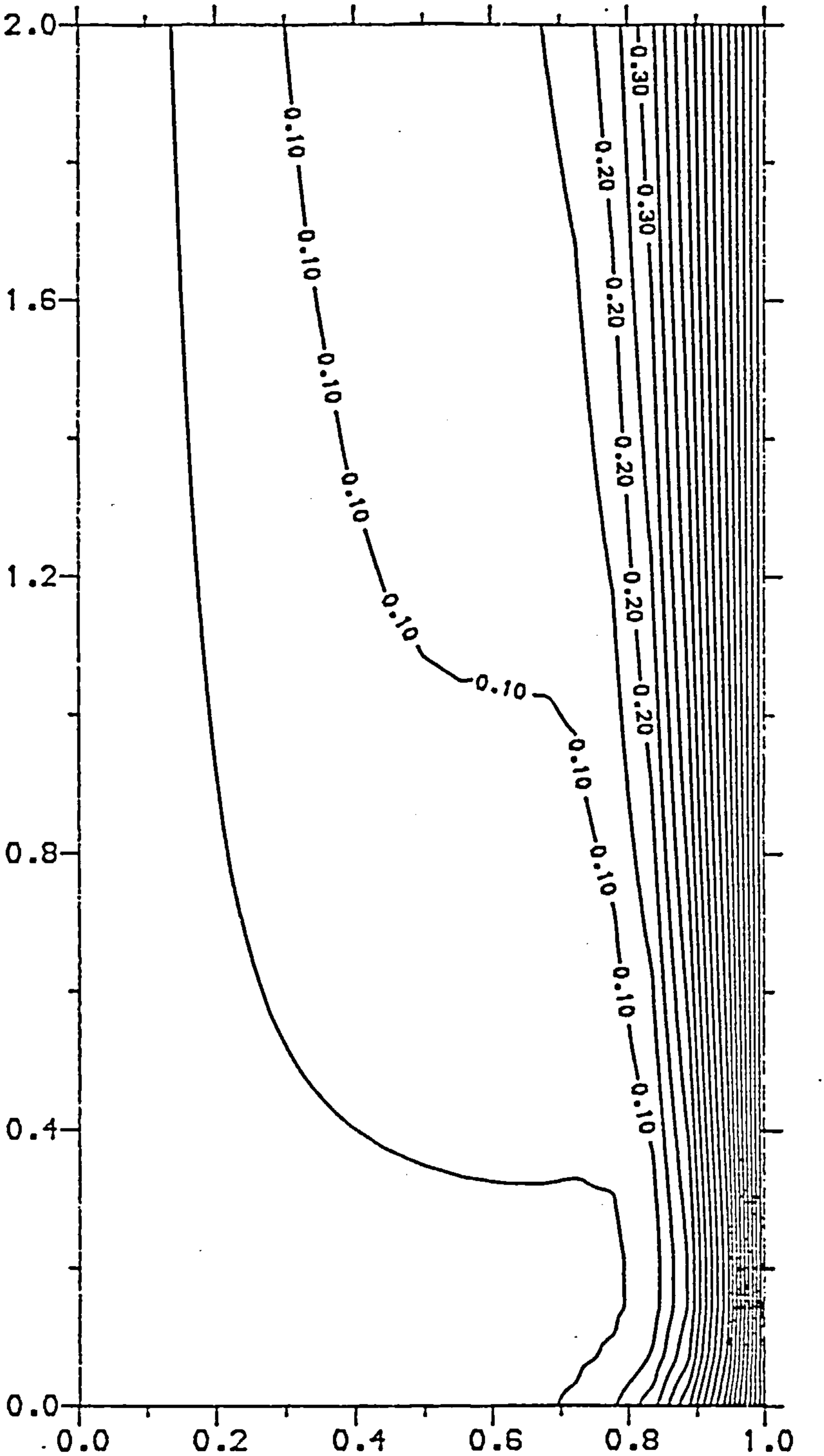

Figure 4.17: Contours of temperature with $\sigma = 6.983$, $A = 30000$ near the bottom of the slot for the insulating case.

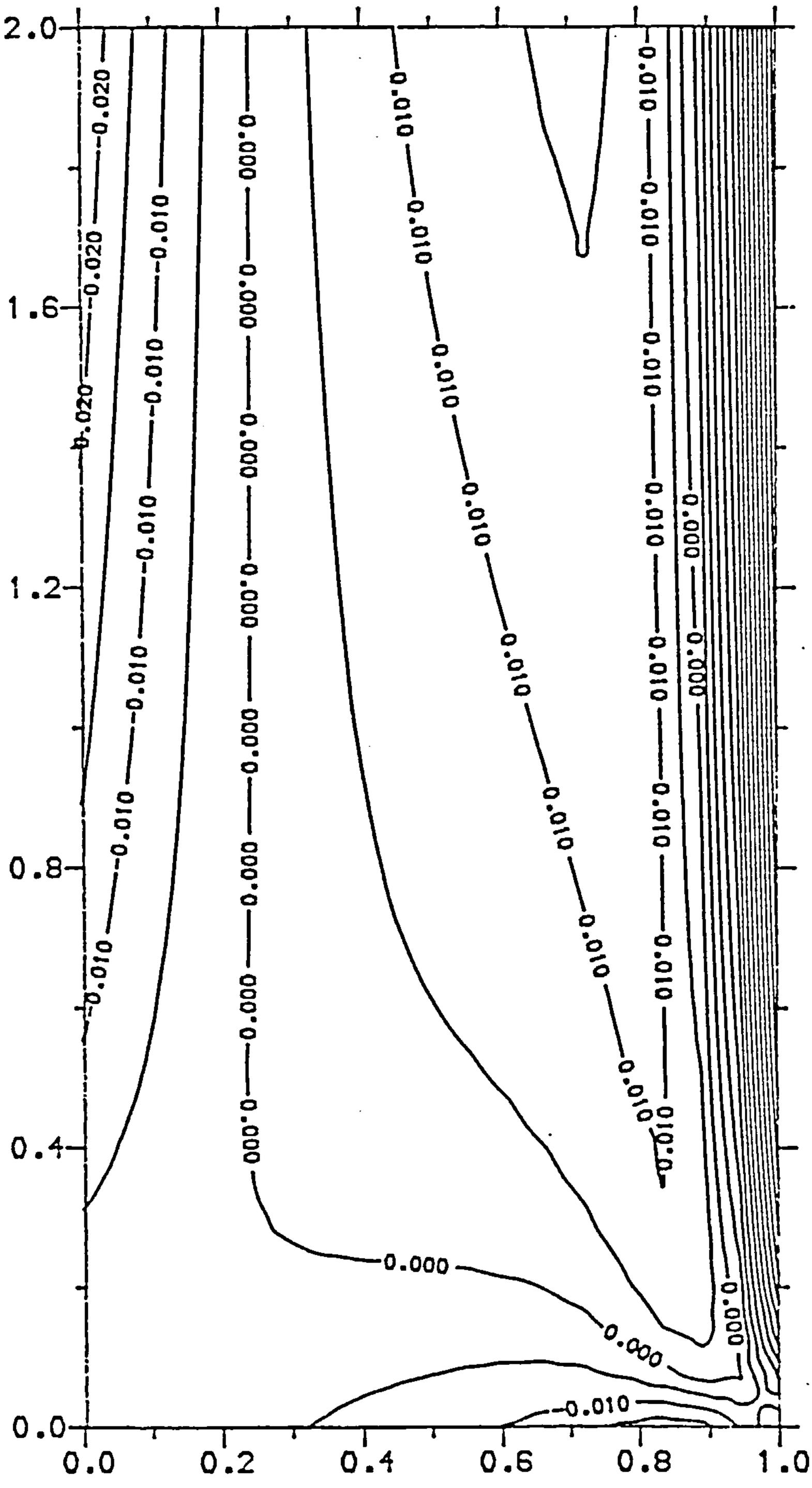

Figure 4.18: Contours of vorticity with $\sigma = 6.983$, $A = 30000$ near the bottom of the slot for the insulating case.

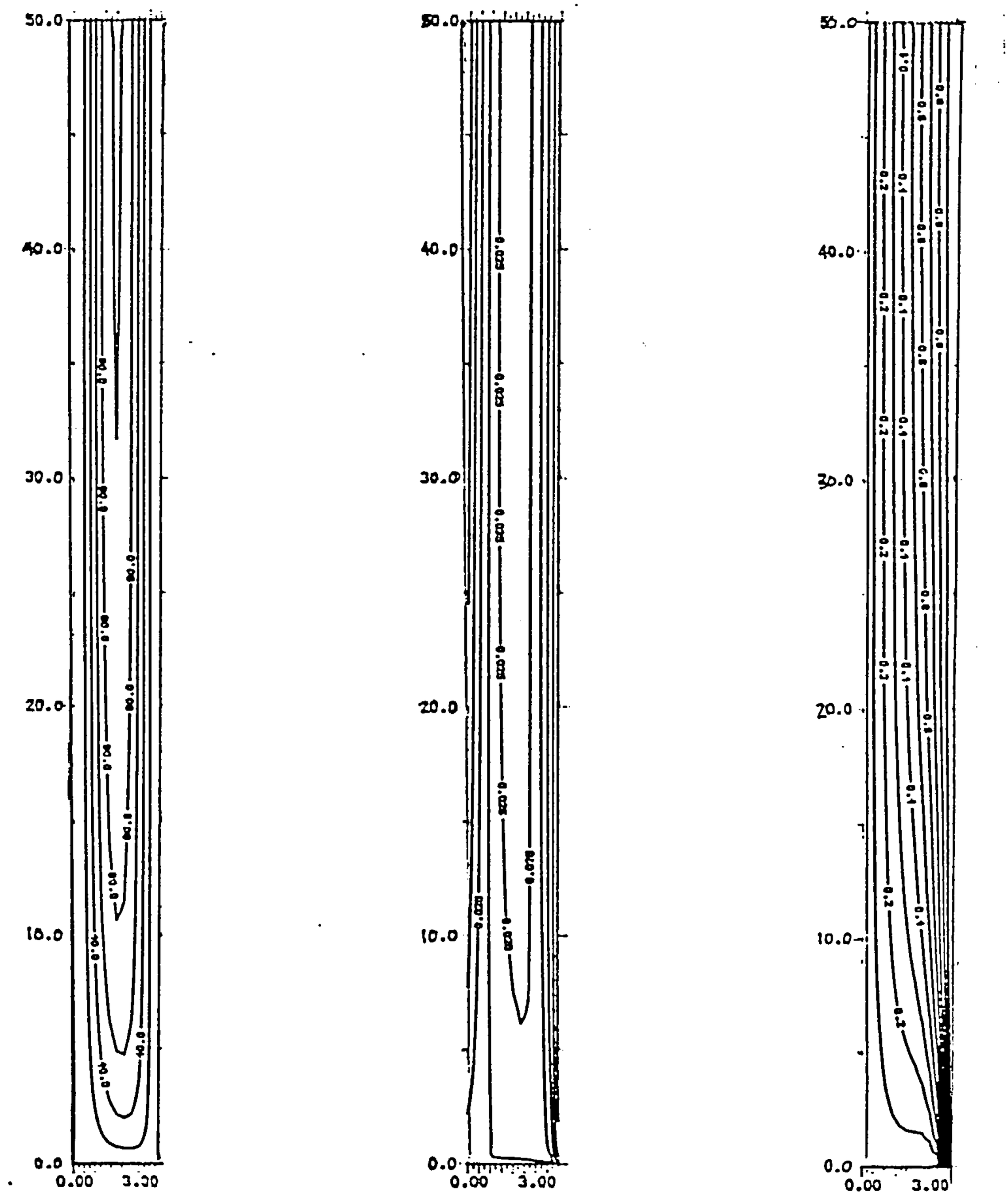

Figure 4.19: Contours of the steady-state solution for (a) stream function, (b) vorticity, (c) temperature, for $\sigma = 6.983$ and $A = 40000$, using a 12×600 computational grid with $z_\infty = 50$.

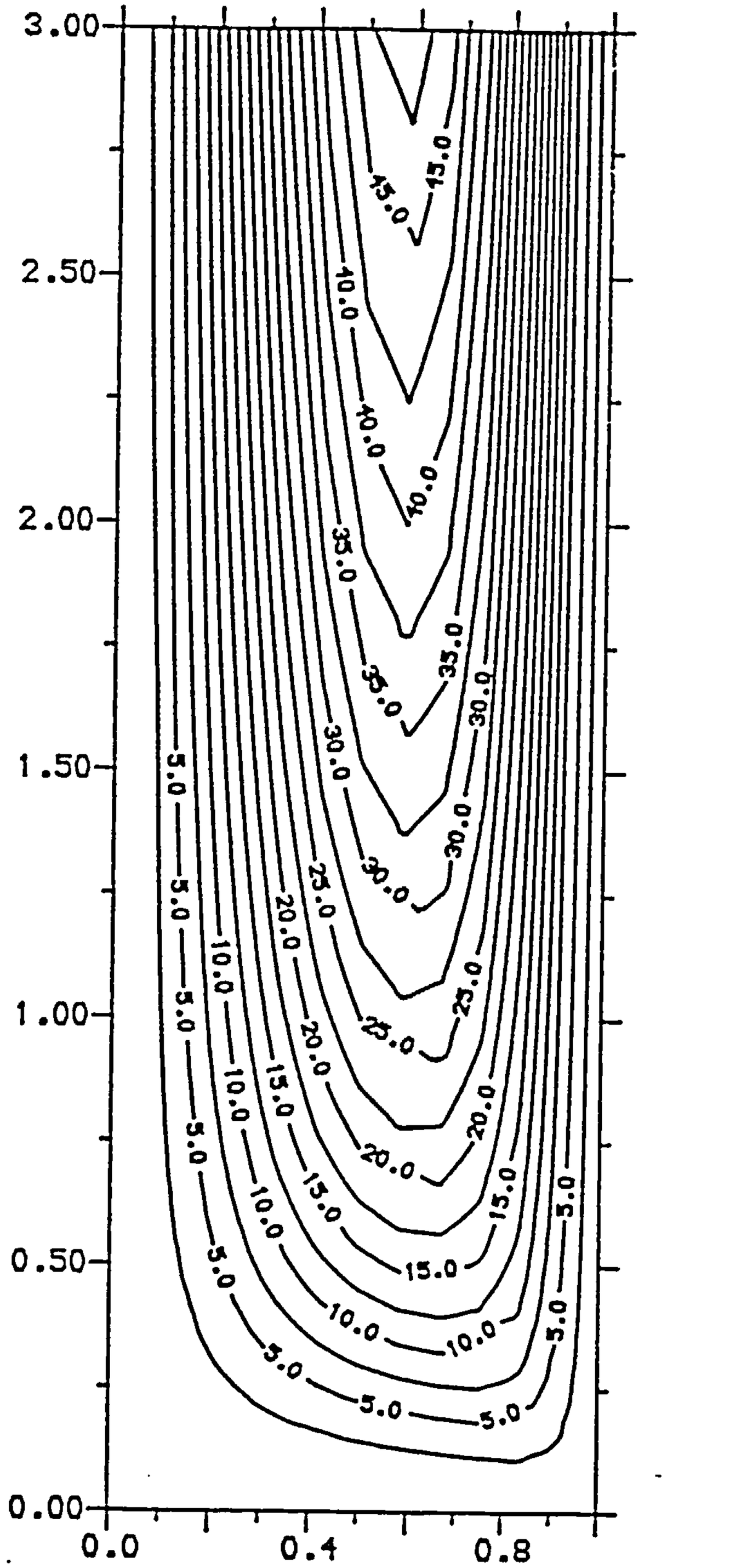

Figure 4.20: Contours of stream function with $\sigma = 6.983$, $A = 40000$ near the bottom of the slot for the insulating case.

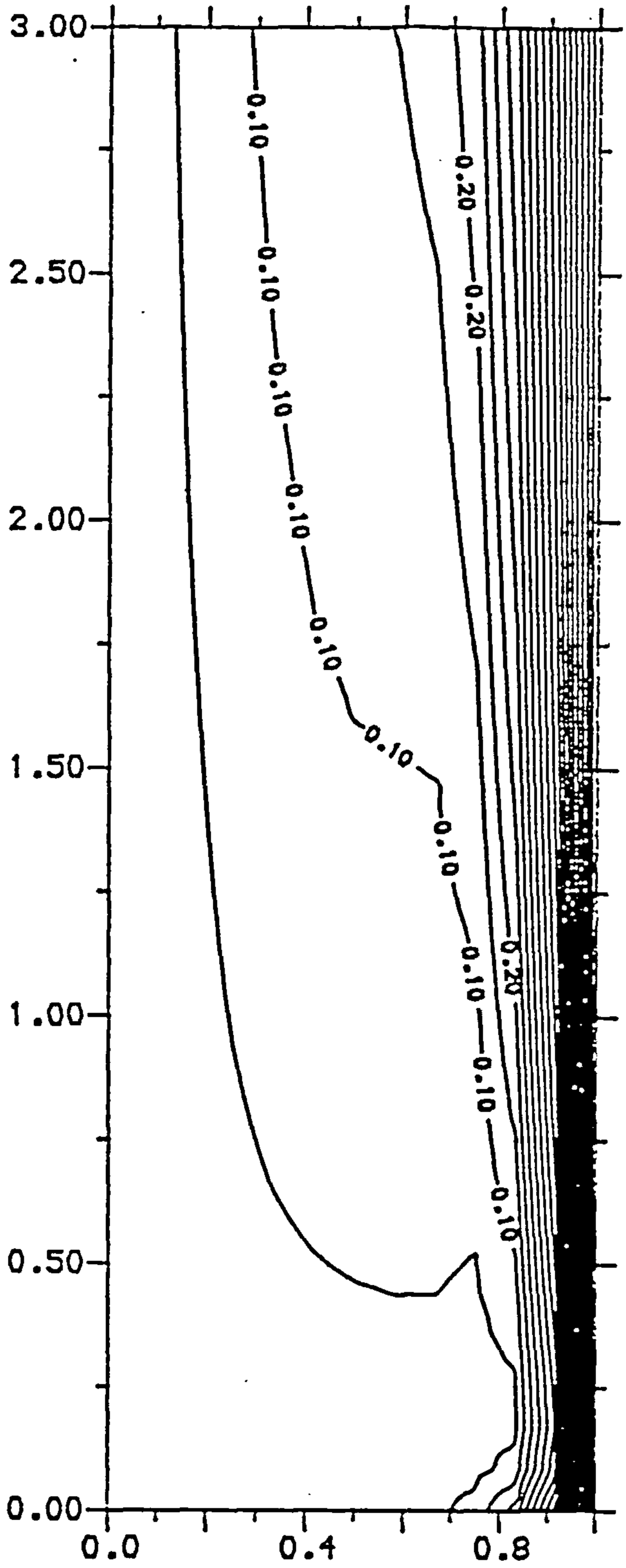

Figure 4.21: Contours of temperature with $\sigma = 6.983$, $A = 40000$ near the bottom of the slot for the insulating case.

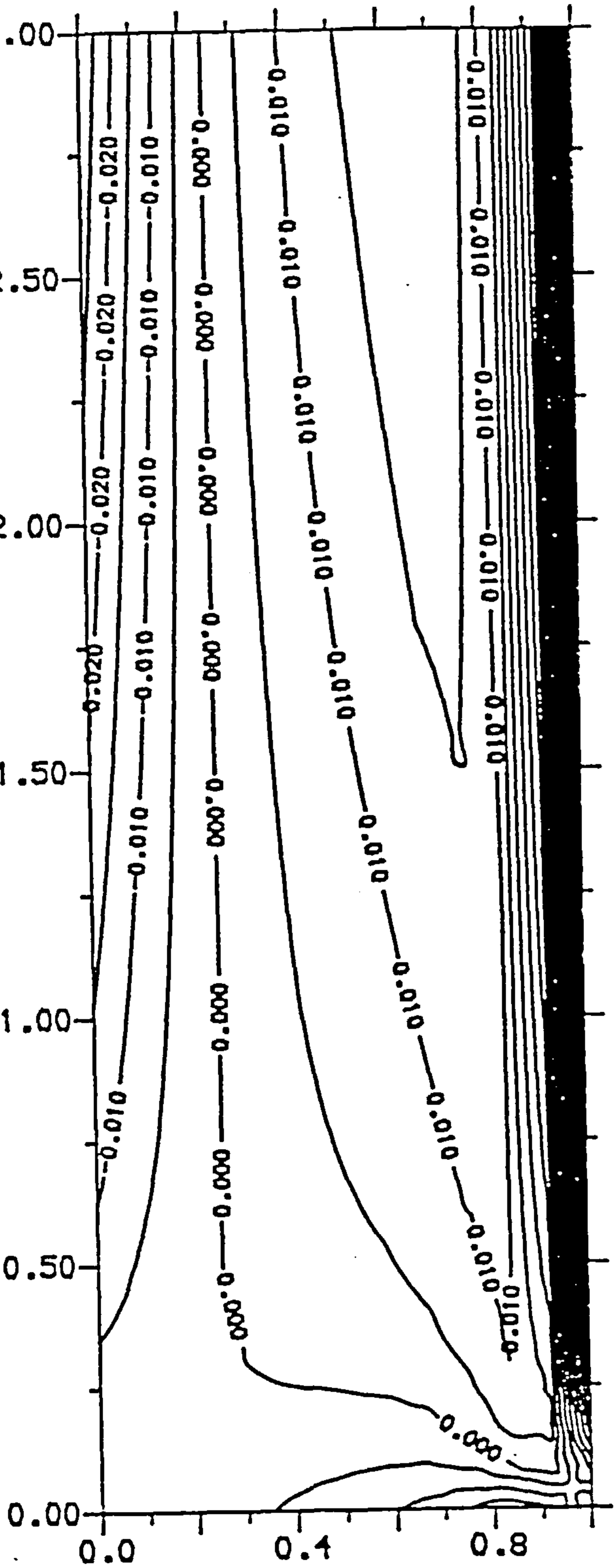

Figure 4.22: Contours of vorticity with $\sigma = 6.983$, $A = 40000$ near the bottom of the slot for the insulating case.

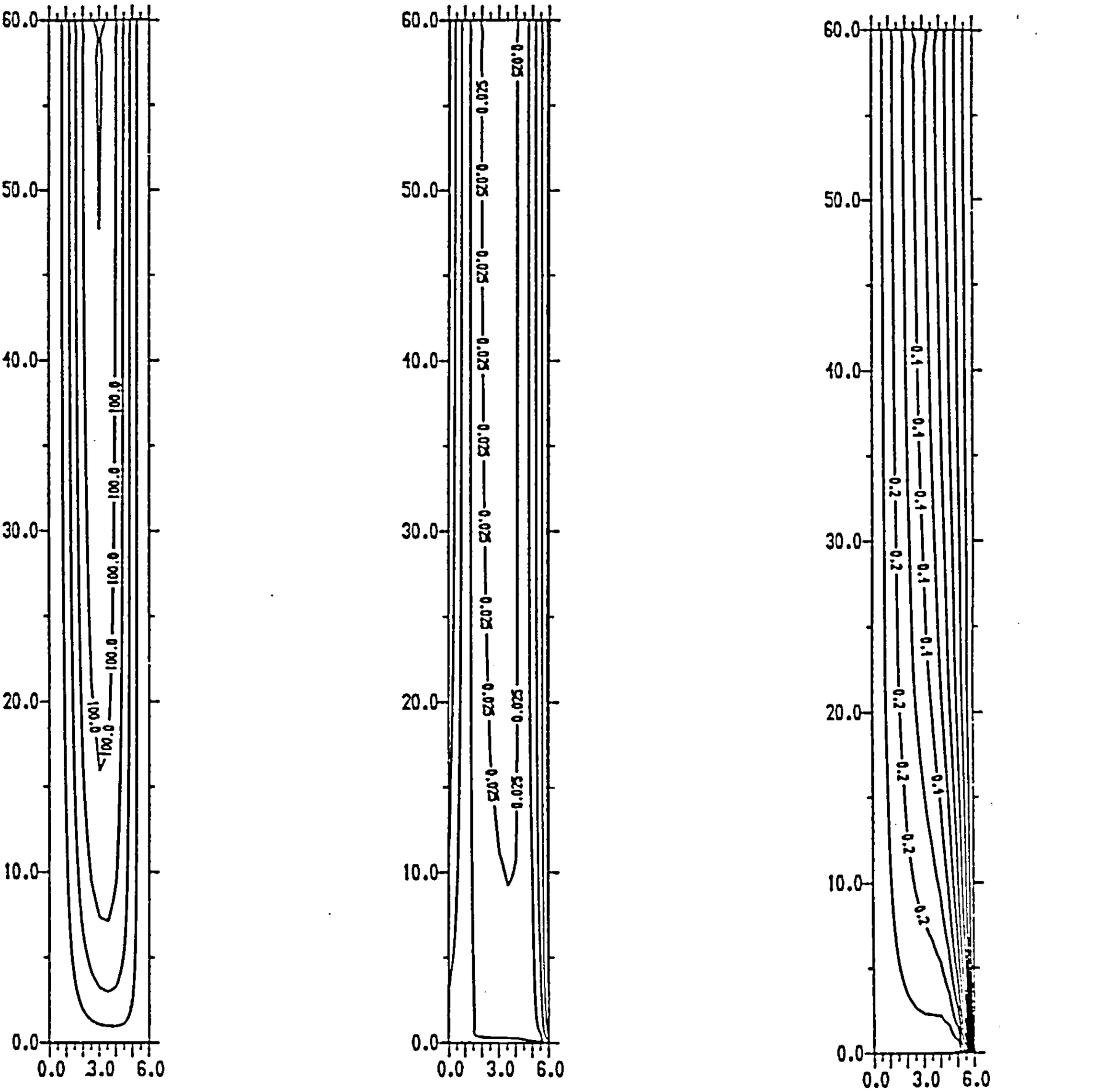

Contour Step 25.00

Contour Step 0.03

Contour Step 0.10

(a)

(b)

(c)

Figure 4.23: Contours of the steady-state solution for (a) stream function , (b) vorticity, (c) temperature, for $\sigma = 6.983$ and $A = 50000$, using a 12×600 computational grid with $z_\infty = 60$.

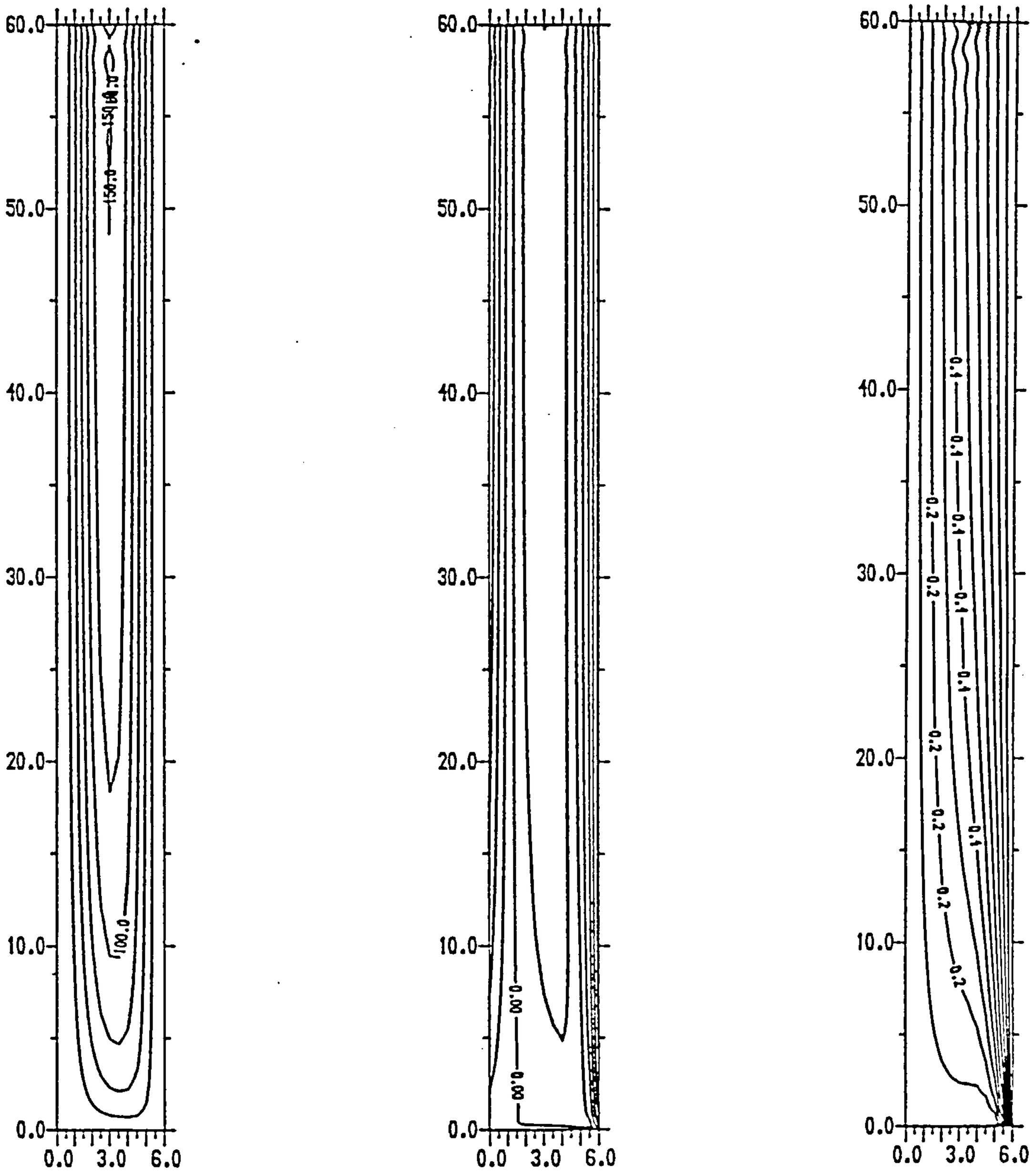

Contour Step 25.00

(a)

Contour Step 0.02

(b)

(c)

Figure 4.24: Contours of the steady-state solution for (a) stream function , (b) vorticity, (c) temperature, for $\sigma = 6.983$ and $A = 60000$, using a 12×600 computational grid with $z_\infty = 60$.

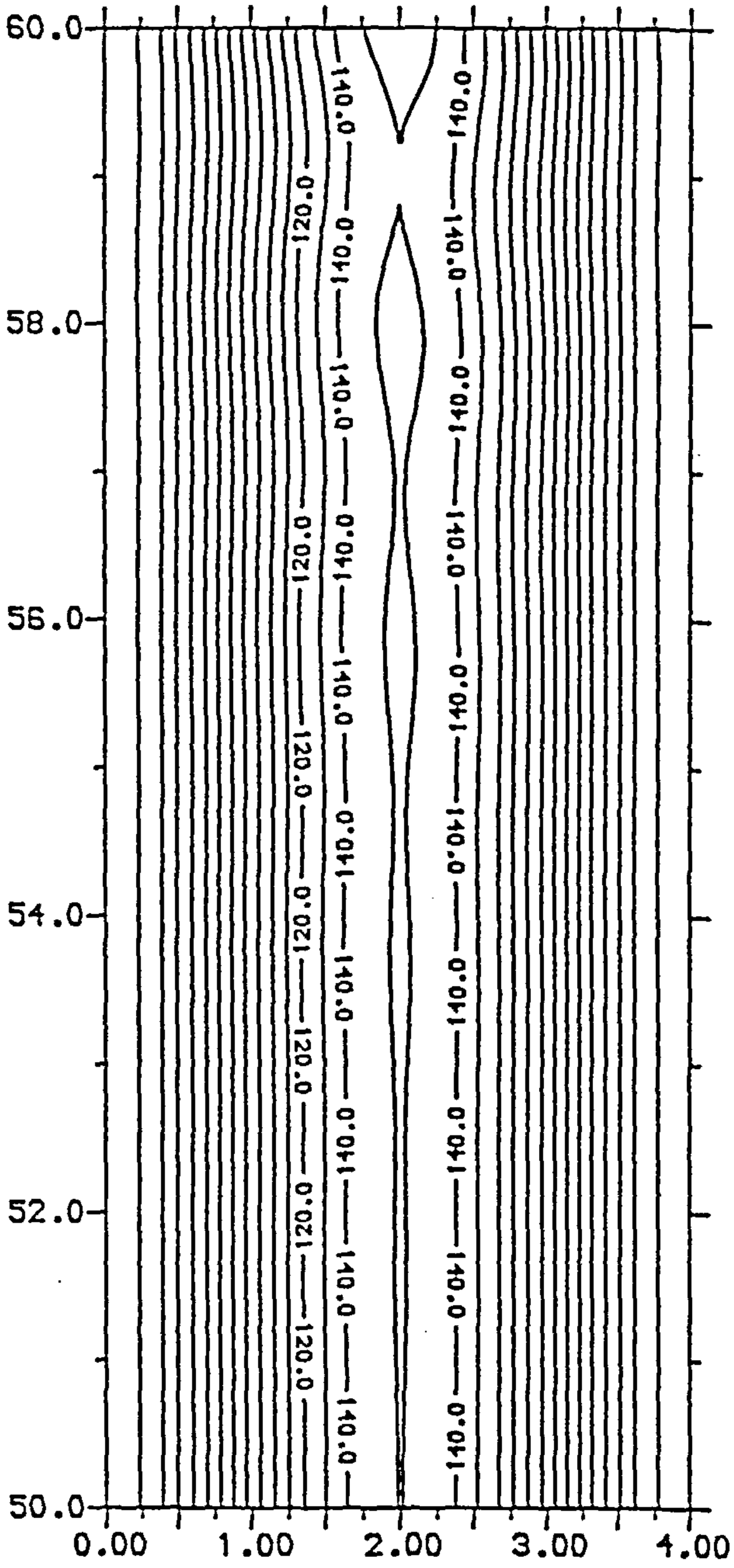

Figure 4.25: Streamlines with $\sigma = 6.983$, $A = 60000$ near the top of the end-zone for the insulating case.

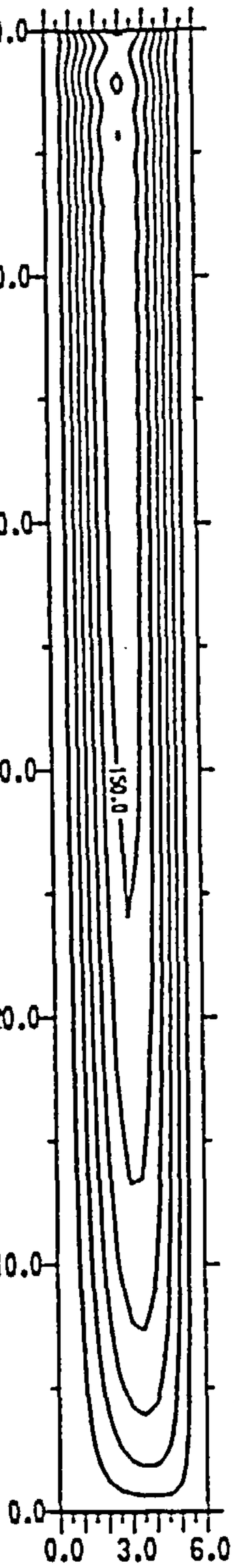

Contour Step 25.00

(a)

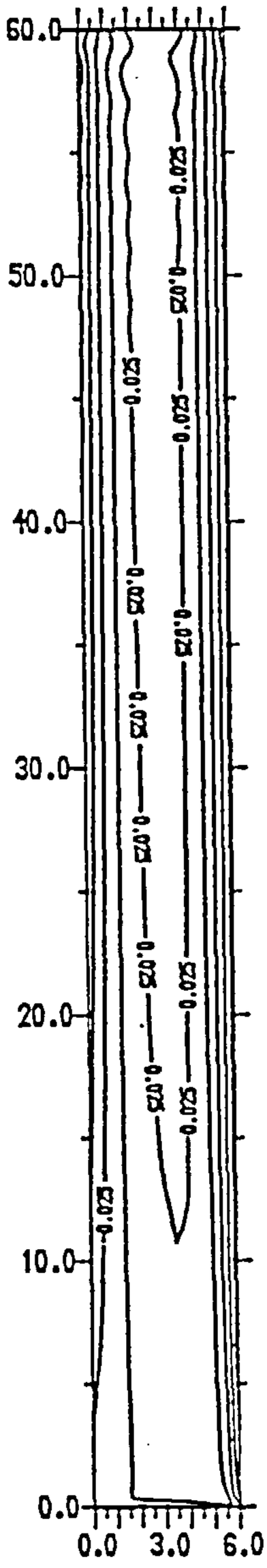

Contour Step 0.03

(b)

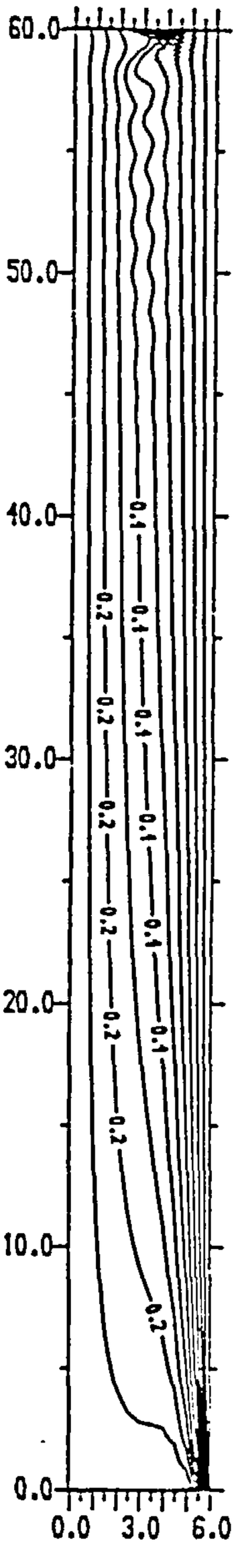

Contour Step 0.10

(c)

Figure 4.26: Contours of the steady-state solution for (a) stream function , (b) vorticity, (c) temperature, for $\sigma = 6.983$ and $A = 70000$, using a 12×600 computational grid with $z_\infty = 60$.

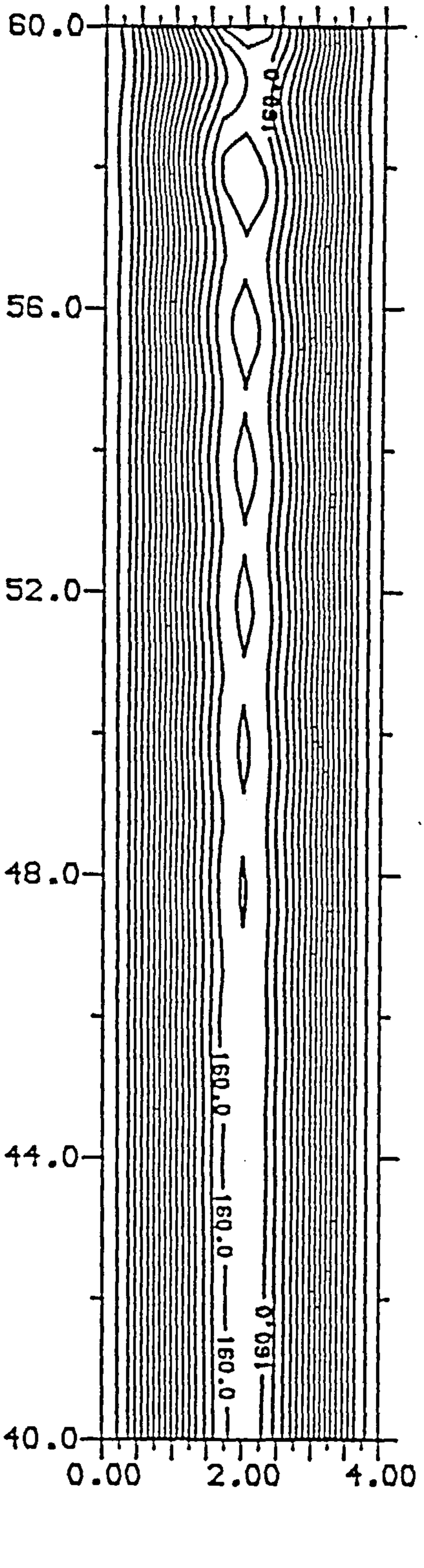

Figure 4.27: Streamlines with $\sigma = 6.983$, $A = 70000$ near the top of the end-zone for the insulating case.

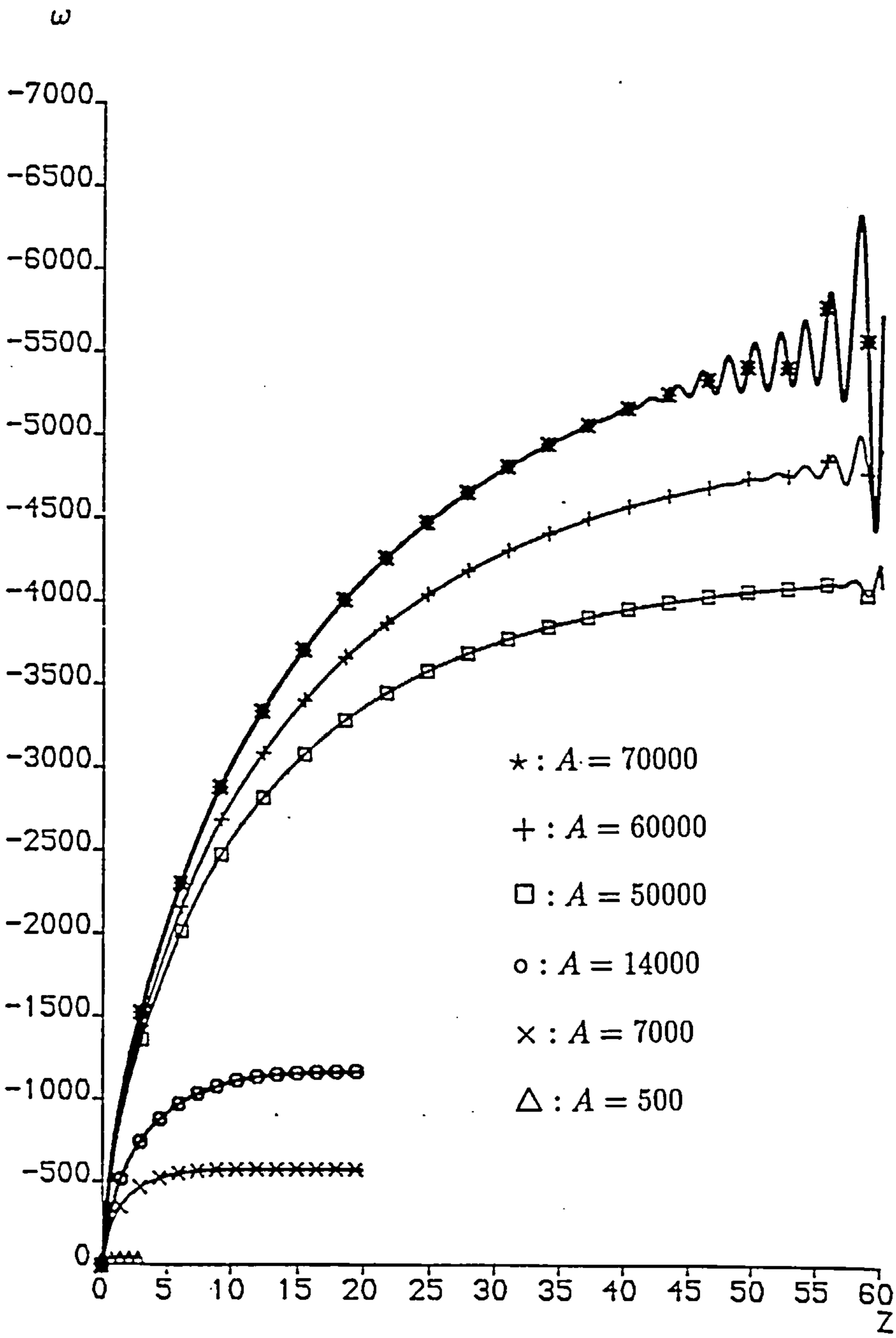

Figure 4.28: The skin friction with $\sigma = 6.983$ for different Rayleigh numbers on the cold wall for the insulating case.

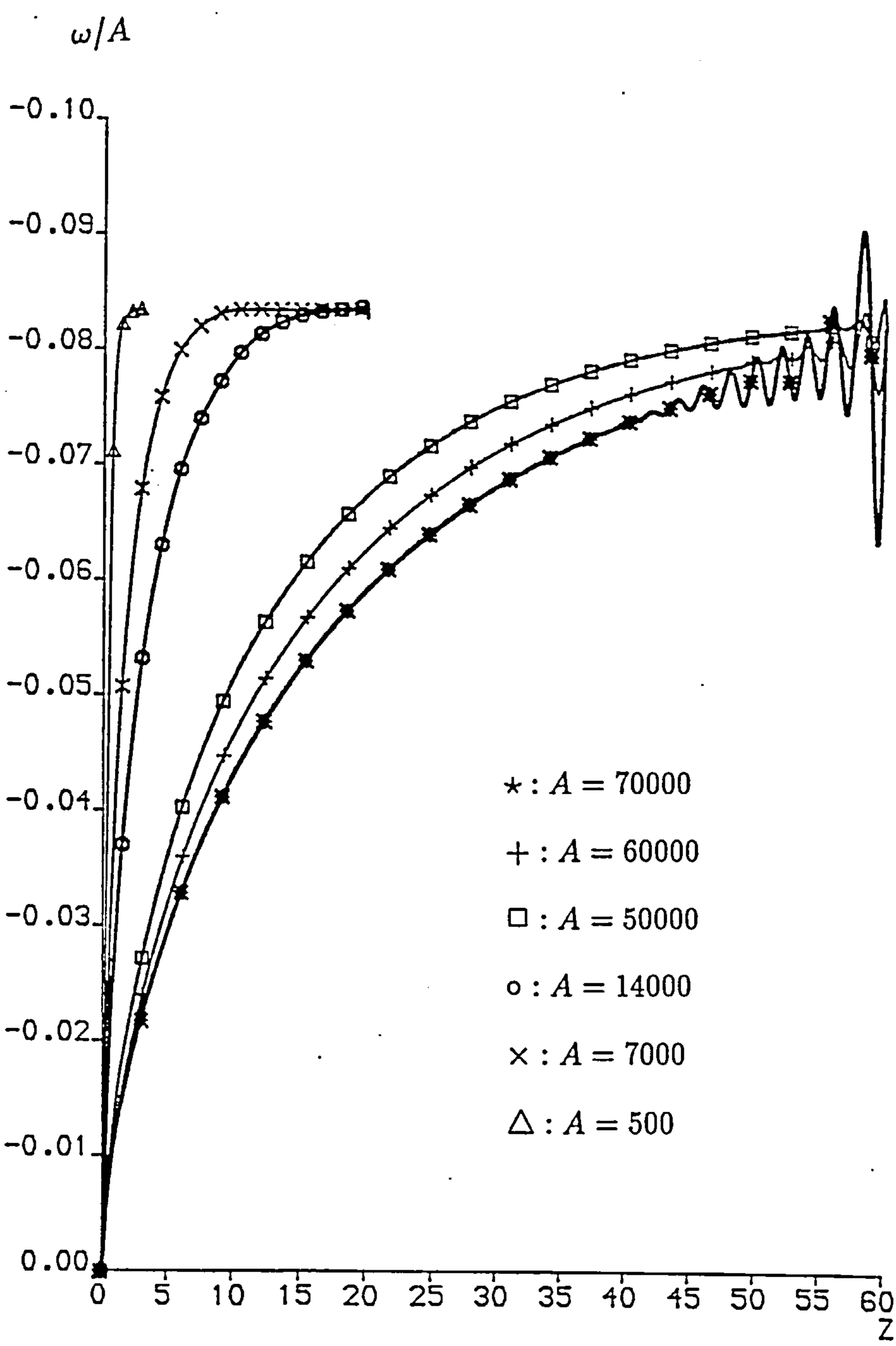

Figure 4.29: The skin friction ω/A with $\sigma = 6.983$ for different Rayleigh numbers on the cold wall for the insulating case.

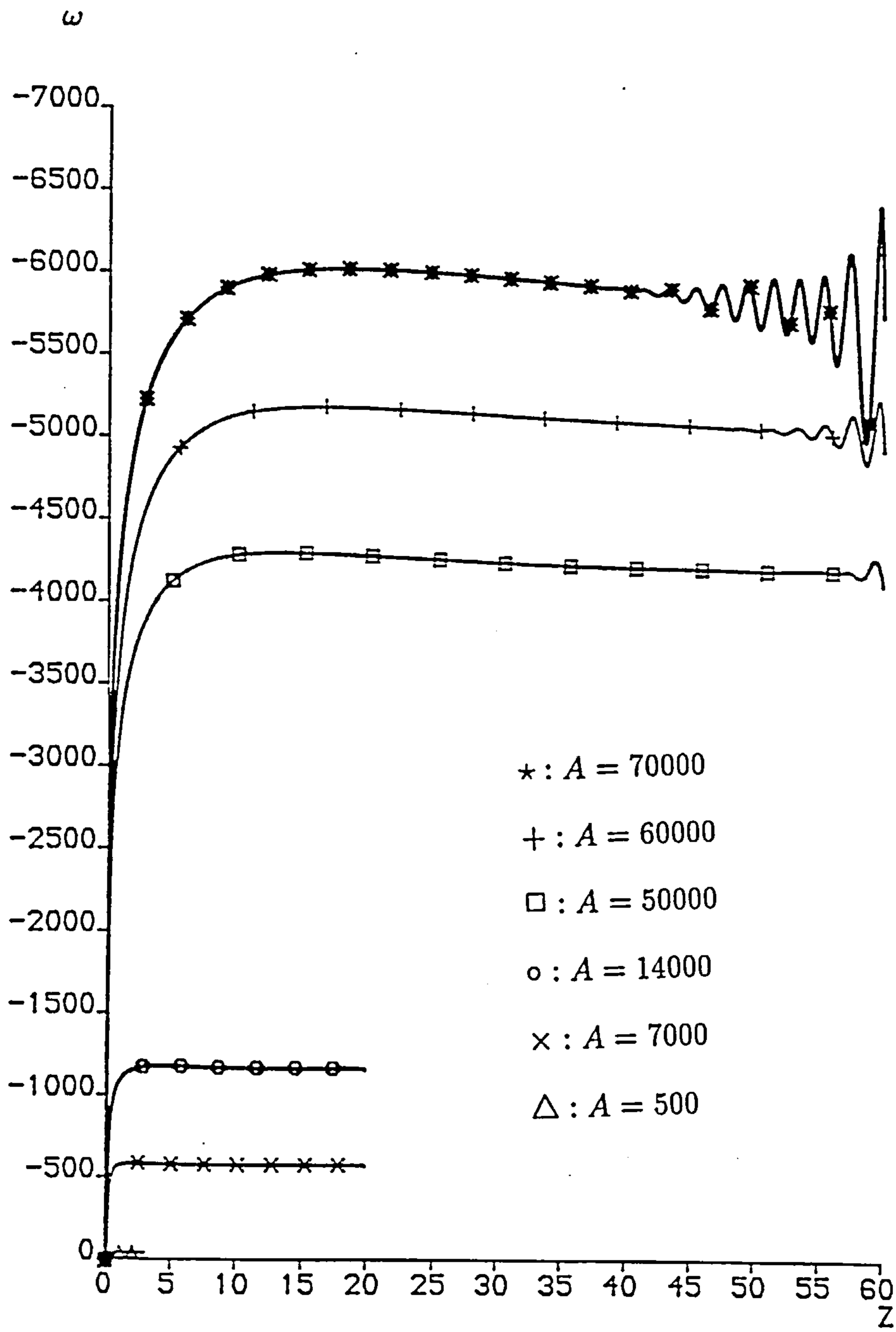

Figure 4.30: The skin friction with $\sigma = 6.983$ for different Rayleigh numbers on the hot wall for the insulating case.

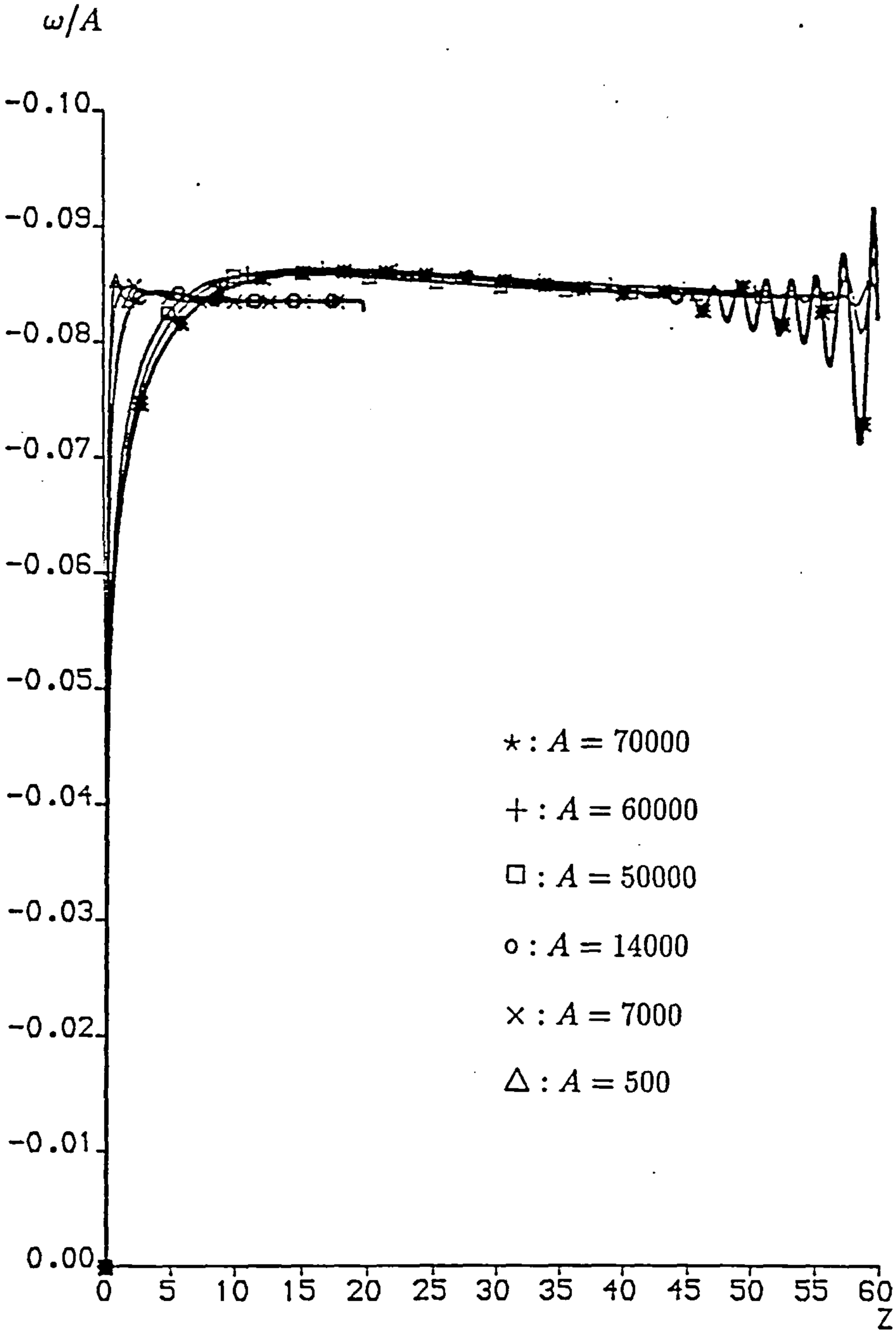

Figure 4.31: The skin friction ω/A with $\sigma = 6.983$ for different Rayleigh numbers on the hot wall for the insulating case.

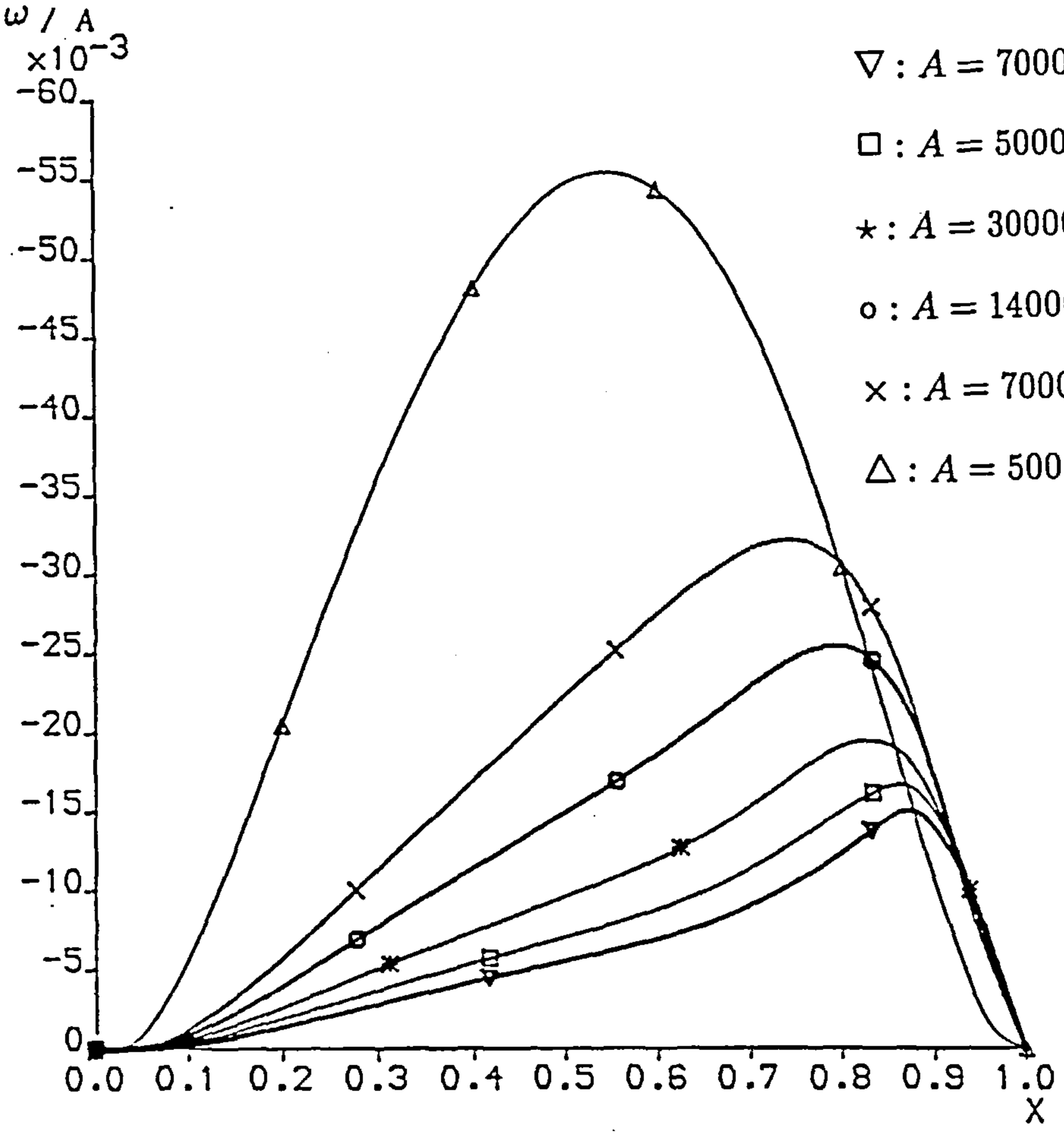

Figure 4.32: The skin friction ω/A with $\sigma = 6.983$ for different Rayleigh numbers on the bottom wall for the insulating case.

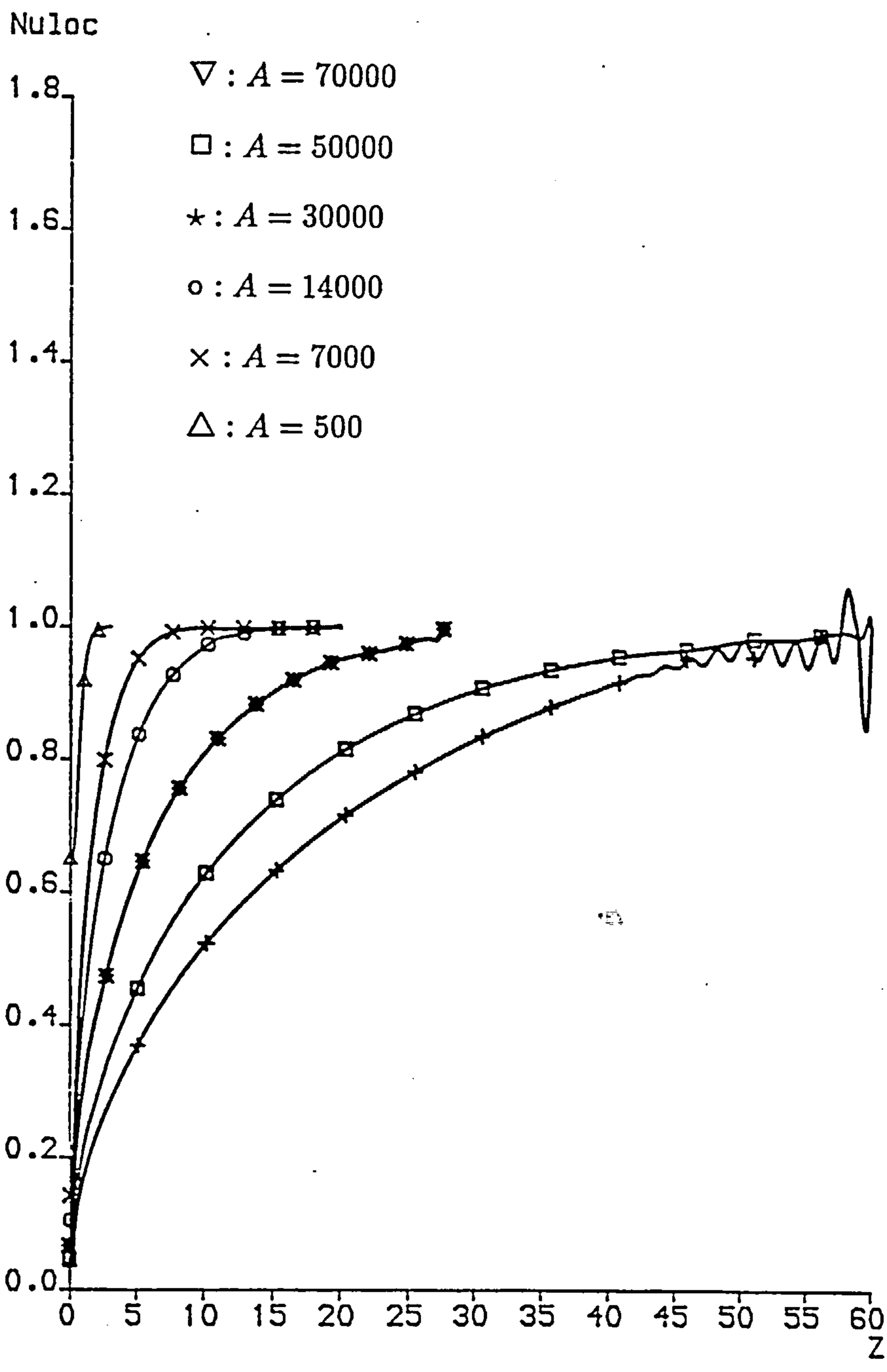

Figure 4.33: The local Nusselt number with $\sigma = 6.983$ for different Rayleigh numbers on the cold wall for the insulating case.

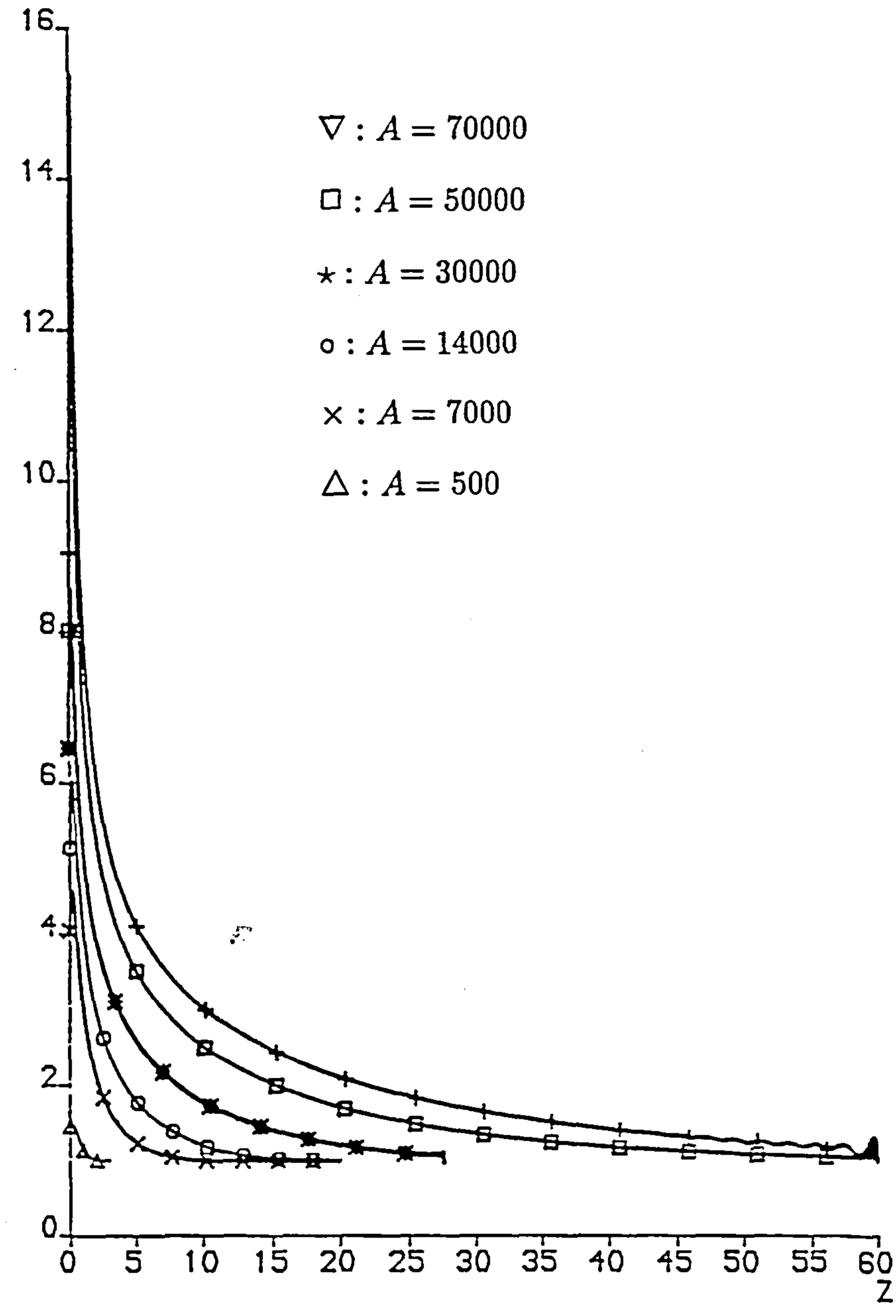

Figure 4.34: The local Nusselt number with $\sigma = 6.983$ for different Rayleigh numbers on the hot wall for the insulating case.

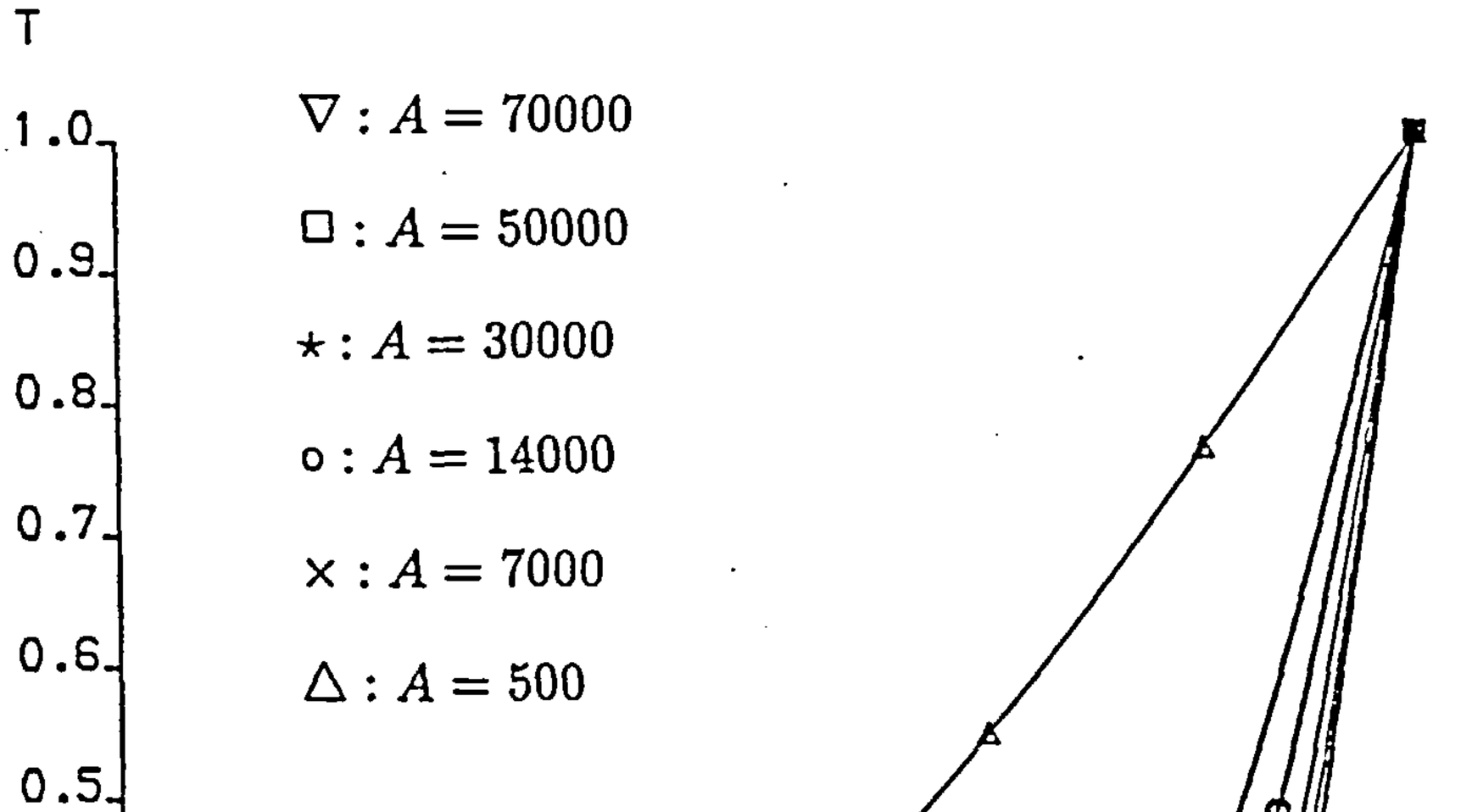

Figure 4.35: The temperature with $\sigma = 6.983$ for different Rayleigh numbers on the bottom wall for the insulating case.

Method	*Researchers*	$A\backslash H$	5	10	15	20	40
Numerical	Present Study	500	1.031	1.0155	1.0103	1.0067	1.0039
Numerical	Present Study	3000	1.41	1.205	1.1367	1.102	1.0512
Numerical	Lee and Korpela (1983)	3000	1.39	1.17	1.129	1.08	1.043
Numerical	Raithby and Wong (1981)	3000	1.40	1.2		1.13	1.045
Experimental	ElSherbiny et al (1982)	3000				1.07	1.01
Numerical	Present Study	5000	1.732	1.366	1.244	1.183	1.0915
Numerical	Lee and Korpela (1983)	5000	1.62	1.338	1.235	1.165	1.08
Experimental	ElSherbiny et al (1982)	5000				1.17	1.04

Table 4.1: Comparison of the average Nusselt number on the cold wall with previous results for air .

A	$\beta - \alpha$	$A/720$	*Discrepancy*
500	0.691	0.694	0.003
3000	4.092	4.167	0.075
5000	6.75	6.955	0.194

Table 4.2: Comparison of the two sides of equation (4.2.17) for air.

Chapter 5

Thermal Convection in a Shallow Laterally Heated Cavity with Conducting Boundaries

5.1 Introduction

This chapter investigates the structure of the flow in a shallow two dimensional rectangular cavity driven by lateral heating. The end walls are maintained at fixed but different temperatures which generate steady two dimensional motions within the cavity. The horizontal boundaries are assumed to be conducting.

The aspect ratio L is assumed to be large so that the cavity is shallow while the Rayleigh number R based on height is $O(L)$. In this range nonlinear effects become significant in end zones near each lateral boundary. For $R \ll L$ the flow is conduction-dominated everywhere with a parallel two-way flow generated throughout most of the cavity by a linear temperature field set up between the vertical end walls. The local solution near the vertical walls satisfies the full nonlinear Boussinesq equations when $R_1 = R/L = O(1)$ which must be solved by numerical methods.

Gargaro (1991) investigated certain properties of the end zone problem including a set of eigensolutions that generally decay away into the core region. The eigensolutions are involved in turning the flow in the end region , but one is associated with a stationary transverse mode of instability (Hart 1972) which can present itself at low Prandtl numbers. The parallel core flow is destroyed by this spatial oscillation, and as the Rayleigh number is increased the instability is forced into the system as a smooth transition emanating from the ends of the cavity.

This chapter describes a numerical solution of the full nonlinear Boussinesq equations in the end zone. Numerical results are compared with the stability theory carried out by Hart (1972, 1983a) and the results of Gargaro (1991).

5.2 Formulation

As in Chapter 2, the flow domain is a rectangular cavity of length l and height h. Two-dimensional motions are generated within the cavity by maintaining the vertical end walls at fixed but different temperatures. The governing equations, subject to the Boussinesq approximation, can be written in non-dimensional form as

$$\sigma^{-1}(\frac{\partial\bar{\omega}}{\partial t} + J(\bar{\omega}, \bar{\psi})) = \nabla^2\bar{\omega} + R\frac{\partial\bar{T}}{\partial x} \quad , \tag{5.2.1}$$

$$\nabla^2\bar{\psi} = -\bar{\omega} \quad , \tag{5.2.2}$$

$$\frac{\partial\bar{T}}{\partial t} + J(\bar{T}, \bar{\psi}) = \nabla^2\bar{T} \quad . \tag{5.2.3}$$

where the Prandtl number σ and the Rayleigh number R based on the height of the cavity are defined by

$$\sigma = \frac{\nu}{\kappa}, \quad R = \frac{g\beta\Delta T h^3}{\kappa\nu} \quad . \tag{5.2.4}$$

Here ν is the kinematic viscosity, κ is the thermal diffusivity, β is the coefficient of thermal expansion, g is the acceleration due to gravity and ΔT is the temperature difference between the end walls. The boundary conditions on the vertical sidewalls

are

$$\bar{\psi} = \frac{\partial \bar{\psi}}{\partial x} = 0 \quad \text{on} \quad x = 0,\, L \quad , \tag{5.2.5}$$

$$\bar{T} = 0 \quad \text{on} \quad x = 0 \quad , \tag{5.2.6}$$

$$\bar{T} = 1 \quad \text{on} \quad x = L \quad . \tag{5.2.7}$$

The horizontal surfaces are assumed to be conducting so that

$$\bar{\psi} = \frac{\partial \bar{\psi}}{\partial z} = 0 \quad \text{on} \quad z = 0,\, 1 \quad , \tag{5.2.8}$$

$$\bar{T} = \frac{x}{L} \quad \text{on} \quad z = 0,\, 1 \tag{5.2.9}$$

where $L = l/h$ is the cavity aspect ratio . These equations and boundary conditions have solutions which possess the centrosymmetric properties

$$\bar{\psi}(x,\, z,\, t) = \bar{\psi}(L - x,\, 1 - z,\, t), \quad \bar{T}(x,\, z,\, t) = 1 - \bar{T}(L - x,\, 1 - z,\, t) \tag{5.2.10}$$

so that in general for the steady state solution only half of the flow domain needs to be considered. The motion is controlled by the three parameters σ, R and L. The Hadley regime (Hadley 1735), defined by $L \to \infty$ with fixed R, has been discussed in detail by Cormack, Leal and Imberger (1974). It can be shown that their approach fails when $R = O(L)$ (Daniels, Blythe and Simpkins 1987), and the present work is concerned with the distinguished limit $L \to \infty$ such that

$$R_1 = \frac{R}{L} = O(1). \tag{5.2.11}$$

Unlike the Hadley structure these flows contain strong nonlinear effects in the end regions.

5.3 Core Solution and End-Zone Structure

Away from the end walls it is appropriate to use as independent variables,

$$\xi = \frac{x}{L}, \quad z = z \tag{5.3.12}$$

and the steady-state solution is found by expanding formally the stream function and the temperature as

$$\left.\begin{aligned}\bar{\psi} &= \psi_0(\xi,z) + L^{-1}\psi_1(\xi,z) + O(L^{-2}) \\ \bar{T} &= T_0(\xi,z) + L^{-1}T_1(\xi,z) + O(L^{-2})\end{aligned}\right\} \quad (L\to\infty) \quad . \tag{5.3.13}$$

Substituting into (5.2.1)-(5.2.3), and using the centrosymmetry relations together with the requirement that

$$T_0 = 0 \quad \text{at} \quad \xi = 0 \tag{5.3.14}$$

gives at leading order

$$T_0 = \xi \quad , \quad \psi_0 = R_1 F(z) \tag{5.3.15}$$

and at second order

$$T_1 = R_1 G(z) \tag{5.3.16}$$

where

$$F(z) = \frac{z^2}{24}(1-z)^2$$

and

$$G(z) = \frac{z^5}{120} - \frac{1}{48}z^4 + \frac{1}{72}z^3 - \frac{1}{720}z.$$

Thus in the core region

$$\left.\begin{aligned}\bar{\psi} &\sim R_1 F(z) \\ \bar{T} &\sim \xi + L^{-1}R_1 G(z)\end{aligned}\right\} \quad , \quad (L\to\infty) \tag{5.3.17}$$

and this solution is actually an exact steady-state solution of the full equations (5.2.1)-(5.2.3). It represents a horizontal two-way flow with fluid moving towards the cold wall in the top half of the cavity ($z > 1/2$) and the hot wall in the bottom half ($z < 1/2$). The temperature field varies linearly with ξ and is also vertically stratified. Near the ends of the cavity the fluid must be turned and the solution (5.3.15) is clearly invalid. The core solution (5.3.17) is only valid if a consistent solution can be found in end-regions near each vertical wall.

Since the overall motion can be assumed centro-symmetric only the solution at the cold end of the cavity needs to considered, where the temperature and stream

function can be expanded in the form

$$\bar{T} = L^{-1}T(x,z,t) + \cdots, \quad \bar{\psi} = \psi(x,z,t) + \cdots, \quad \bar{\omega} = \omega(x,z,t) + \cdots. \tag{5.3.18}$$

It then follows from (5.3.17) that the motion is governed by the full nonlinear Boussinesq equations

$$\sigma^{-1}(\frac{\partial \omega}{\partial t} + J(\omega, \psi)) = \nabla^2\omega + R_1\frac{\partial T}{\partial x} \quad , \tag{5.3.19}$$

$$\nabla^2\psi = -\omega \quad , \tag{5.3.20}$$

$$\frac{\partial T}{\partial t} + J(T, \psi) = \nabla^2 T \quad , \tag{5.3.21}$$

in the region $x \geq 0$, $0 \leq z \leq 1$ with boundary conditions

$$\psi = \frac{\partial \psi}{\partial z} = 0, \quad z = 0, 1 \quad , \tag{5.3.22}$$

$$\psi = \frac{\partial \psi}{\partial x} = 0 \quad \text{on} \quad x = 0 \quad , \tag{5.3.23}$$

$$T = 0, \quad x = 0, \tag{5.3.24}$$

$$T = x \quad , z = 0, 1 \tag{5.3.25}$$

and

$$\psi \to R_1F(z), \quad T \sim x + R_1G(z) \quad (x \to \infty) \quad . \tag{5.3.26}$$

Here (5.3.22)-(5.3.25) are the relevant boundary conditions on the cavity walls while (5.3.26) ensures that the solution matches with that in the core. Thus the regime where R_1 is $O(1)$ is identified by the presence of nonlinear inertial and convective effects in roughly square zones at each end of the cavity and the flow is determined by the solution of the full Boussinesq system (5.3.19)-(5.3.26) , which in general needs to be solved by a numerical technique. This is considered in the next section.

Certain properties of the end -zone problem have been studied by Gargaro (1991) who considered the manner in which the steady solution approaches the parallel core flow (5.3.17). This is found by considering the forms

$$\left.\begin{aligned} \psi &\sim R_1F(z) + \phi(z)exp(-\alpha x) \\ T &\sim x + R_1G(z) + \theta(z)exp(-\alpha x) \end{aligned}\right\} \quad (x \to \infty). \tag{5.3.27}$$

Substitution into (5.3.19)-(5.3.21) shows that the eigenvalue α is determined by the solution of the system

$$\phi'''' + 2\alpha^2\phi'' + \alpha^4\phi + \alpha R_1\theta = \alpha R_1(F'''\phi - F'(\phi'' + \alpha^2\phi))/\sigma \tag{5.3.28}$$

$$\theta'' + \alpha^2\theta - \phi' = \alpha R_1(G'\phi - F'\theta) \tag{5.3.29}$$

with

$$\theta = \phi = \phi' = 0 \quad \text{on} \quad z = 0, 1. \tag{5.3.30}$$

A triply-infinite family of eigenvalues α with positive real part is found to exist for $R_1 < R_{1c}(\sigma)$, indicating that an end-zone solution can then be found consistent with exponential decay to the parallel core flow. At the critical Rayleigh number R_{1c}, the real part of the leading eigenvalue tends to zero, leaving a purely imaginary solution $\alpha = i\alpha_c$, equivalent to oscillatory behaviour associated with instability of the parallel core flow in the form of transverse rolls (Hart 1972), and for $R_1 > R_{1c}(\sigma)$, the parallel flow is destroyed by multiple eddies which are forced into the core from the end zones. The function $R_{1c}(\sigma)$ is given by Gargaro (1991) and exists only in the region $0 \leq \sigma \leq 0.27$, tending to infinity as $\sigma \to 0.27$ and approaching 7980σ as $\sigma \to 0$ (Hart 1972). For $\sigma > 0.27$ an end-zone solution consistent with a smooth approach (5.3.17) to a parallel core flow is possible for any Rayleigh number R_1. For lower Prandtl numbers the outer behaviour (5.3.17) is only possible when $R_1 < R_{1c}(\sigma)$.

For low Rayleigh numbers $R_1 \to 0$, the steady solution of the end zone problem can be developed as a power series in R_1 in the manner described by Cormack, Leal and Imberger (1974). In this case

$$T = x + R_1T_1(x, z) + \cdots, \quad \psi = R_1\psi_1(x, z) + \cdots \tag{5.3.31}$$

where ψ_1 satisfies the equation

$$\nabla^4\psi_1 = 1 \tag{5.3.32}$$

with boundary conditions

$$\psi_1 = \frac{\partial\psi_1}{\partial z} = 0, \quad z = 0, 1, \tag{5.3.33}$$

$$\psi_1 = \frac{\partial \psi_1}{\partial x} = 0, \quad x = 0, \tag{5.3.34}$$

$$\psi_1 \to F(z) \quad (x \to \infty). \tag{5.3.35}$$

The solution given by Cormack et al (1974) is equivalent to a symmetric turning motion and is also relevant at small Rayleigh numbers ($A \ll 1$) in the end zones of the tall cavity problems considered in Chapters 3 and 4.

5.4 Numerical Scheme for the End-Zone Problem

The system (5.3.19)-(5.3.26) can be solved numerically using the scheme developed in earlier chapters and a finite computational domain $0 \leq x \leq x_\infty$, $0 \leq z \leq 1$ with x_∞ chosen sufficiently large to accommodate the solution. As in the tall cavity problem, at high Rayleigh numbers a long range in the x direction is required for the solution to attain the parallel core flow, with the leading eigenvalue α in (5.3.28)-(5.3.30) proportional to R_1^{-1} as $R_1 \to \infty$ when $\sigma > 0.27$ (Gargaro 1991). Therefore, a large outer boundary is required for high Rayleigh numbers.

The numerical scheme of Chapter 2 is used for the end-zone problem, with modifications to account for the new outer boundary condition at x_∞, where (5.3.17) is applied in the form

$$\psi = R_1 F(z), \quad \frac{\partial T}{\partial x} = 1 \quad . \tag{5.4.1}$$

Thus in the numerical scheme the thermal boundary conditions become

$$T_{i,0} = T_{i,N_z} = i\Delta x, \quad (i = 0, 1, 2, ..., N_x), \tag{5.4.2}$$

$$T_{0,j} = 0, \quad (j = 0, 1, \cdots, N_z) \tag{5.4.3}$$

and

$$T_{N_x,j} = \Delta x + T_{N_x-1,j}, \quad (j = 0, 1, \cdots, N_z) \tag{5.4.4}$$

for all time levels. Here $N_z = \frac{1}{\Delta z}$, $N_x = \frac{x_\infty}{\Delta x}$, and Δx, Δz are the space steps.

For the vorticity, the method used here is similar to that of the finite cavity problem except that the formala

$$\omega_{N_x,j} = -R_1 F''(j\Delta z), \quad (j = 0, 1, 2, ..., N_z) \tag{5.4.5}$$

is used for all time levels to appoximate the outer boundary conditon for ω.

For the stream function, ψ, (5.3.22), (5.3.23) and (5.3.26) give

$$\psi_{0,j} = 0, \quad \psi_{N_x,j} = R_1 F(j\Delta z), \quad (j = 0, 1, 2, ..., N_z) \tag{5.4.6}$$

$$\psi_{i,0} = 0, \quad \psi_{i,N_z} = 0, \quad (i = 0, 1, 2, ..., N_x) \tag{5.4.7}$$

for all time levels.

The heat transfer along the cold, top and bottom walls is characterised by the local Nusselt numbers,

$$Nu_{loc} = \frac{\partial T}{\partial x}|_{x=0},$$

$$Nu_{loc} = \frac{\partial T}{\partial z}|_{z=1},$$

$$Nu_{loc} = \frac{\partial T}{\partial z}|_{z=0}.$$

Numerically these are approximated by Taylor series expansions so that for the cold wall

$$\frac{\partial T}{\partial x}|_{x=0} = \frac{18T_{1,j} - 9T_{2,j} + 2T_{3,j} - 11T_{0,j}}{6\Delta x}, \quad (j = 0, 1, 2, ..., N_z) \tag{5.4.8}$$

where $T_{0,j} = 0$; for the top wall

$$\frac{\partial T}{\partial z}|_{z=1} = -\frac{18T_{i,N_x-1} - 9T_{i,N_x-2} + 2T_{i,N_x-3} - 11T_{i,N_x}}{6\Delta z}, \quad (i = 0, 1, 2, ..., N_x) \tag{5.4.9}$$

where $T_{i,N_x} = i\Delta x$ and for the bottom wall

$$\frac{\partial T}{\partial z}|_{z=0} = \frac{18T_{i,1} - 9T_{i,2} + 2T_{i,3} - 11T_{i,0}}{6\Delta z}, \quad (i = 0, 1, 2, ..., N_x) \tag{5.4.10}$$

where $T_{i,0} = i\Delta x$. For a steady-state solution, integration of the heat equation

$$\nabla^2 T = \frac{\partial(T, \psi)}{\partial(x, z)} \tag{5.4.11}$$

over the end zone gives

$$\int_0^\infty \int_0^1 \nabla^2 T dx dz = \int_0^\infty \int_0^1 \frac{\partial(T,\psi)}{\partial(x,z)} dx dz. \tag{5.4.12}$$

Using the outer form (5.3.17) yields

$$\begin{aligned} \int_0^1 \frac{\partial T}{\partial x}|_{x=0} dz - \int_0^\infty (\frac{\partial T}{\partial z}|_{z=1} - \frac{\partial T}{\partial z}|_{z=0}) dx &= 1 + \int_0^1 \psi \frac{\partial T}{\partial z}|_{x=\infty} dz \\ &= 1 + \frac{R_1^2}{1209600}. \end{aligned} \tag{5.4.13}$$

Once a steady-state numerical solution of the end zone is obtained, the integrals on the left hand side of equation (5.4.13) can be calculated using Simpson's rule . The above relation can then be used to provide a check on the accuracy of the numerical solution.

The steady-state solution is computed by starting from the following state:

$$\left.\begin{aligned} T &= x \\ \psi &= 0 \\ \omega = u &= w = 0 \end{aligned}\right\} (0 \le x < x_\infty), \quad (0 \le z \le 1) \tag{5.4.14}$$

$$\left.\begin{aligned} \frac{\partial T}{\partial x} &= 1 \\ \psi &= R_1 F(z) \\ \omega &= -R_1 F''(z) \\ u &= w = 0 \end{aligned}\right\} (x = x_\infty), \quad (0 \le z \le 1). \tag{5.4.15}$$

Apart from modifications already noted, the overall scheme of computation is the same as that in Chapter 2 for a finite cavity except that R is replaced by R_1 .

5.5 Numerical Results and Discussion

This section presents the results of numerical experiments conducted for the end zone problem for two Prandtl numbers, $\sigma = 0.05$ and $\sigma = 0.733$, and for a range of Rayleigh numbers, R_1. The outer boundary is varied according to the values of the Rayleigh number in order to accommodate the outer boundary condition (5.3.17).

For low Prandtl number ($\sigma = 0.05$) there is the possibility of spatial oscillations when the Rayleigh number R_1 reaches the critical value $R_{1c}(0.05) \approx 455$ (Gargaro 1991). Contour plots of streamfunction, vorticity and temperature with $\sigma = 0.05$ and different Rayleigh numbers ranging from 200 to 600 are shown in Figures 5.1-5.4. Here, an outer boundary $x_\infty = 6$ is used. Figure 5.1 shows the near-symmetric flow associated with the low Rayleigh number limit (5.3.31); the temperature field is primarily linear in x together with a small vertical gradient associated with the term $R_1 G(z)$. In Figure 5.2, where the Rayleigh number is increased to 400, the streamline field indicates the development of weak eddies along $z = 0.5$. This secondary flow increases in amplitude as the Rayleigh number increases, as shown for $R_1 = 500$ and $R_1 = 600$ in Figures 5.3 and 5.4. The critical Rayleigh number for the onset of transverse rolls is $R_{1c}(0.05) = 455$ and the critical wavelength is $z = 2\pi/\alpha_c = 2.33$, consistent with the evidence of the numerical results obtained here. The numerical results are also in good agreement with those obtained by Drummond and Korpela (1985) by solving the full cavity problem for a range of large aspect ratios.

Numerical results have been obtained for air ($\sigma = 0.733$) for a range of Rayleigh numbers from 500 to 14000. Outer boundaries $x_\infty = 3, 7$ were chosen for the computations. Figures 5.5-5.8 illustrate the contour fields of stream function, vorticity and temperature in the end region. These flow patterns are different from those with $\sigma = 0.05$ and, in particular, the flow is free from multiple eddies (since $\sigma > 0.27$). In Figure 5.5, where $R_1 = 500$, the flow approximates the symmetric low Rayleigh number form (5.3.31) and the main turning motion occurs in the region $0 \leq x < 1$ close to the cold wall. As the Rayleigh number is increased, an inward penetration of nonlinear convective effects from the end of the cavity is observed. The non-parallel region extends into the cavity, as shown in the results for $3000 \leq R_1 \leq 14000$ in Figures 5.6-5.8. The vertical temperature variation increases and there is a tendency for the turning motion to dip towards the lower boundary near the cold wall. Profiles of the skin friction on the bottom wall (Figure 5.9) show a sharp change close to the cold wall and at higher Rayleigh numbers there is a further sharp decrease

just dowmstream, suggesting the possibility of a flow separation on the bottom wall at sufficiently high Rayleigh number. Figures 5.10-5.11 show the skin friction on the top and cold walls respectively.

Local Nusselt numbers for the cold, top and bottom walls are shown in Figures 5.12-5.14. The heat flux changes remarkably little on the top wall for different Rayleigh numbers (Figure 5.13), but on the bottom wall, there are significant changes near the cold corner (Figure 5.14) where heat is transferred out of the cavity for Rayleigh numbers greater than about 3000. The local Nusselt number on the cold wall is shown in Figure 5.12 and indicates how the outward heat transfer is significantly enhanced as R_1 increases; the overall Nusselt number for the cold wall is given in Table 5.1. Formula (5.4.13) was used to test the accuracy of the numerical results, and values of each side of the equation are listed in Table 5.2. This indicates good consistency, discrepancies being attributable to the limitation in the number of grid points and the finite extent of the outer boundary at $x = x_\infty$.

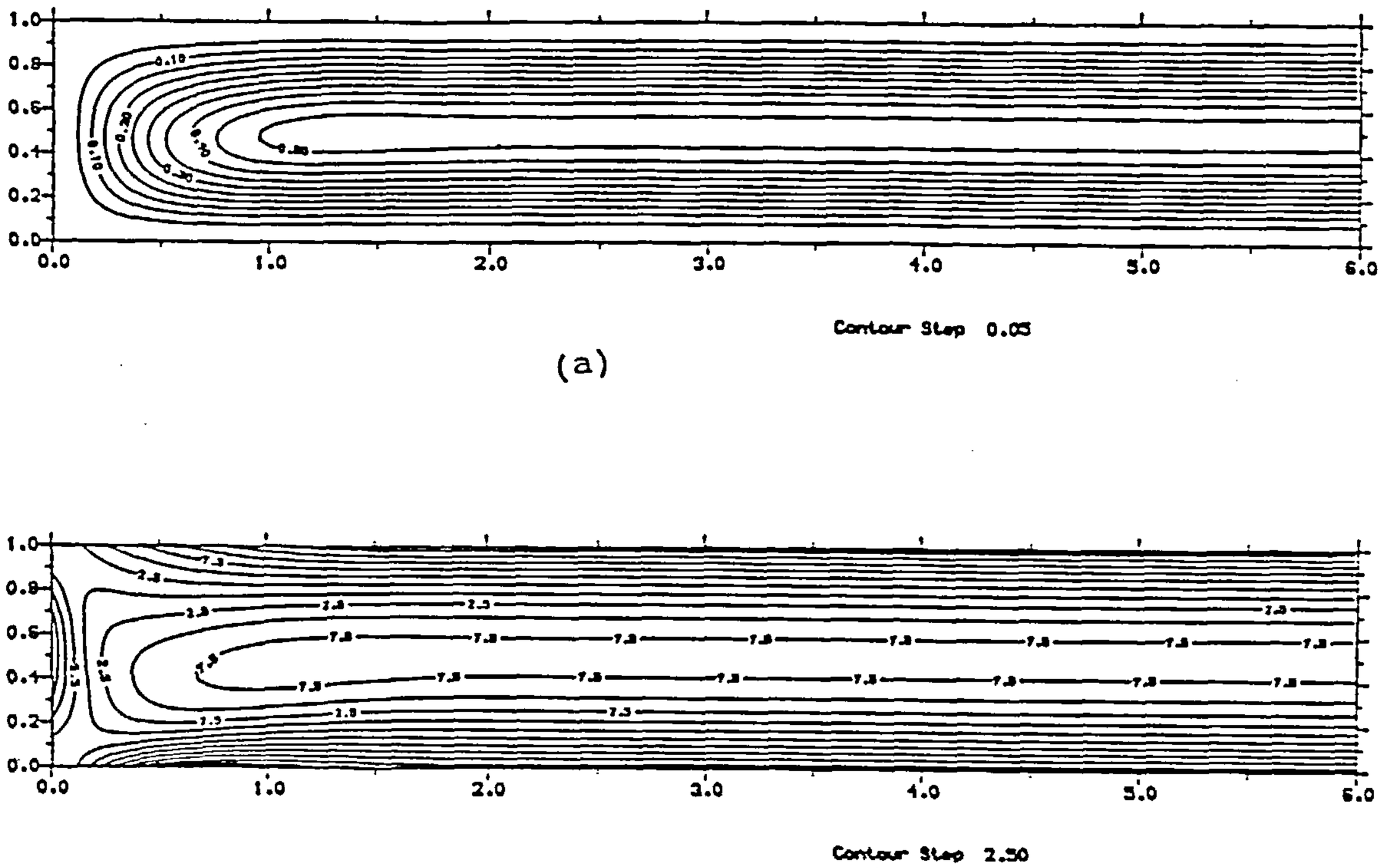

Figure 5.1: Contours of the steady-state solution for (a) stream function , (b) vorticity, (c) temperature, for $\sigma = 0.05$ and $R_1 = 200$, using a 180×30 computational grid with $x_\infty = 6$.

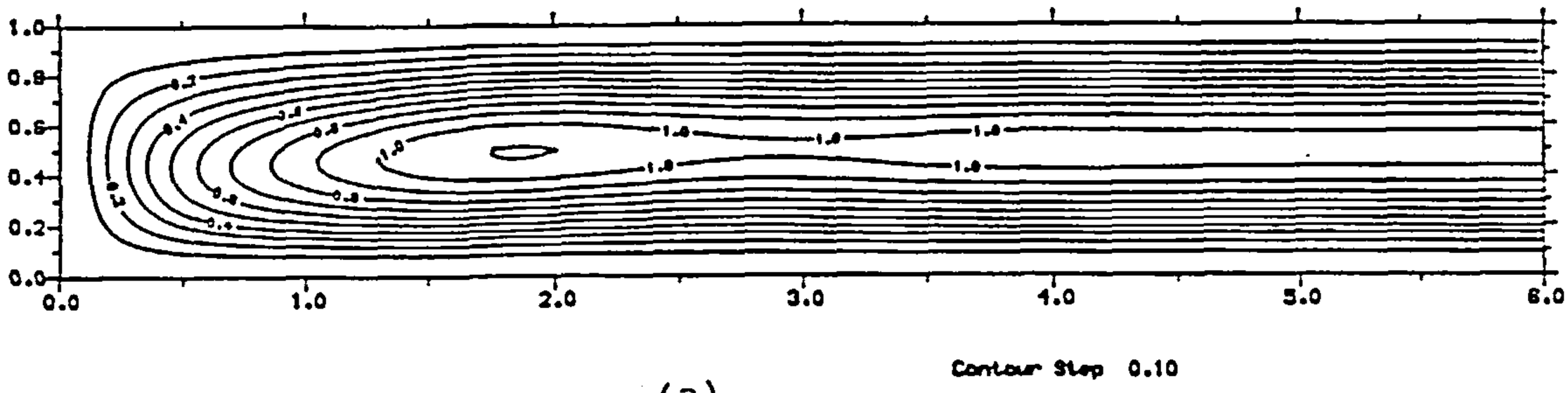

(a)

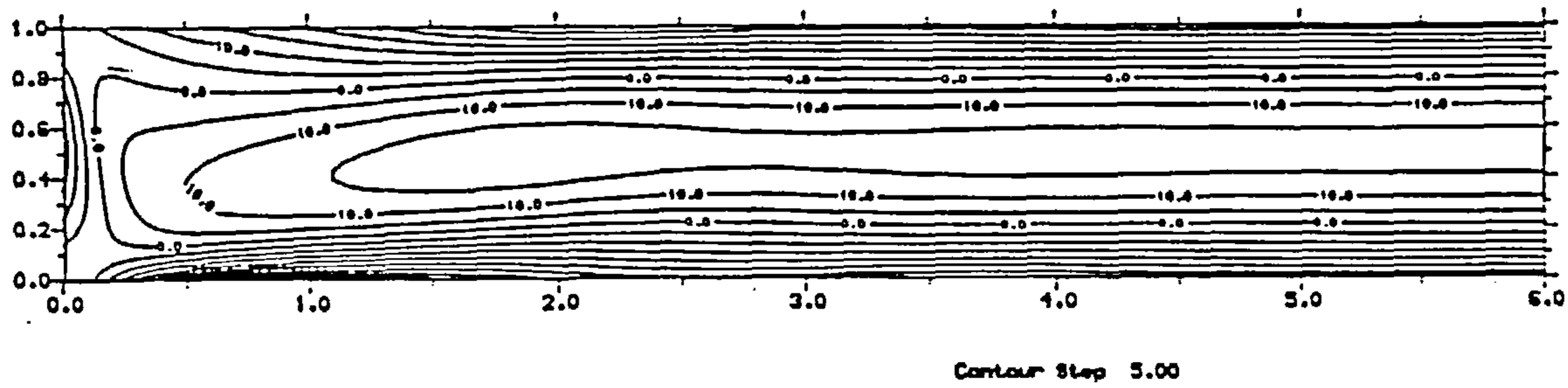

(b)

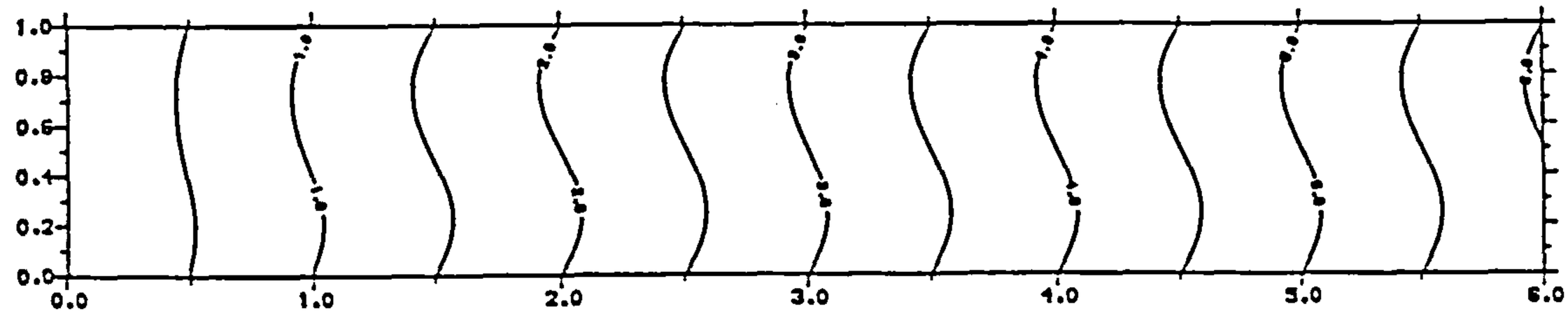

(c) Contour Step 0.50

Figure 5.2: Contours of the steady-state solution for (a) stream function , (b) vorticity, (c) temperature, for $\sigma = 0.05$ and $R_1 = 400$, using a 180×30 computational grid with $x_\infty = 6$.

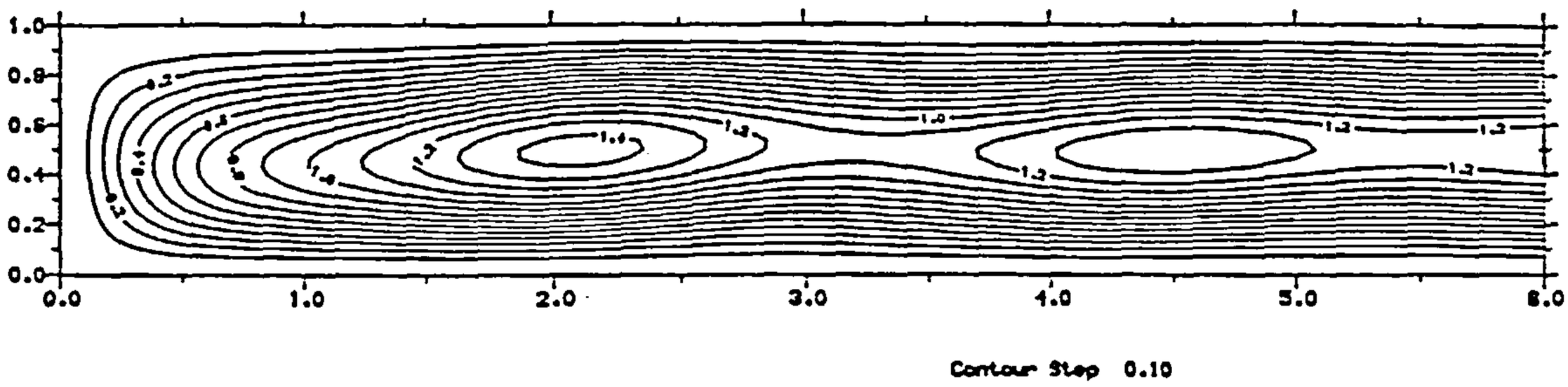

(a)

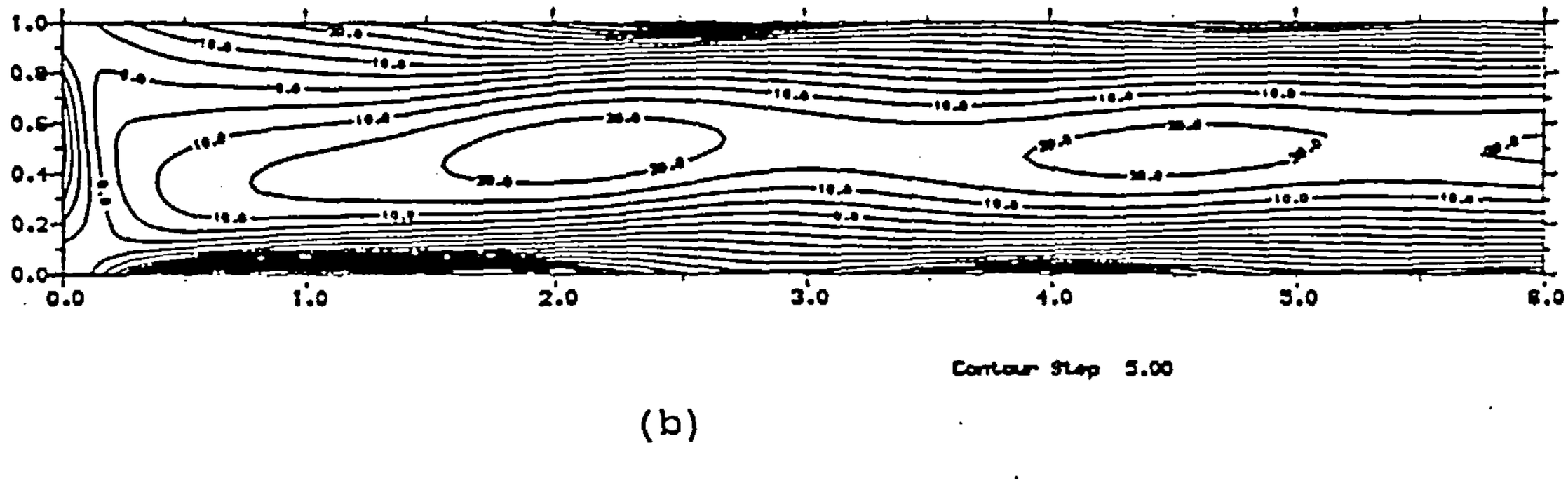

(b)

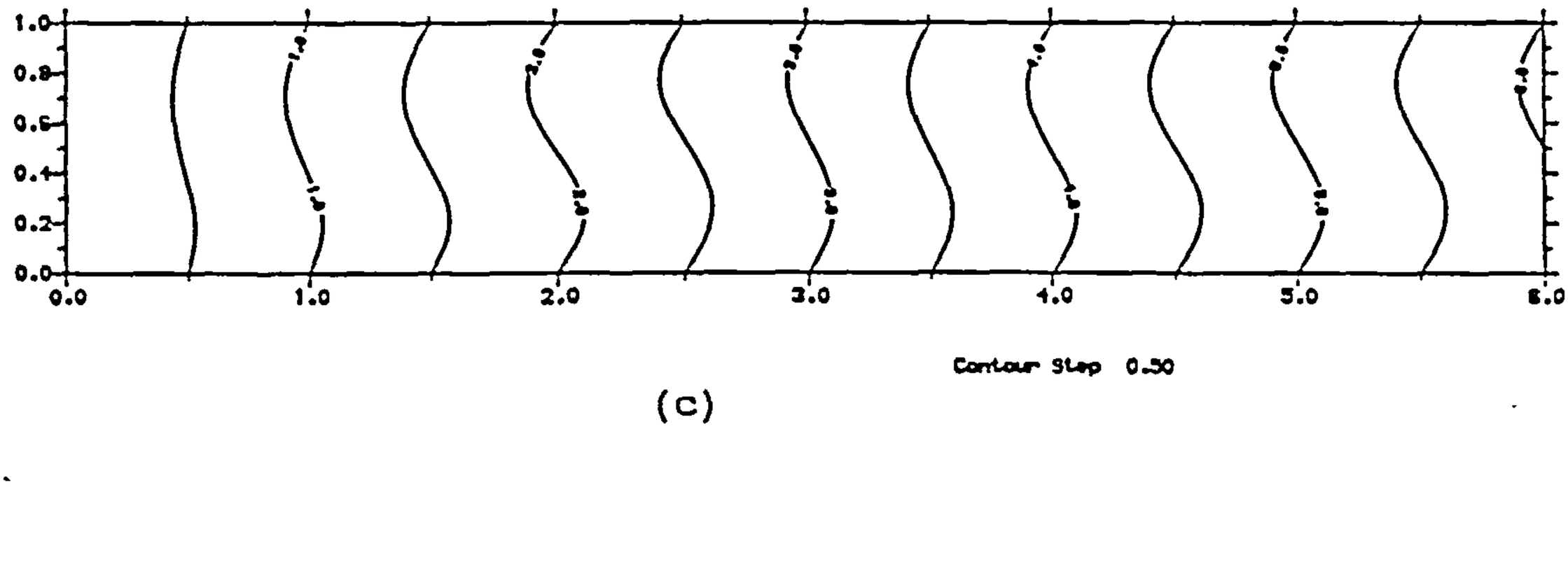

(c)

Figure 5.3: Contours of the steady-state solution for (a) stream function , (b) vorticity, (c) temperature, for $\sigma = 0.05$ and $R_1 = 500$, using a 180×30 computational grid with $x_\infty = 6$.

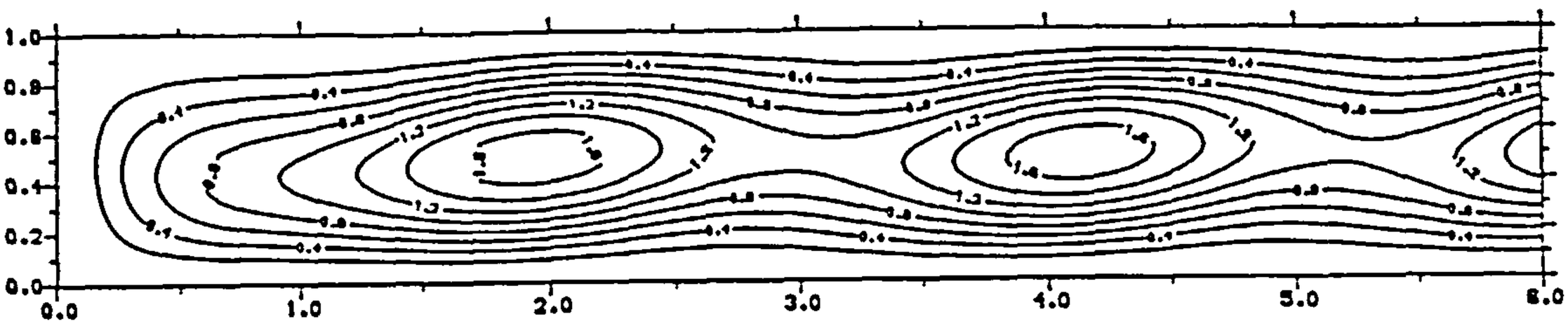

(a)

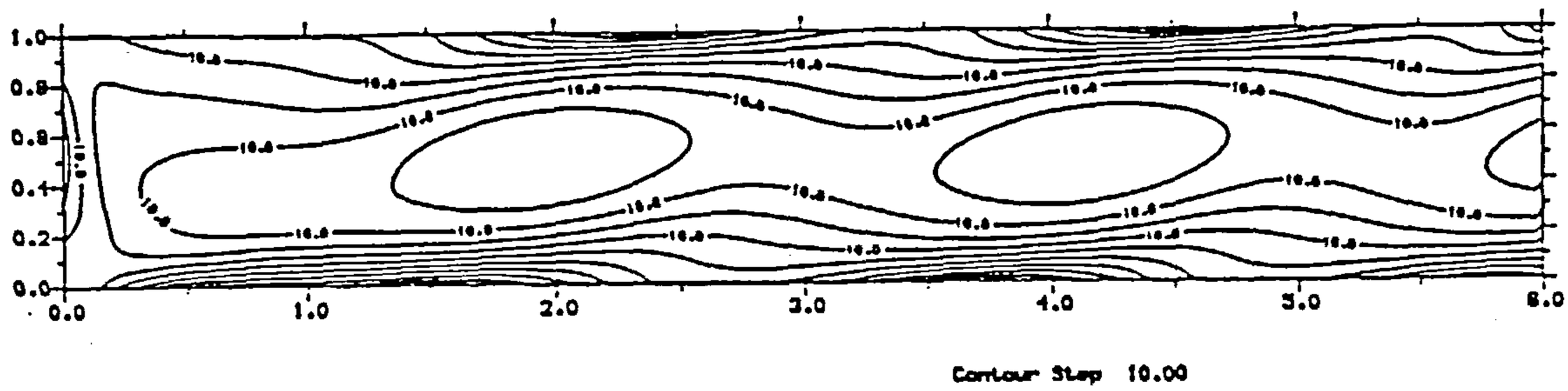

(b)

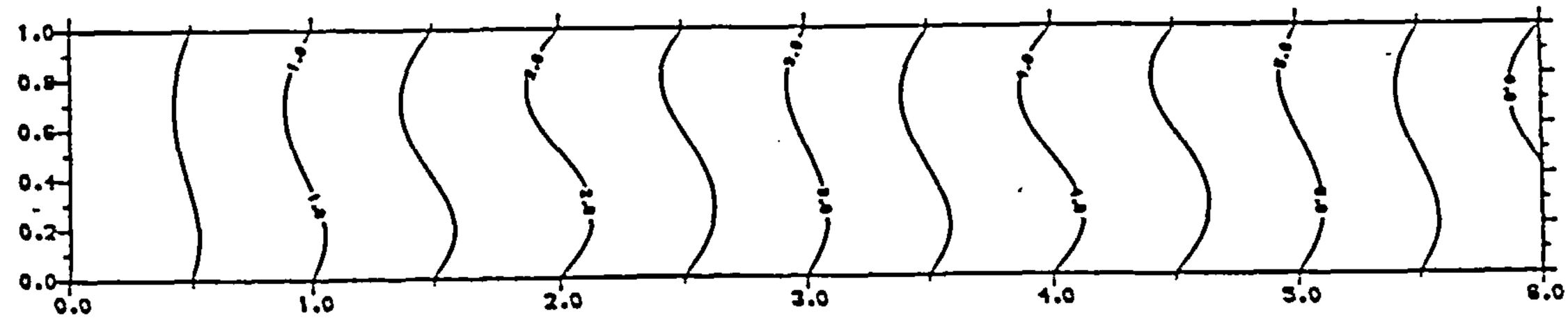

(C) Contour Step 0.30

Figure 5.4: Contours of the steady-state solution for (a) stream function , (b) vorticity, (c) temperature, for $\sigma = 0.05$ and $R_1 = 600$, using a 180×30 computational grid with $x_\infty = 6$.

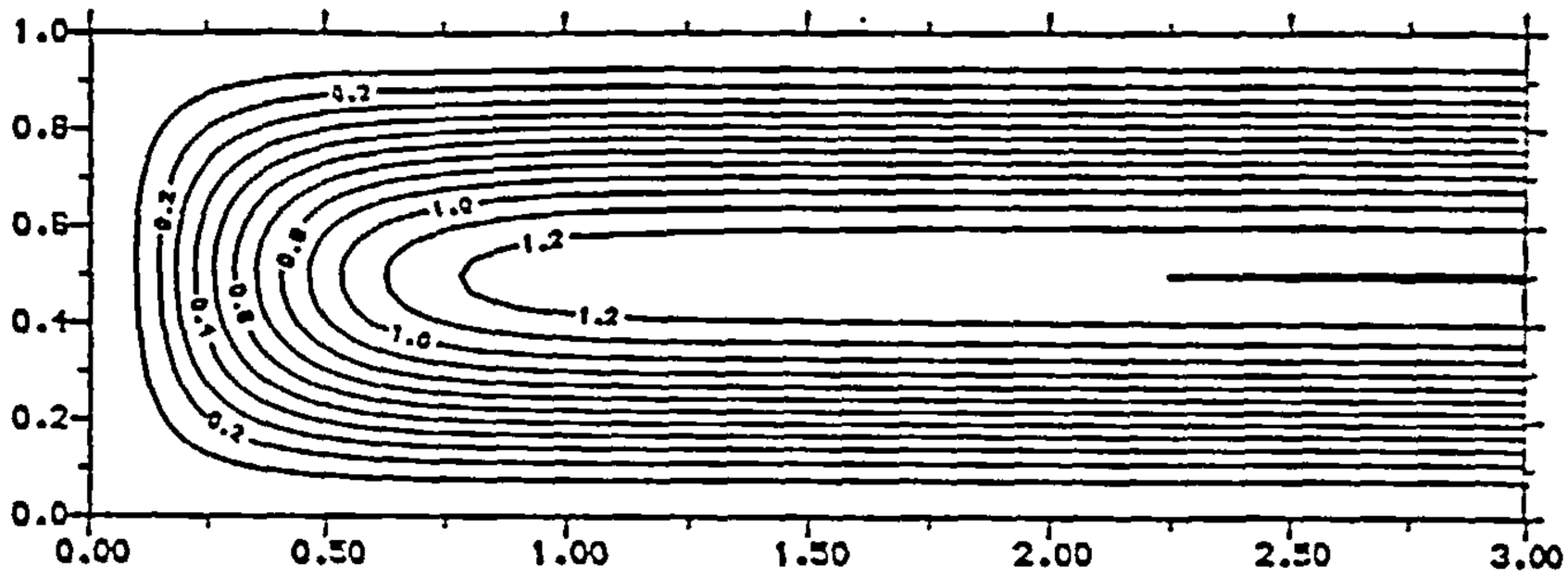

(a) Contour Step 0.10

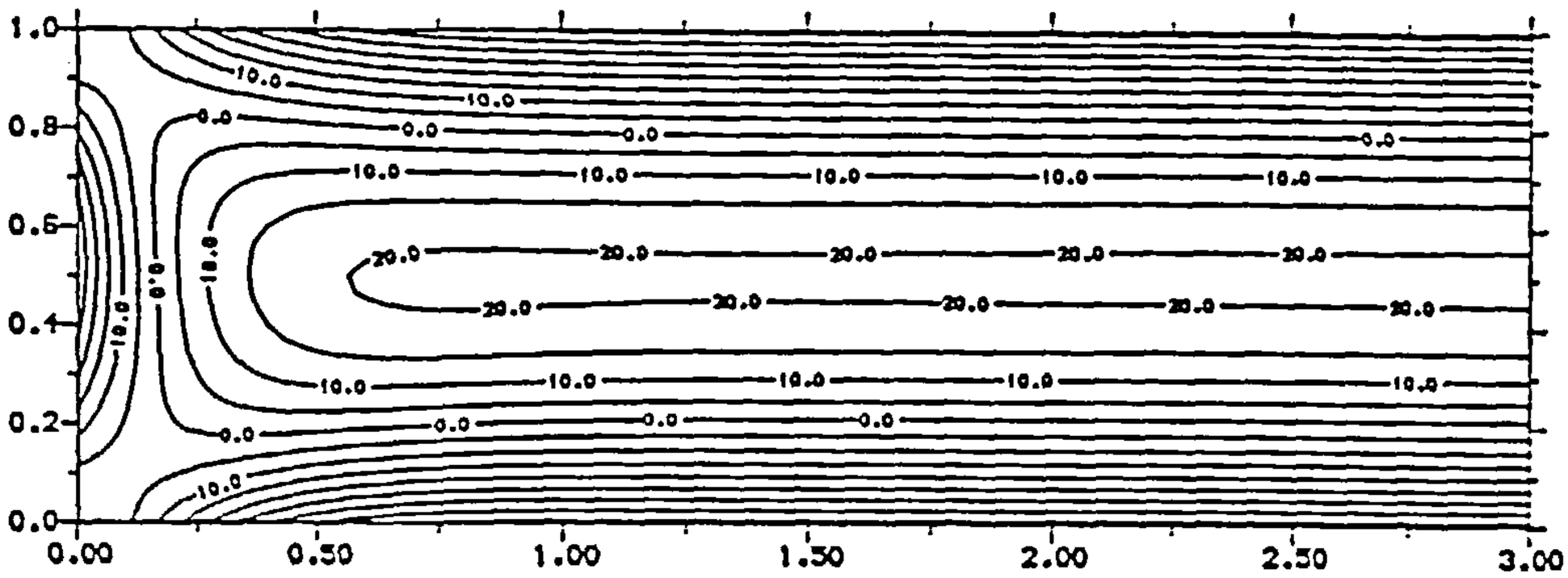

(b) Contour Step 5.00

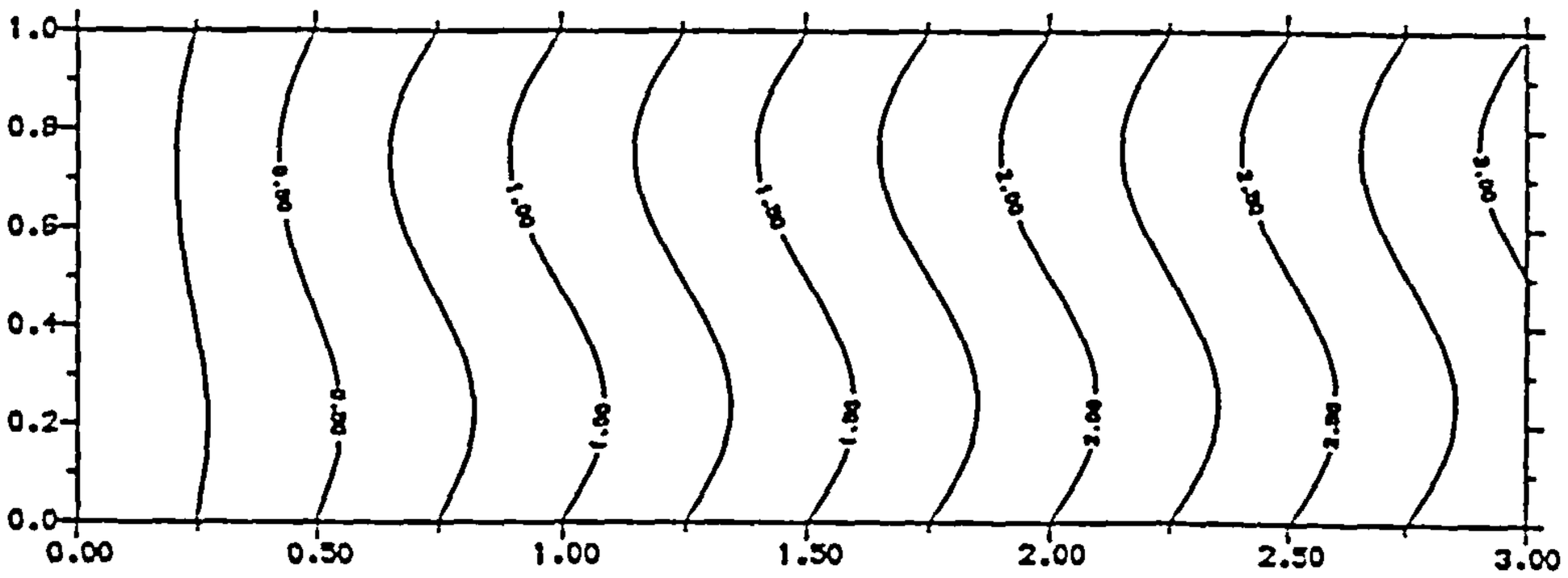

(c) Contour Step 0.25

Figure 5.5: Contours of the steady-state solution for (a) stream function , (b) vorticity, (c) temperature, for $\sigma = 0.733$ and $R_1 = 500$, using a 90×30 computational grid with $x_\infty = 3$.

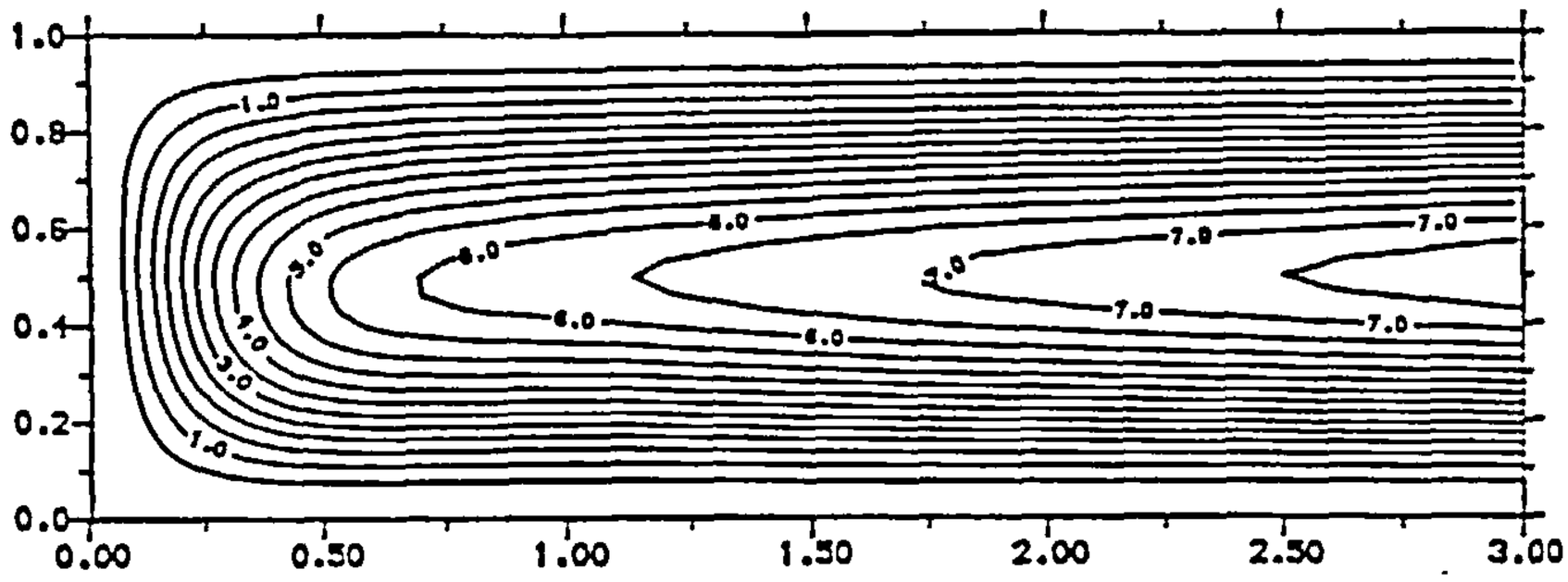

(a) Contour Step 0.50

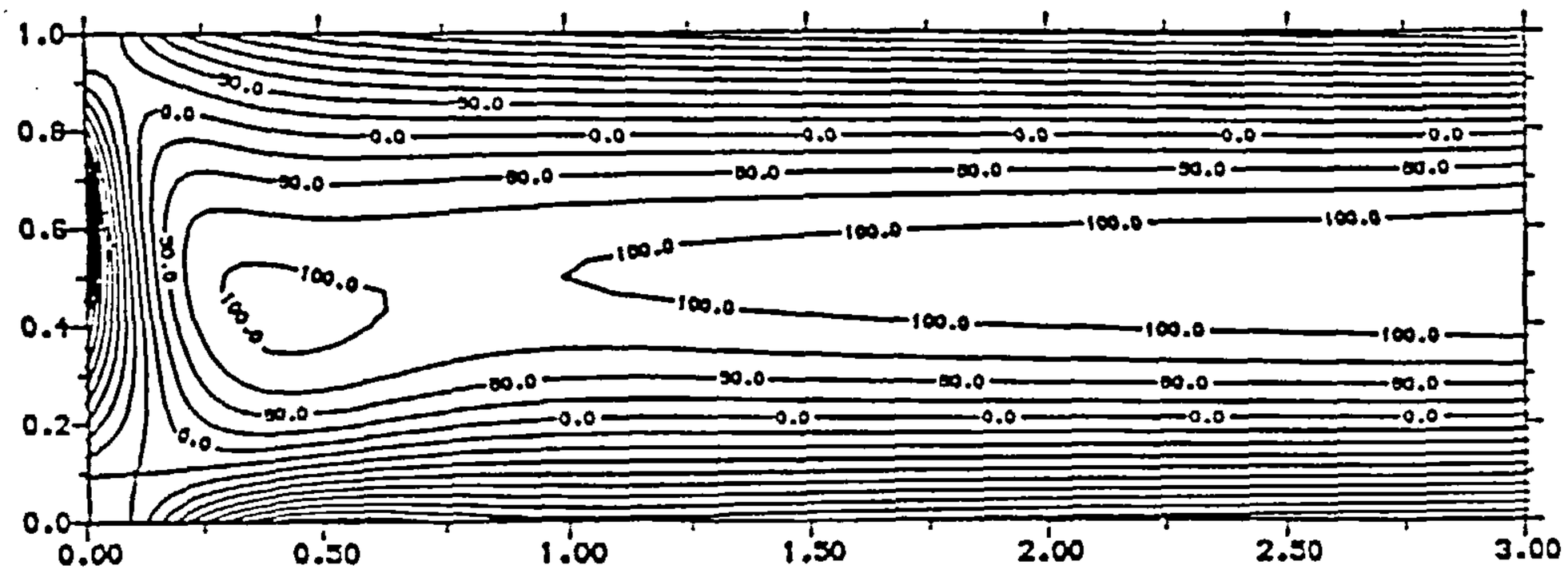

(b) Contour Step 25.00

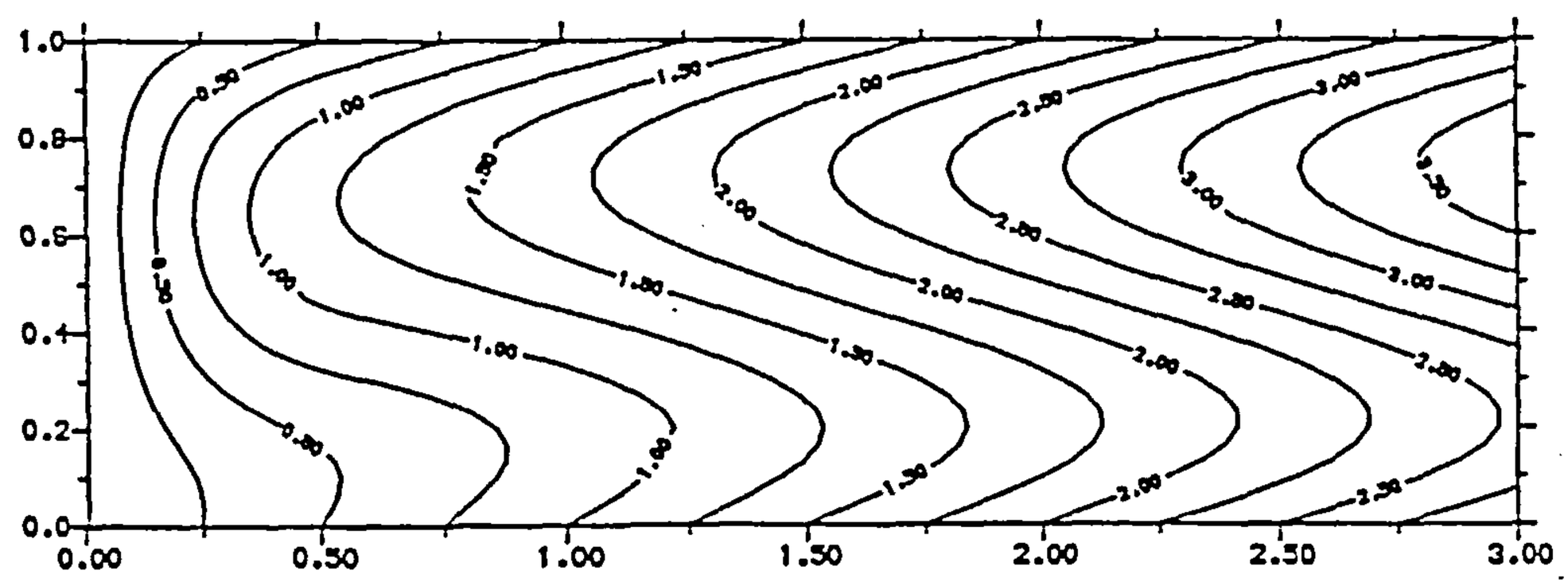

(C) Contour Step 0.25

Figure 5.6: Contours of the steady-state solution for (a) stream function , (b) vorticity, (c) temperature, for $\sigma = 0.733$ and $R_1 = 3000$, using a 90×30 computational grid with $x_\infty = 3$.

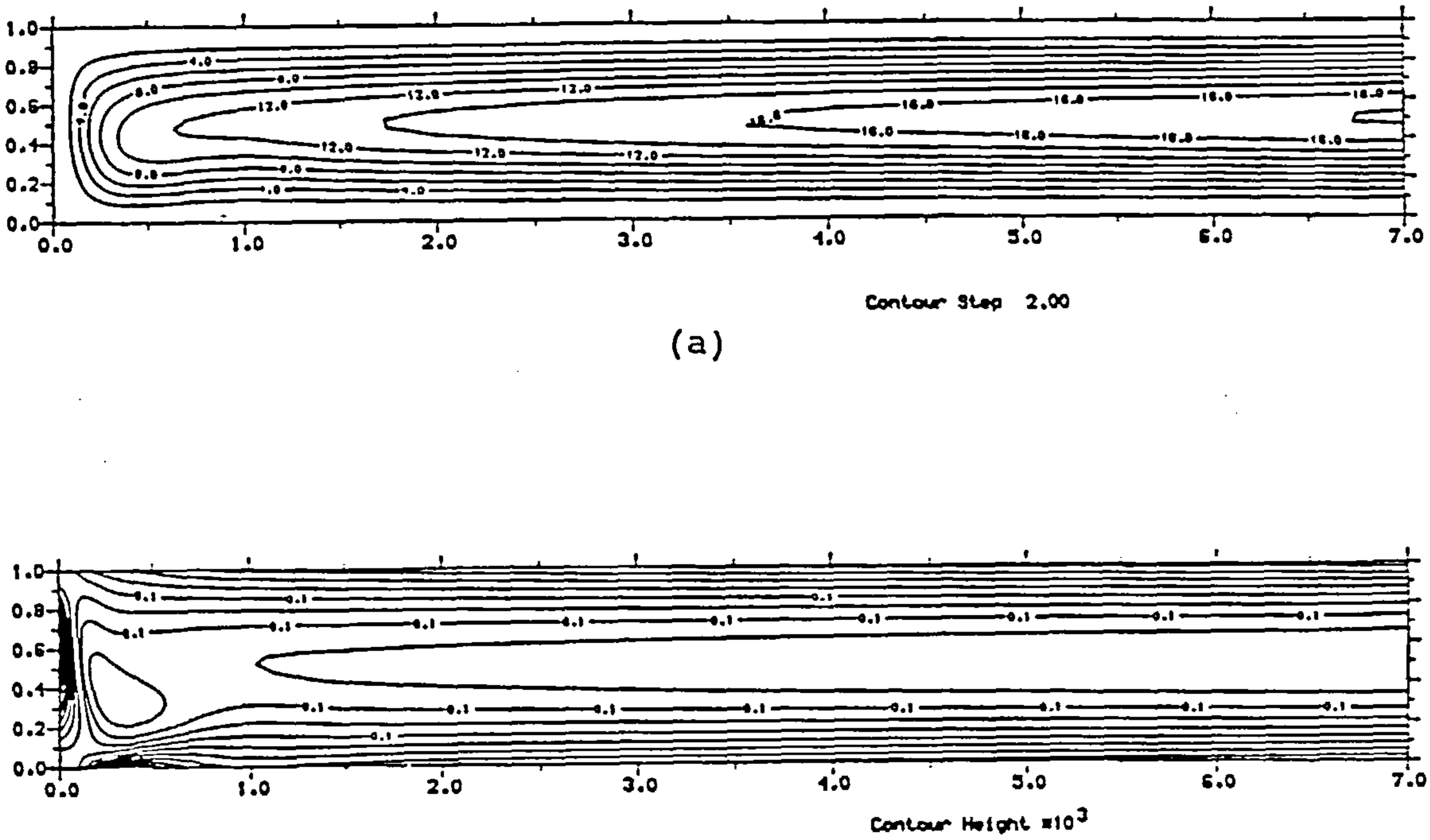

Figure 5.7: Contours of the steady-state solution for (a) stream function , (b) vorticity, (c) temperature, for $\sigma = 0.733$ and $R_1 = 7000$, using a 175×25 computational grid with $x_\infty = 7$.

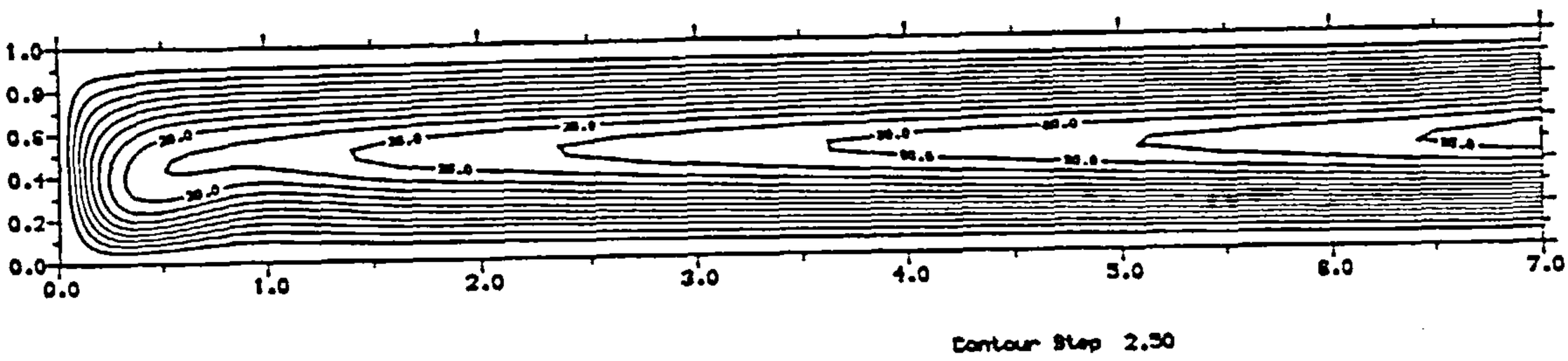

(a)

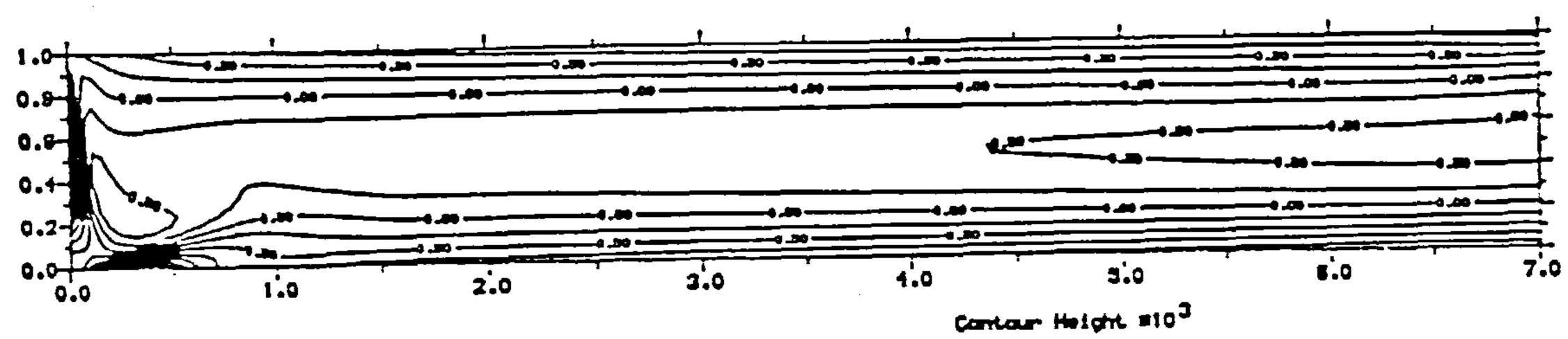

(b)

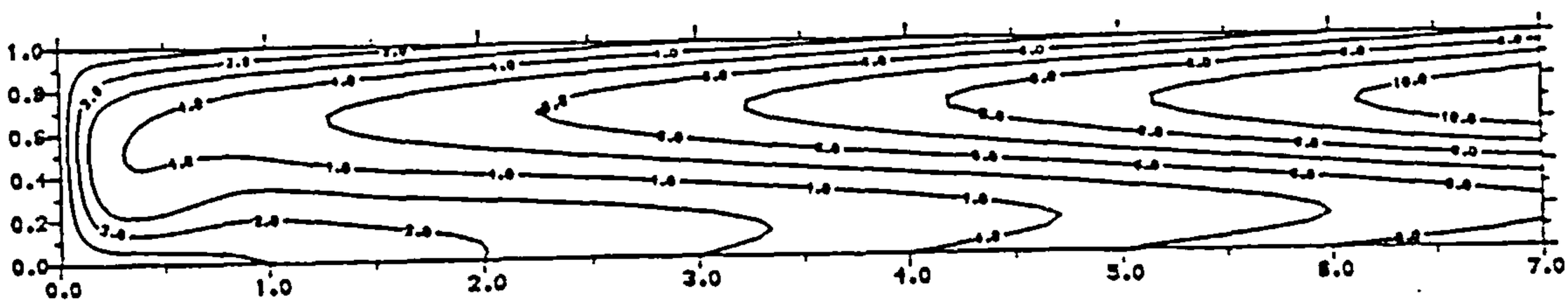

(c)

Figure 5.8: Contours of the steady-state solution for (a) stream function , (b) vorticity, (c) temperature, for $\sigma = 0.733$ and $R_1 = 14000$, using a 175×25 computational grid with $x_\infty = 7$.

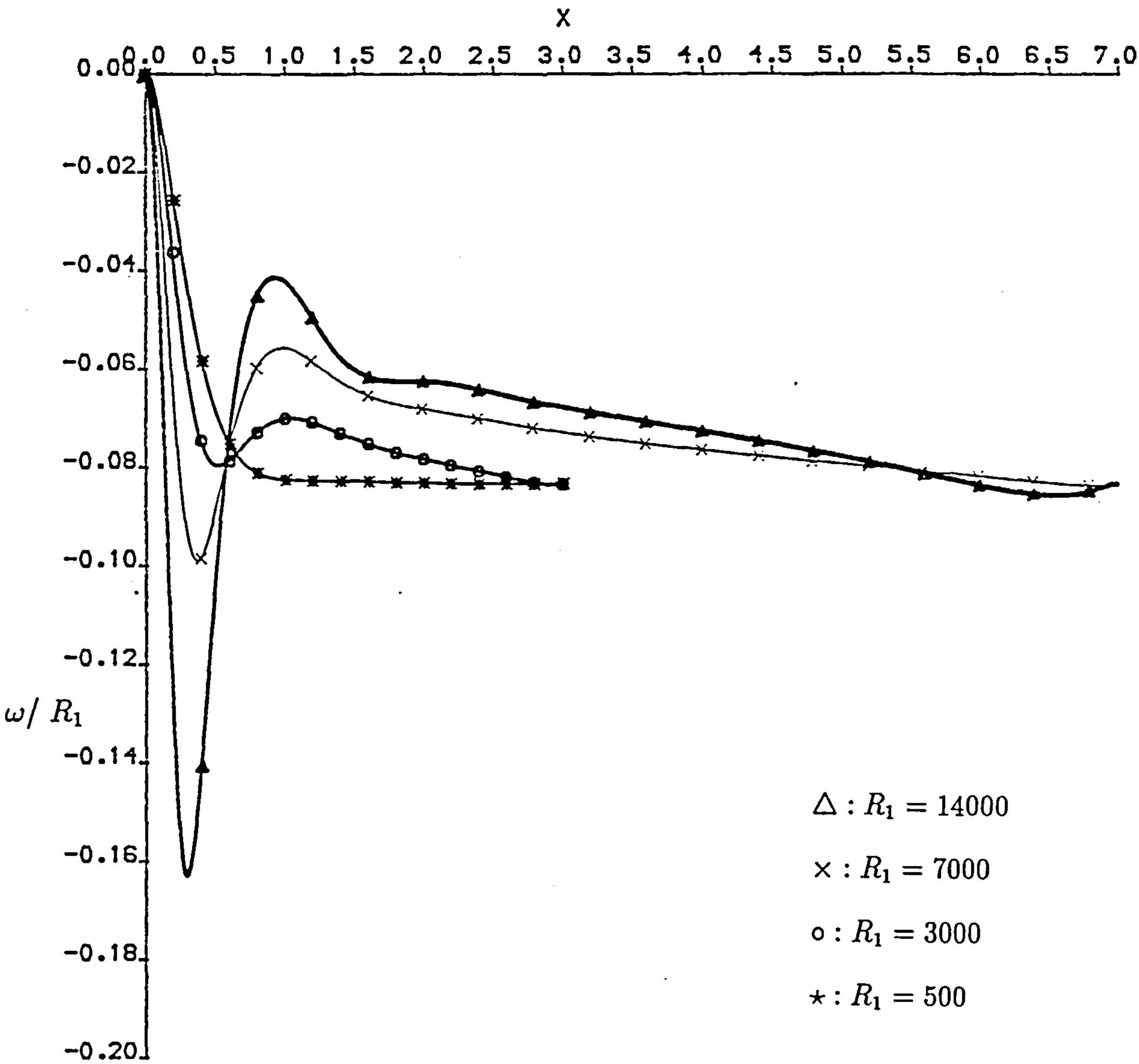

Figure 5.9: The skin friction ω/R_1 with $\sigma = 0.733$ for different Rayleigh numbers on the bottom wall for the conducting case.

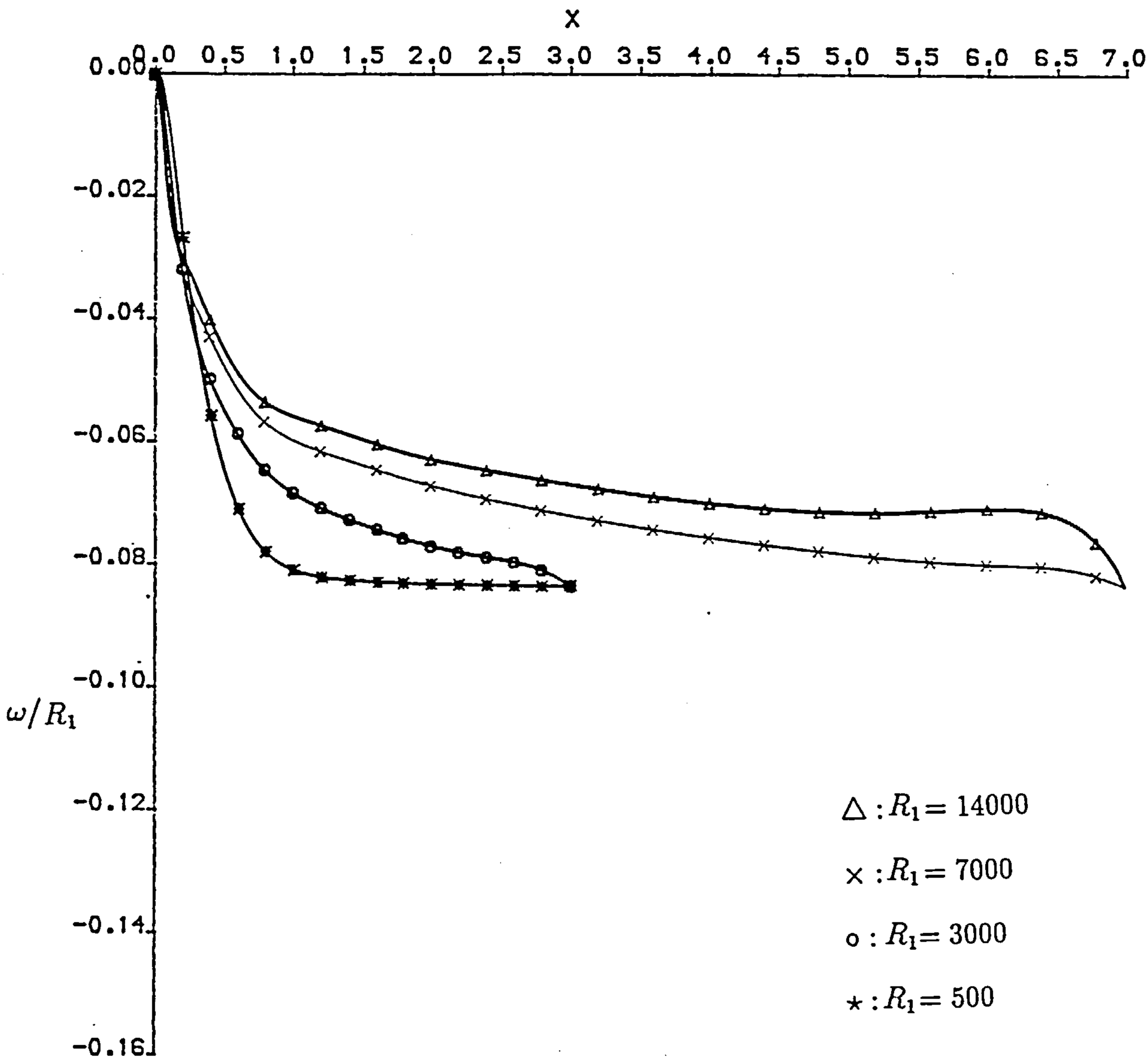

Figure 5.10: The skin friction ω/R_1 with $\sigma = 0.733$ for different Rayleigh numbers on the top wall for the conducting case.

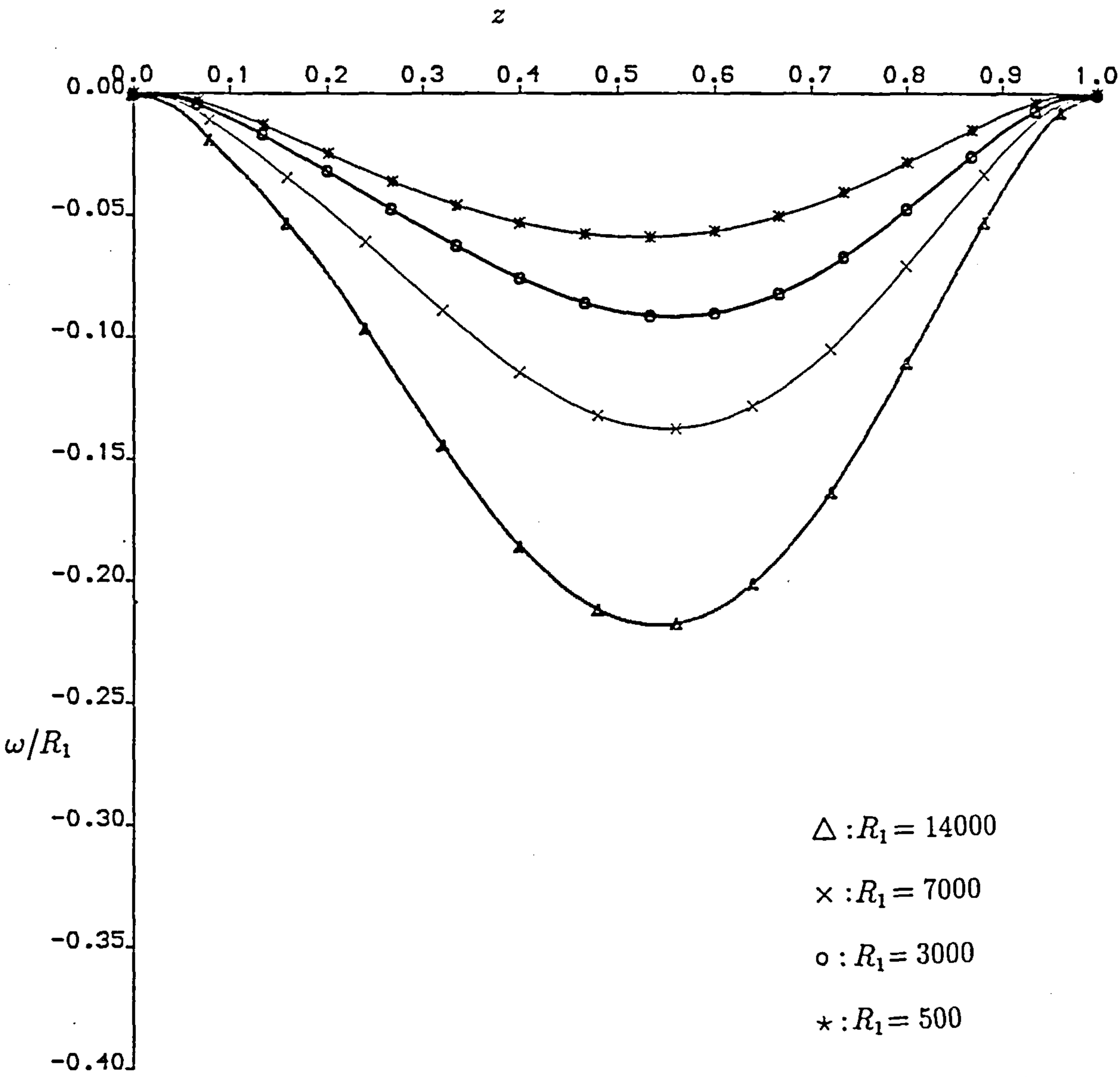

Figure 5.11: The skin friction ω/R_1 with $\sigma = 0.733$ for different Rayleigh numbers on the cold wall for the conducting case.

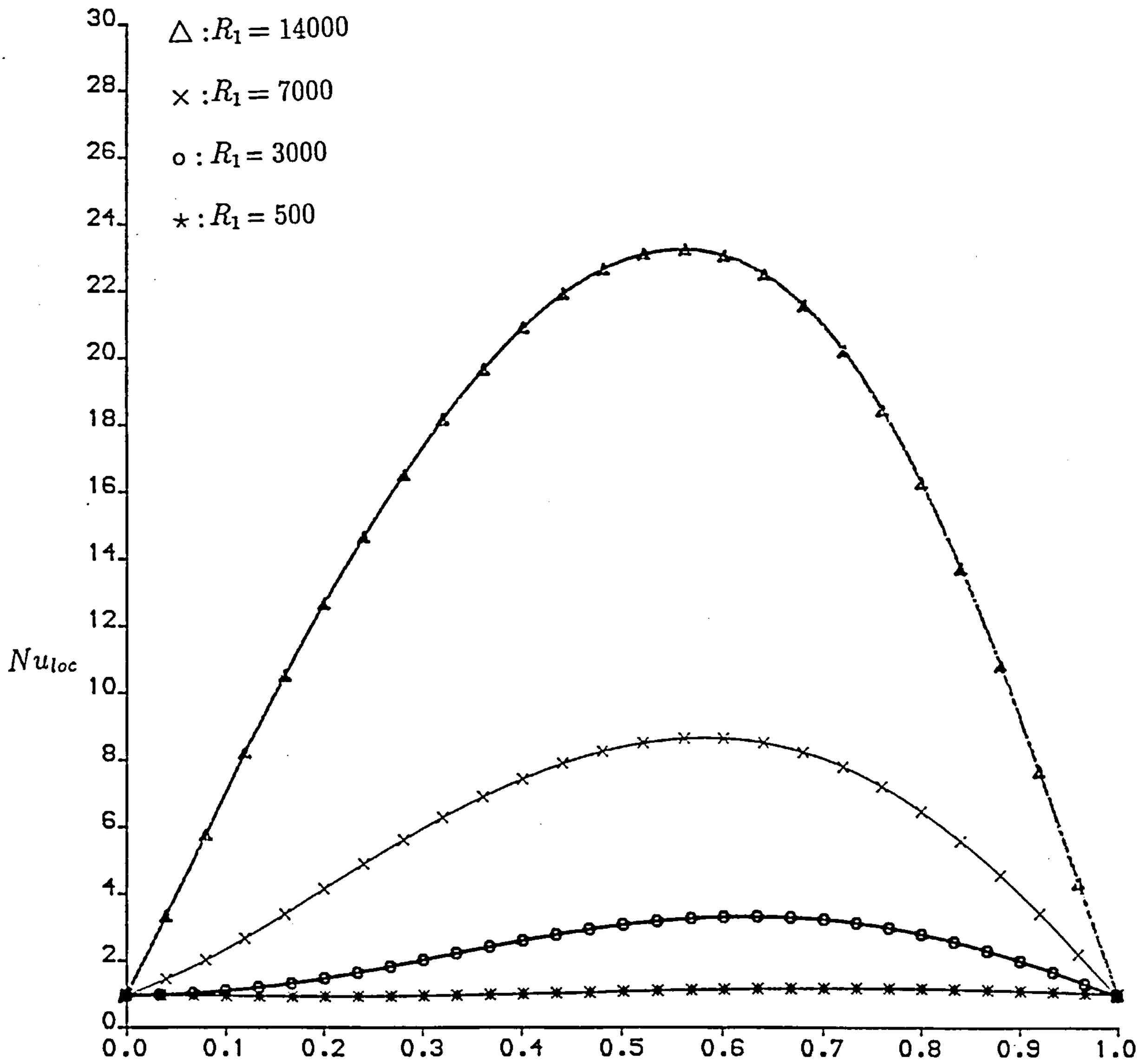

Figure 5.12: The local Nusselt number with $\sigma = 0.733$ for different Rayleigh numbers on the cold wall for the conducting case.

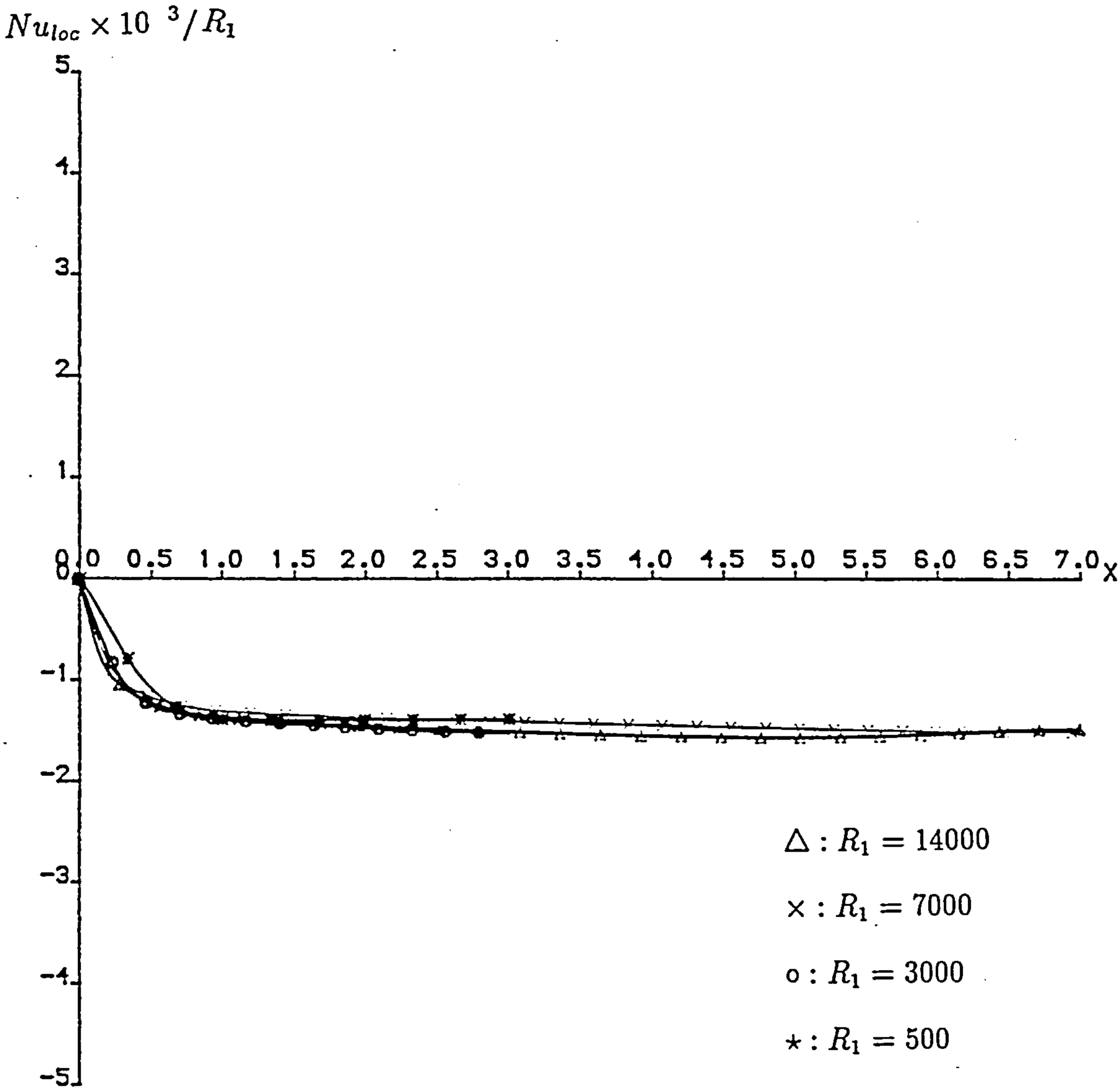

Figure 5.13: The local Nusselt number with $\sigma = 0.733$ for different Rayleigh numbers on the top wall for the conducting case.

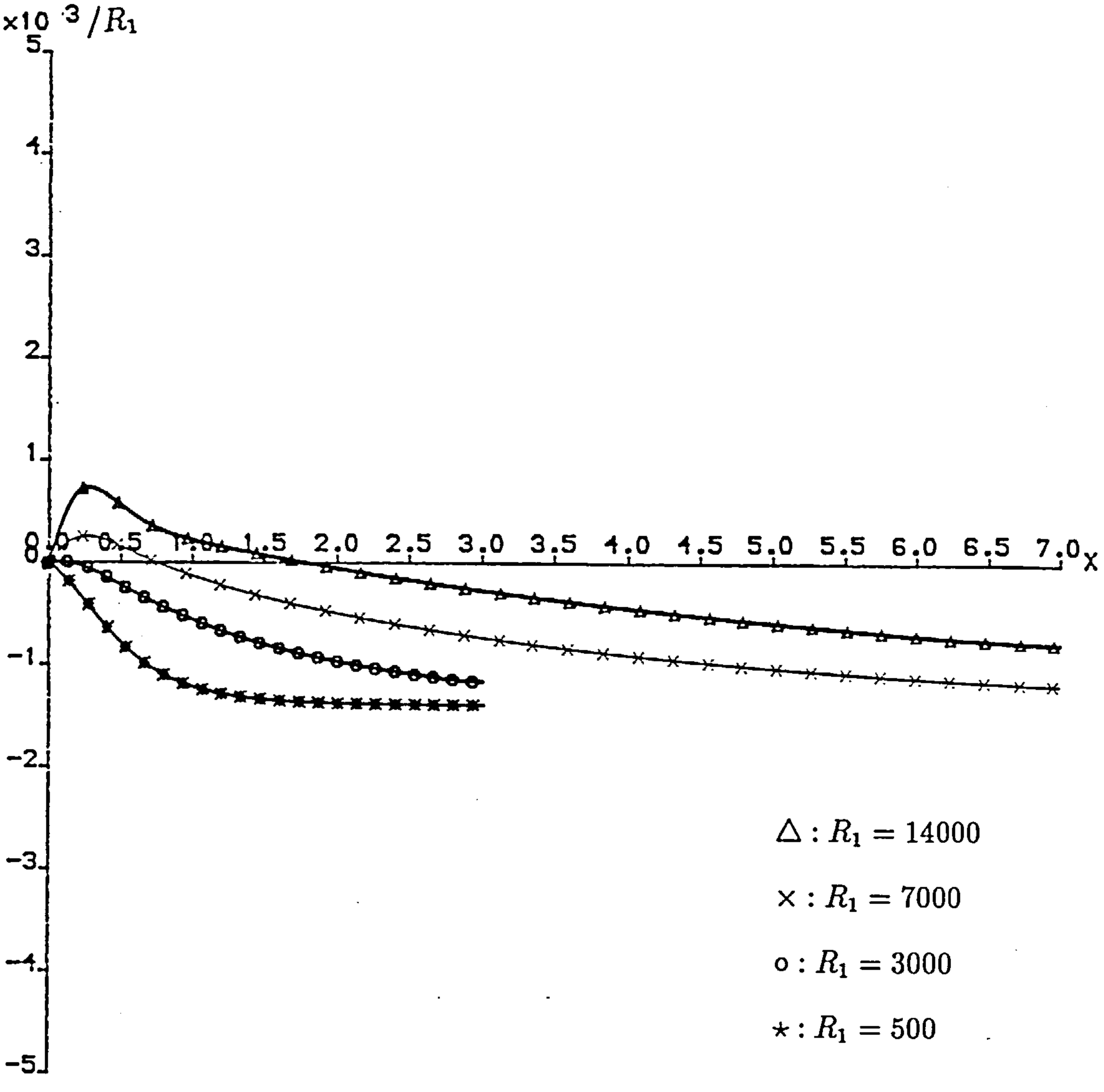

Figure 5.14: The local Nusselt number with $\sigma = 0.733$ for different Rayleigh numbers on the bottom wall for the conducting case.

R_1	$\int_0^1 \frac{\partial T}{\partial x}\|_{x=0} dz$
500	1.0733
3000	2.3418
7000	5.7074
14000	15.2633

Table 5.1: The overall Nusselt number at the cold wall for air.

R_1	σ	*Left-hand side*	*Right-hand side*	*Discrepancy*
500	0.733	1.22624	1.20668	0.01956
3000	0.733	8.06246	8.44047	-0.37801
7000	0.733	39.1836	41.5092	-2.3256
14000	0.733	130.48	163.037	-32.557
200	0.05	1.05495	1.03307	0.02188
400	0.05	1.15291	1.13227	0.02064
500	0.05	1.22333	1.20667	0.0166
600	0.05	1.28574	1.29761	-0.01187

Table 5.2: Comparison of the two sides of equation (5.4.13) for different Rayleigh numbers and Prandtl numbers.

Chapter 6

Thermal Convection in a Shallow Laterally Heated Cavity with Adiabatic Boundaries

6.1 Introduction

In this chapter the structure of the flow in a shallow laterally heated cavity with adiabatic horizontal surfaces is considered. In general, the flow structure is determined by the Rayleigh number, Prandtl number and aspect ratio. Here the main results for Rayleigh numbers $R_1 = R/L = O(1)$ and the limit $L \to \infty$ are reviewed, the end zone structure being similar to that of the conducting case. Convective flow in the end zone is studied numerically for a range of Rayleigh numbers R_1, and Prandtl numbers σ.

In Section 6.2, a mathematical formulation of the shallow cavity flow with insulated boundaries is described, along with the appropriate parallel flow solution in the core region . The end zone problem is also set up and the instability of the flow is discussed. Section 6.3 describes the form of the end zone solution for large

Rayleigh numbers $R_1 \gg 1$, as predicted by asymptotic analysis (Daniels, Blythe and Simpkins 1987a, Gargaro 1991). One of the main features is the formation of a vertical boundary layer on the cold wall, whose properties are discussed in detail. In Section 6.4 a numerical method for solving the end zone problem is described. The results are presented in Sections 6.5 and 6.6 for a range of Rayleigh numbers and Prandtl numbers and detailed comparisons are made with the predictions of the asymptotic theory for large values of R_1.

6.2 Formulation, Core Flow and End-Zone Structure

The governing equations for the overall cavity flow, from Chapter 5, are

$$\sigma^{-1}\left(\frac{\partial \bar{\omega}}{\partial t} + J(\bar{\omega}, \bar{\psi})\right) = \nabla^2 \bar{\omega} + R\frac{\partial \bar{T}}{\partial x} \quad , \tag{6.2.1}$$

$$\nabla^2 \bar{\psi} = -\bar{\omega} \quad , \tag{6.2.2}$$

$$\frac{\partial \bar{T}}{\partial t} + J(\bar{T}, \bar{\psi}) = \nabla^2 \bar{T} \quad . \tag{6.2.3}$$

The boundary conditions on the vertical sidewalls are

$$\bar{\psi} = \frac{\partial \bar{\psi}}{\partial x} = 0 \quad \text{on} \quad x = 0, L \quad , \tag{6.2.4}$$

$$\bar{T} = 0 \quad \text{on} \quad x = 0 \quad , \tag{6.2.5}$$

$$\bar{T} = 1 \quad \text{on} \quad x = L \quad . \tag{6.2.6}$$

The horizontal surfaces are assumed to be insulated so that

$$\bar{\psi} = \frac{\partial \bar{\psi}}{\partial z} = \frac{\partial \bar{T}}{\partial z} = 0 \quad \text{on} \quad z = 0, 1 \quad . \tag{6.2.7}$$

The boundary conditions and governing equations are consistent with Gill's (1966) centrosymmetry relations

$$\bar{\psi}(x, z, t) = \bar{\psi}(L - x, 1 - z, t), \tag{6.2.8}$$

$$\bar{T}(x, z, t) = 1 - \bar{T}(L - x, 1 - z, t) \tag{6.2.9}$$

and for a steady-state solution only one half of the flow domain needs to be considered.

The structure of the solution for $L \to \infty$ and

$$R_1 = \frac{R}{L} = O(1) \quad , \tag{6.2.10}$$

is similar to that of the conducting case considered in Chapter 5 and Daniels et al (1987) outlined the formal asymptotic expansions. The core region, where the steady-state flow is dependent on the variables

$$\xi = \frac{x}{L}, \quad z = z \tag{6.2.11}$$

is dominated by lateral conduction associated with a Hadley circulation and the appropriate solution expanded in inverse powers of L is

$$\bar{T} = \xi + L^{-1}\{(\xi - \frac{1}{2})c_1(R_1, \sigma) + R_1 G(z)\} + O(L^{-2}) \tag{6.2.12}$$

and

$$\bar{\psi} = R_1\{1 + L^{-1}c_1(R_1, \sigma)\}F(z) + O(L^{-2}) \tag{6.2.13}$$

as $L \to \infty$, with

$$G(z) = \frac{z^5}{120} - \frac{1}{48}z^4 + \frac{1}{72}z^3 - \frac{1}{1440} \quad . \tag{6.2.14}$$

$c_1(R_1, \sigma)$ is a constant contribution which must be determined by matching with solutions near the end walls. Note that here the definition of $G(z)$ is different from that used in Chapter 5.

Near the cold wall, the solution adjusts to the boundary conditions on the wall in an approximately square zone where x, z are O(1). Here

$$\bar{T} = L^{-1}T(x, z, t) + \cdots, \quad \bar{\psi} = \psi(x, z, t) + \cdots \tag{6.2.15}$$

and substitution into (6.2.1)-(6.2.3) gives

$$\sigma^{-1}(\frac{\partial \omega}{\partial t} + J(\omega, \psi)) = \nabla^2 \omega + R_1 \frac{\partial T}{\partial x} \quad , \tag{6.2.16}$$

$$\nabla^2 \psi = -\omega \quad , \tag{6.2.17}$$

$$\frac{\partial T}{\partial t} + J(T, \psi) = \nabla^2 T \quad . \tag{6.2.18}$$

From (6.2.4)-(6.2.7) these equations are to be solved subject to

$$\psi = \frac{\partial \psi}{\partial x} = T = 0 \quad \text{on} \quad x = 0 \quad , \tag{6.2.19}$$

$$\psi = \frac{\partial \psi}{\partial z} = \frac{\partial T}{\partial z} = 0 \quad \text{on} \quad z = 0,\ 1 \tag{6.2.20}$$

and to match with the core solution

$$T \sim x + c + R_1 G(z), \quad \psi \to R_1 F(z) \quad , \quad (x \to \infty). \tag{6.2.21}$$

The core temperature is determined to $O(L^{-1})$ through the matching requirement

$$c_1 = -2c. \tag{6.2.22}$$

The value of c can only be determined by solving the end zone problem (6.2.16)-(6.2.21). At small values of R_1 , results given by Cormack et al (1974) are equivalent to the behaviour

$$c(R_1, \sigma) \sim 1.74 \times 10^{-6} R_1^2 \quad \text{as} \quad R_1 \to 0, \tag{6.2.23}$$

while at general values of R_1 and σ, numerical solutions are required to determine the value of c. This is one of the main aims of the present chapter. Predictions of the form of c as $R_1 \to \infty$ can also be made, using an asymptotic analysis of the end-zone system (6.2.15)- (6.2.21), which is described in Section 6.3.

It should also be noted here that as in the conducting problem of Chapter 5, the parallel core flow is susceptible to instability in the form of stationary transverse rolls at low values of the Prandtl number and the end-zone system then no longer has a steady solution consistent with the behaviour (6.2.21). Calculations determining the region of (R_1, σ) parameter space for which parallel core structures do exist have been discussed by Hart (1972, 1983) and Daniels, Blythe and Simpkins (1987). Their calculations suggest that the end zone problem remains consistent at all Rayleigh numbers if the Prandtl number of the fluid is greater than about 0.12. For Prandtl

numbers less than 0.12, multiple eddies are forced into the core of the cavity when the Rayleigh number exeeds a critical value $R_{1c}(\sigma)$ (see Daniels, Blythe and Simpkins 1987) and the entire flow structure then becomes nonlinear. Hart (1983) obtained numerical results for low Prandtl number to illustrate this phenomenon and found solutions consistent with the stability theory which fixes $R_{1c}(\sigma)$. Provided $\sigma > 0.12$ the steady-state end zone solution should remain intact for all Rayleigh numbers, allowing its asymptotic structure to be analysed as $R_1 \rightarrow \infty$. This is the subject of the next section.

6.3 Asymptotic Structure, $R_1 \rightarrow \infty$

In this section the asymptotic structure of the steady-state solution is described for large Rayleigh numbers. At general R_1, integration of the energy equation (6.2.3) using (6.2.7) gives an expression for the horizontal heat transfer balance

$$\int_0^1 (\frac{\partial T}{\partial x} + \psi \frac{\partial T}{\partial z}) dz = Q \qquad (6.3.1)$$

where Q is a constant. Assuming a parallel flow structure exists as $x \rightarrow \infty$ and using the outer form (6.2.21),Q can be evaluated as

$$Q = R_1^2 Q_0 + 1 \quad , \qquad (6.3.2)$$

where

$$Q_0 = \int_0^1 F^2 dz = \frac{1}{362880} \quad . \qquad (6.3.3)$$

The convective term supplies the major contribution to the left-hand side of (6.3.1) at large distances from the end wall when $R_1 \gg 1$. At the wall ψ is zero and the lateral conduction term must dominate, requiring that locally

$$T = O(xR_1^2). \qquad (6.3.4)$$

In a vertical boundary layer adjacent to the wall, a balance between conduction and convection in the energy equation, and viscosity and buoyancy in the vorticity

equation, requires

$$x\psi = O(1) \quad \text{and} \quad \psi = O(R_1 T x^3) \tag{6.3.5}$$

which suggests the scalings

$$T \sim R_1^{7/5} T_1, \quad \psi \sim R_1^{3/5} \psi_1, \quad x = R_1^{-3/5} x_1 \tag{6.3.6}$$

for the vertical boundary layer, as $R_1 \to \infty$. Other possibilities involving $\psi = O(R_1)$, $x = O(R_1^{-1})$, or a larger local temperature, $T = O(R_1^3)$, appear to lead to contradictions. The results (6.3.6) are of particular significance because the scalings of both T and ψ differ from those of order R_1 naively suggested by the outer condition (6.2.21). A consequence is that the order $R_1^{7/5}$ temperature field outside the vertical boundary layer must be constant and form the leading term in the expansion of $c(R_1, \sigma)$ as $R_1 \to \infty$:

$$c(R_1, \sigma) = R_1^{7/5} c_0(\sigma) + \cdots \tag{6.3.7}$$

The governing equations and boundary conditions in the vertical boundary layer are therefore

$$\frac{\partial^4 \psi_1}{\partial x_1^4} = \frac{\partial T_1}{\partial x_1} + \frac{1}{\sigma}\left[\frac{\partial^3 \psi_1}{\partial x_1^3}\frac{\partial \psi_1}{\partial z} - \frac{\partial^3 \psi_1}{\partial x_1^2 \partial z}\frac{\partial \psi_1}{\partial x_1}\right] \tag{6.3.8}$$

and

$$\frac{\partial^2 T_1}{\partial x_1^2} = \frac{\partial(T_1, \psi_1)}{\partial(x_1, z)}, \tag{6.3.9}$$

with

$$T_1 \to c_0, \quad \frac{\partial \psi_1}{\partial x_1} \to 0 \quad \text{as} \quad x_1 \to \infty, \tag{6.3.10}$$

$$\psi_1 = \frac{\partial \psi_1}{\partial x_1} = T_1 = 0 \quad \text{on} \quad x_1 = 0. \tag{6.3.11}$$

A solution to (6.3.8)-(6.3.11) is the similarity form

$$T_1 = c_0 g(\eta), \quad \psi_1 = c_0^{1/4}(1-z)^{3/4} f(\eta), \tag{6.3.12}$$

where

$$\eta = \frac{c_0^{1/4} x_1}{(1-z)^{1/4}},$$

as discussed by Squire, see Goldstein (1938). The functions f and g satisfy

$$f''' + \sigma^{-1}(\frac{3}{4}ff' - \frac{1}{2}f'^2) - g + 1 = 0 \quad , \tag{6.3.13}$$

$$g'' + \frac{3}{4}fg' = 0 \quad , \tag{6.3.14}$$

with

$$f = f' = g = 0 \quad (\eta = 0) \quad ; \quad g \to 1, \quad f' \to 0 \quad (\eta \to \infty). \tag{6.3.15}$$

The boundary conditions at $\eta = 0$ are obtained from the end wall conditions (6.3.11), and the conditions at $\eta = \infty$ from (6.3.10) which is based on the assumption that there is no vertical external flow of magnitude $R_1^{6/5}$. Numerical solutions of (6.3.13)-(6.3.15) have been obtained by Ostrach (1952); the main property required here is the wall heat transfer, which can be approximated to within 0.5% by the formula

$$\lambda = g'(0) = \frac{3}{4}\sigma^{1/4}(2.436 + 4.884\sigma^{1/2} + 4.952\sigma)^{-1/4}, \tag{6.3.16}$$

for all values of the Prandtl number. The heat transferred through the cold wall from the vertical boundary layer,

$$R_1^2 \int_0^1 \frac{\partial T_1}{\partial x_1}(0, z)dz \quad ,$$

is the dominant contribution to the left-hand side of (6.3.1) at $x_1 = 0$ so that, from (6.3.12),

$$\frac{4}{3}c_0^{5/4}\lambda = Q_0 \tag{6.3.17}$$

and hence

$$c_0 = (3Q_0/4\lambda)^{4/5} \quad . \tag{6.3.18}$$

At the base of the vertical boundary layer the wall heat transfer has been converted into a convective transfer

$$\begin{aligned} R_1^2 \int_0^\infty \psi_1 \frac{\partial T_1}{\partial x_1}(x_1, 0)dx_1 &= R_1^2 c_0^{5/4} \int_0^\infty fg'd\eta \\ &= \frac{4}{3}R_1^2 c_0^{5/4}\lambda, \end{aligned} \tag{6.3.19}$$

which must be carried with the isotherms and streamlines around the corner into a horizontal boundary layer. This conversion to a horizontal transfer

$$\int \psi \frac{\partial T}{\partial z} dz \sim \frac{4}{3} R_1^2 c_0^{5/4} \lambda \tag{6.3.20}$$

near the base of the cavity, consistent with (6.3.1), accomplishes the necessary transfer of (negative) heat energy, via a horizontal boundary layer structure, into the main outer part of the end zone where $x = O(R_1)$. Further details are given by Daniels, Blythe and Simpkins (1987a). The above structure as $R_1 \to \infty$ is consistent with the global constraint imposed by (6.3.1) and leads to an unexpectedly large contribution of order $R_1^{7/5}$ to the local temperature field T in the end zone. The corresponding prediction of the form of c as $R_1 \to \infty$ given by (6.3.7) and (6.3.18) is one which can be tested against a numerical solution of the end zone problem. This solution is discussed in the next section.

6.4 Numerical Scheme for the End-Zone Problem

In this section, a numerical scheme for solving the end zone problem (6.2.16)-(6.2.21) is described . The main scheme is the same as that in Chapter 2, apart from the outer boundary condition which is applied at $x = x_\infty$. In the computation, this outer boundary varies typically from 3 to 20 according to the value of the Rayleigh number. For high Rayleigh numbers, the numerical computation is difficult because the thin vertical boundary layer formed near the cold wall necessitates the use of a fine grid, while a large outer boundary is also required to accommodate the spread of the end zone on a lateral scale proportional to R_1. Thus accurate high Rayleigh number computations are expensive in both CPU time and memory.

The main difference from the scheme of Chapter 2 is associated with application of the outer condition (6.2.21) which is applied in the form

$$\psi = R_1 F(z) \quad , \quad \frac{\partial T}{\partial x} = 1 \quad \text{at} \quad x = x_\infty. \tag{6.4.1}$$

Thus for the temperature, the outer boundary condition takes the discretised form

$$T_{N_x,j} = \Delta x + T_{N_x-1,j}, \quad j = 0, 1, 2, \cdots, N_z \tag{6.4.2}$$

for all time levels. Here $N_z = \frac{1}{\Delta z}$, $N_x = x_\infty/\Delta x$, and Δx, Δz are the space steps. For the vorticity, the outer boundary condition is applied in the form

$$\omega_{N_x,j} = -R_1 F''(i\Delta z), \quad j = 0, 1, 2, \cdots, N_z \tag{6.4.3}$$

for all time levels, where F'' is given by

$$F''(z) = \frac{1}{2}z^2 - \frac{1}{2}z + \frac{1}{12} \quad .$$

For the stream function ψ, the outer boundary condition is applied in the form

$$\psi_{N_x,j} = R_1 F(i\Delta z), \quad j = 0, 1, 2, \cdots, N_z \tag{6.4.4}$$

for all time levels.

The local heat flux on the cold wall is calculated by the formula given in Chapter 5 and steady-state solutions are computed from the following initial conditions :

$$\left.\begin{aligned} T &= x \\ \psi &= 0 \\ \omega = u &= w = 0 \end{aligned}\right\} \quad (0 \le x < x_\infty), \quad (0 \le z \le 1) \tag{6.4.5}$$

$$\left.\begin{aligned} \tfrac{\partial T}{\partial x} &= 1 \\ \psi &= R_1 F(z) \\ \omega &= -R_1 F''(z) \\ u &= w = 0 \end{aligned}\right\} \quad (x = x_\infty), \quad (0 \le z \le 1). \tag{6.4.6}$$

The overall scheme of computation is the same as that in Chapter 2 for the finite cavity problem. The heat transfer integral (6.3.1) is used to monitor the accuracy of the converged steady-state solution by calculating its value at several x stations and comparing with the value given by (6.3.2).

6.5 Numerical Results for Low Prandtl Number

In this section, numerical solutions of the end zone problem are reported for $\sigma = 0.05$ and a range of Rayleigh numbers varying from 200 to 600. Outer boundaries $x_\infty = 6$ and $x_\infty = 7$ were used for the computations.

The flow patterns are presented in Figures 6.1-6.3, which show the effect of the Rayleigh number on the flow structure. In Figure 6.1, the fluid travels along the top boundary, and falls as it rejects heat to the cold wall, then travels away along the bottom of the cavity. The turning motion is limited to a range defined approximately by $0 < x < 2$, with the flow beyond $x = 2$ having attained the cubic polynomial form of the core profile. With an increase in Rayleigh number ($R_1 = 400$) in Figure 6.2, a closed cell develops in the streamline field near the cold wall and further cells develop at higher Rayleigh numbers ($R_1 = 600$, Figure 6.3). This shows the onset of secondary flow consistent with linear stability analysis for a stationary mode of the form $e^{i\alpha x}$.

For low Prandtl number fluids, ($\sigma \leq 0.12$) this analysis predicts the onset of secondary flow for $R_1 > R_{1c}(\sigma)$ where $R_{1c}(0.05) \approx 610$ (Hart 1972, Daniels, Blythe and Simpkins 1987). This is consistent with the behaviour observed in Figures 6.1-6.3. The corresponding critical wavenumber of the instability, $\alpha_c(\sigma)$ is given by $\alpha_c(0.05) \approx 2.65$ and this is also in reasonable agreement with the wavelength between the centres of neighbouring cells measured in Figure 6.3, approximately 2.39. This should be compared with the value of $2\pi/\alpha_c \approx 2.37$. The observed behaviour tends to confirm Hart's (1983) conclusion that the bifurcation which occurs in the solution is an imperfect one and from Figures 6.2-6.3, it can be seen that the end cells experience the strongest circulation as the Rayleigh number increases. The results are also in reasonable agreement with simulations of the full cavity flow by Drummond and Korpela (1985).

Flow properties on the walls are illustrated in Figures 6.4-6.9 . These figures show the skin friction on each wall of the end zone, indicating the effect of the

Rayleigh number on the flow near each wall. On the bottom wall , the skin friction has a strong gradient near the corner of the cold wall, and when the Rayleigh number reaches the critical value $R_{1c}(\sigma)$, oscillations are observed starting from the end and spreading away to the core, in agreement with the linear stability analysis.

The local heat transfer at the cold wall is shown in Figure 6.7. It is evident that a higher Rayleigh number leads to a larger Nusselt number, and near the top corner where sharp horizontal temperature gradients occur, the heat transfer is larger than near the lower corner. Temperature profiles for the upper and lower walls are presented in Figures 6.8-6.9. On the bottom wall, the temperature has a near-linear form while on the top wall larger variations develop near the cold wall as the Rayleigh number increases (Figure 6.9).

6.6 Numerical Results for Air and Water

Extensive numerical investigations were carried out for a wide range of Rayleigh numbers with $\sigma = 0.733$ (air) and further results were also obtained for $\sigma = 6.983$ (water). Attention is focused on the case of air, where results were obtained for $100 \leq R_1 \leq 20000$ using outer boundaries varying from 3 to 20. Figures 6.10-6.18 show the flow patterns for different Rayleigh numbers. In Figures 6.12-6.15 , the results are shown in the region $0 < x < 4$ although an outer boundary $x_\infty = 7$ was used in the numerical computations. Also Figures 6.16-6.18 show flow patterns in the region $0 < x < 1$ although an outer boundary $x_\infty = 20$ was used in the computation. These parts of the flow, near the cold wall, are where the most interesting behaviour takes place.

Figures 6.10-6.18 show the influence of the Rayleigh number R_1 on the flow structure. For low Rayleigh numbers in Figures 6.10-6.11, roughly less than 1000, the non-parallel flow is restricted to a square area near the cold wall, and away from that the flow is approximately parallel to the horizontal boundaries. When R_1 increases to

5000 or more (Figures 6.12-6.15), the flow patterns change dramatically. A vertical thermal boundary layer is gradually formed on the cold wall, with a horizontal width $x \ll 1$, while away from the cold wall the flow requires an increasingly large distance $x \gg 1$ to achieve the outer form associated with the parallel core flow. At the higher Rayleigh numbers, the vertical boundary layer is much thinner, and the strongest horizontal temperature gradients are set up near the top corner of the cold wall, where there is vigorous convection down the wall. In Figures 6.13-6.15 when $R_1 \geq 6000$, a small eddy occurs in the streamline field near the lower cold corner, and the flow is slightly divergent away from the lower horizontal boundary, consistent with theoretical analysis of a possible horizontal boundary- layer structure there in the limit $R_1 \rightarrow \infty$ (Daniels and Gargaro 1992a,b). Further quantitative comparisons with the proposed high-Rayleigh number limit structure (Section 6.3) are discussed below. Numerical results were also obtained for $R_1 = 20000$ and detailed pictures of the flow and temperature fields are presented in Figures 6.16-6.18. Note how the isotherms descending the cold wall follow the streamlines near the base of the wall, indicating that the flow there is convectively-dominated at large Rayleigh numbers. Note also that most of the mass flux in the vertical boundary layer is conveyed to the base of the layer, consistent with the similarity solution of Section 6.3.

The skin friction on the top and bottom walls is shown for different Rayleigh numbers in Figures 6.19 and 6.20. On the top wall, there is a strong variation close to $x = 0$ indicating the boundary layer structure of the flow at high Rayleigh numbers. On the bottom wall, the skin friction develops both minimum and maximum values in the range $0 < x < 1$, before reaching a constant asymptotic form as $x \rightarrow \infty$. This is associated with the complex flow near the bottom of the cold wall and suggests the possibility of flow separation on the bottom wall for $R_1 > 20000$.

The temperatures of the top and bottom walls are illustrated in Figures 6.21-6.22. These show that the temperature increases as R_1 increases, and for higher Rayleigh numbers a sharp variation occurs near the top of the cold wall with almost linear behaviour beyond. On the lower boundary, a much larger scale in x is needed

for the temperature to attain its linear form, this scale increasing with R_1. The local heat flux at the cold wall is shown in Figure 6.23, and is seen to increase with Rayleigh number, especially near the top of the cold wall, where the vertical boundary layer solution described in Section 6.3 would actually correspond to an infinite form $\partial T/\partial x \propto (1-z)^{-1/4}$ as $z \to 1$. Of course the boundary layer approximation breaks down very close to the corner, reflecting the local behaviour described in the numerical computations shown in Figure 6.23.

Quantitative comprisons were made with the asymptotic structure outlined in Section 6.3 in three areas, relating to the form of the parameter $c(R_1, \sigma)$ as $R_1 \to \infty$ and to specific properties of the vertical boundary layer solution. Figure 6.24 shows the computed values of c based on the temperature profile (6.2.21) obtained in the numerical solution at $x = x_\infty$. According to (6.3.7) the quantity $c/R_1^{7/5}$ should approach a constant limiting form $c_0(\sigma)$ as $R_1 \to \infty$, where

$$c_0 = (\frac{3Q_0}{4\lambda})^{4/5} \tag{6.6.1}$$

with $Q_0 = 1/362880$ and

$$\lambda = g'(0) = \frac{3}{4}\sigma^{1/4}(2.436 + 4.884\sigma^{1/2} + 4.952\sigma)^{-1/4}.$$

For the present case where $\sigma = 0.733$ it follows that

$$c_0 = 6.04353 \times 10^{-5}$$

and this horizontal asymptote is shown in Figure 6.24. There appears to be excellent agreement with the trend of the numerical solution. It should also be mentioned that at low Rayleigh numbers the asymptotic form predicted by Cormack, Leal and Imberger (1974)

$$c \sim 1.74 \times 10^{-6} R_1^2 \tag{6.6.2}$$

is in excellent agreement with the value $c = 1.617 \times 10^{-2}$ obtained from the present computation with $R_1 = 100$. The value predicted by (6.6.2) is $c = 1.74 \times 10^{-2}$.

Figures 6.25 and 6.26 show comparisons of the vertical boundary layer structure for $R_1 \gg 1$ proposed in Section 6.3 with the numerical results. The boundary

layer theory predicts that the skin friction on the cold wall should approach a form proportional to $R_1^{9/5}$ as $R_1 \rightarrow \infty$, or more specifically,

$$R_1^{-9/5}\frac{\partial w}{\partial x}\,|_{x=0} \rightarrow -c_0^{3/4}(1-z)^{1/4}f''(0) = -2Kc_0^{3/4}(1-z)^{1/4}, \quad R_1 \rightarrow \infty, \quad (6.6.3)$$

where $K = f''(0)/2 = 0.4483$ is the value obtained by Gargaro (1991). In Figure 6.25 the right-hand side of (6.6.3) with c_0 given by (6.3.18) is compared with the computed values of the left-hand side for each Rayleigh number. This suggests that the Rayleigh number scaling is correct and that the quantitative comparison is reasonable, especially for the top half of the vertical boundary layer. The discrepancy in the bottom half is thought to be due to the corner structure at the bottom of the cold wall which may only be attained for exceptionally high Rayleigh numbers, if the type of structure envisaged by Smith and Duck (1977) is valid there. The present computations indicate the right trend, but results need to be obtained for much higher Rayleigh numbers to confirm the asymptotic prediction.

For the heat transfer, the boundary layer theory predicts a form proportional to R_1^2 as $R_1 \rightarrow \infty$, or more specifically

$$R_1^{-2}\frac{\partial T}{\partial x}|_{x=0} \rightarrow \lambda c_0^{5/4}(1-z)^{-1/4}, \quad R_1 \rightarrow \infty, \quad (6.6.4)$$

where λ is given by (6.3.16). In Figure 6.26 the right-hand side of (6.6.4) with c_0 given by (6.3.18) is compared with the computed values of the left-hand side for each Rayleigh number. Again this suggests that the Rayleigh number scaling is correct and the comparison for the region $z \geq 0.3$ is quite convincing. Again a corner structure may be responsible for the discrepancy observed in the region close to $z = 0$.

Other general features of the computations at high Rayleigh numbers are encouraging in terms of the proposed asymptotic structure. Apart from the vertical boundary layer structure, the asymptotic theory predicts that the flow must turn the corner at the base of the cold wall and then develop within a horizontal layer where the isotherms descending the cold wall attach to the bottom wall of the cavity. The horizontal structure eventually merges with the main recirculatory flow in

the end zone on the long scale $x = O(R_1)$ as $R_1 \to \infty$. This scale is observed in the numerical computations, and the isotherm patterns of Figures 6.15 , 6.17 are consistent with the expected behaviour.

Finally, Figures 6.27-6.28 show some results for the case of water ($\sigma = 6.983$). At low Rayleigh numbers the flow patterns are similar to those for air. More work is needed to obtain results for high Rayleigh numbers to compare with the asymptotic theory.

In conclusion, a detailed numerical study of the end zone flow in a shallow cavity with insulated boundaries has been carried out. For low Prandtl number fluids, secondary flow is seen to appear near $R_1 \approx 500$ with $\sigma = 0.05$ in the form of stationary transverse cells , in good agreement with the value of $R_{1c}(0.05) \approx 610$ predicted by linear stability theory and consistent with the onset of secondary flow as a result of an imperfect bifurcation (Hart 1983). At low Rayleigh numbers, the present computation of c in the temperature field of the core flow is in good agreement with the theoretical prediction of c by Cormack et al (1974), while at high Rayleigh numbers, the numerical solutions appear to be in good agreement with the theoretical prediction of c for the case of air ($\sigma = 0.733$) based on boundary-layer theory.

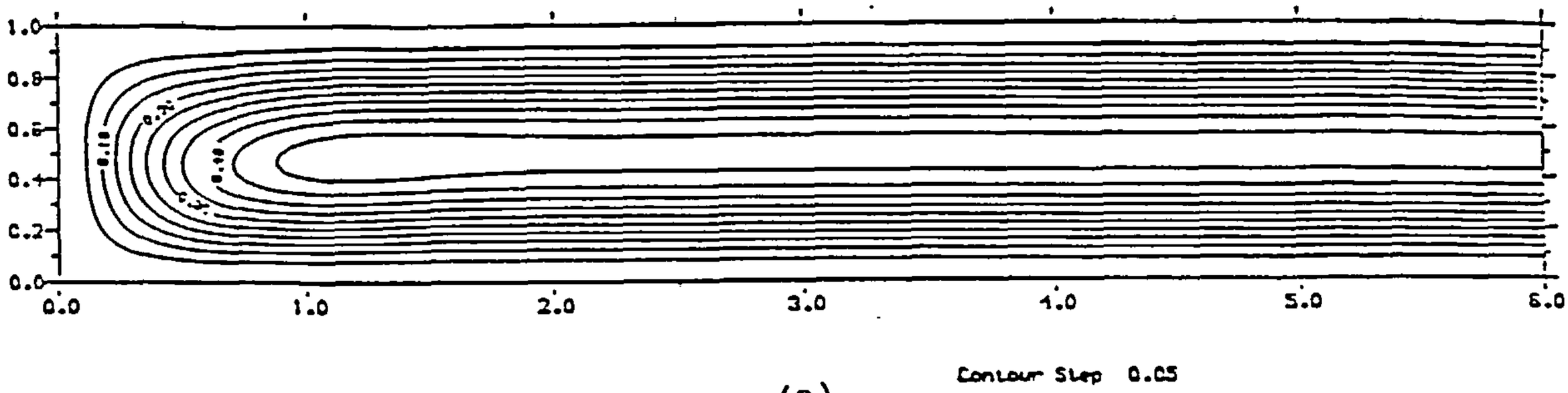

(a)

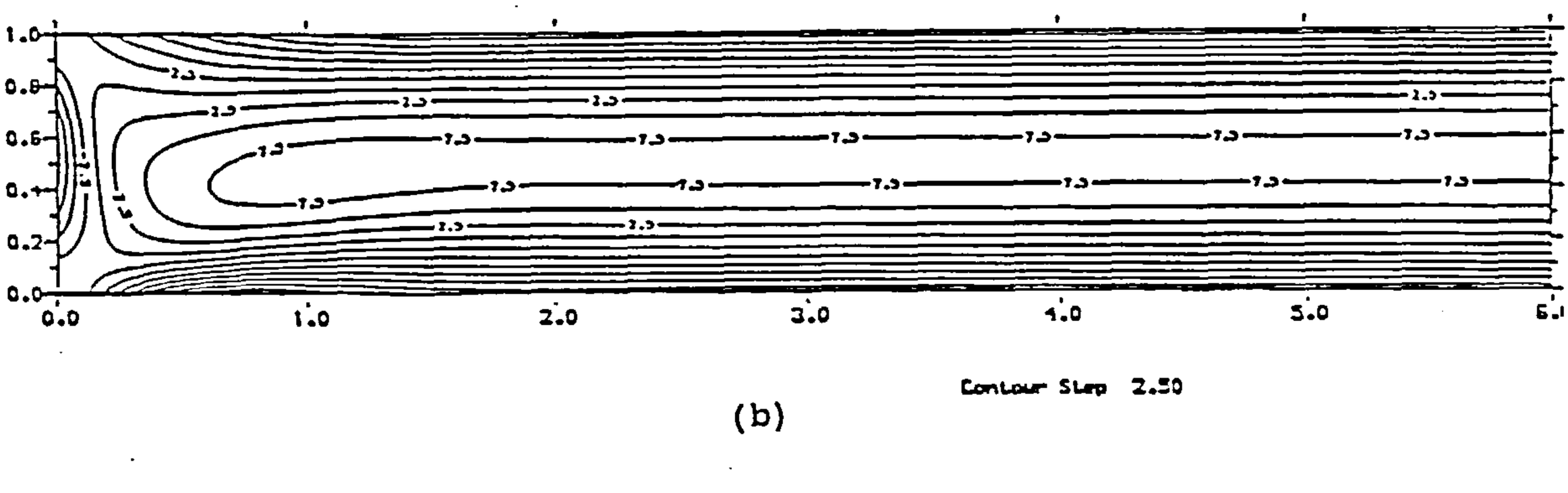

(b)

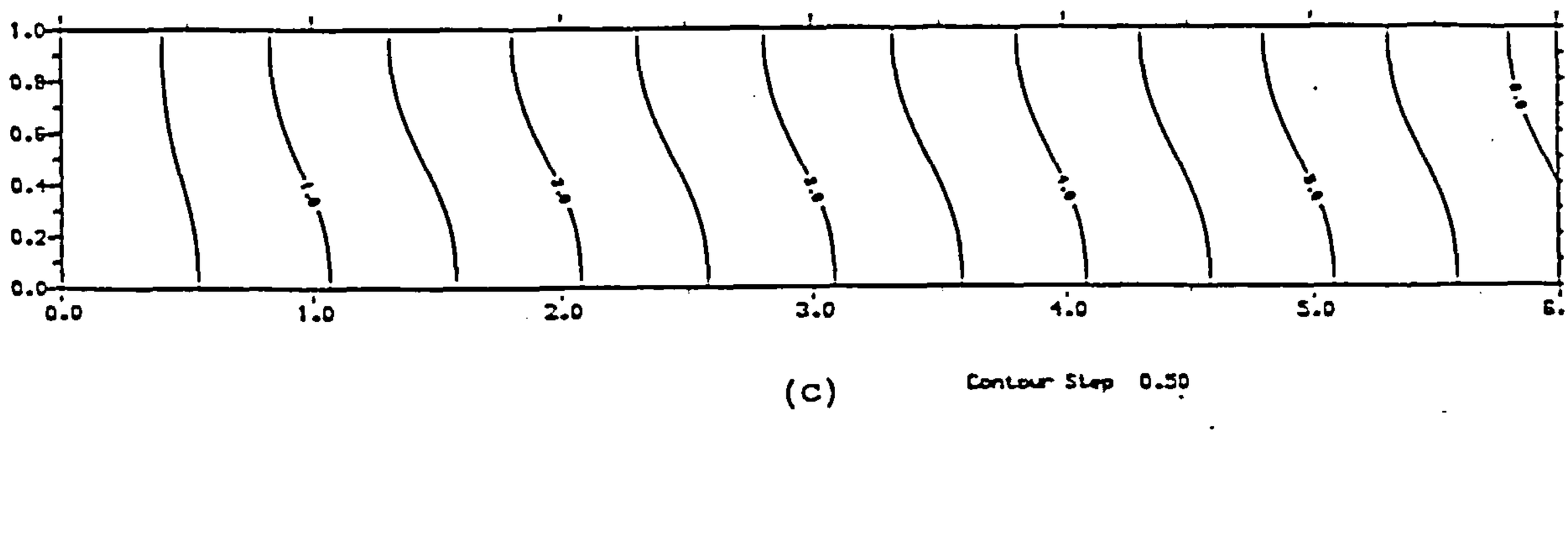

(c)

Figure 6.1: Contours of the steady-state solution for (a) stream function , (b) vorticity, (c) temperature, for $\sigma = 0.05$ and $R_1 = 200$, using a 180×30 computational grid with $x_\infty = 6$.

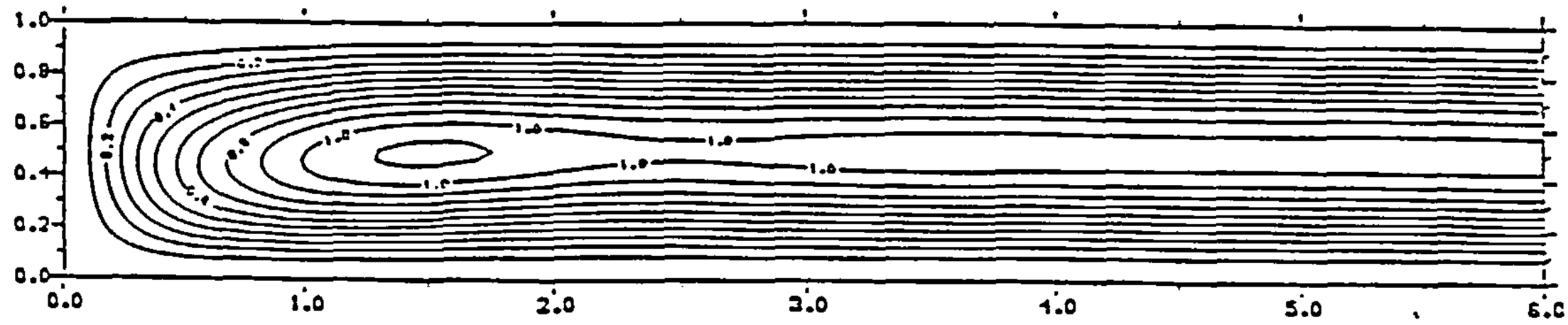

Contour Step 0.10

(a)

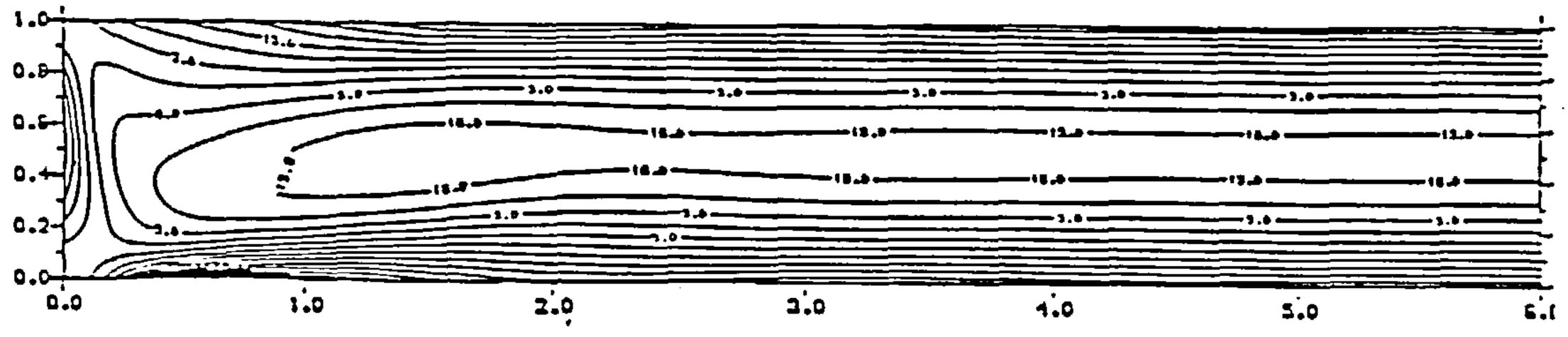

Contour Step 5.00

(b)

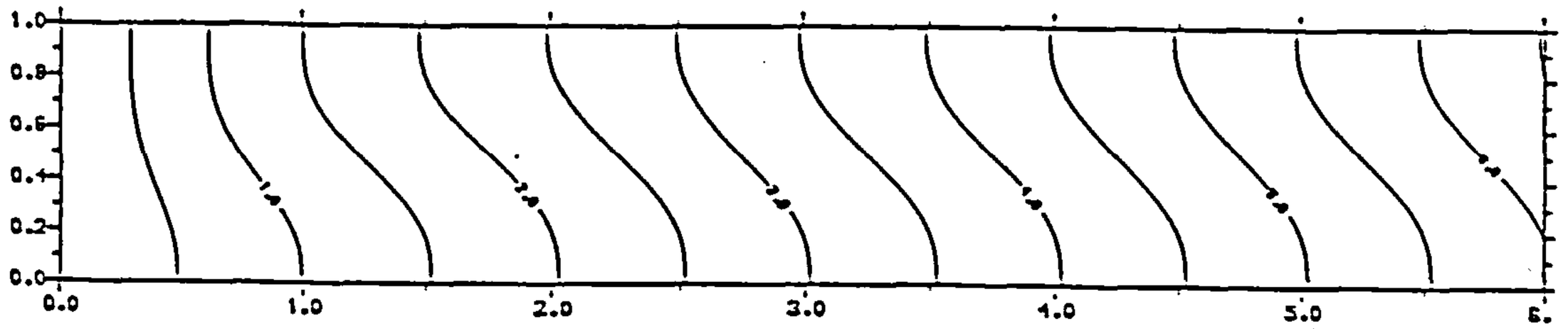

Contour Step 0.50

(c)

Figure 6.2: Contours of the steady-state solution for (a) stream function , (b) vorticity, (c) temperature, for $\sigma = 0.05$ and $R_1 = 400$, using a 180×30 computational grid with $x_\infty = 6$.

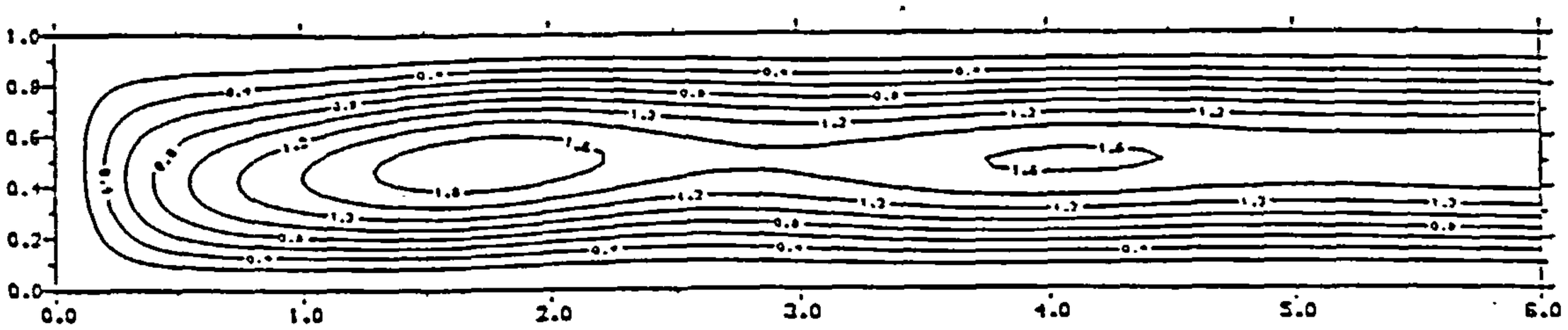

(a)

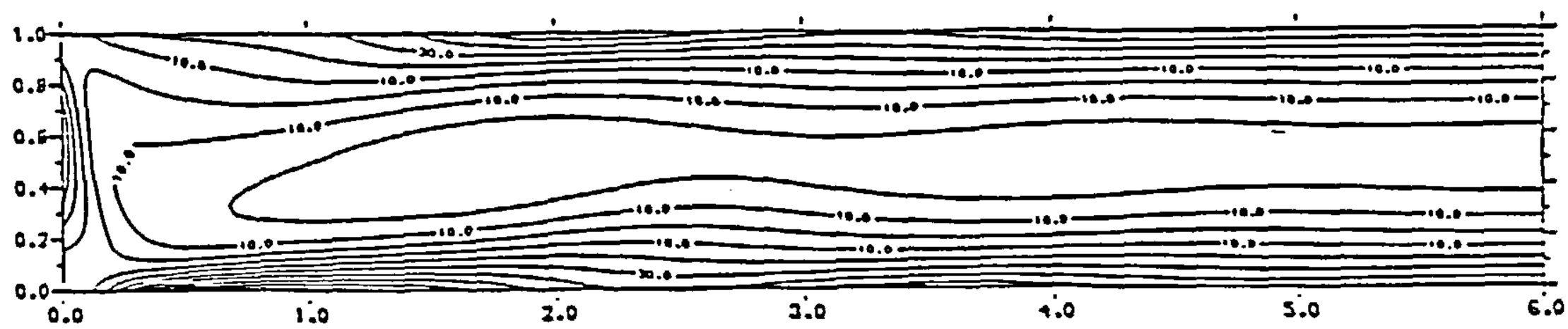

(b)

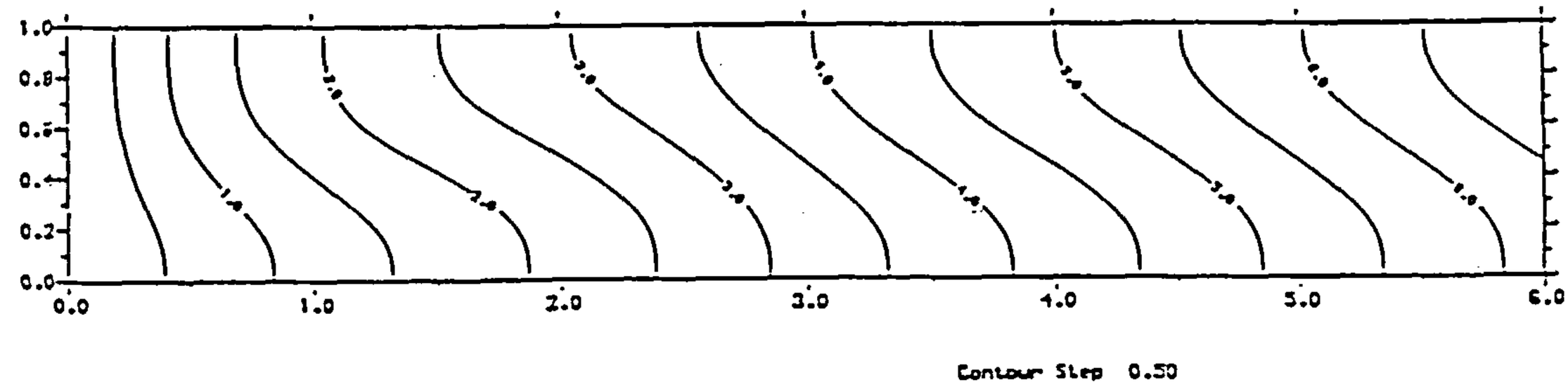

(c)

Figure 6.3: Contours of the steady-state solution for (a) stream function , (b) vorticity, (c) temperature, for $\sigma = 0.05$ and $R_1 = 600$, using a 180×30 computational grid with $x_\infty = 7$.

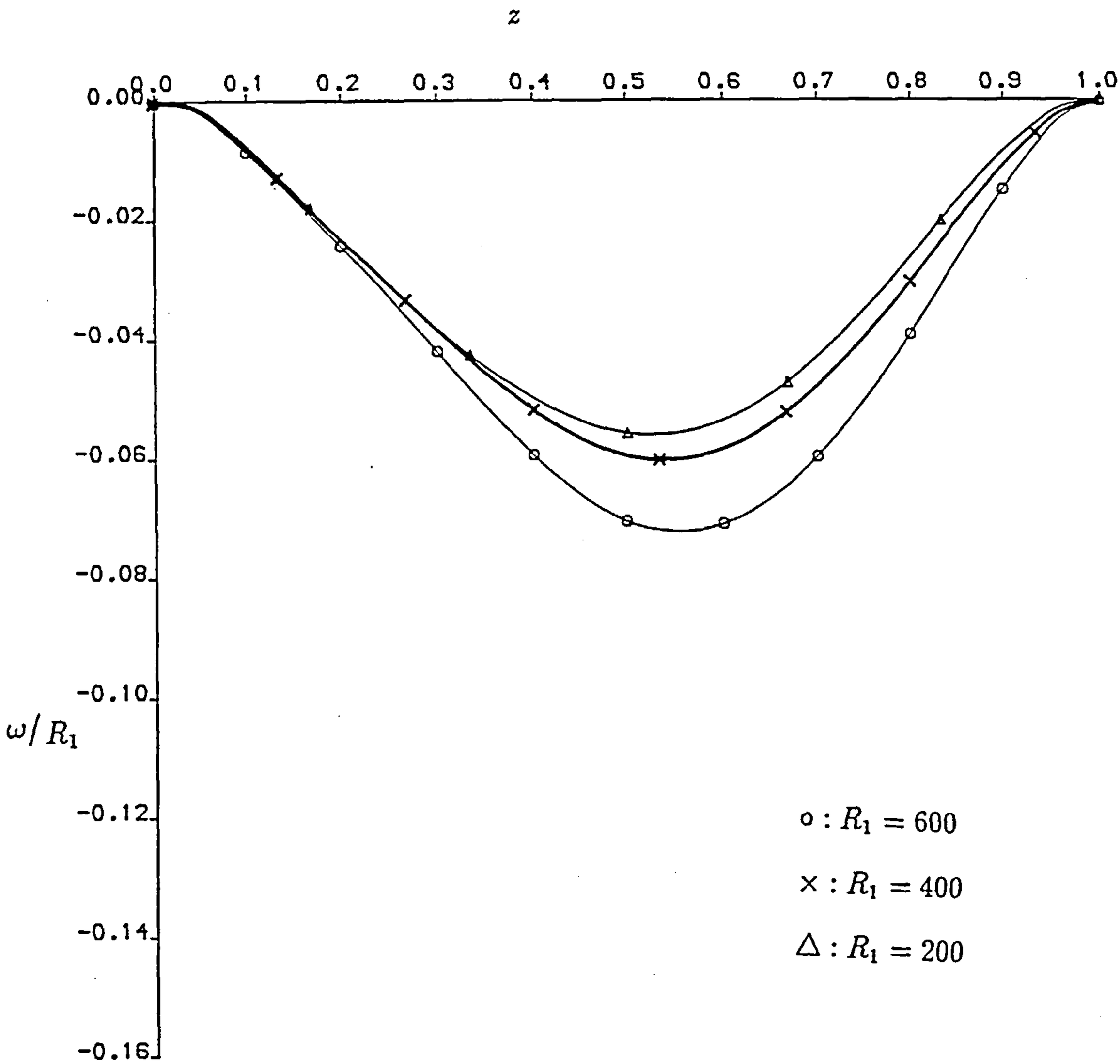

Figure 6.4: The skin friction ω/R_1 with $\sigma = 0.05$ for different Rayleigh numbers on the cold wall for the insulating case.

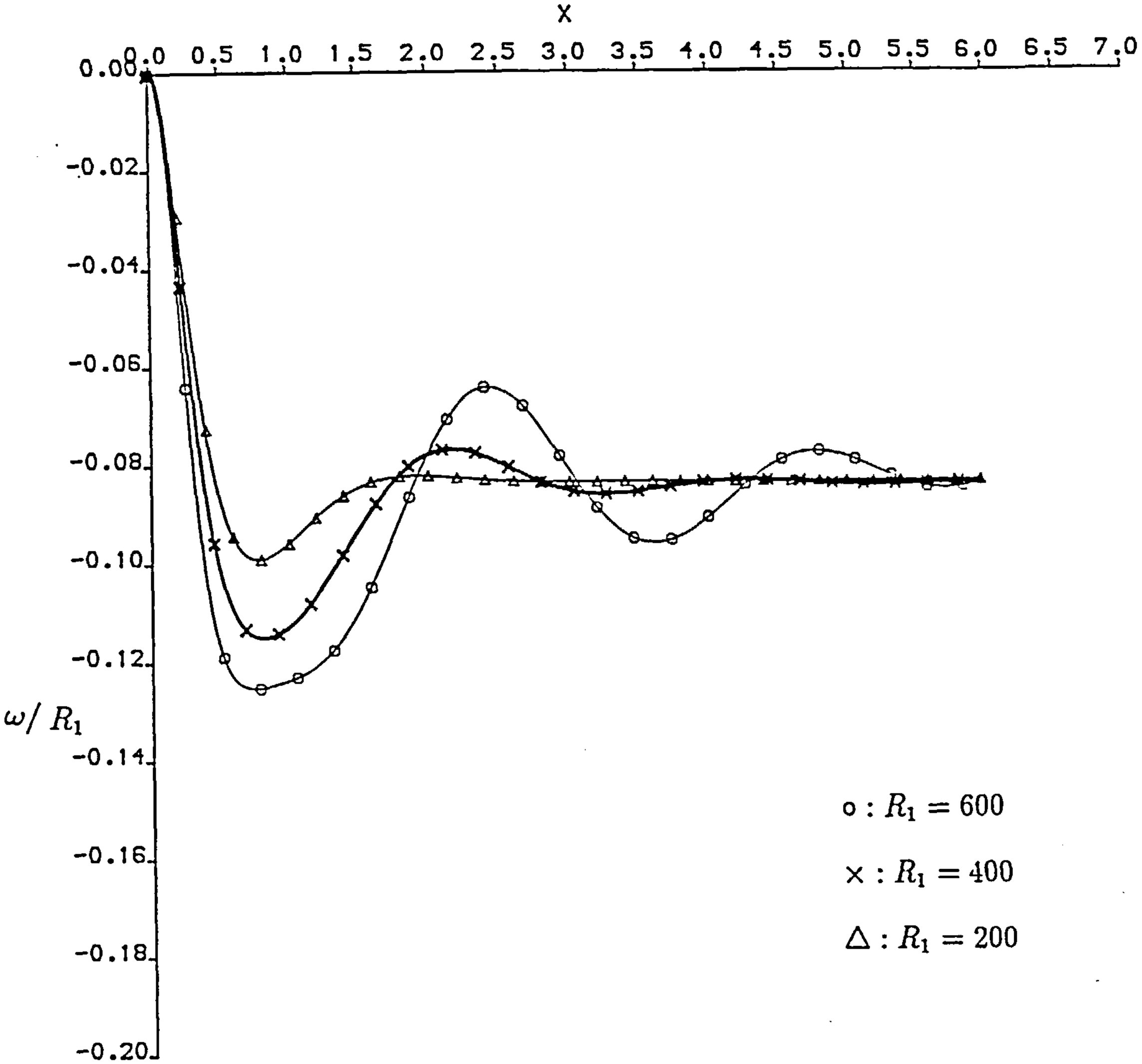

Figure 6.5: The skin friction ω/R_1 with $\sigma = 0.05$ for different Rayleigh numbers on the bottom wall for the insulating case.

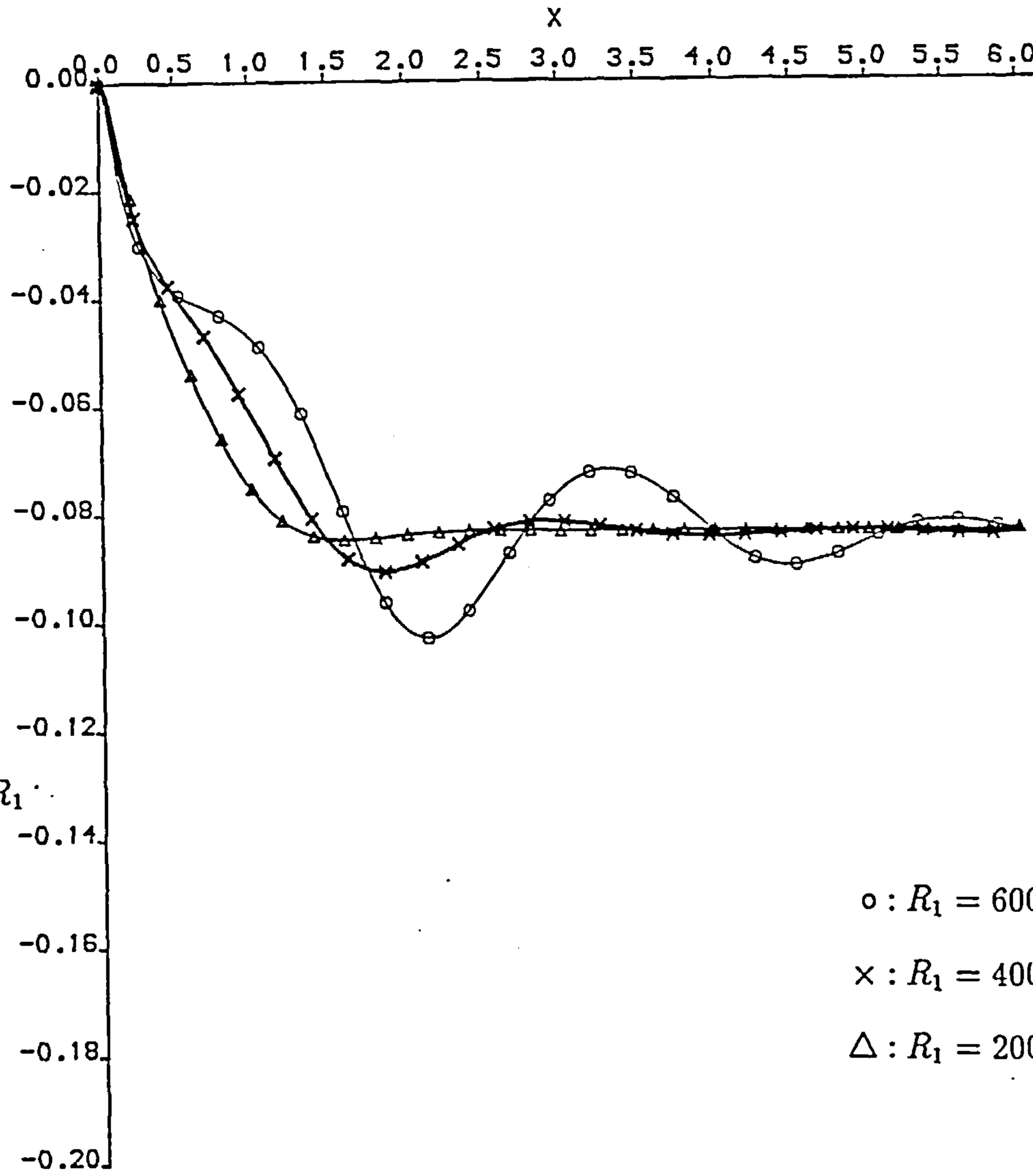

Figure 6.6: The skin friction ω/R_1 with $\sigma = 0.05$ for different Rayleigh numbers on the top wall for the insulating case.

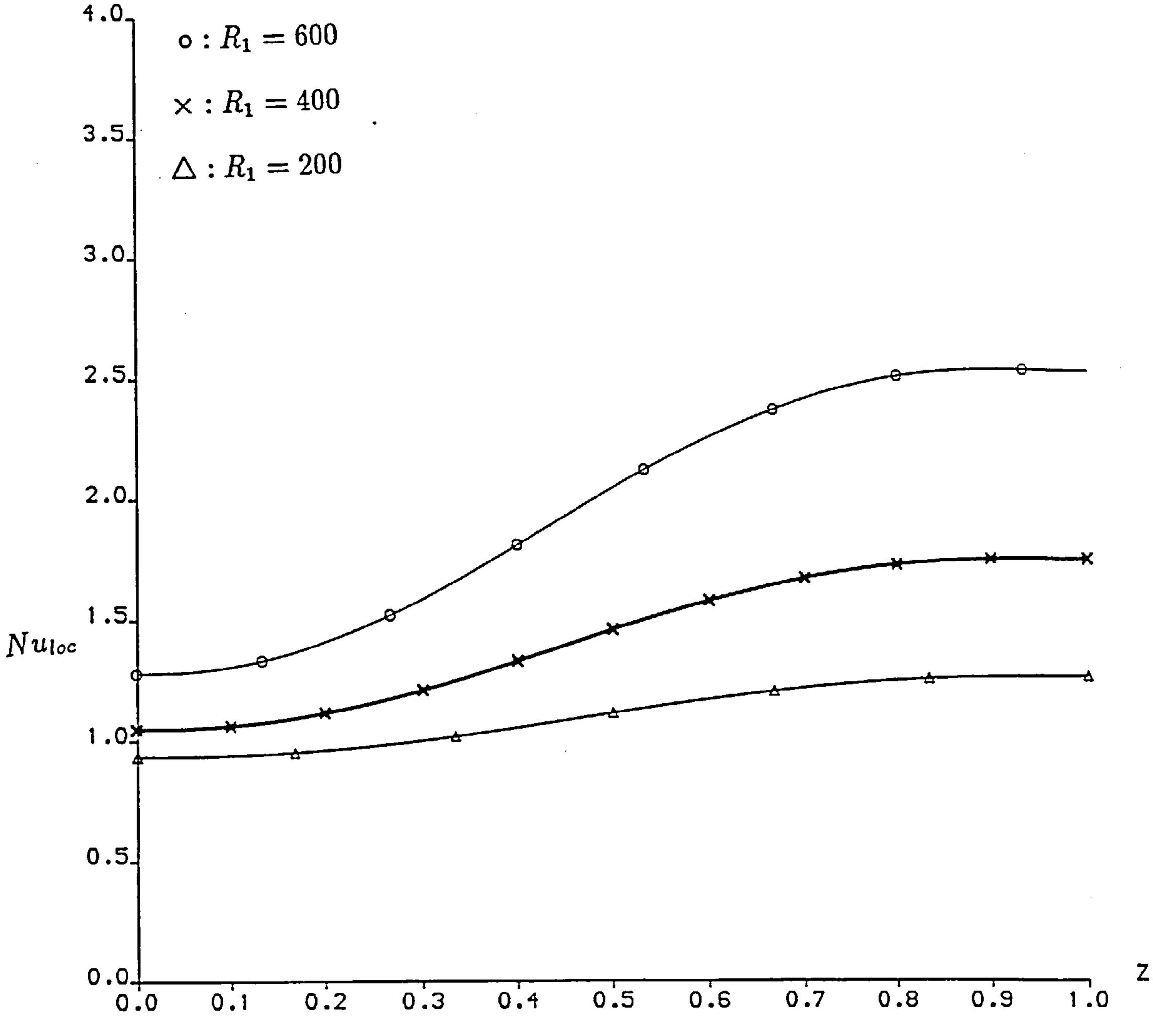

Figure 6.7: The local Nusselt number with $\sigma = 0.05$ for different Rayleigh numbers on the cold wall for the insulating case.

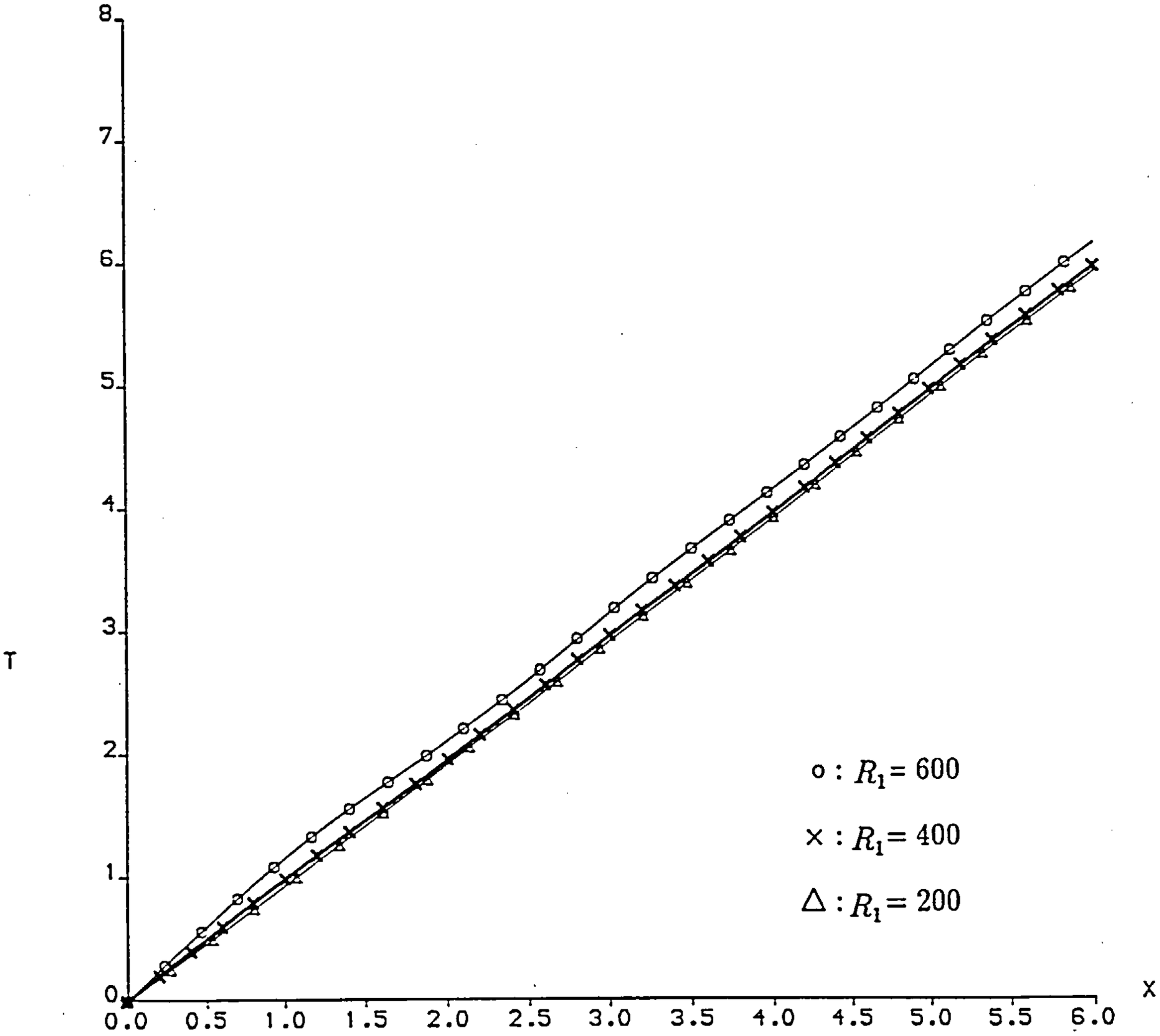

Figure 6.8: The temperature with $\sigma = 0.05$ for different Rayleigh numbers on the bottom wall for the insulating case.

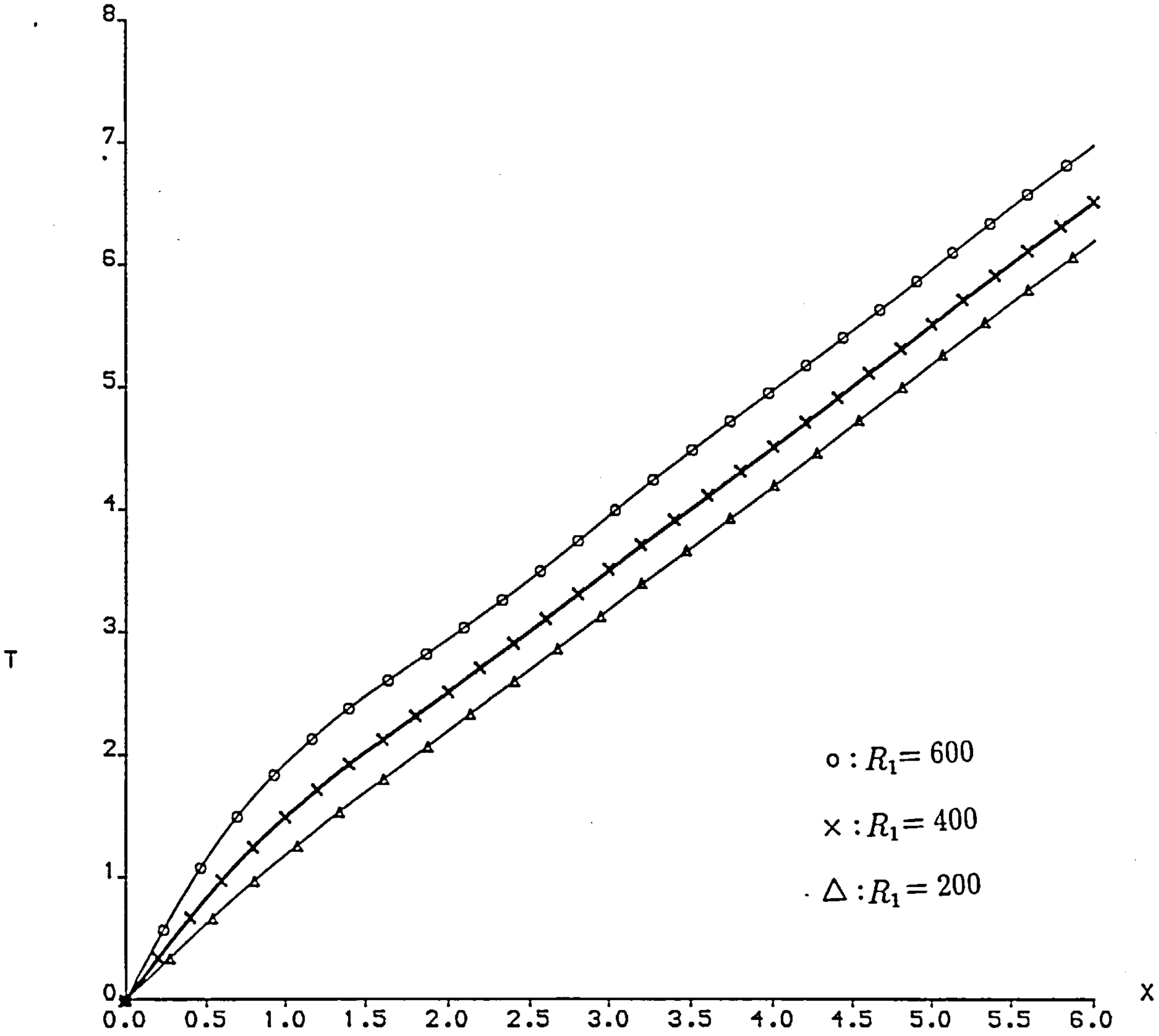

Figure 6.9: The temperature with $\sigma = 0.05$ for different Rayleigh numbers on the top wall for the insulating case.

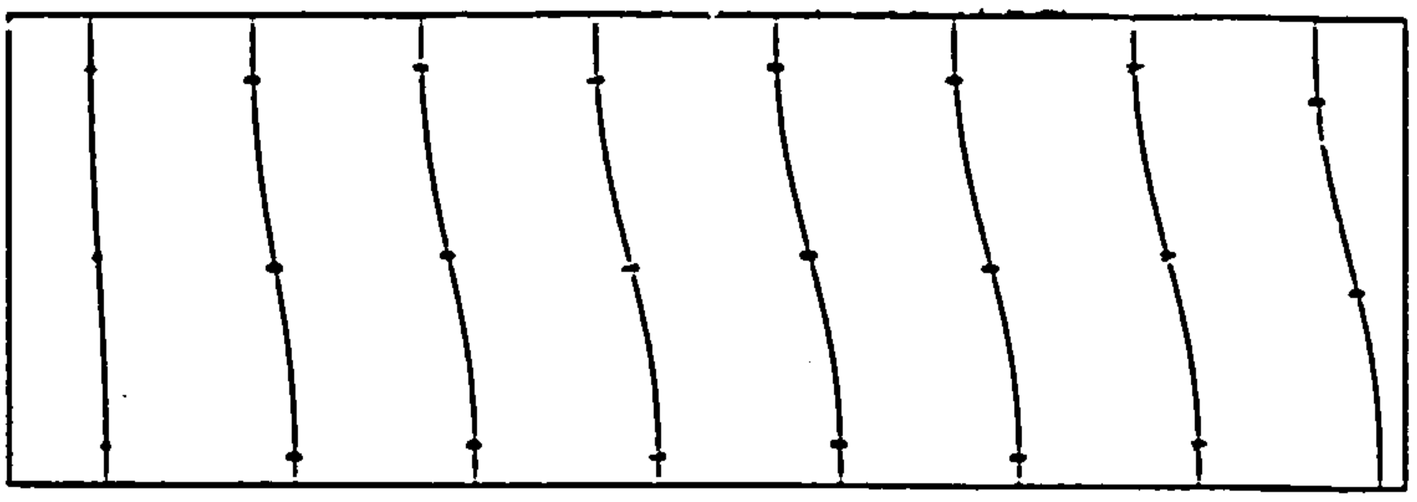

CONTOUR KEY	
1	0.1927726
2	0.5783179
3	0.9638632
4	1.3494085
5	1.7349537
6	2.1204990
7	2.5060443
8	2.8915896

(c)

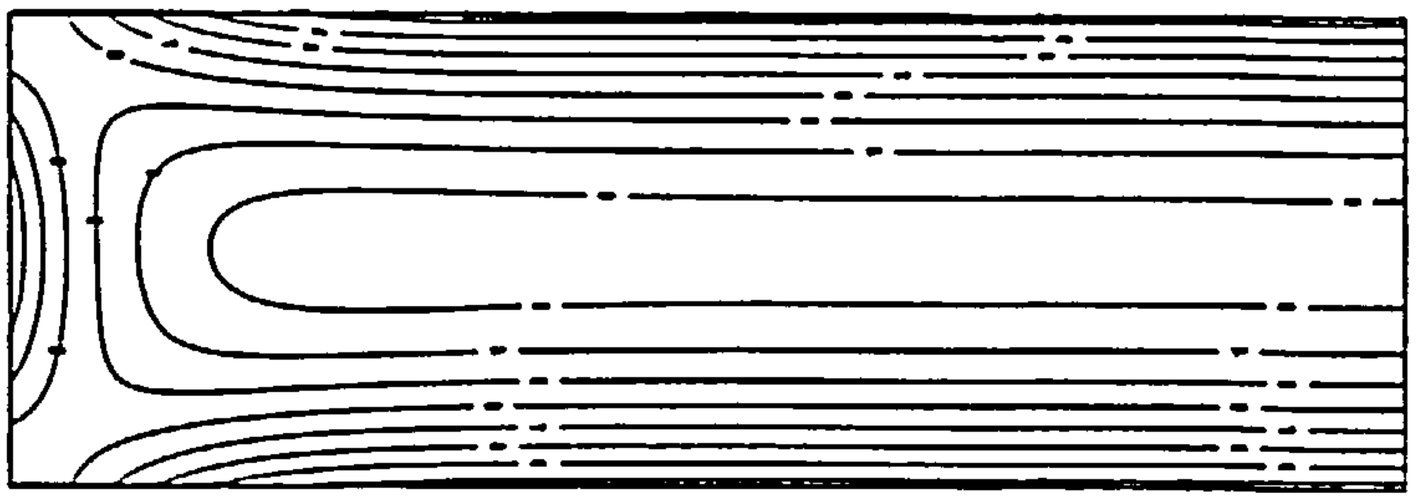

CONTOUR KEY	
1	-7.5077839
2	-6.0177461
3	-4.4277083
4	-2.8376705
5	-1.2476327
6	0.3424051
7	1.9324429
8	3.5224807

(b)

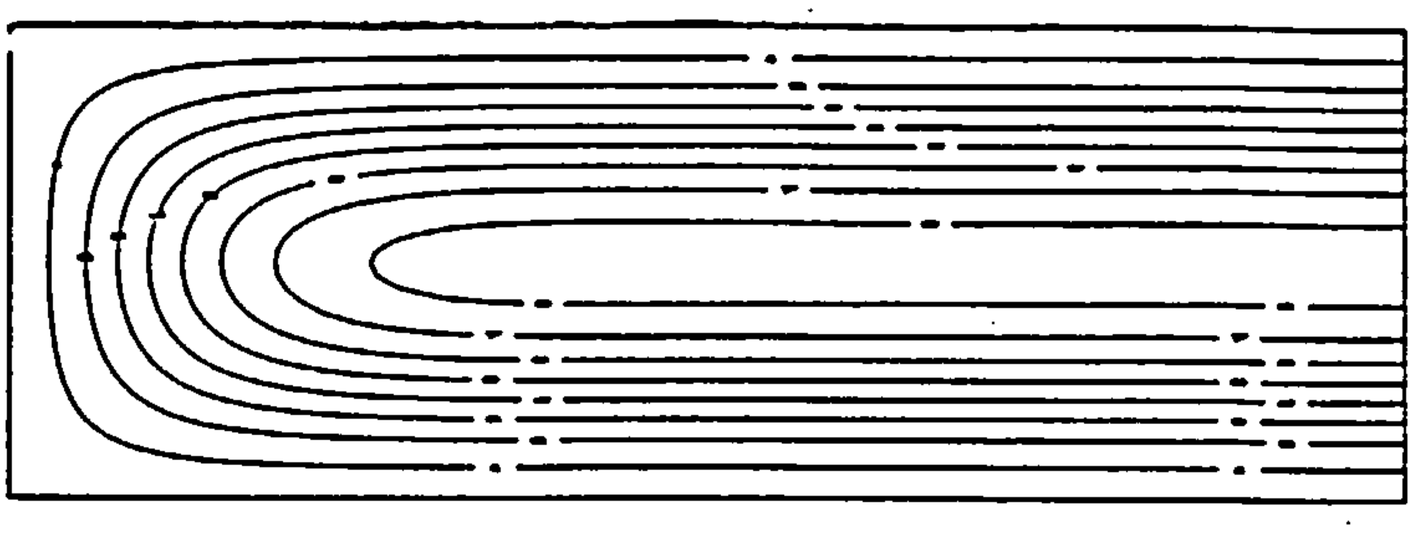

CONTOUR KEY	
1	0.0153358
2	0.0490103
3	0.0815839
4	0.1143575
5	0.1470310
6	0.1797045
7	0.2123782
8	0.2450517

(a)

Figure 6.10: Contours of the steady-state solution for (a) stream function , (b) vorticity, (c) temperature, for $\sigma = 0.733$ and $R_1 = 100$, using a 120×40 computational grid with $x_\infty = 3$.

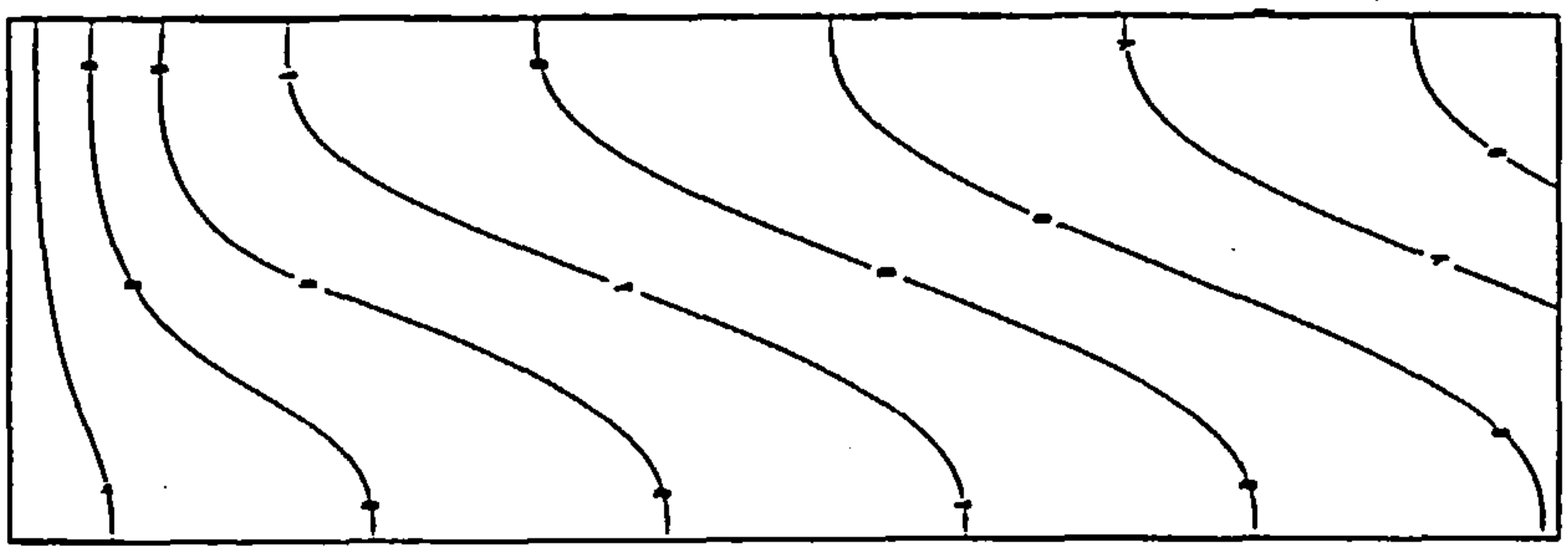

CONTOUR KEY	
1	0.2797350
2	0.8392049
3	1.3986748
4	1.9581447
5	2.5176147
6	3.0770846
7	3.6365545
8	4.1960244

(c)

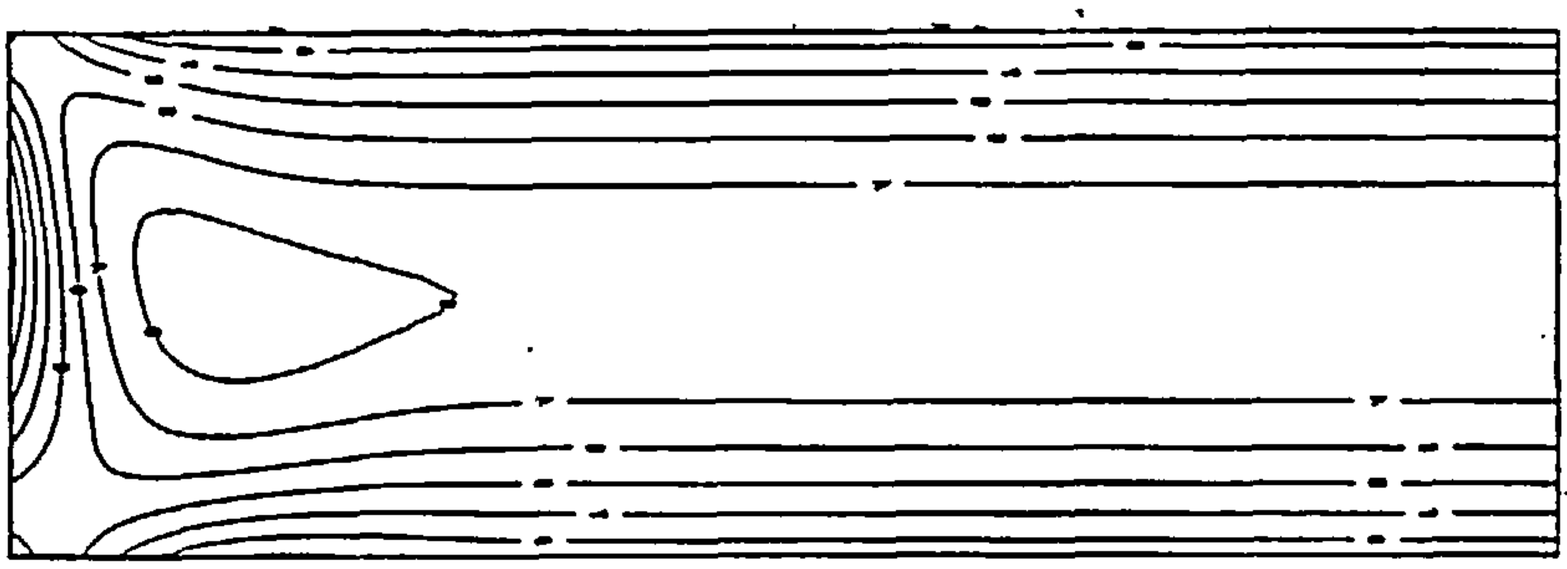

CONTOUR KEY	
1	-114.3717932
2	-91.9586629
3	-69.5455326
4	-47.1324022
5	-24.7192719
6	-2.3061415
7	20.1069888
8	42.5201191

(b)

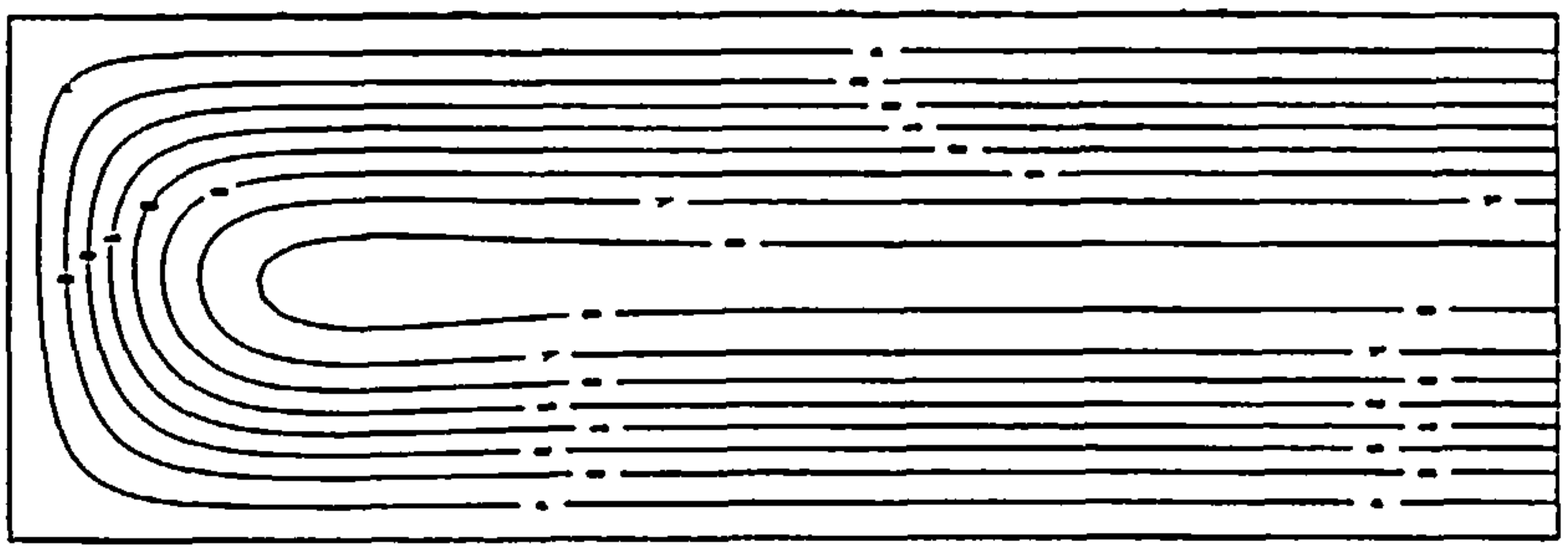

CONTOUR KEY	
1	0.1680012
2	0.5040036
3	0.8400061
4	1.1760085
5	1.5120109
6	1.8480133
7	2.1840158
8	2.5200182

(a)

Figure 6.11: Contours of the steady-state solution for (a) stream function , (b) vorticity, (c) temperature, for $\sigma = 0.733$ and $R_1 = 1000$, using a 90×30 computational grid with $x_\infty = 3$.

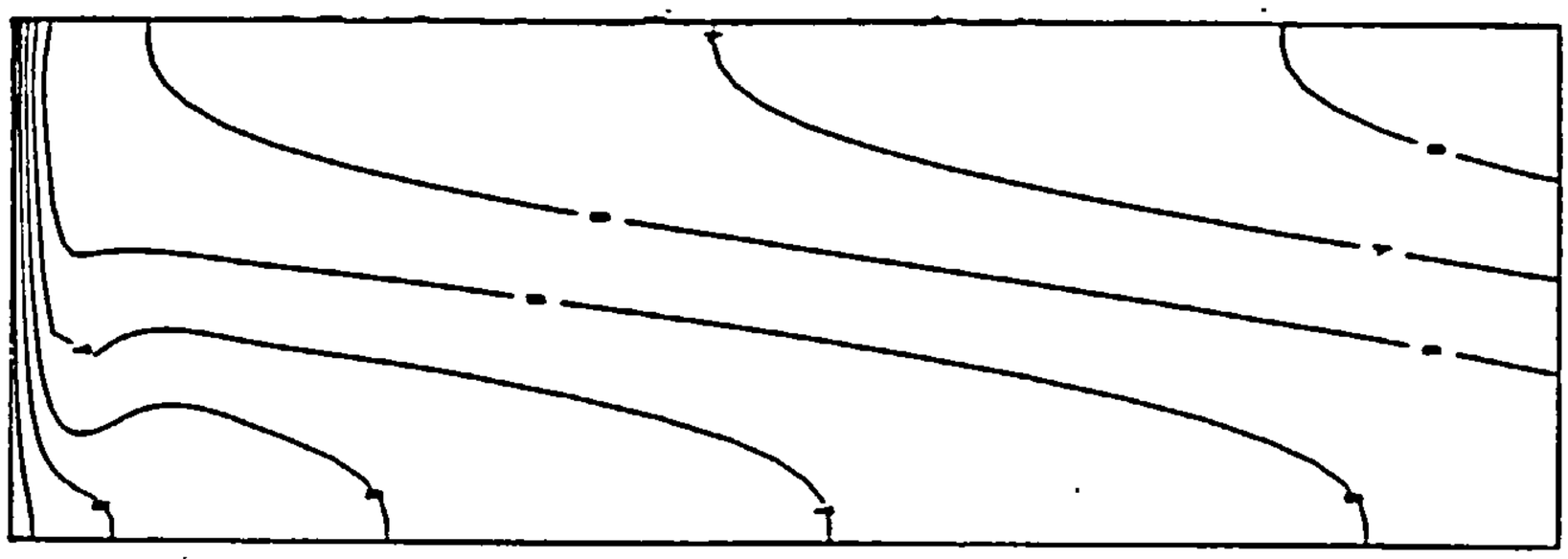

CONTOUR KEY	
1	1.082044
2	3.246132
3	5.410219
4	7.574307
5	9.738395
6	11.902483
7	14.066570
8	16.230658

(c)

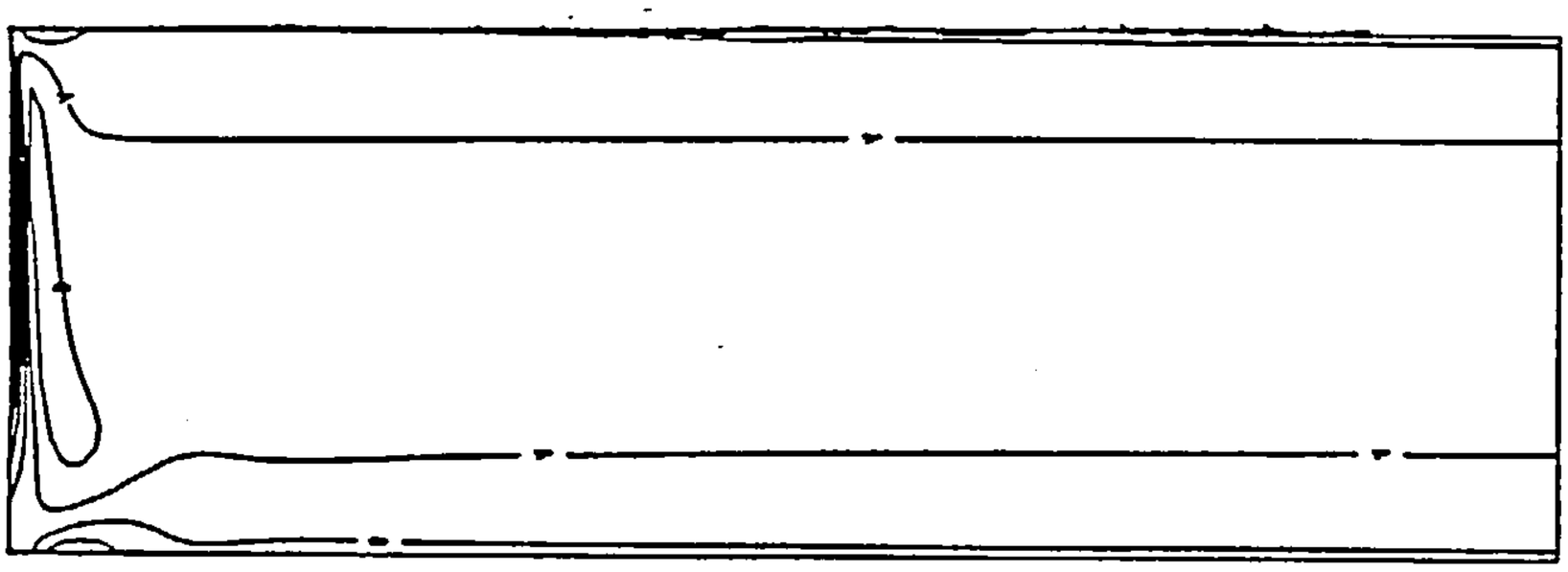

CONTOUR KEY	
1	-2176.102964
2	-1816.096022
3	-1456.089079
4	-1096.082137
5	-736.075195
6	-376.068253
7	-16.061310
8	343.945632

(b)

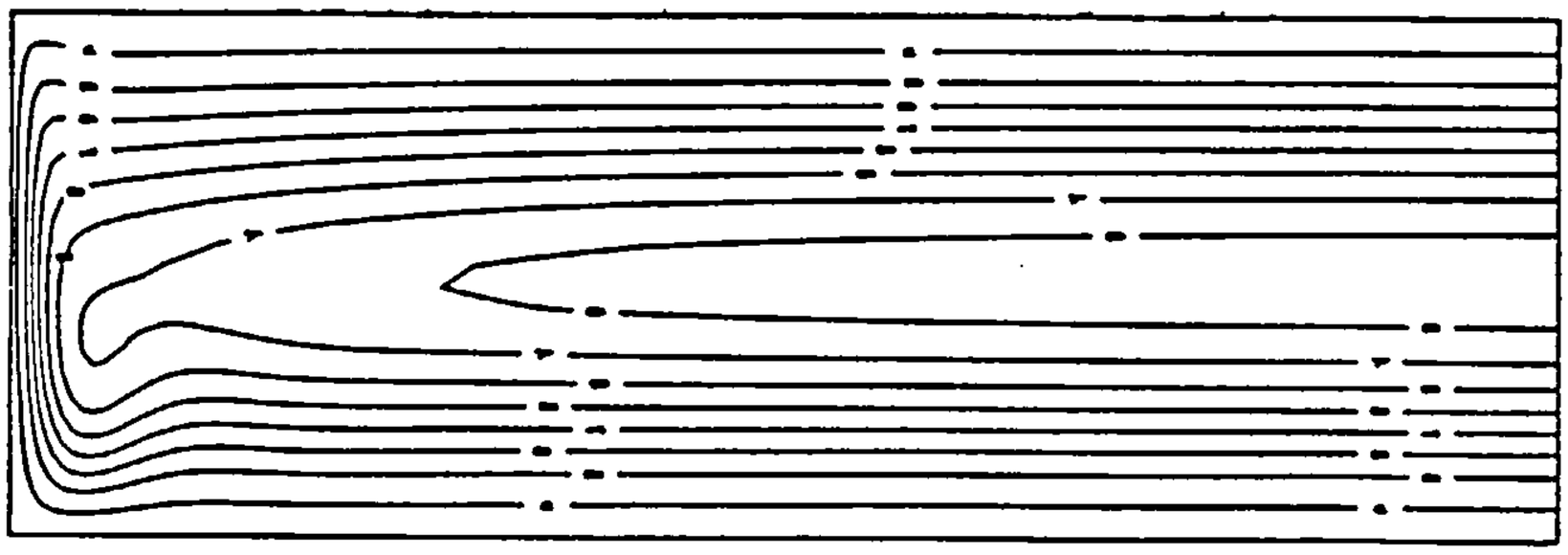

CONTOUR KEY	
1	0.811200
2	2.433600
3	4.056000
4	5.678400
5	7.300800
6	8.923200
7	10.545600
8	12.168000

(a)

Figure 6.12: Contours of the steady-state solution for (a) stream function , (b) vorticity, (c) temperature, for $\sigma = 0.733$ and $R_1 = 5000$, using a 150×25 computational grid with $x_\infty = 3$.

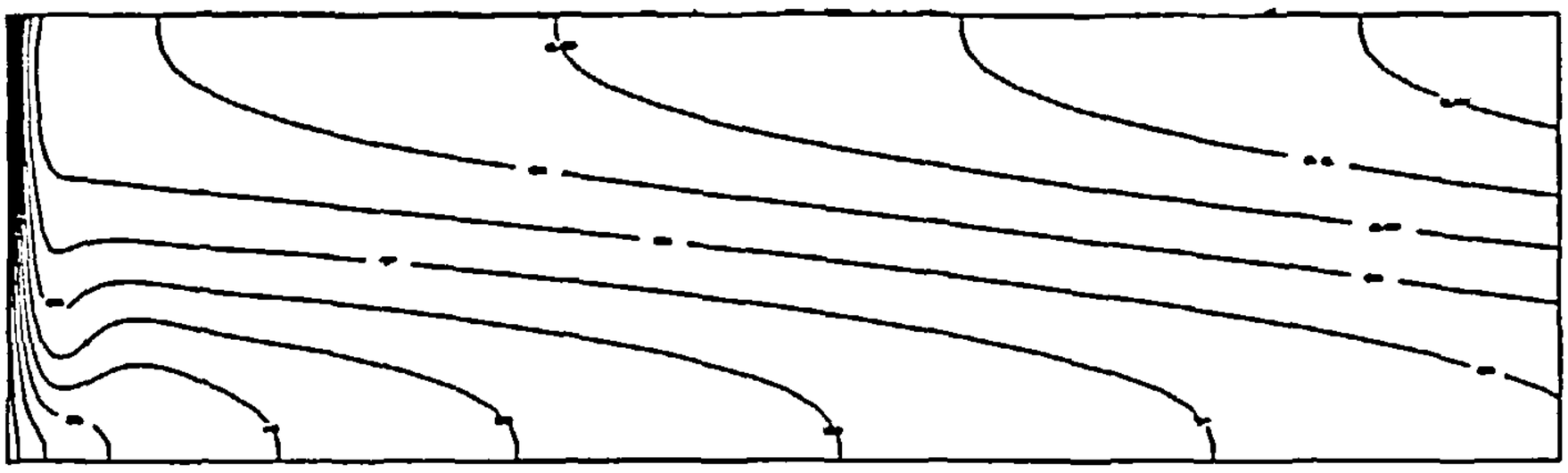

CONTOUR KEY	
1	0.888914
2	2.666743
3	4.444571
4	6.222400
5	8.000229
6	9.778057
7	11.555886
8	13.333714
9	15.111543
10	16.889372
11	18.667200
12	20.445029

(c)

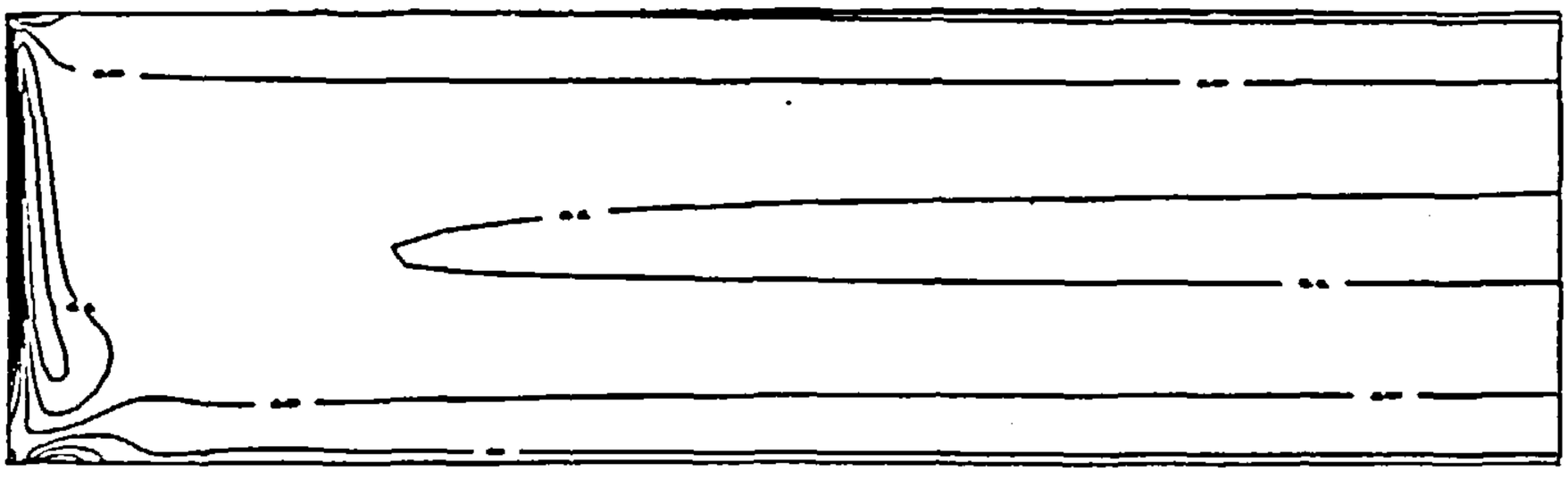

CONTOUR KEY	
1	-3110.307301
2	-2777.268397
3	-2444.229493
4	-2111.190589
5	-1778.151685
6	-1445.112781
7	-1112.073878
8	-779.034974
9	-445.996070
10	-112.957166
11	220.081738
12	553.120642

(b)

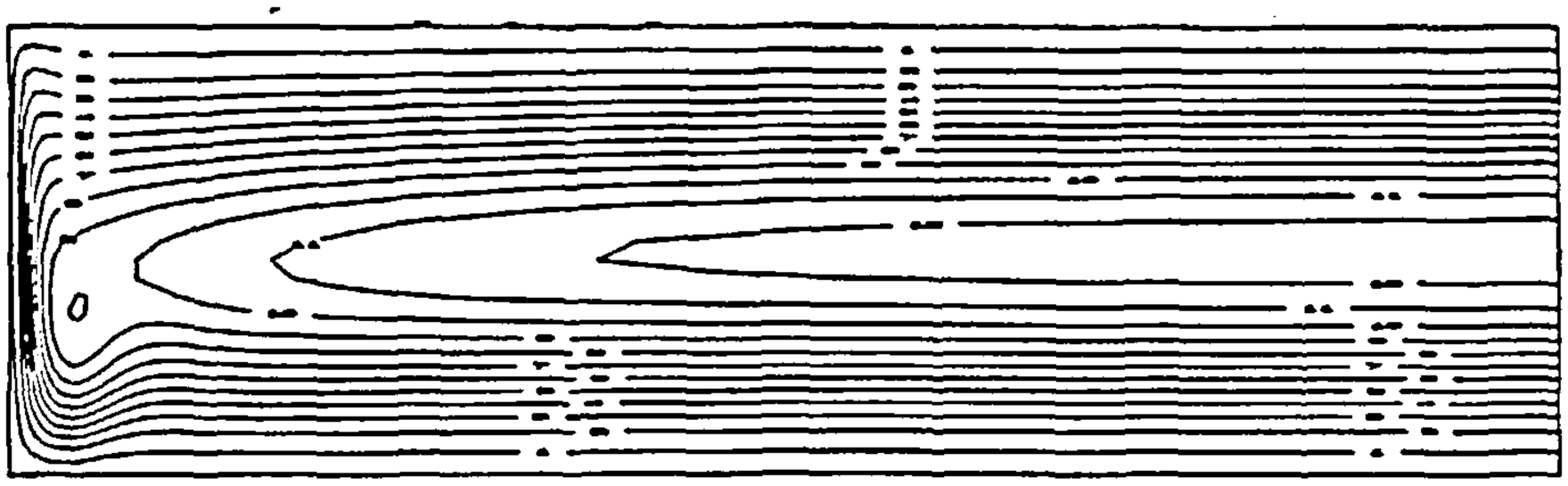

CONTOUR KEY	
1	0.648960
2	1.946880
3	3.244800
4	4.542720
5	5.840640
6	7.138560
7	8.436480
8	9.734400
9	11.032320
10	12.330240
11	13.628160
12	14.926080

(a)

Figure 6.13: Contours of the steady-state solution for (a) stream function , (b) vorticity, (c) temperature, for $\sigma = 0.733$ and $R_1 = 6000$, using a 175×25 computational grid with $x_\infty = 7$.

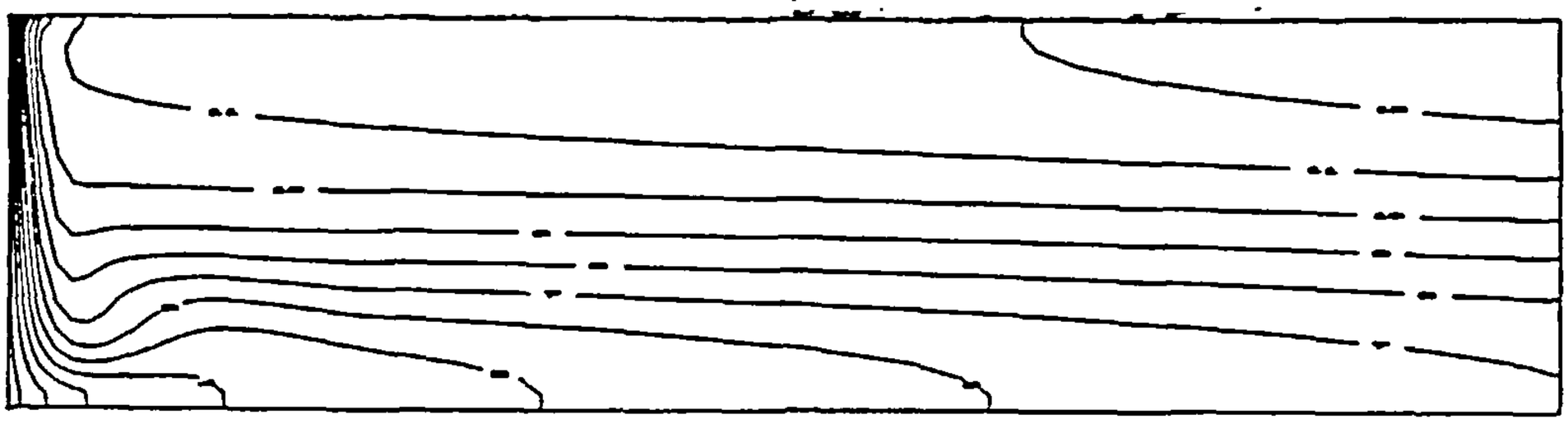

CONTOUR KEY	
1	1.388585
2	4.165756
3	6.942927
4	9.720097
5	12.497268
6	15.274439
7	18.051609
8	20.828780
9	23.605951
10	26.383121
11	29.160292
12	31.937463

(c)

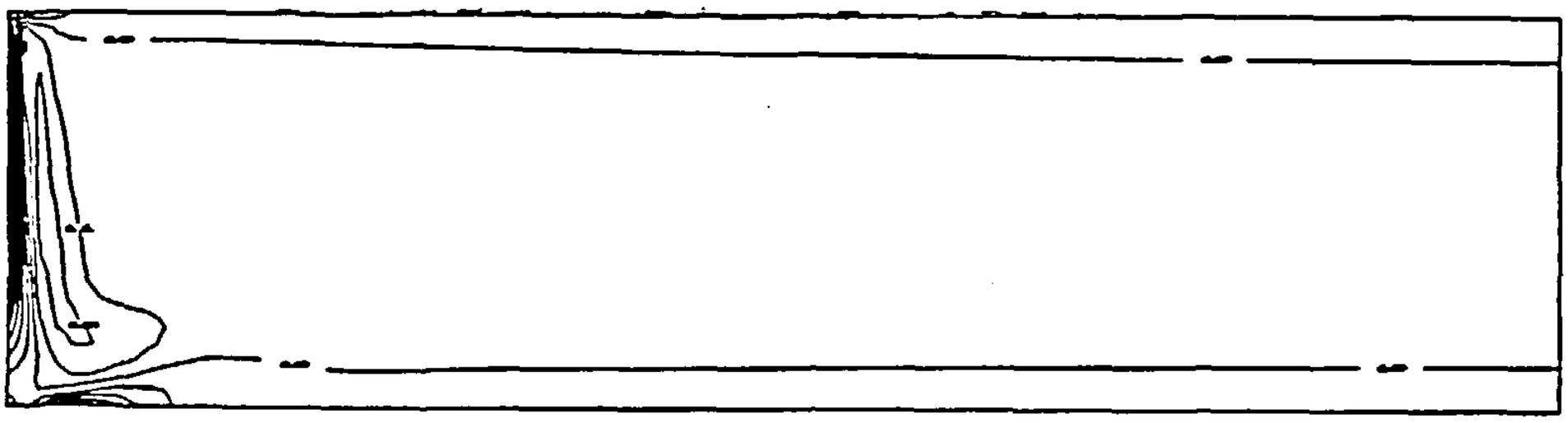

CONTOUR KEY	
1	-8142.757583
2	-7272.706311
3	-6402.655039
4	-5532.603767
5	-4662.552495
6	-3792.501223
7	-2922.449952
8	-2052.398680
9	-1182.347408
10	-312.296136
11	557.755136
12	1427.806408

(b)

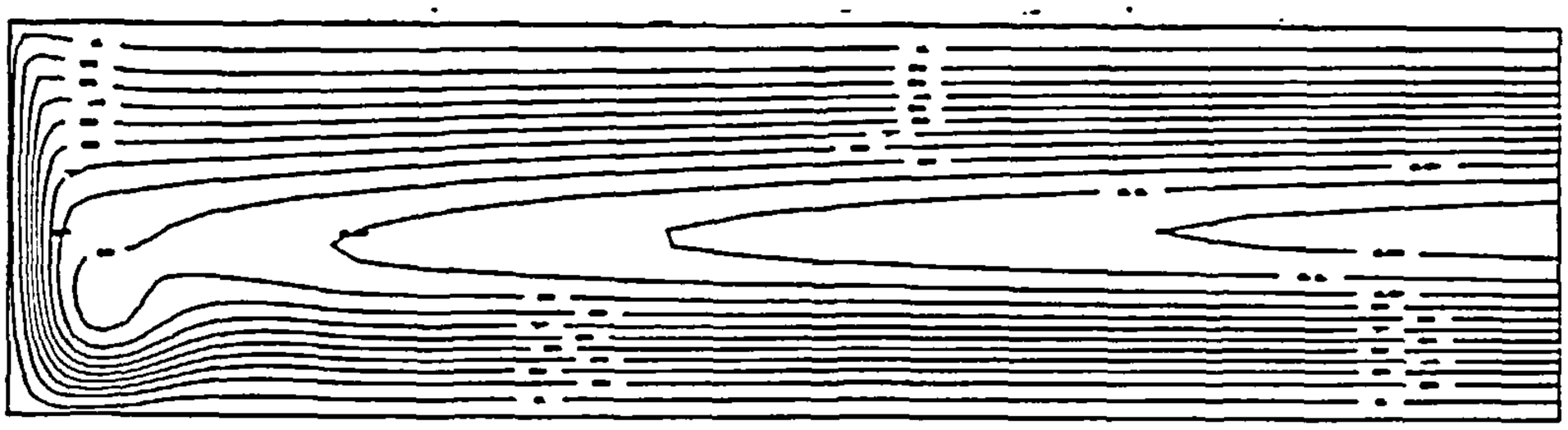

CONTOUR KEY	
1	1.030884
2	3.092651
3	5.154419
4	7.216186
5	9.277953
6	11.339721
7	13.401488
8	15.463256
9	17.525023
10	19.586790
11	21.648558
12	23.710325

(a)

Figure 6.14: Contours of the steady-state solution for (a) stream function , (b) vorticity, (c) temperature, for $\sigma = 0.733$ and $R_1 = 10000$, using a 175×25 computational grid with $x_\infty = 7$.

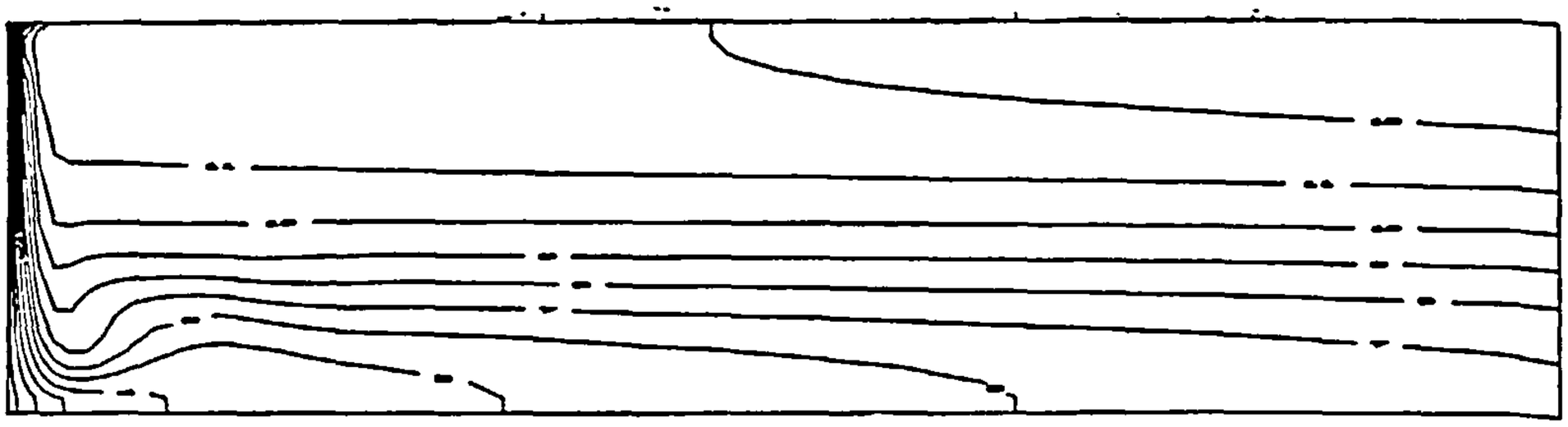

CONTOUR KEY	
1	2.276628
2	6.829883
3	11.383139
4	15.936394
5	20.489649
6	25.042905
7	29.596160
8	34.149416
9	38.702671
10	43.255926
11	47.809182
12	52.362437

(c)

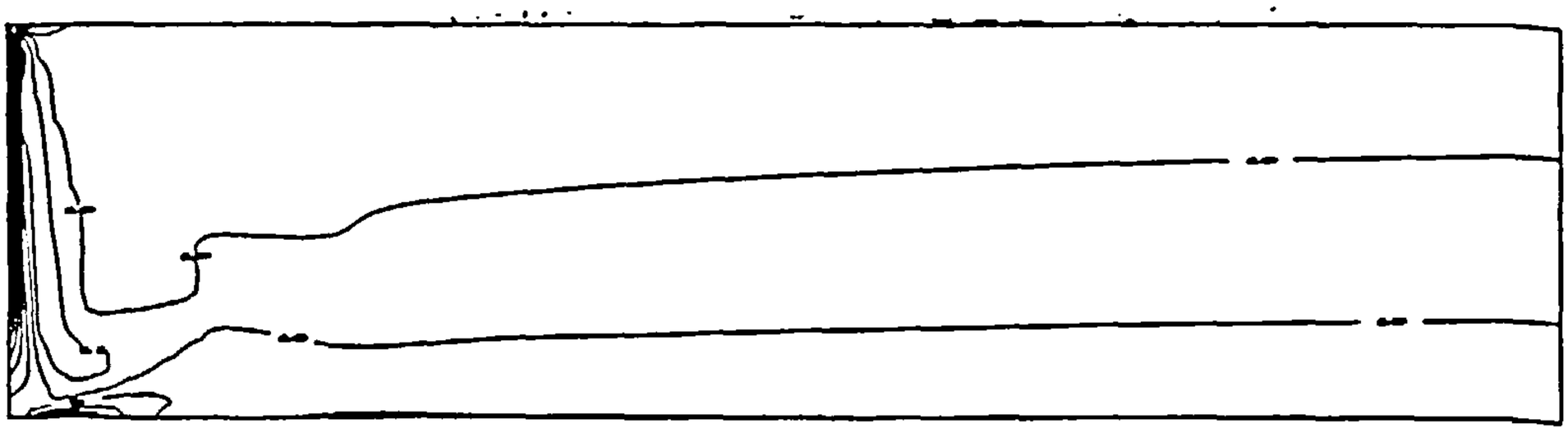

CONTOUR KEY	
1	-16191.362921
2	-14361.175530
3	-12530.988138
4	-10700.800747
5	-8870.613355
6	-7040.425964
7	-5210.238572
8	-3380.051181
9	-1549.863789
10	280.323602
11	2110.510994
12	3940.698385

(b)

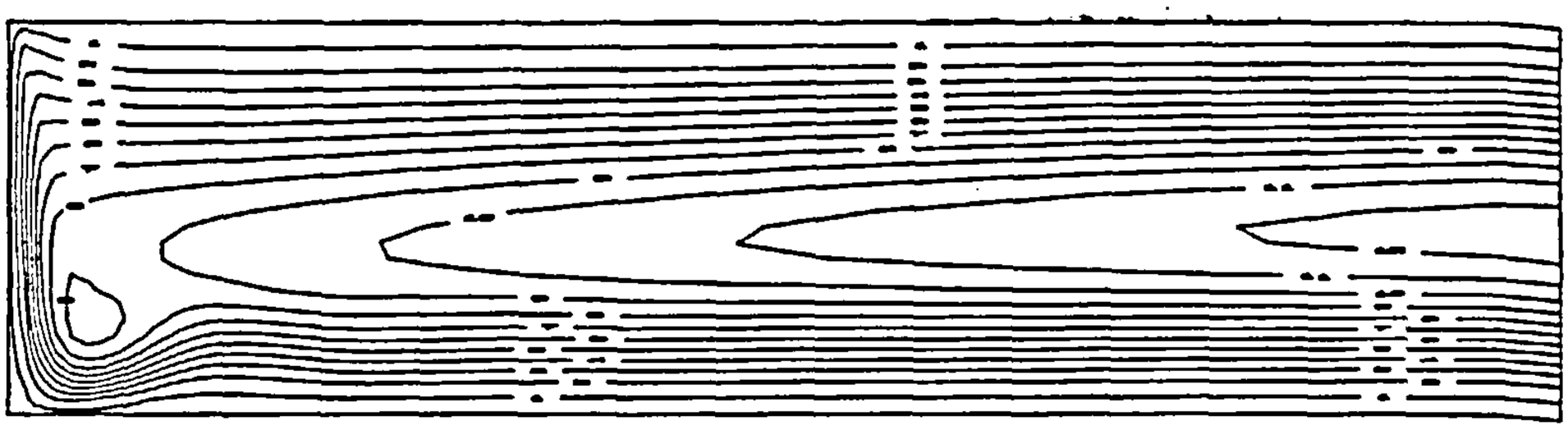

CONTOUR KEY	
1	1.405267
2	4.215800
3	7.026334
4	9.836868
5	12.647401
6	15.457935
7	18.268469
8	21.079002
9	23.889536
10	26.700070
11	29.510603
12	32.321137

(a)

Figure 6.15: Contours of the steady-state solution for (a) stream function , (b) vorticity, (c) temperature, for $\sigma = 0.733$ and $R_1 = 14000$, using a 175×25 computational grid with $x_\infty = 7$.

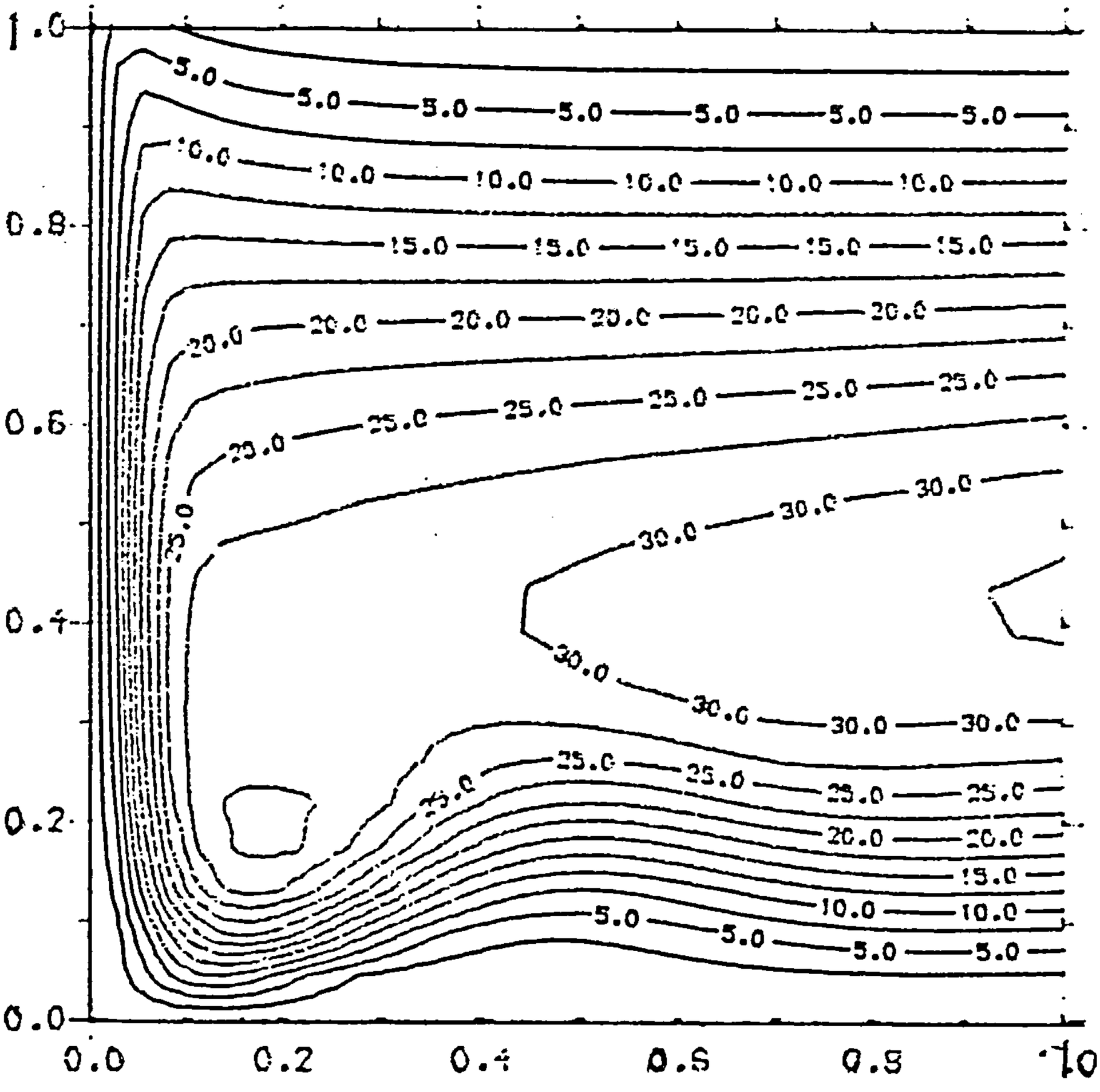

Figure 6.16: Contours of stream function with $\sigma = 0.733$, $R_1 = 20000$ near the cold wall of the cavity for the insulating case.

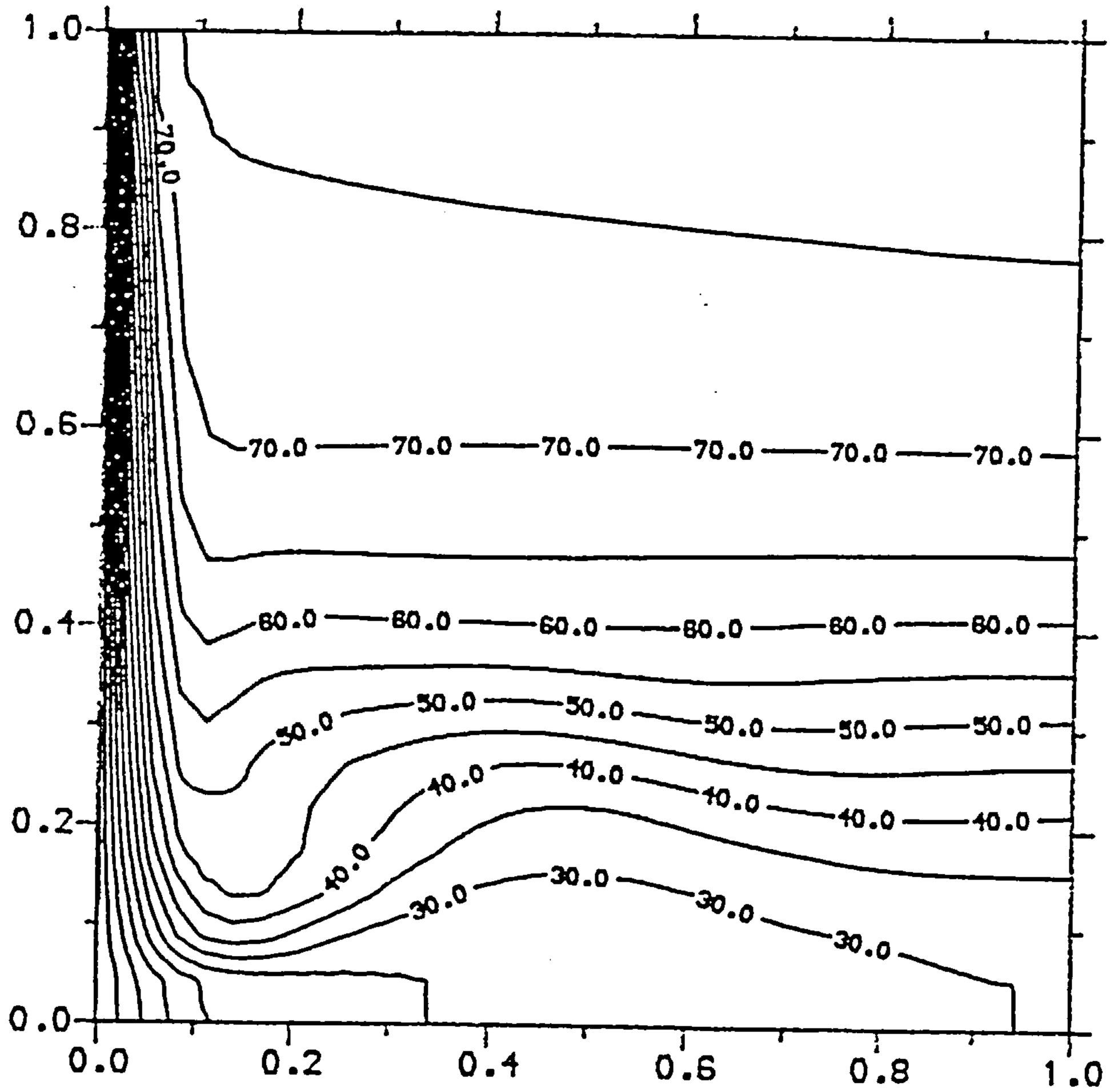

Figure 6.17: Contours of temperature with $\sigma = 0.733$, $R_1 = 20000$ near the cold wall of the cavity for the insulating case.

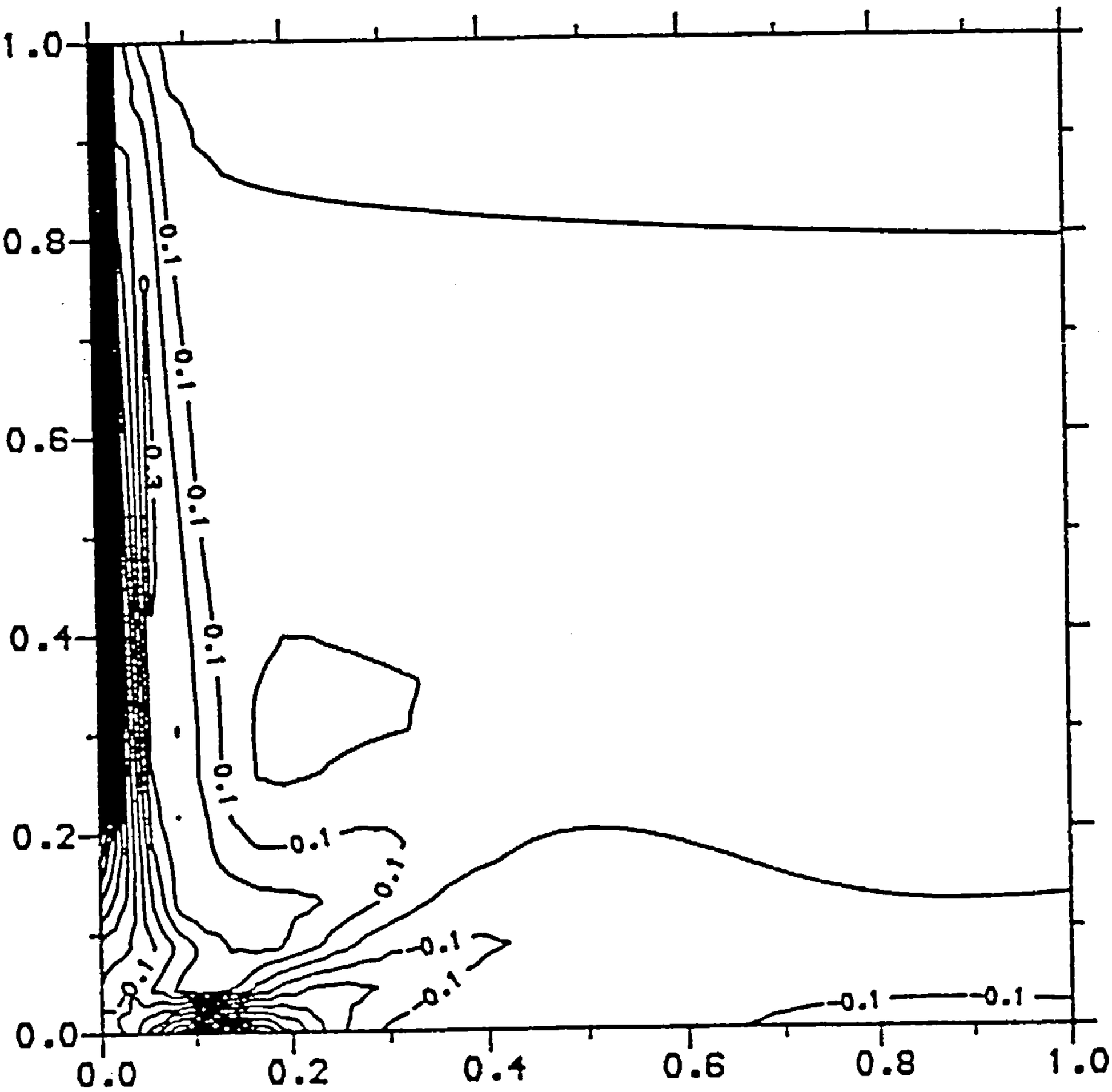

Figure 6.18: Contours of vorticity with $\sigma = 0.733$, $R_1 = 20000$ near the cold wall of the cavity for the insulating case.

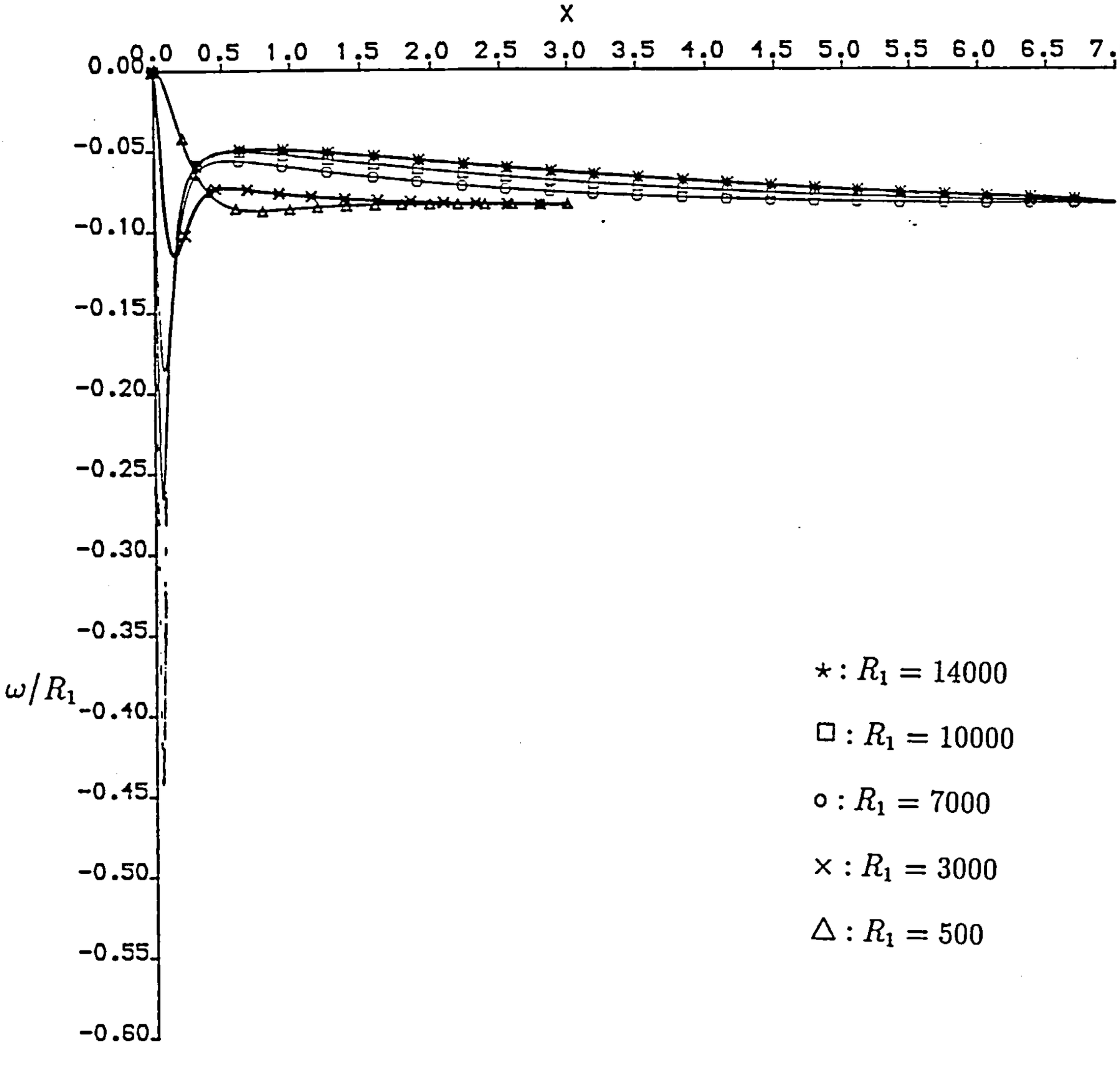

Figure 6.19: The skin friction ω/R_1 with $\sigma = 0.733$ for different Rayleigh numbers on the top wall for the insulating case.

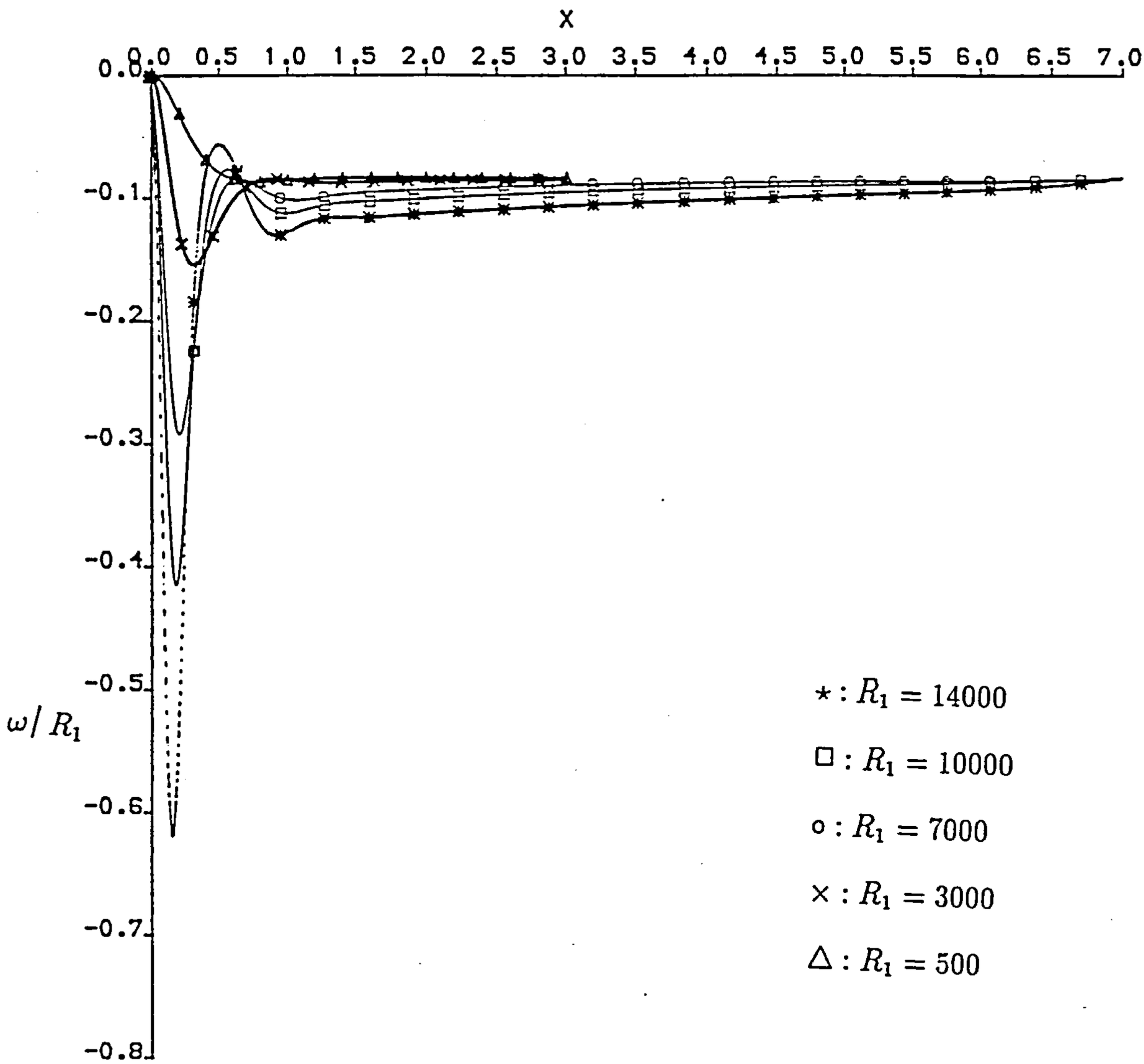

Figure 6.20: The skin friction ω/R_1 with $\sigma = 0.733$ for different Rayleigh numbers on the bottom wall for the insulating case.

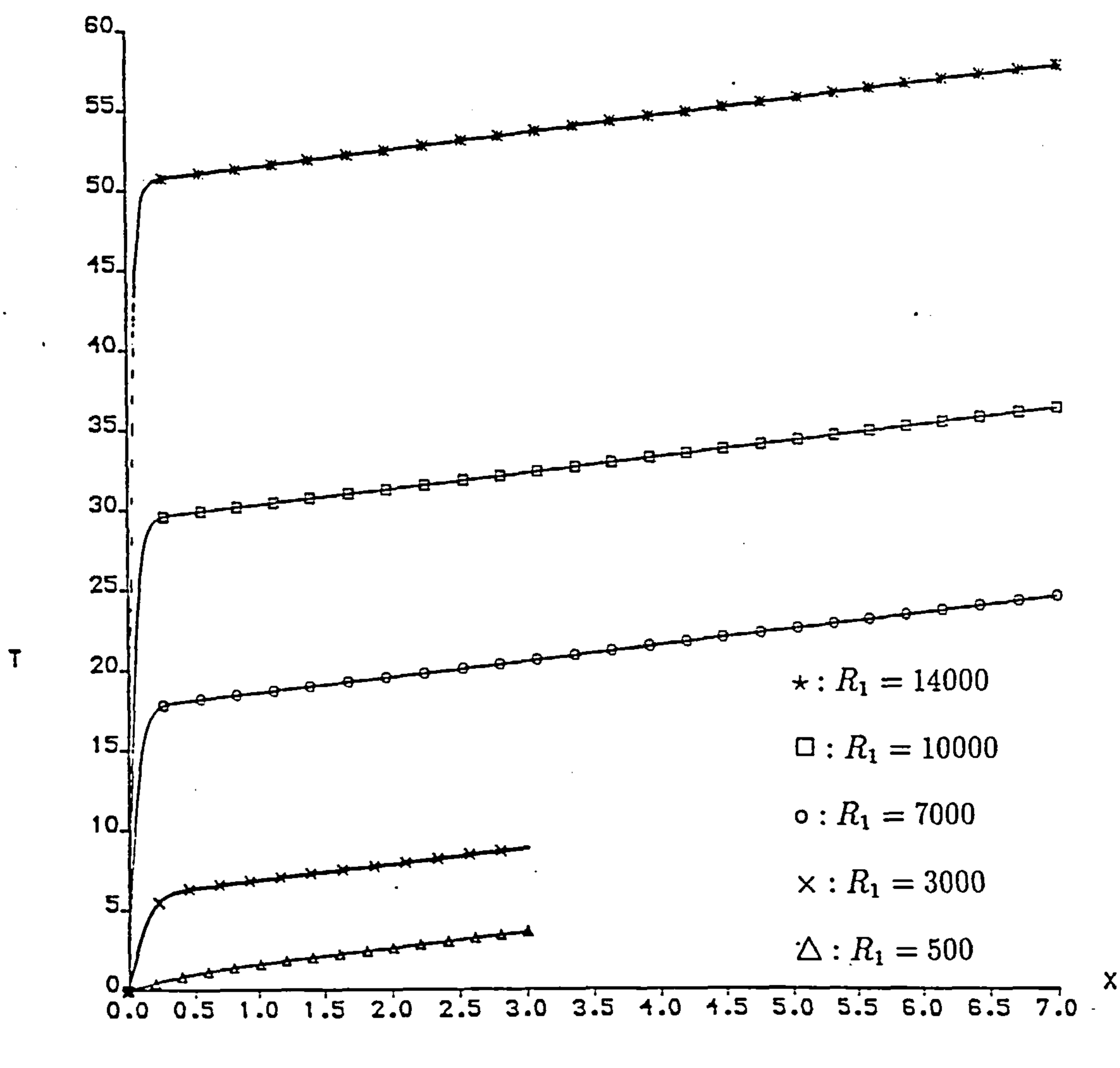

Figure 6.21: The temperature with $\sigma = 0.733$ for different Rayleigh numbers on the top wall for the insulating case.

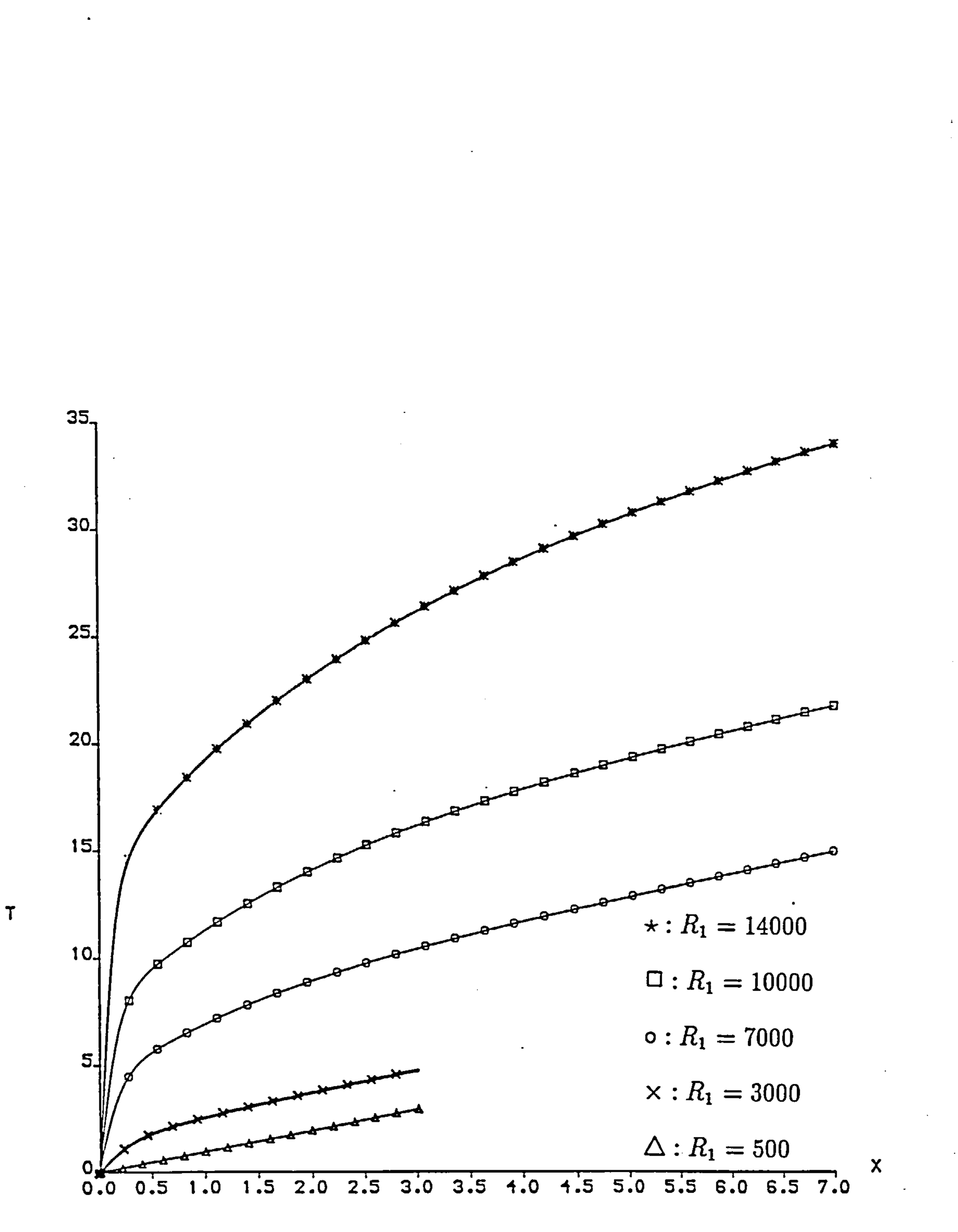

Figure 6.22: The temperature with $\sigma = 0.733$ for different Rayleigh numbers on the bottom wall for the insulating case.

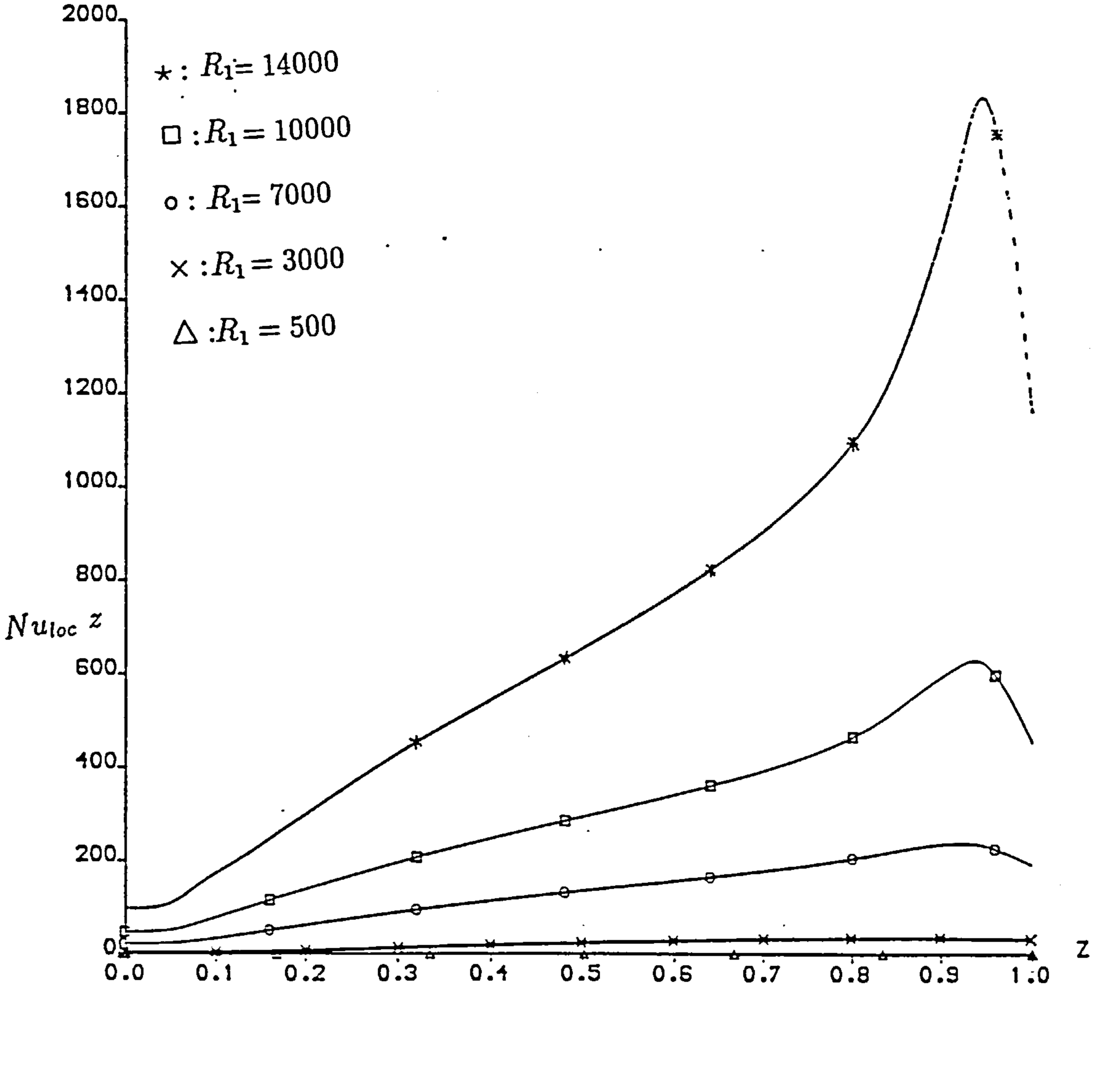

Figure 6.23: The local Nusselt number with $\sigma = 0.733$ for different Rayleigh numbers on the cold wall for the insulating case.

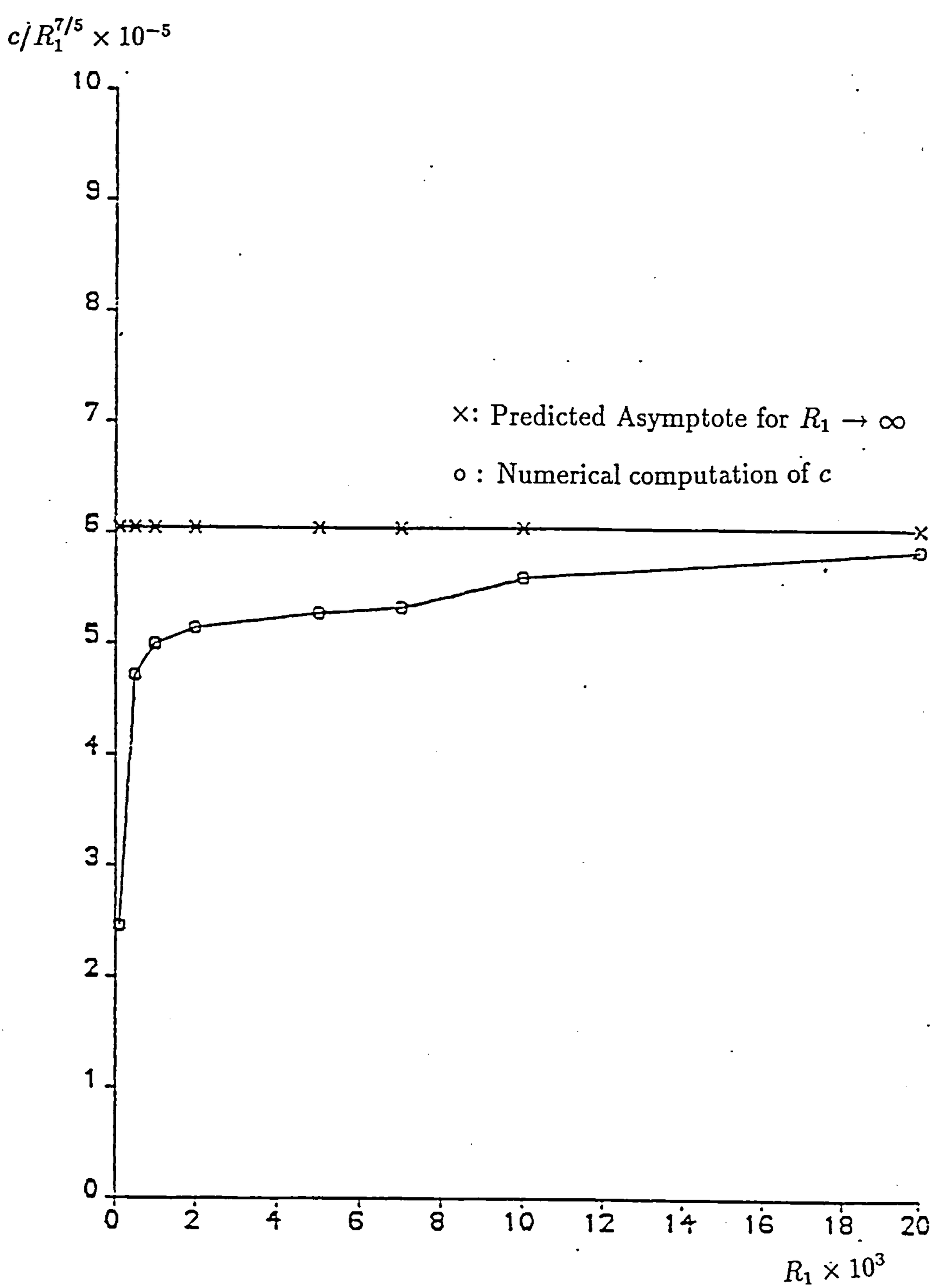

Figure 6.24: The numerical computation of c for $\sigma = 0.733$ and the asymptote predicted by boundary-layer theory.

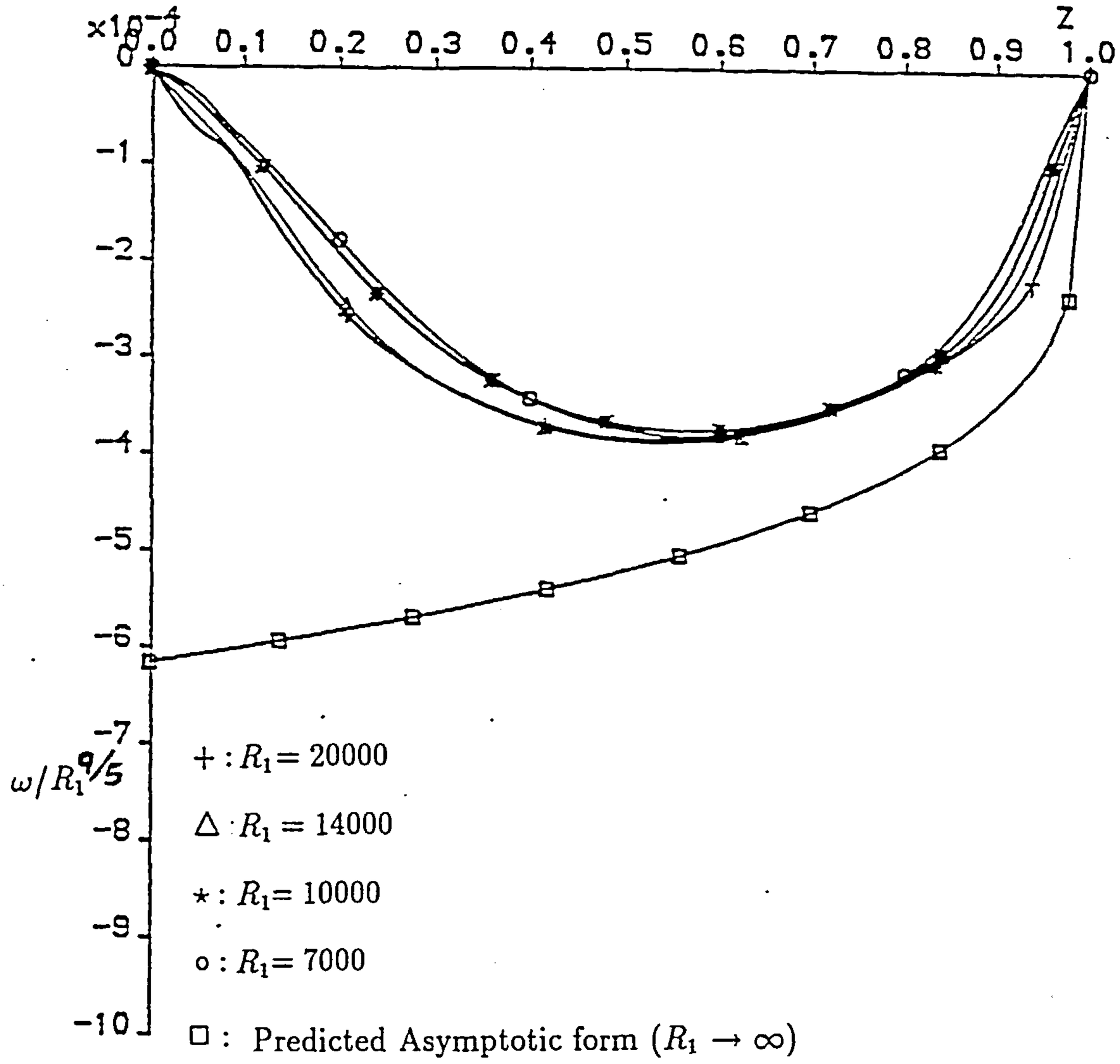

Figure 6.25: The numerical computation of the skin friction on the cold wall, showing $\omega/R_1^{9/5}$ for $\sigma = 0.733$ and the asymptotic form for $R_1 \to \infty$ predicted by (6.6.3).

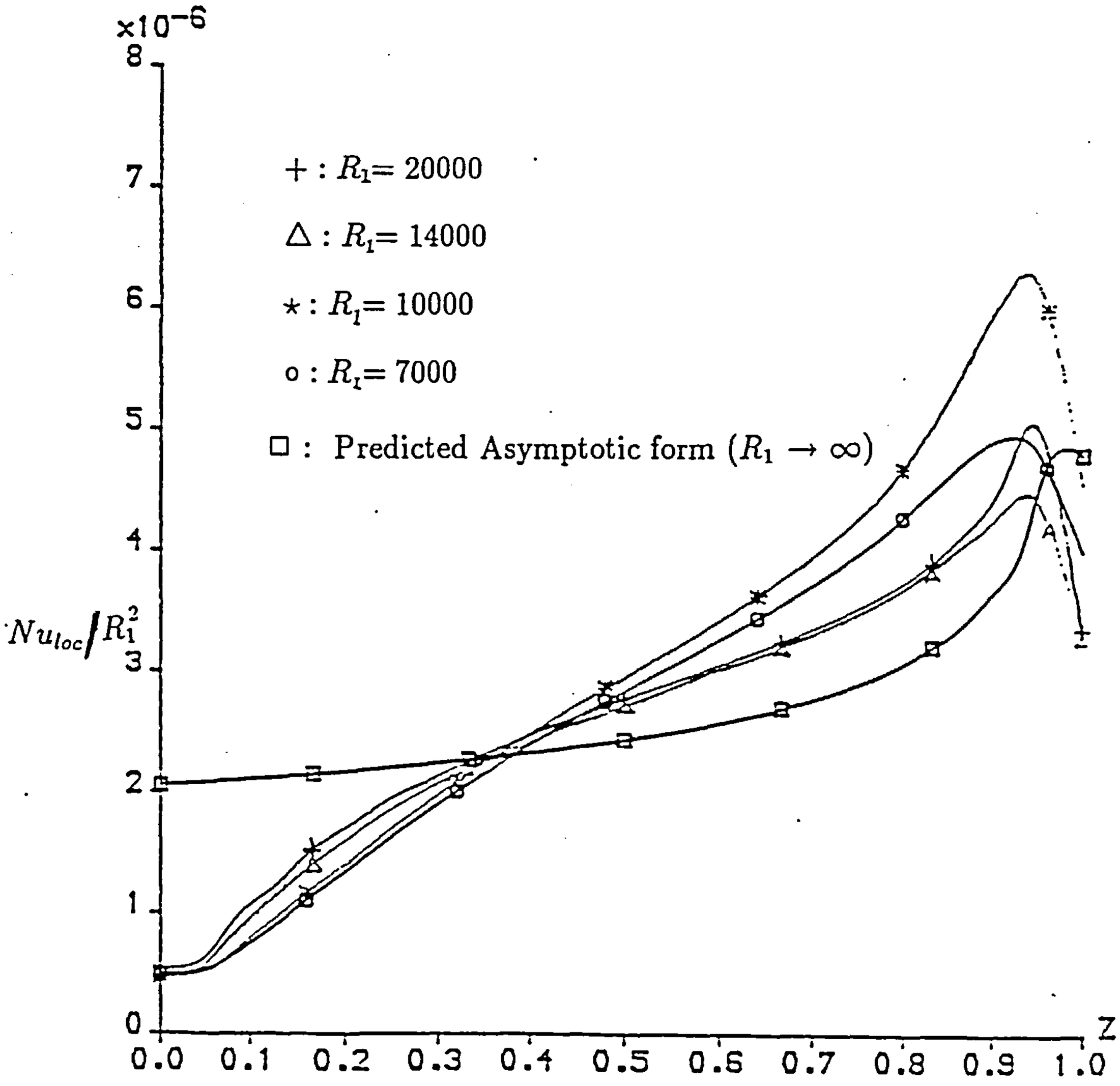

Figure 6.26: The numerical computation of the local Nusselt number on the cold wall, showing Nu_{loc}/R_1^2 for $\sigma = 0.733$ and the asymptotic form predicted by (6.6.3).

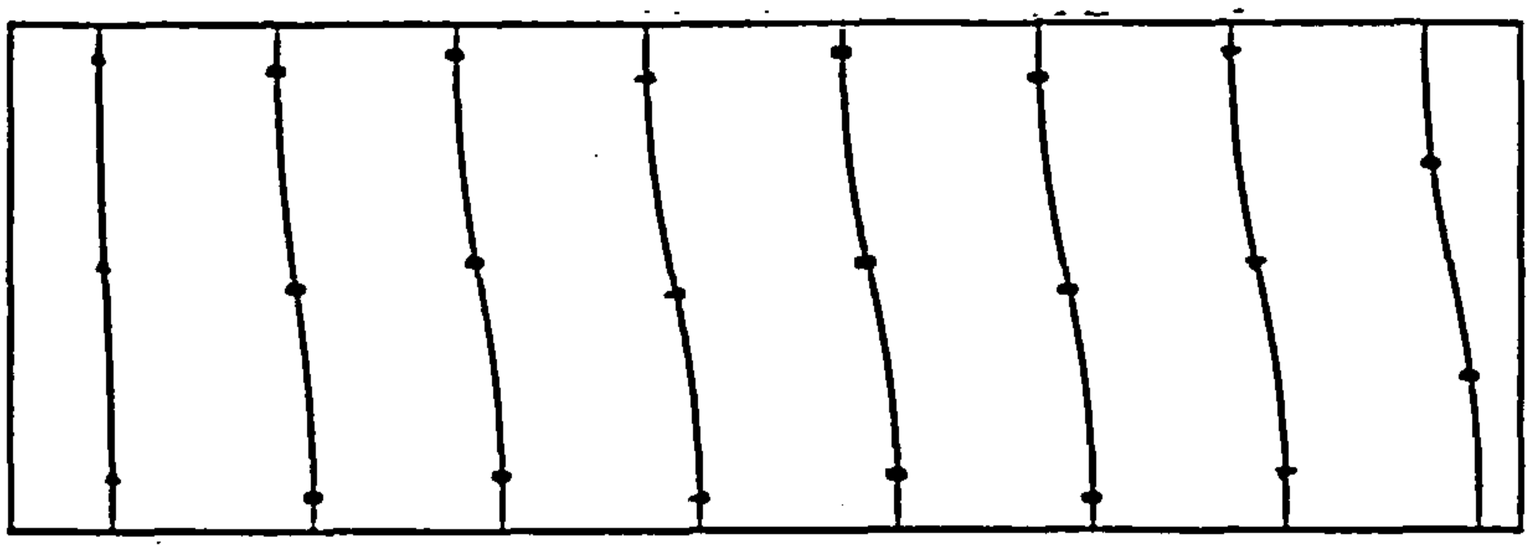

CONTOUR KEY	
1	0.1907926
2	0.5723777
3	0.9539628
4	1.3355479
5	1.7171331
6	2.0987182
7	2.4803033
8	2.8618884

(c)

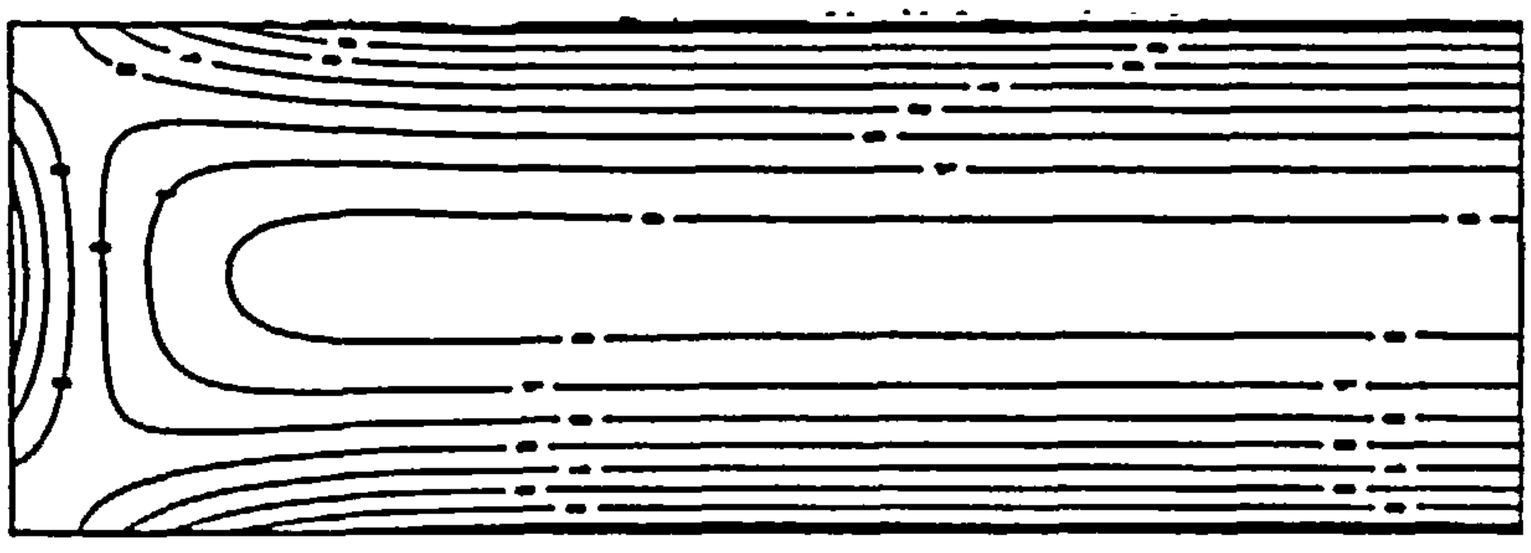

CONTOUR KEY	
1	-7.5906084
2	-6.0079813
3	-4.4253542
4	-2.8427271
5	-1.2600999
6	0.3225272
7	1.9051543
8	3.4877814

(b)

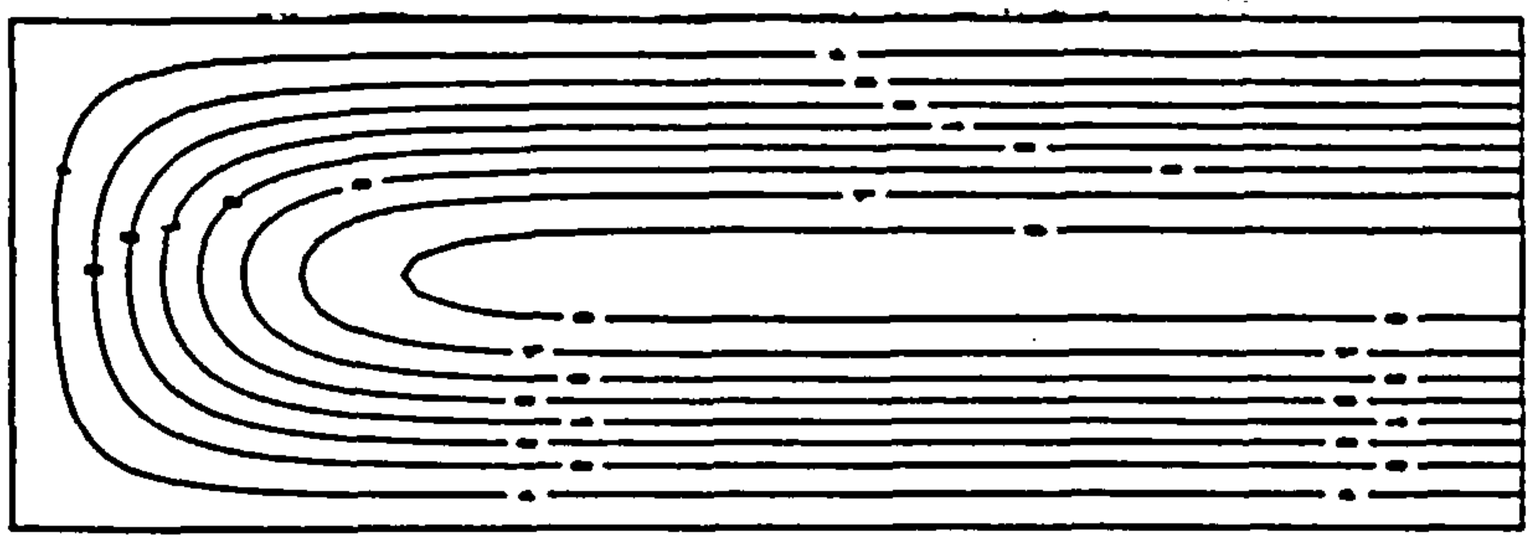

CONTOUR KEY	
1	0.0163120
2	0.0489360
3	0.0815600
4	0.1141840
5	0.1468080
6	0.1794320
7	0.2120560
8	0.2446800

(a)

Figure 6.27: Contours of the steady-state solution for (a) stream function , (b) vorticity, (c) temperature, for $\sigma = 6.983$ and $R_1 = 100$, using a 90×30 computational grid with $x_\infty = 3$.

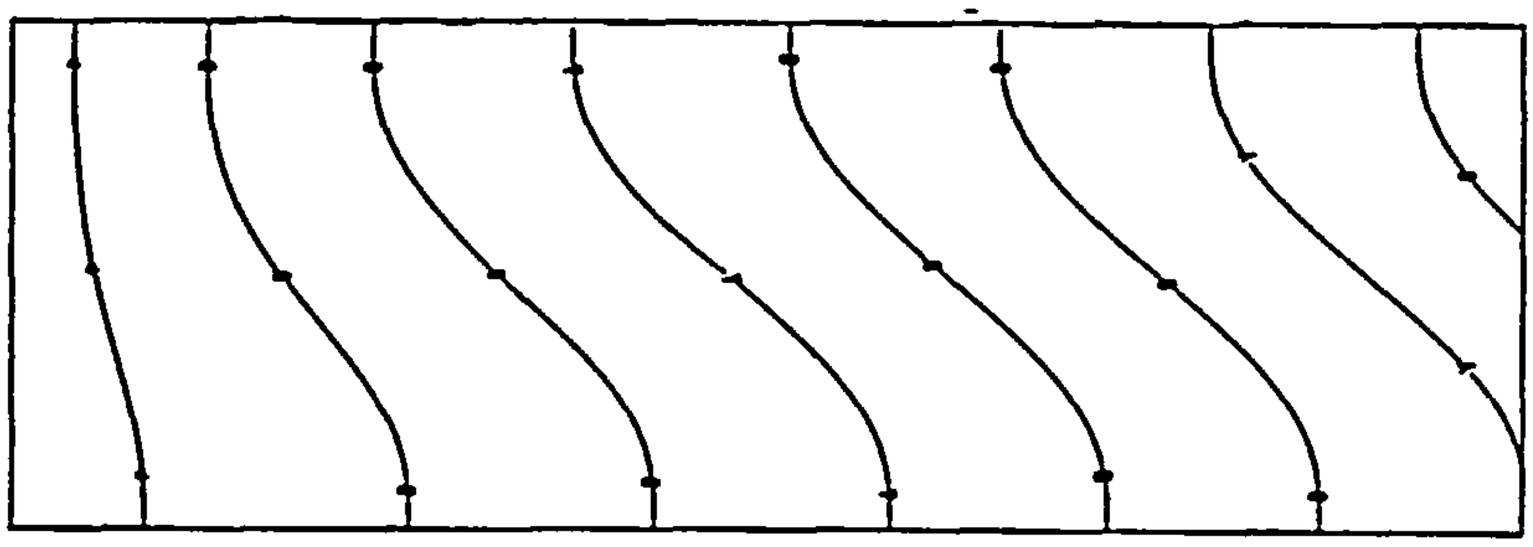

CONTOUR KEY	
1	0.2074567
2	0.6223701
3	1.0372834
4	1.4521968
5	1.8671102
6	2.2820236
7	2.6969369
8	3.1118503

(c)

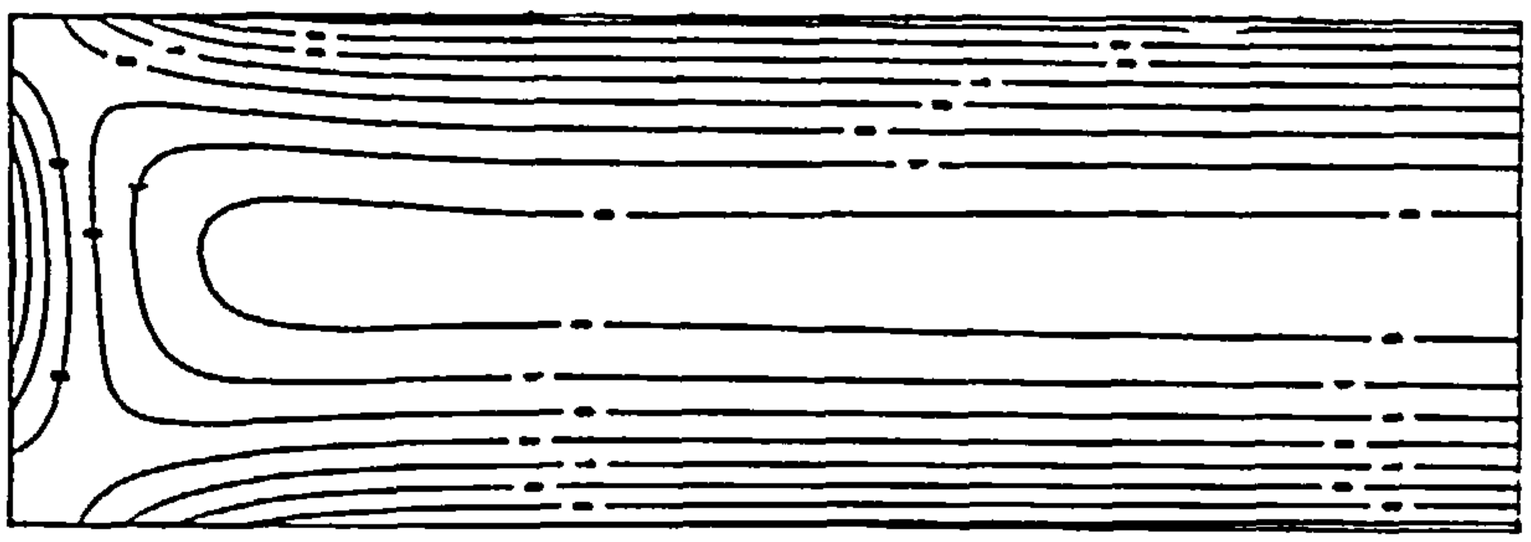

CONTOUR KEY	
1	-37.7871123
2	-29.9710529
3	-22.1549936
4	-14.3389342
5	-6.5228748
6	1.2931846
7	9.1092439
8	16.9253033

(b)

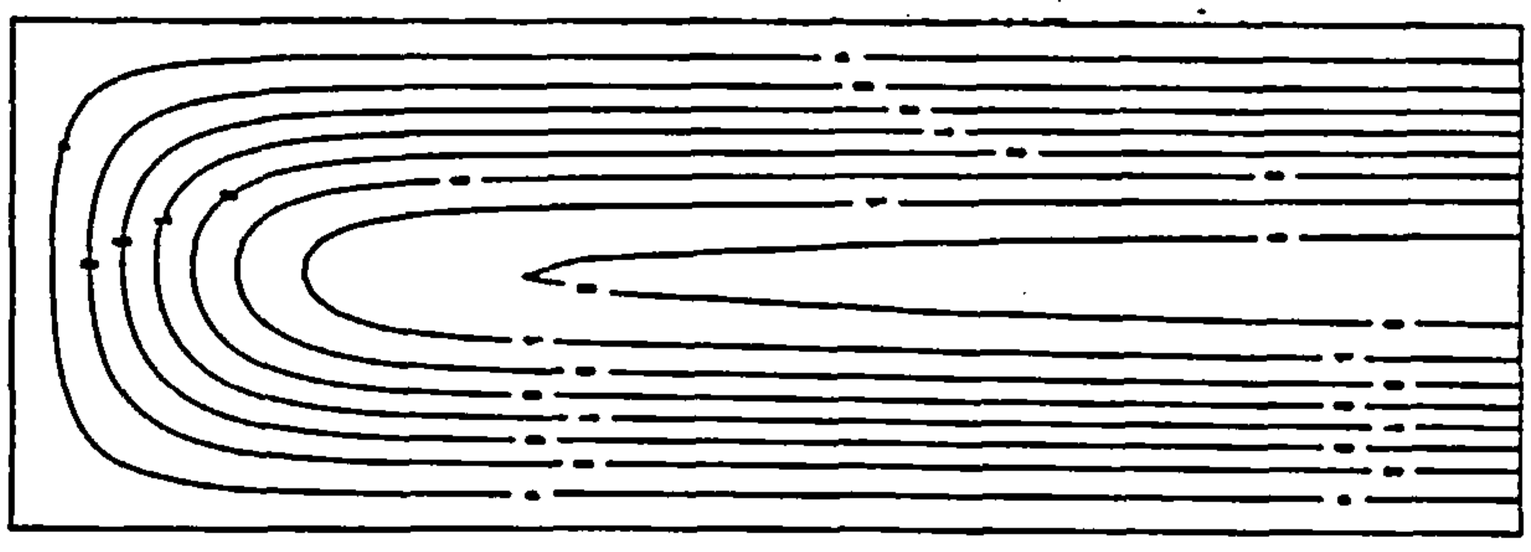

CONTOUR KEY	
1	0.0813802
2	0.2441406
3	0.4069009
4	0.5696613
5	0.7324217
6	0.8951821
7	1.0579424
8	1.2207028

(a)

Figure 6.28: Contours of the steady-state solution for (a) stream function , (b) vorticity, (c) temperature, for $\sigma = 6.983$ and $R_1 = 500$, using a 90×30 computational grid with $x_\infty = 3$.

Chapter 7

Time-Dependent Thermally-Driven Shallow Cavity Flows

7.1 Introduction

In previous chapters, we have discussed the steady-state form of thermally-driven slender cavity flows. In this chapter the evolution of the flow structure with time is considered for shallow cavity flows with insulated boundaries. New theoretical and numerical solutions are found by analytical and computational methods, and are discussed in the light of the steady-state solutions found in Chapter 6.

The problem is formulated in Section 7.2. Sections 7.3-7.5 are concerned with analytical properties of the time-dependent flow starting from an initial configuration in which the fluid is at rest with a linear, conductive temperature profile across the cavity and for which $R_1 = R/L = O(1)$. The evolution of the flow is found to occur on two main scales, $t = O(1)$, and $t = O(L^2)$ where L is the aspect ratio of the cavity, assumed large. The main core flow develops on the time scale $t = O(1)$ and

is discussed in Section 7.3 and this in turn generates flow in roughly square zones near each end of the cavity. The solutions there for the time scale $t = O(1)$ are discussed in Section 7.4 , with particular emphasis on the structure which emerges as $t \to \infty$. In general a numerical solution is required and results are obtained, using the previously developed time-stepping code,in Section 7.5. The end zone behaviour as $t \to \infty$ creates a reaction in the core region which then adjusts on a long time scale $t = O(L^2)$ considered in Section 7.6 and which ultimately leads to the type of steady-state solution found in Chapter 6. Finally, Section 7.7 considers more general initial configurations and the analytical and numerical results of the previous sections are extended to include these.

7.2 Formulation

Time-dependent flow in a cavity $0 \leq x \leq L, 0 \leq z \leq 1$ is governed by the non-dimensional equations

$$\frac{\partial \bar{u}}{\partial x} + \frac{\partial \bar{w}}{\partial z} = 0, \tag{7.2.1}$$

$$\frac{1}{\sigma}\left(\frac{\partial \bar{u}}{\partial t} + \bar{u}\frac{\partial \bar{u}}{\partial x} + \bar{w}\frac{\partial \bar{u}}{\partial z}\right) = -\frac{\partial \bar{p}}{\partial x} + \nabla^2 \bar{u}, \tag{7.2.2}$$

$$\frac{1}{\sigma}\left(\frac{\partial \bar{w}}{\partial t} + \bar{u}\frac{\partial \bar{w}}{\partial x} + \bar{w}\frac{\partial \bar{w}}{\partial z}\right) = -\frac{\partial \bar{p}}{\partial z} + \nabla^2 \bar{w} + R\,\bar{T}, \tag{7.2.3}$$

$$\frac{\partial \bar{T}}{\partial t} + \bar{u}\frac{\partial \bar{T}}{\partial x} + \bar{w}\frac{\partial \bar{T}}{\partial z} = \nabla^2 \bar{T}. \tag{7.2.4}$$

The rigid end walls are maintained at fixed temperatures while the horizontal boundaries are assumed to be insulating, equivalent to the boundary conditions

$$\bar{\psi} = \frac{\partial \psi}{\partial x} = \bar{T} = 0 \quad (x = 0), \tag{7.2.5}$$

$$\bar{\psi} = \frac{\partial \bar{\psi}}{\partial x} = 0, \quad \bar{T} = 1 \quad (x = L), \tag{7.2.6}$$

$$\bar{\psi} = \frac{\partial \bar{\psi}}{\partial z} = \frac{\partial \bar{T}}{\partial z} = 0 \quad (z = 0, 1). \tag{7.2.7}$$

In Sections 7.3-7.6 of this chapter the evolution of the flow is considered, starting from an initial state

$$\bar{T} = x/L, \quad \bar{u} = \bar{w} = 0, \quad (t = 0) \tag{7.2.8}$$

throughout the cavity. Because this state is centrosymmetric, the time- dependent motion which ensues can also be assumed centro-symmetric,

$$\bar{T}(x, z, t) = 1 - \bar{T}(L - x, 1 - z, t), \tag{7.2.9}$$

$$\bar{\psi}(x, z, t) = \bar{\psi}(L - x, 1 - z, t), \tag{7.2.10}$$

allowing only half of the flow domain to be considered. It will also be assumed that the Rayleigh number and aspect ratio are such that $R_1 = R/L = O(1)$.

7.3 Core Solution for $t = O(1)$

In the core region away from the end walls, it is appropriate to use as independent variables,

$$\xi = x/L, \quad z = z$$

as in the steady-state solution of Chapter 6. In the limit as $L \to \infty$

$$\bar{T} = \xi + L^{-1} T_1(\xi, z, t) + \cdots, \tag{7.3.1}$$

$$\bar{\psi} = \psi_1(\xi, z, t) + \cdots, \tag{7.3.2}$$

$$\bar{u} = u_1(\xi, z, t) + \cdots, \tag{7.3.3}$$

$$\bar{p} = \xi R_1 L z + LP(\xi, t) + p_1(\xi, z, t) + \cdots, \tag{7.3.4}$$

with the leading terms in the temperature and pressure reflecting the fact that the initial temperature profile is given by (7.2.8). This generates a flow field $\bar{\psi}$ of order one as $L \to \infty$.

Substitution into (7.2.1) — (7.2.4) gives

$$\frac{1}{\sigma}\frac{\partial u_1}{\partial t} = -R_1 z + \frac{\partial^2 u_1}{\partial z^2} - \frac{\partial P}{\partial \xi} \quad , \tag{7.3.5}$$

$$0 = -\frac{\partial p_1}{\partial z} + R_1 T_1 \quad , \tag{7.3.6}$$

$$\frac{\partial T_1}{\partial t} + u_1 = \frac{\partial^2 T_1}{\partial z^2} \quad . \tag{7.3.7}$$

Thus the stream function ψ_1 satisfies the system

$$\frac{1}{\sigma}\frac{\partial^2 \psi_1}{\partial z \partial t} = -R_1 z + \frac{\partial^3 \psi_1}{\partial z^3} - \frac{\partial P}{\partial \xi} \quad , \tag{7.3.8}$$

$$\psi_1 = \frac{\partial \psi_1}{\partial z} = 0 \quad (z = 0, 1) \quad , \tag{7.3.9}$$

$$\psi_1 = 0 \quad (t = 0) \quad . \tag{7.3.10}$$

It may be assumed that in the core a parallel flow is generated independent of ξ and (by centrosymmetry) such that ψ_1 is an even function of z. This indicates that $P = p_0 \xi$, where $p_0 = -\frac{1}{2} R_1$, so that

$$\frac{1}{\sigma}\frac{\partial^2 \psi_1}{\partial z \partial t} = -R_1 (z - \frac{1}{2}) + \frac{\partial^3 \psi_1}{\partial z^3} \tag{7.3.11}$$

and then $u_1 = \partial \psi_1 / \partial z$ satisfies

$$\frac{1}{\sigma}\frac{\partial u_1}{\partial t} = -R_1 (z - \frac{1}{2}) + \frac{\partial^2 u_1}{\partial z^2} \quad , \tag{7.3.12}$$

with

$$u_1 = 0 \quad (z = 0, 1),$$

$$u_1 = 0 \quad (t = 0).$$

Thus

$$u_1 = R_1 \left(\frac{z^3}{6} - \frac{z^2}{4} + \frac{z}{12} \right) + R_1 U(z, t), \tag{7.3.13}$$

where U satisfies the system

$$\frac{1}{\sigma}\frac{\partial U}{\partial t} = \frac{\partial^2 U}{\partial z^2} \quad , \tag{7.3.14}$$

$$U = 0 \quad (z = 0, 1) \quad , \tag{7.3.15}$$

$$U = \left(-\frac{z^3}{6} + \frac{z^2}{4} - \frac{z}{12} \right), \quad (t = 0) \quad . \tag{7.3.16}$$

The solution of (7.3.14) – (7.3.16) is

$$U(z, t) = -\sum_{n=1}^{\infty} \frac{1}{4n^3 \pi^3} e^{-4n^2 \pi^2 \sigma t} \sin(2n\pi z), \tag{7.3.17}$$

so that

$$u_1 = R_1\left(\frac{z^3}{6} - \frac{z^2}{4} + \frac{z}{12}\right) - R_1\sum_{n=1}^{\infty}\frac{1}{4n^3\pi^3}e^{-4n^2\pi^2\sigma t}\sin(2n\pi z) \tag{7.3.18}$$

and

$$\psi_1 = \int_0^z u_1 dz = R_1\tilde{F}(z,t), \tag{7.3.19}$$

where

$$\tilde{F}(z,t) = \frac{z^2}{24}(1-z)^2 + \sum_{n=1}^{\infty}\frac{e^{-4n^2\pi^2\sigma t}}{8(n\pi)^4}(\cos(2n\pi z) - 1) \quad . \tag{7.3.20}$$

The energy equation (7.3.7) can be solved by setting $T_1 = R_1\tilde{G}(z,t)$ so that $\tilde{G}$ satisfies

$$\frac{\partial\tilde{G}}{\partial t} - \frac{\partial^2\tilde{G}}{\partial z^2} = -\frac{\partial\tilde{F}}{\partial z} \quad , \tag{7.3.21}$$

$$\frac{\partial\tilde{G}}{\partial z} = 0 \quad (z = 0,1) \quad , \tag{7.3.22}$$

$$\tilde{G} = 0 \quad (t = 0) \quad . \tag{7.3.23}$$

The solution of (7.3.21) — (7.3.23) can be written in the form

$$\tilde{G} = G(z) + \sum_{n=1}^{\infty} g_n(z)e^{-4n^2\pi^2\sigma t} + G_1(z,t) \tag{7.3.24}$$

where the first and second terms are particular solutions generated by the two parts of $\tilde{F}$,

$$G = \frac{z^5}{120} - \frac{z^4}{48} + \frac{z^3}{72} - \frac{1}{1440} \tag{7.3.25}$$

and

$$g_n'' + 4n^2\pi^2\sigma g_n = -\frac{1}{4n^3\pi^3}\sin(2n\pi z), \tag{7.3.26}$$

$$g_n' = 0 \quad (z = 0,1). \tag{7.3.27}$$

The solution for $g_n(z)$ is

$$g_n(z) = \frac{1}{16n^5\pi^5(\sigma-1)}\left(\frac{\sin(2n\pi\sqrt{\sigma}(z-\frac{1}{2}))}{\sqrt{\sigma}\cos(n\pi\sqrt{\sigma})} - \sin(2n\pi z)\right). \tag{7.3.28}$$

Finally, the complementary solution G_1 must satisfy

$$\frac{\partial G_1}{\partial t} = \frac{\partial^2 G_1}{\partial z^2} \tag{7.3.29}$$

$$\frac{\partial G_1}{\partial z} = 0 \qquad (z = 0, 1) \tag{7.3.30}$$

$$G_1 = -G - \sum_{n=1}^{\infty} g_n \quad (t = 0) \tag{7.3.31}$$

so that

$$G_1 = \sum_{k=1}^{\infty} A_k e^{-k^2\pi^2 t} \cos k\pi z \tag{7.3.32}$$

where A_k is determined by the initial condition (7.3.22) as

$$A_k = -2\int_0^1 G(z)\cos(k\pi z)dz - 2\sum_{n=1}^{\infty}\int_0^1 g_n(z)\cos(k\pi z)dz \tag{7.3.33}$$

which in general gives

$$A_k = 0 \quad (k \quad \text{even}) \tag{7.3.34}$$

$$= -\frac{4}{k^6\pi^6}\left(\frac{k^2\pi^2}{12} - 1\right) + \frac{1}{16\pi^6(1-\sigma)}\sum_{m=1}^{\infty}\frac{1}{m^4(4m^2\sigma - k^2)} \quad (k \quad \text{odd}) \tag{7.3.35}$$

In summary, the solution in the core region for $t = O(1)$ can be written as

$$\left.\begin{aligned} \bar{T} &= \xi + L^{-1}R_1\tilde{G}(z,t) + O(L^{-2}) \\ \bar{\psi} &= R_1\tilde{F}(z,t) + O(L^{-1}) \end{aligned}\right\} \tag{7.3.36}$$

where

$$\begin{aligned} \tilde{G}(z,t) &= G(z) + \sum_{n=1}^{\infty} g_n(z)e^{-4n^2\pi^2\sigma t} + \sum_{n=0}^{\infty} A_{2n+1}e^{-(2n+1)^2\pi^2 t}\cos((2n+1)\pi z), \\ \tilde{F}(z,t) &= F(z) + \sum_{n=1}^{\infty}\frac{e^{-4n^2\pi^2\sigma t}}{8(n\pi)^4}(\cos(2n\pi z) - 1) \end{aligned} \tag{7.3.37}$$

and

$$F(z) = \frac{1}{24}z^2(1-z)^2.$$

7.4 End Zone Problem for $t = O(1)$

At each end of the cavity the time-dependent core flow is turned in regions that are approximately square. The solution in the end zone at the cold wall may be expanded as

$$\left.\begin{aligned} \bar{T} &= L^{-1}T(x,z,t) + \cdots \quad , \\ \bar{\psi} &= \psi(x,z,t) + \cdots \end{aligned}\right\} \tag{7.4.1}$$

and after elimination of the pressure in (7.2.1) — (7.2.4) the flow is governed by

$$\frac{1}{\sigma}\left(\frac{\partial \nabla^2\psi}{\partial t} + \frac{\partial(\nabla^2\psi,\psi)}{\partial(x,z)}\right) = \nabla^4\psi - R_1\frac{\partial T}{\partial x} \quad , \tag{7.4.2}$$

$$\frac{\partial T}{\partial t} + \frac{\partial(T,\psi)}{\partial(x,z)} = \nabla^2 T \quad , \tag{7.4.3}$$

$$\psi = \frac{\partial\psi}{\partial x} = T = 0 \qquad \text{on} \quad x = 0 \quad , \tag{7.4.4}$$

$$\psi = \frac{\partial\psi}{\partial z} = \frac{\partial T}{\partial z} = 0 \qquad \text{on} \quad z = 0,1, \tag{7.4.5}$$

together with the requirement that the solution matches with that (7.3.36) in the core:

$$\left.\begin{aligned} T &\sim x + R_1 G(z,t) \\ \psi &\sim R_1 \tilde{F}(z,t) \end{aligned}\right\} \qquad (x \to \infty) \tag{7.4.6}$$

and with initial conditions

$$T = x, \qquad \psi = 0 \qquad (t = 0). \tag{7.4.7}$$

In general this system must be solved by a computational method, which is discussed in Section 7.5. Here we consider the form that the end-zone solution is likely to assume at large times t. As $t \to \infty$, we expect the solution to divide into two main regions

$x \sim 1$ $z \sim 1$	$x \sim t^{1/2}$ $z \sim 1$
I	II

where the inner region (I) is equivalent to the steady-state structure identified in Chapter 6. Thus in region I, we expect that as $t \to \infty$

$$\psi \sim \psi_0(x,z) + \cdots, \tag{7.4.8}$$

$$T \sim T_0(x,z) + \cdots, \tag{7.4.9}$$

where ψ_0, T_0 is the steady-state solution of Chapter 6, such that

$$\left.\begin{aligned} \psi_0 &\to R_1 F(z) \\ T_0 &\sim x + c + R_1 G(z) \end{aligned}\right\} \quad (x \to \infty) \tag{7.4.10}$$

and where c is the parameter found previously. This does not however satisfy the outer boundary condition (7.4.6), requiring the presence of the outer region II where $x \sim t^{1/2}$. This allows the solution to adjust to the form (7.4.6) at the edge of the end zone.

In region II, the solution can be obtained for large times in the form:

$$\left.\begin{aligned} \psi &= R_1 F(z) + t^{-1/2}\psi_1(z,\eta) + t^{-1}\psi_2(z,\eta) + \cdots \\ T &= x + R_1 G(z) + T_0(z,\eta) + t^{-1/2}T_1(z,\eta) + t^{-1}T_2(z,\eta) + \cdots \end{aligned}\right\} \quad (t \to \infty) \tag{7.4.11}$$

where $\eta = x/t^{1/2}$. Substitution into (7.4.2) - (7.4.3) and equating terms of like order in t yields a sequence of coupled equations for the unknown functions ψ_i and $T_{i-1}, i = 1, 2, \ldots$. Here we list these together with the relevant boundary conditions up to $O(t^{-1})$.

At $O(1)$

$$R_1 G'' + \frac{\partial^2 T_0}{\partial z^2} = R_1 F' \quad , \tag{7.4.12}$$

$$F'''' - 1 = 0 \quad . \tag{7.4.13}$$

This indicates that

$$\partial^2 T_0 / \partial z^2 = 0$$

and since

$$\partial T_0 / \partial z = 0 \quad \text{at} \quad z = 0 \quad \text{and} \quad z = 1$$

it follows that

$$T_0 = T_0(\eta) \tag{7.4.14}$$

At $O(t^{-1/2})$

$$\frac{\partial \psi_1}{\partial z} + R_1 F' \frac{dT_0}{d\eta} = \frac{\partial^2 T_1}{\partial z^2} \quad , \tag{7.4.15}$$

$$\frac{\partial^4 \psi_1}{\partial z^4} = R_1 \frac{dT_0}{d\eta}, \tag{7.4.16}$$

with

$$\psi_1 = \frac{\partial \psi_1}{\partial z} = \frac{\partial T_1}{\partial z} = 0 \quad (z = 0, 1), \tag{7.4.17}$$

so that

$$\psi_1 = \frac{dT_0}{d\eta} R_1 F, \tag{7.4.18}$$

$$T_1 = 2GR_1 \frac{dT_0}{d\eta} + \hat{T}_1(\eta), \tag{7.4.19}$$

where $\hat{T}_1$ is an unknown function of η.

At $O(t^{-1})$, T_2 satisfies

$$\frac{d^2 T_0}{d\eta^2} + \frac{\partial^2 T_2}{\partial z^2} = -\frac{1}{2}\eta \frac{dT_0}{d\eta} + \frac{\partial \psi_2}{\partial z} + \frac{dT_0}{d\eta}\frac{\partial \psi_1}{\partial z} + R_1 F' \frac{\partial T_1}{\partial \eta} - R_1 G' \frac{\partial \psi_1}{\partial \eta}, \tag{7.4.20}$$

$$\psi_2 = \frac{\partial \psi_2}{\partial z} = \frac{\partial T_2}{\partial z} = 0 \quad (z = 0, 1). \tag{7.4.21}$$

Substituting for ψ_1 and T_1 from (7.4.18)-(7.4.19) gives

$$\frac{d^2 T_0}{d\eta^2} + \frac{\partial^2 T_2}{\partial z^2} = -\frac{1}{2}\eta \frac{dT_0}{d\eta} + \frac{\partial \psi_2}{\partial z} + \frac{dT_0}{d\eta}\frac{\partial \psi_1}{\partial z} + 2R_1^2 F' G \frac{d^2 T_0}{d\eta^2} - R_1^2 G' F \frac{d^2 T_0}{d\eta^2} \tag{7.4.22}$$

and now integrating from $z = 0$ to $z = 1$ and using the conditions (7.4.17), (7.4.21) shows that T_0 satisfies the equation

$$(1 + 3R_1^2 Q_0)\frac{d^2 T_0}{d\eta^2} + \frac{1}{2}\eta \frac{dT_0}{d\eta} = 0, \tag{7.4.23}$$

where $Q_0 = \int_0^1 G'^2 dz = \frac{1}{362880}$. The solution must match with the inner behaviour (7.4.10) as $\eta \to 0$, requiring that

$$T_0 = c \quad \text{at} \quad \eta = 0 \quad , \tag{7.4.24}$$

and must be consistent with the outer boundary condition (7.4.6) as $\eta \to \infty$, equivalent to the requirement that

$$T_0 \to 0 \quad \text{as} \quad \eta \to \infty \quad . \tag{7.4.25}$$

The appropriate solution is therefore

$$T_0(\eta) = c - c\frac{2}{\sqrt{\pi}} \int_0^{\frac{\eta}{2(1+3R_1^2Q_0)^{1/2}}} e^{-u^2} du, \tag{7.4.26}$$

$$= c \quad erfc(\frac{\eta}{2(1+3R_1^2Q_0)^{1/2}}). \tag{7.4.27}$$

In summary, the solution in region II is expected to take the form

$$\psi \sim R_1 F(z) + O(t^{-1/2}), \tag{7.4.28}$$

$$T \sim x + R_1 G(z) + c \quad erfc(\frac{\eta}{2(1+3R_1^2Q_0)^{1/2}}), \tag{7.4.29}$$

at $t \to \infty$. Thus the end-zone spreads into the core on the scale $x \sim t^{1/2}$ as $t \to \infty$, eventually modifying the solution outlined in Section 7.3.

7.5 Numerical Solution of the End-Zone Problem for $t = O(1)$

In general, the end-zone problem (7.4.2)-(7.4.6) needs to be solved numerically. As the equations are the same as those of Chapter 6 , the same numerical method can be used, taking into account the new time-dependent outer behaviour (7.4.6) and the appropriate initial state (7.4.7). It was decided to obtain results for one of the cases considered in Chapter 6, namely

$$R_1 = 500, \quad \sigma = 0.733$$

and computations were carried out with an outer boundary $x_\infty = 60$. This large value is needed to encompass the spread of the solution with time, as identified in the previous section.

The computational results are presented using contours of temperature, vorticity and stream function for different times. Figures 7.1-7.4 show the evolution of the flow structure with time from $t = 0.005$ to $t = 50$. The temperature starts from $T = x$ as $t = 0$, and gradually develops the vertical gradient associated with the steady-state solution of Chapter 6. The flow field increases in amplitude, driven by the developing core flow (7.4.6), with the position of maximum stream function moving from the core region to a position near the wall as $t \to \infty$. Eventually the solution near the wall attains the steady-state form obtained in Chapter 6.However, further from the wall, the solution continues to change with time, as shown by profiles of $T - x$ on the centre-line $z = 1/2$ for successive times in Figure 7.5. Near the wall the observed maximum is associated with the behaviour

$$T - x \sim c \quad (1 \ll x \ll t^{1/2}),$$

the solution approaching the value $c(R_1, \sigma) = c(500, 0.733) \approx 0.36295$ as $t \to \infty$. At large distances,

$$T - x \to 0 \quad (x \gg t^{1/2}),$$

as required by the outer boundary condition (7.4.6) and in the region where $x \sim t^{1/2}$, the solution, as given by (7.4.29), approximates the form $T - x \sim cerfc(\frac{\eta}{2(1+3R_1^2Q_0)^{1/2}})$ at large times. A rough estimate of the decay of the error function suggests that the outer behaviour is reached close to $\eta = 2$, equivalent to

$$x \sim 4t^{1/2}\left(1 + \frac{3R_1^2}{362880}\right)^{1/2}.$$

This is in good agreement with the computed solution shown in Figure 7.5. As t increases, the numerical solution can, in fact, no longer be accommodated without increasing x_∞ beyond 60, leading to the spurious behaviour evident in the region $x \geq 40$.

7.6 Core Solution for $t = O(L^2)$

As the two end zones spread into the core, the solution there is modified when the lateral scale $x \sim t^{1/2}$ is comparable with the cavity width, L, i.e. when $t = O(L^2)$.

In order to determine the solution in the core on the large time scale $t = O(L^2)$ the solution there is expanded in the form

$$\bar{T} = \xi + L^{-1}T_1(\xi, z, \tau) + L^{-2}T_2(\xi, z, \tau) + L^{-3}T_3(\xi, z, \tau) + \cdots,$$

$$\bar{\psi} = R_1 F(z) + L^{-1}\psi_1(\xi, z, \tau) + L^{-2}\psi_2(\xi, z, \tau) + L^{-3}\psi_3(\xi, z, \tau) + \cdots,$$

where $\xi = x/L$ and $\tau = L^{-2}t$. Substituting into the governing equations and boundary conditions

$$\nabla^4\bar{\psi} - R_1 L\frac{\partial\bar{T}}{\partial x} = \frac{1}{\sigma}\left(\frac{\partial(\nabla^2\bar{\psi}, \bar{\psi})}{\partial(x, z)} + \frac{\partial\nabla^2\bar{\psi}}{\partial t}\right), \tag{7.6.1}$$

$$\nabla^2\bar{T} = \frac{\partial(\bar{T}, \bar{\psi})}{\partial(x, z)} + \frac{\partial\bar{T}}{\partial t}, \tag{7.6.2}$$

$$\bar{\psi} = \frac{\partial\bar{\psi}}{\partial z} = \frac{\partial\bar{T}}{\partial z} = 0 \text{ on} \quad z = 0, 1, \tag{7.6.3}$$

obtained from (7.2.1)-(7.2.4) and equating terms of like order in L we obtain the following results.

At $O(1)$

$$F'''' = 1, \tag{7.6.4}$$

with

$$F = F' = 0 \quad \text{at} \quad z = 0, 1, \tag{7.6.5}$$

consistent with the previous solution for F.

At $O(L^{-1})$

$$\frac{\partial^4\psi_1}{\partial z^4} = R_1\frac{\partial T_1}{\partial\xi}, \tag{7.6.6}$$

$$R_1 F' = \frac{\partial^2 T_1}{\partial z^2}, \tag{7.6.7}$$

with boundary conditions

$$\psi_1 = \frac{\partial\psi_1}{\partial z} = \frac{\partial T_1}{\partial z} = 0 \quad (z = 0, 1). \tag{7.6.8}$$

The relevant solutions are

$$\psi_1 = R_1\frac{\partial A}{\partial\xi}F(z), \tag{7.6.9}$$

$$T_1 = R_1 G(z) + A(\xi, \tau), \tag{7.6.10}$$

where $A(\xi,\tau)$ is an unknown function of ξ and τ.

At $O(L^{-2})$, T_2 satisfies

$$R_1F'\frac{\partial T_1}{\partial \xi}+\frac{\partial \psi_1}{\partial z}=\frac{\partial^2 T_2}{\partial z^2}, \tag{7.6.11}$$

with boundary conditions

$$\psi_2=\frac{\partial \psi_2}{\partial z}=\frac{\partial T_2}{\partial z}=0 \quad (z=0,1), \tag{7.6.12}$$

giving

$$T_2=2GR_1\frac{\partial T_1}{\partial \xi}+B(\xi,\tau), \tag{7.6.13}$$

where $B(\xi,\tau)$ is an unknown function of ξ and τ.

At $O(L^{-3})$, T_3 satisfies

$$\frac{\partial^2 T_3}{\partial z^2}+\frac{\partial^2 T_1}{\partial \xi^2}=R_1F'\frac{\partial T_2}{\partial \xi}+\frac{\partial T_1}{\partial \xi}\frac{\partial \psi_1}{\partial z}+\frac{\partial T_1}{\partial \tau}-\frac{\partial \psi_1}{\partial \xi}\frac{\partial T_1}{\partial z}+\frac{\partial \psi_2}{\partial z} \tag{7.6.14}$$

with boundary conditions

$$\frac{\partial T_3}{\partial z}=0 \quad (z=0,1) \quad . \tag{7.6.15}$$

Substituting (7.6.9) – (7.6.10) into (7.6.14) gives

$$\frac{\partial^2 T_3}{\partial z^2}+\frac{\partial^2 T_1}{\partial \xi^2}=(2R_1^2F'G-R_1^2FG')\frac{\partial^2 T_1}{\partial \xi^2}+\frac{\partial T_1}{\partial \tau}+\frac{\partial T_1}{\partial \xi}\frac{\partial \psi_1}{\partial z}+\frac{\partial \psi_2}{\partial z} \tag{7.6.16}$$

and integrating (7.6.16) from $z=0$ to $z=1$ yields an equation for $A(\xi,\tau)$:

$$(1+3R_1^2Q_0)\frac{\partial^2 A}{\partial \xi^2}=\frac{\partial A}{\partial \tau}, \tag{7.6.17}$$

where $Q_0=\int_0^1 G'^2dz=1/362880$. The solution for T_1 must match with that in each end zone , where the relevant solution on the long time scale $t=O(L^2)$ is the steady-state solution associated with region I (Section 7.3). Thus

$$A(0,\tau)=c \tag{7.6.18}$$

and similarly for the other end of the cavity

$$A(1,\tau)=-c. \tag{7.6.19}$$

As $\tau \to 0$, the solution must match with that given by (7.4.6) as $t \to \infty$, which requires that

$$A(\xi, 0) = 0 \quad . \tag{7.6.20}$$

The solution for A can now be written

$$A = c(1 - 2\xi) + \bar{A}(\xi, \tau),$$

where $\bar{A}$ satisfies

$$\begin{aligned} k^2 \frac{\partial^2 \bar{A}}{\partial \xi^2} &= \frac{\partial \bar{A}}{\partial \tau}, & (7.6.21)\\ \bar{A}(0, \tau) &= 0, & (7.6.22)\\ \bar{A}(1, \tau) &= 0, & (7.6.23)\\ \bar{A}(\xi, 0) &= -c + 2c\xi, & (7.6.24) \end{aligned}$$

with $k = \sqrt{1 + 3R_1^2 Q_0}$.

The solution is

$$\bar{A} = -\frac{c}{2} \sum_{n=1}^{\infty} \frac{1}{n\pi} e^{-4n^2 k^2 \pi^2 \tau} \sin 2n\pi\xi \tag{7.6.25}$$

so that finally

$$A = c - 2\xi c - \frac{c}{2} \sum_{n=1}^{\infty} \frac{1}{n\pi} e^{-4n^2 \pi^2 k^2 \tau} \sin 2n\pi\xi \tag{7.6.26}$$

and the core solution for $t = O(L^2)$ takes the form

$$\bar{T} = \xi + L^{-1} \left(R_1 G(z) + c - 2\xi c - \frac{c}{2} \sum_{n=1}^{\infty} \frac{1}{n\pi} e^{-4n^2 \pi^2 (1 + 3R_1^2 Q_0)\tau} \sin 2n\pi\xi \right) + O(L^{-2}) \tag{7.6.27}$$

$$\bar{\psi} = R_1 F(z) + L^{-1} R_1 F \left(-2c - c \sum_{n=1}^{\infty} e^{-4n^2 \pi^2 (1 + 3R_1^2 Q_0)\tau} \cos 2n\pi\xi \right) + O(L^{-2}). \tag{7.6.28}$$

As $\tau \to \infty$, this solution approaches the steady-state core solution already identified in Chapter 6 (see(6.2.12)-(6.2.13)).

7.7 Other Initial States

In this section, initial states of the form

$$\bar{T} = \left(1 - \frac{a}{L}\right)\frac{x}{L} + \frac{a}{2L}, \quad \bar{\psi} = 0 \quad \text{at} \quad t = 0 \tag{7.7.1}$$

are considered, where a is a finite constant. The case $a = 0$ corresponds to the situation considered in Sections 7.2-7.6 while increasing values of a correspond to a weaker initial temperature gradient, so that there is a jump in temperature at $t = 0$ at each end wall. In such cases the initial evolution is not so gradual and indeed the case $a = L$ would correspond to starting from $\bar{T} = 1/2$ throughout the cavity with the motion generated by the sudden change in temperature to $\bar{T} = 0$ and $\bar{T} = 1$ at the end walls. This leads to initial motions near the end walls which for large values of a take the form of wall jets generated by the sudden heating. Provided a is finite the analysis of Sections 7.2-7.4 and 7.6 can easily be extended to incorporate the class of initial profile (7.7.1). The core solution for $t = O(1)$ simply becomes

$$\bar{T} = \xi + L^{-1}\left(-a\xi + \frac{a}{2} + R_1\tilde{G}(z,t)\right) + \cdots, \tag{7.7.2}$$

$$\bar{\psi} = R_1\tilde{F}(z,t) + \cdots, \tag{7.7.3}$$

where $\tilde{G}$ and $\tilde{F}$ are the same as before, and for $t = O(L^2)$ the core solution is

$$\bar{T} = \xi + L^{-1}\left(R_1 G(z) + c - 2\xi c - \sum_{n=1}^{\infty} -\frac{2c-a}{4n\pi} e^{-4n^2\pi^2(1+3R_1^2Q_0)\tau}\sin 2n\pi\xi\right) + O(L^{-2}),$$

$$\bar{\psi} = R_1 F(z) + L^{-1}R_1 F\left(-2c - \frac{2c-a}{2}\sum_{n=1}^{\infty} e^{-4n^2\pi^2(1+3R_1^2Q_0)\tau}\cos 2n\pi\xi\right) + O(L^{-2}),$$

indicating that as $\tau \to \infty$, the same steady- state flow is achieved.

Interest centres, however, on the manner in which the end-zone flow develops, particularly for large values of a. The end-zone problem is as stated in (7.4.2)-(7.4.6) except that the initial profile is

$$T = x + \frac{1}{2}a, \quad \psi = 0 \quad \text{at} \quad t = 0$$

and the outer condition (7.4.6) is replaced by

$$\left.\begin{aligned} T &\sim x + \tfrac{1}{2}a + R_1\tilde{G}(z,t) \\ \psi &\sim R_1\tilde{F}(z,t) \end{aligned}\right\} \quad (x \to \infty). \tag{7.7.4}$$

Numerical solutions were obtained for $a = 1$ and $a = 4$ with $R_1 = 500$ and $\sigma = 0.733$.

Figures 7.6 - 7.9 show contours of temperature, vorticity and stream function at different times. At early times, the flow contains stronger horizontal gradients near the wall than in the case $a = 0$ but the effect weakens rapidly as time increases and the outer core flow takes over as the main driving force. In the vorticity field, there is a closed contour near the wall at early times which is not found in the case $a = 0$. For higher values of a the end-wall effect is much easier to observe. In Figure 7.10, for $a = 4$, the contours indicate a very strong nonlinearity near the wall, with a local circulation generated by the sudden heating at $t = 0$. This is clearly shown in Figure 7.11 by profiles of the vertical velocity w near the wall for different values of a, indicating the jet-like motion for $a = 4$. Further results for an alternative initial state

$$T = 0 \quad \text{on} \quad (0, x_0), \tag{7.7.5}$$

$$T = x + \frac{1}{2} \quad \text{on} \quad (x_0, \infty), \tag{7.7.6}$$

are shown in Figure 7.12.

Figure 7.13 shows how the new initial state with $a = 1$ affects the evolution of $T - x$ along the centre-line of the end zone, in contrast to the result obtained for $a = 0$ in Figure 7.5. At large $x \gg t^{1/2}$, $T - x$ must now approach the value $a/2 = 1/2$ while for $1 \ll x \ll t^{1/2}$ the plateau value $c \approx 0.36295$ must emerge as $t \to \infty$. This is consistent with the behaviour shown in Figure 7.13. The outer section where $x \sim t^{1/2}$ eventually develops into part of the core solution on the long-time scale $t = O(L^2)$ which then adjusts to the steady-state form $T \sim \xi + L^{-1}c(1 - 2\xi)$, independent of a, when $\tau = L^{-2}t \gg 1$. The solution which evolves in the inner part of the end zone as $t \to \infty$ is already independent of the initial state and is shown in Figure 7.14.

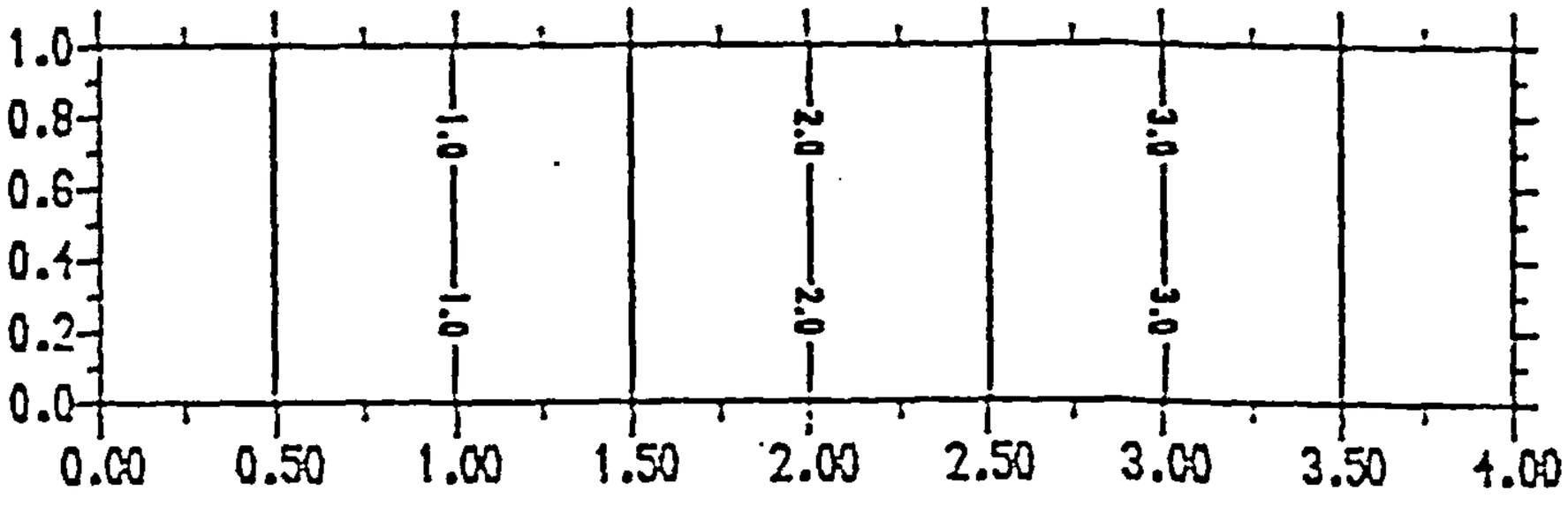

(c)

Contour Step 0.50

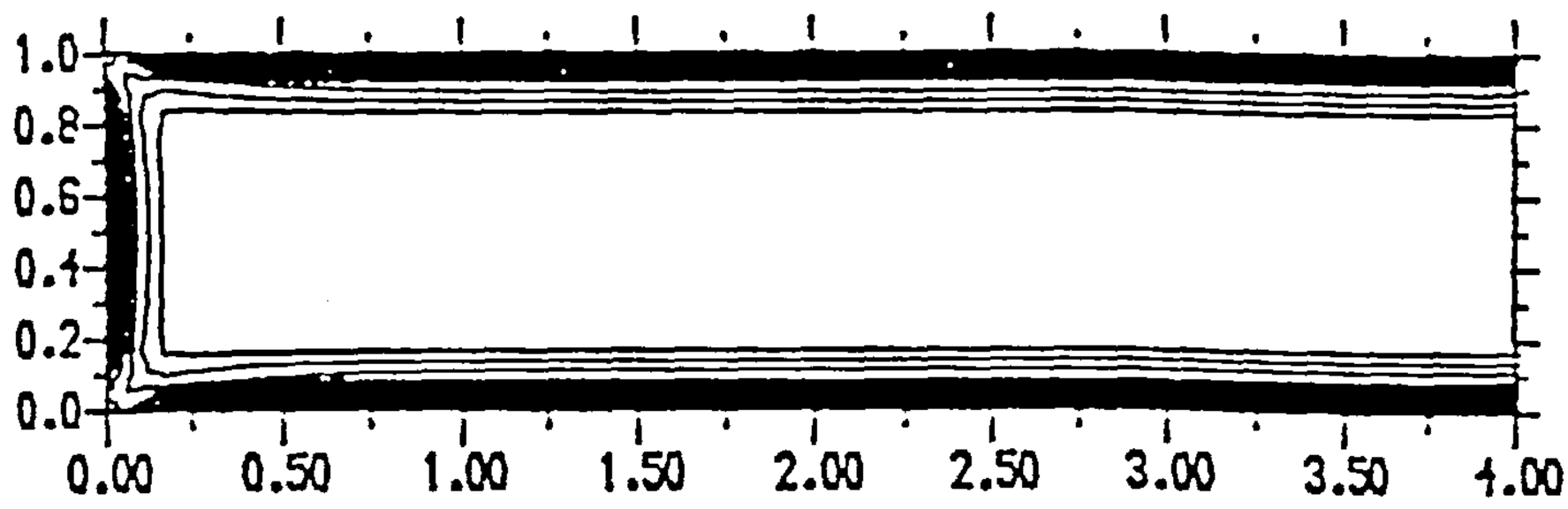

(b)

Contour Step 0.00

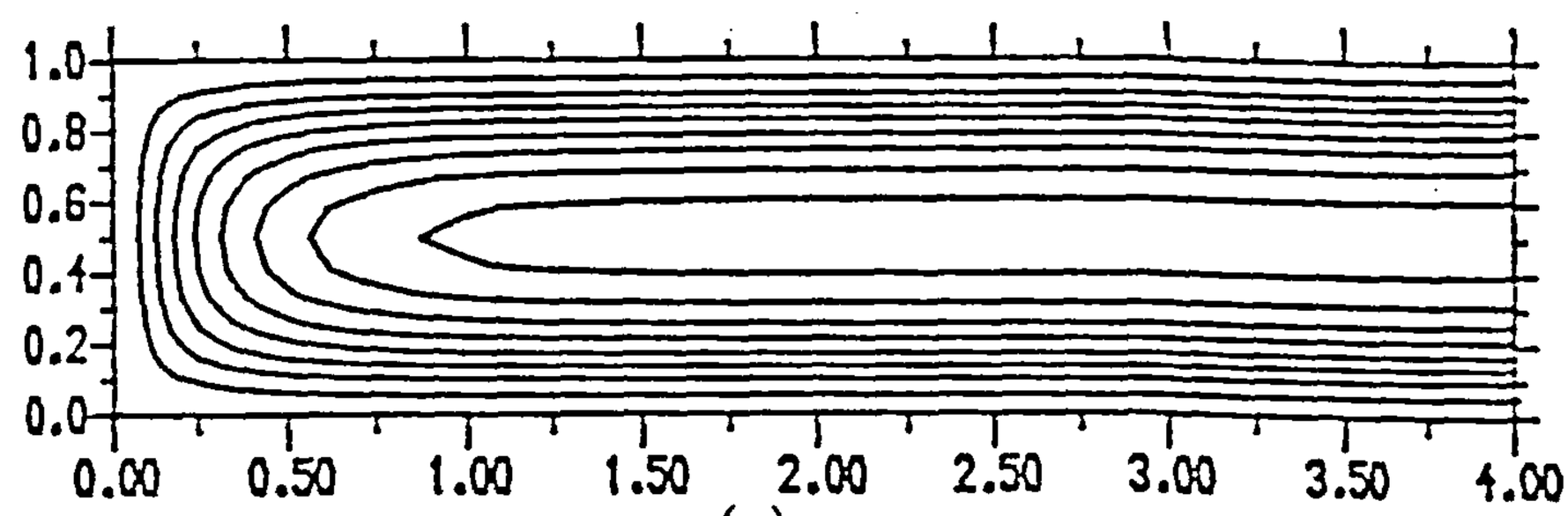

(a)

Figure 7.1: Contours at $t = 0.005$ of (a) stream function , (b) vorticity, (c) temperature, for $\sigma = 0.733$, $R_1 = 500$, using a 750×12 computational grid with $x_\infty = 60$ and the initial condition $T = x, u = w = 0$ at $t = 0$ for the insulating case.

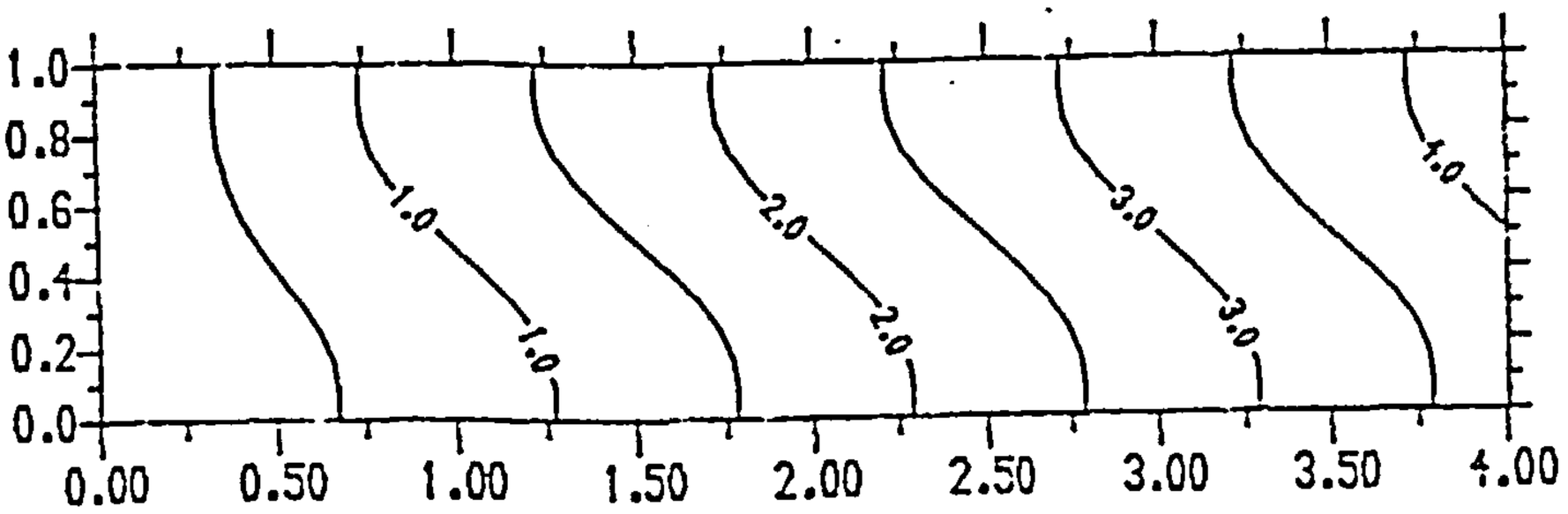

(c)

Contour Step 0.50

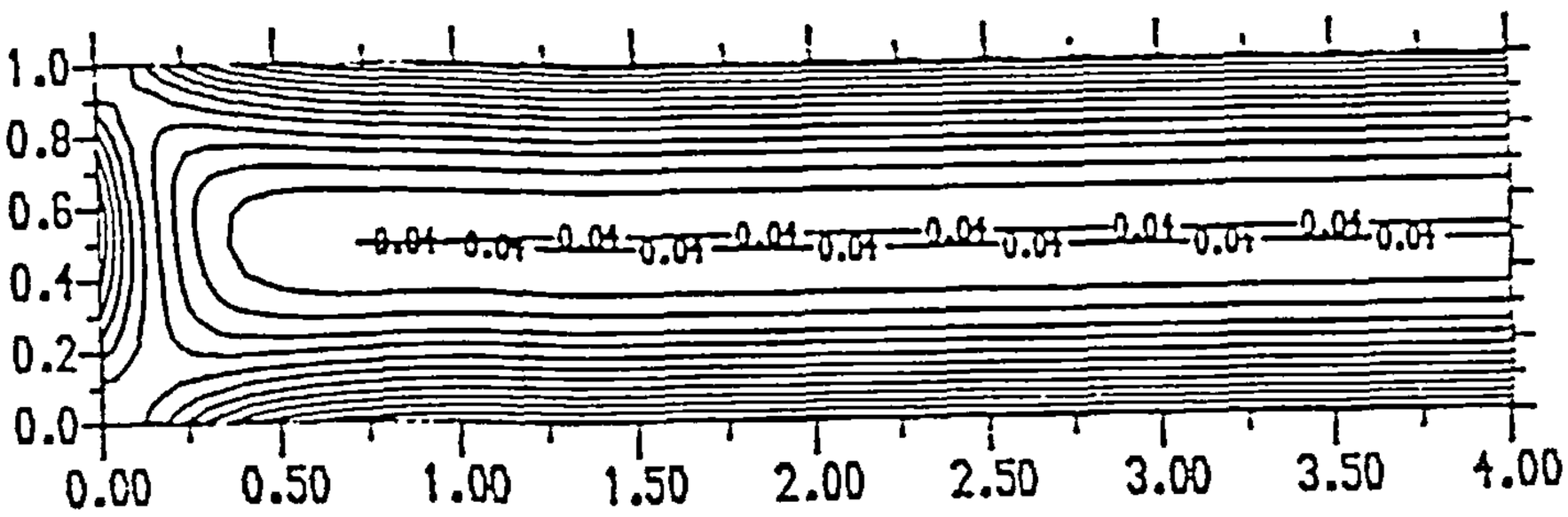

(b) Contour Step 0.01

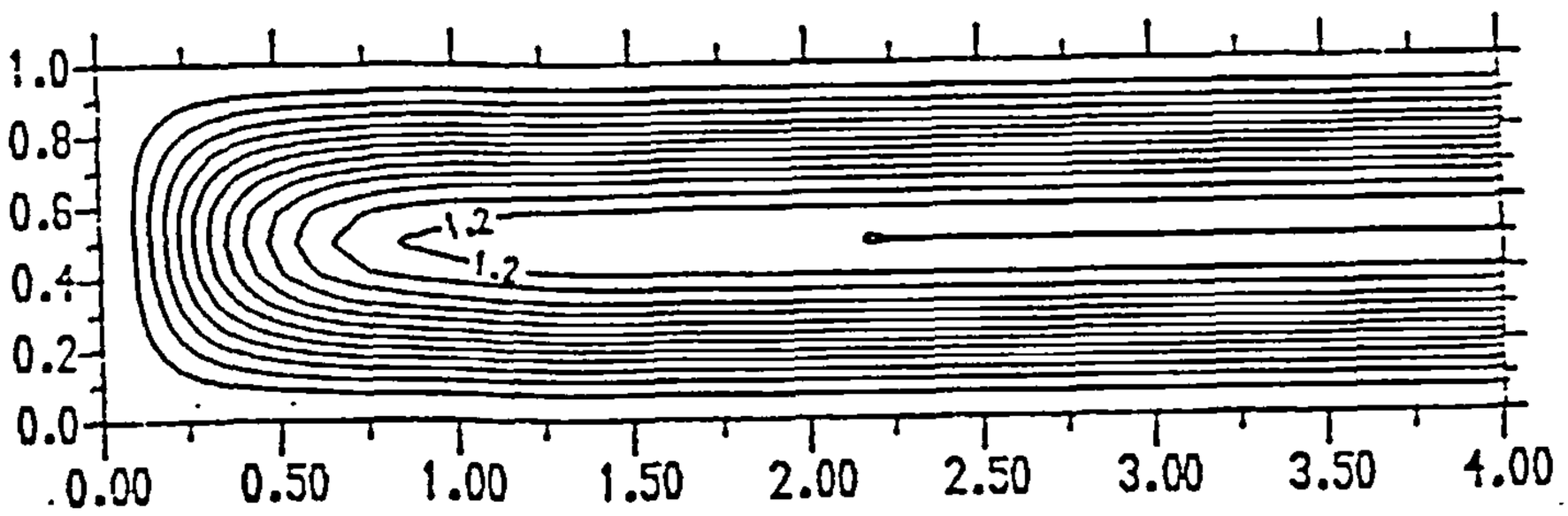

(a)

Contour Step 0.10

Figure 7.2: Contours at $t = 0.2$ of (a) stream function , (b) vorticity, (c) temperature, for $\sigma = 0.733$, $R_1 = 500$, using a 750×12 computational grid with $x_\infty = 60$ and the initial condition $T = x, u = w = 0$ at $t = 0$ for the insulating case.

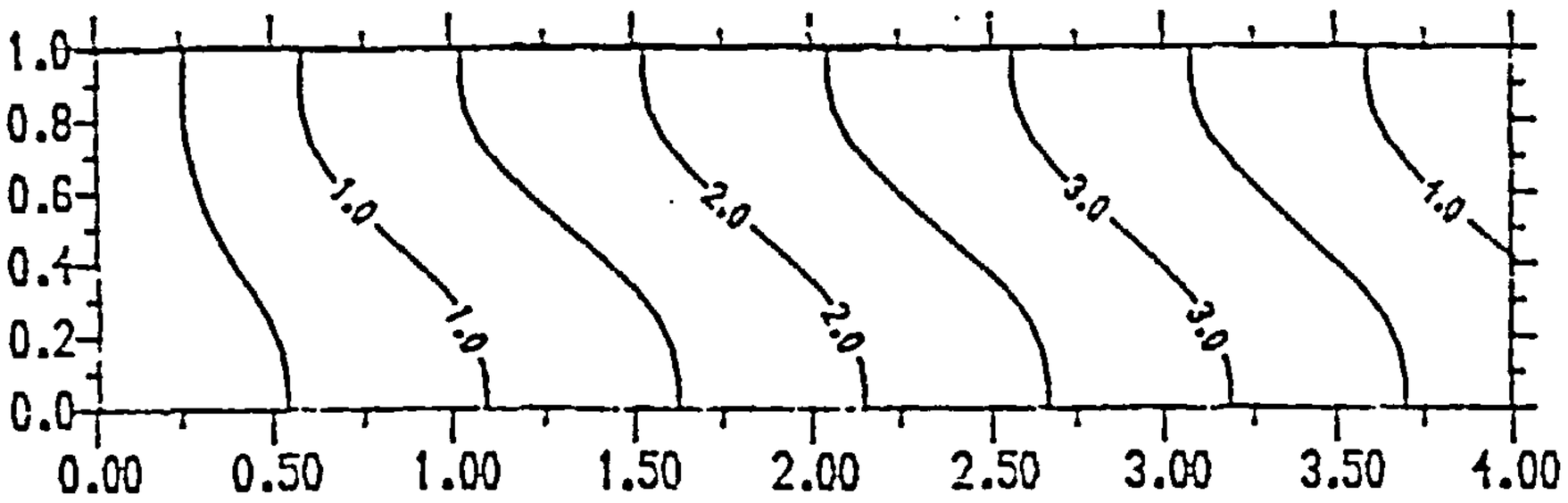

(c) Contour Step 0.50

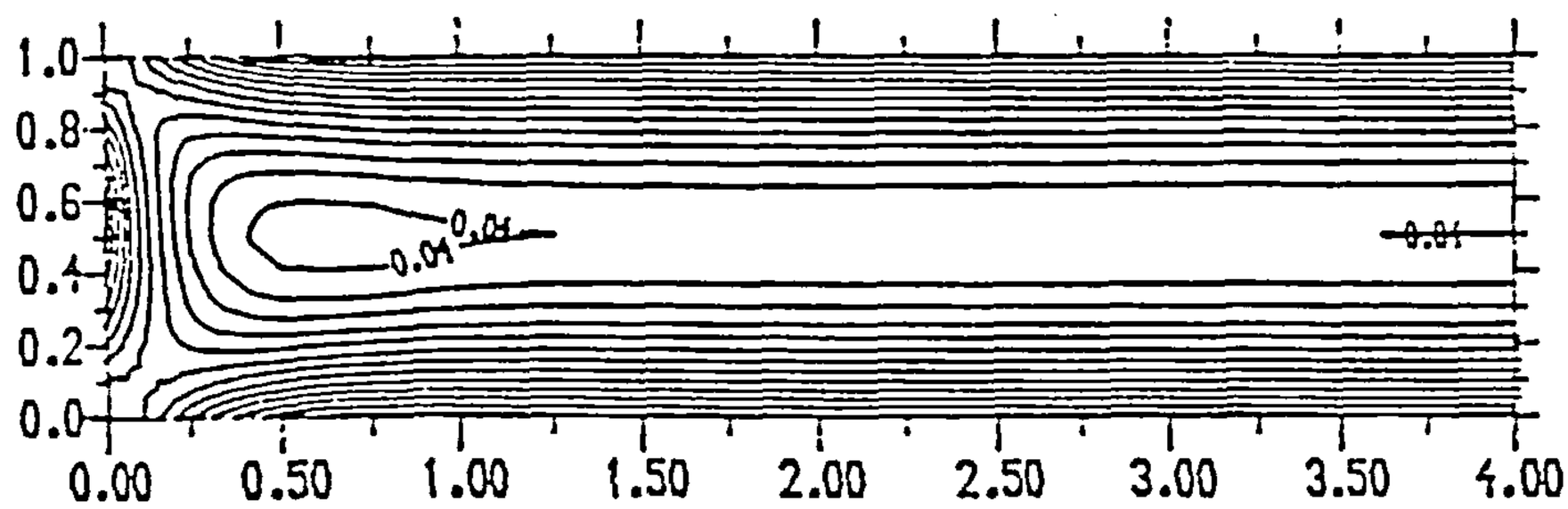

(b) Contour Step 0.01

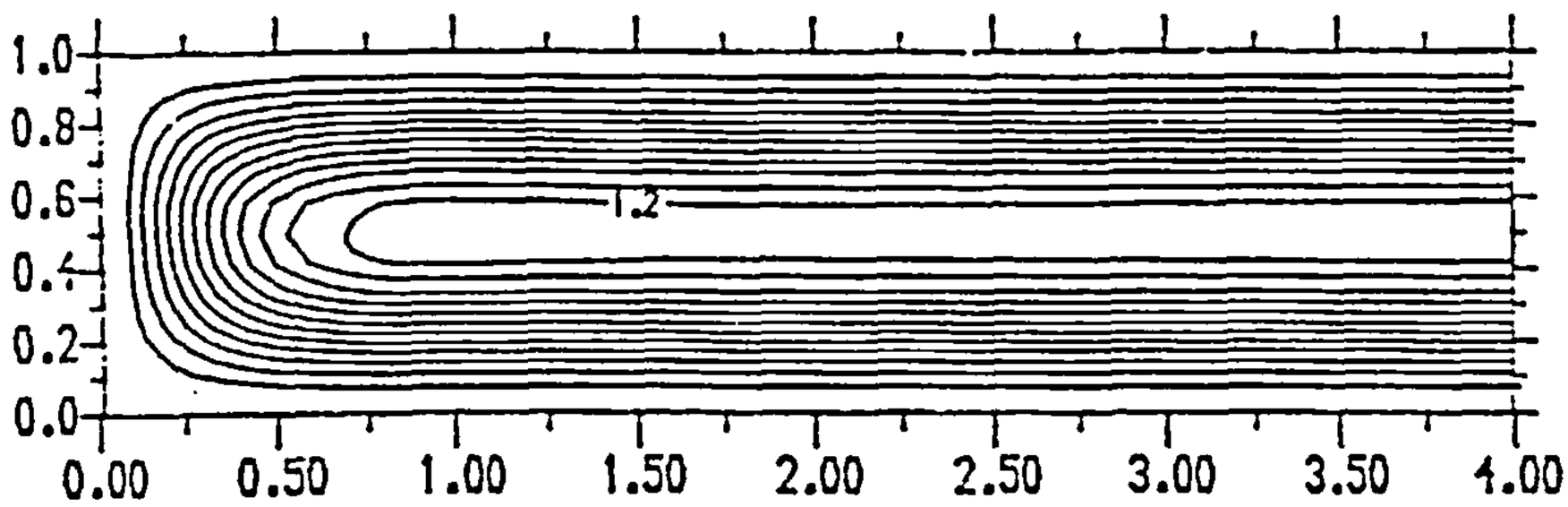

(a) Contour Step 0.10

Figure 7.3: Contours at $t = 5$ of (a) stream function , (b) vorticity, (c) temperature, for $\sigma = 0.733$, $R_1 = 500$, using a 750×12 computational grid with $x_\infty = 60$ and the initial condition $T = x, u = w = 0$ at $t = 0$ for the insulating case.

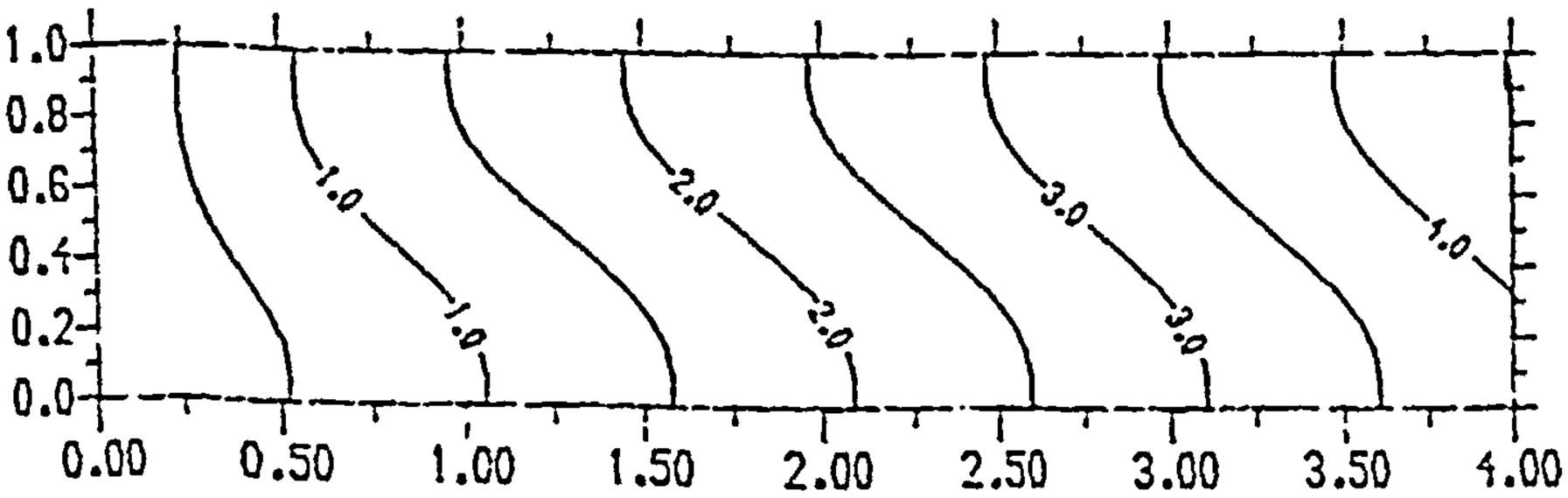

(c) Contour Step 0.50

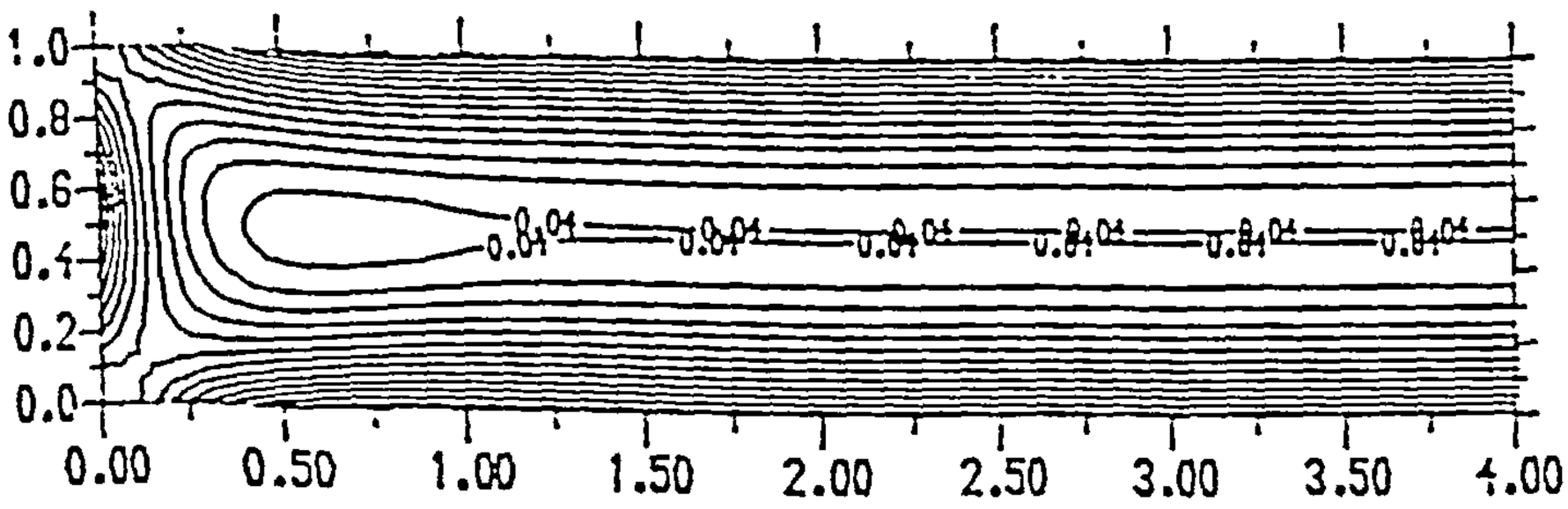

(b) Contour Step 0.01

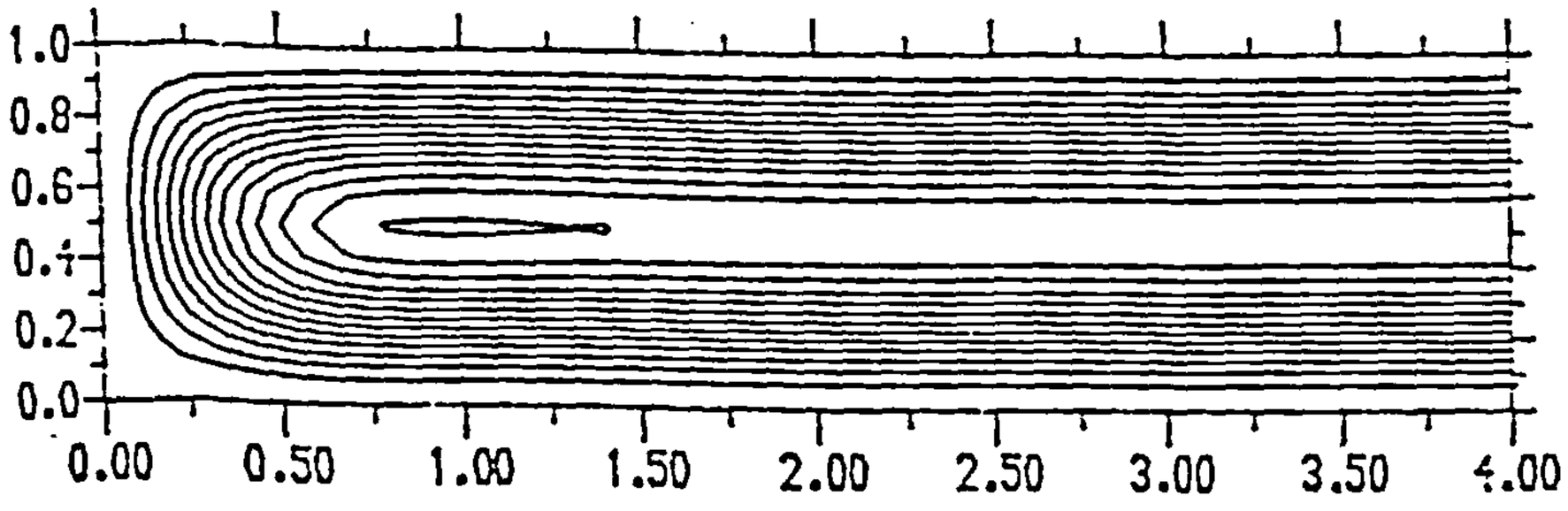

(a) Contour Step 0.10

Figure 7.4: Contours at $t = 50$ of (a) stream function , (b) vorticity, (c) temperature, for $\sigma = 0.733$, $R_1 = 500$, using a 750×12 computational grid with $x_\infty = 60$ and the initial condition $T = x, u = w = 0$ at $t = 0$ for the insulating case.

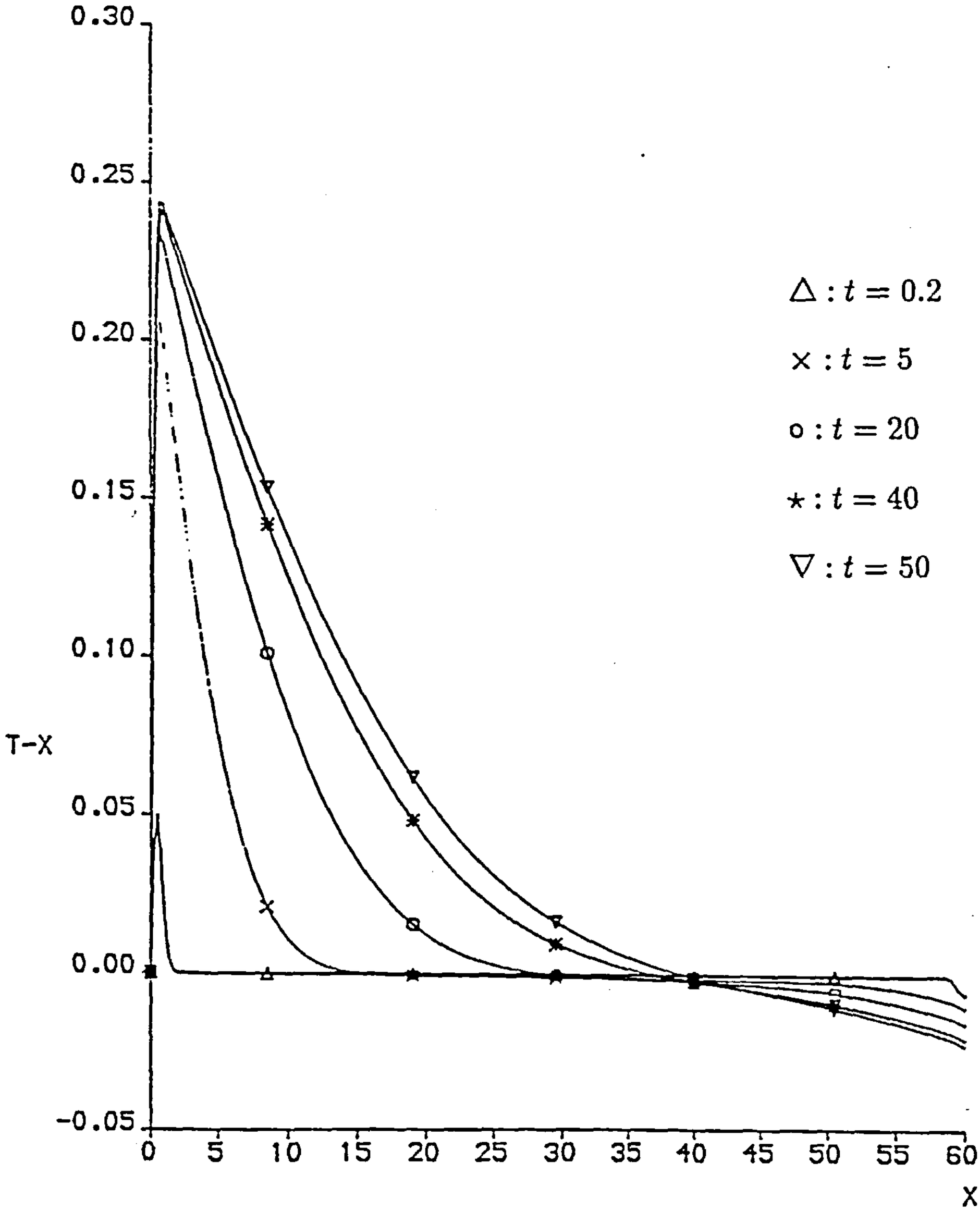

Figure 7.5: The function $T - x$ on $z = 1/2$ for $\sigma = 0.733$, $R_1 = 500$ at different time steps for the initial condition $T = x, \quad u = w = 0$ at $t = 0$ in the insulating case.

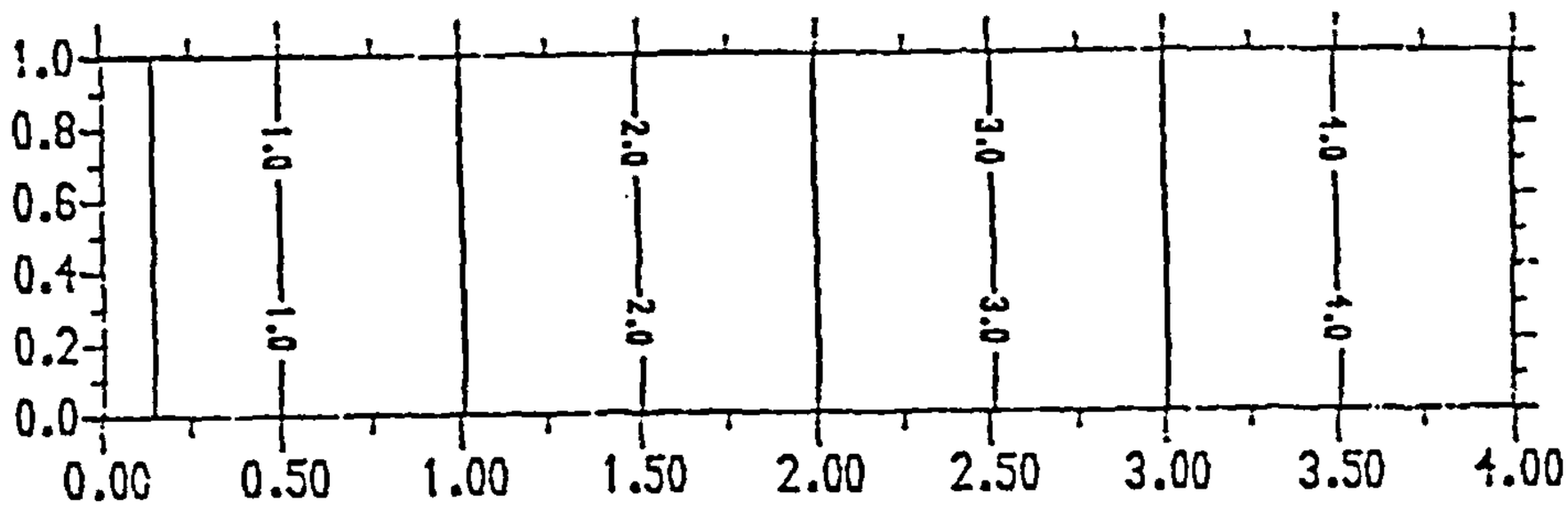

(c)

Contour Step 0.50

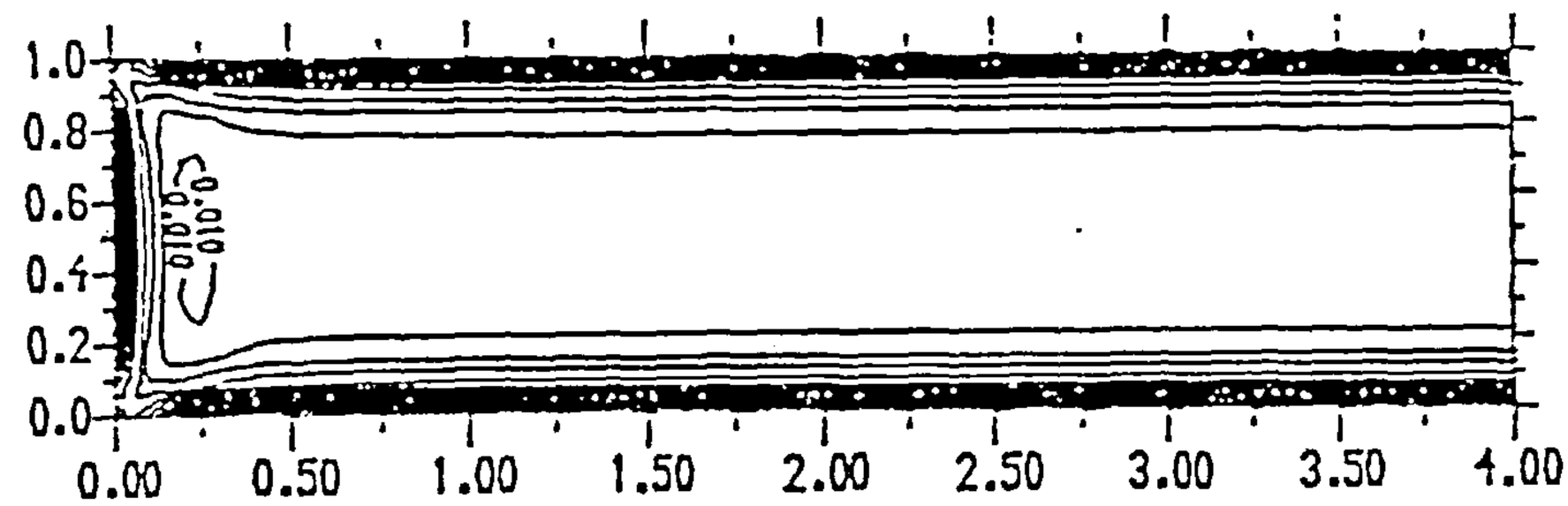

(b)

Contour Step 0.00

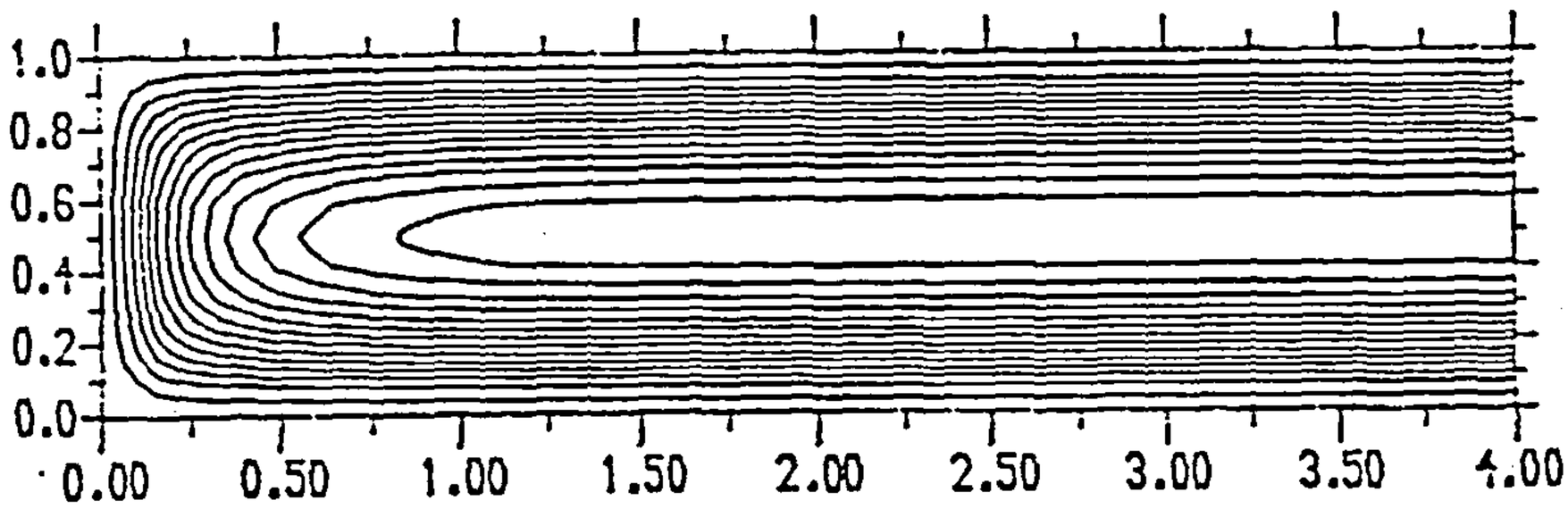

(a)

Contour Step 0.03

Figure 7.6: Contours at $t = 0.01$ of (a) stream function , (b) vorticity, (c) temperature, for $\sigma = 0.733$, $R_1 = 500$, using a 750×12 computational grid with $x_\infty = 60$ and the initial condition $T = x + 0.5, u = w = 0$ at $t = 0$ for the insulating case.

(c) Contour Step 0.50

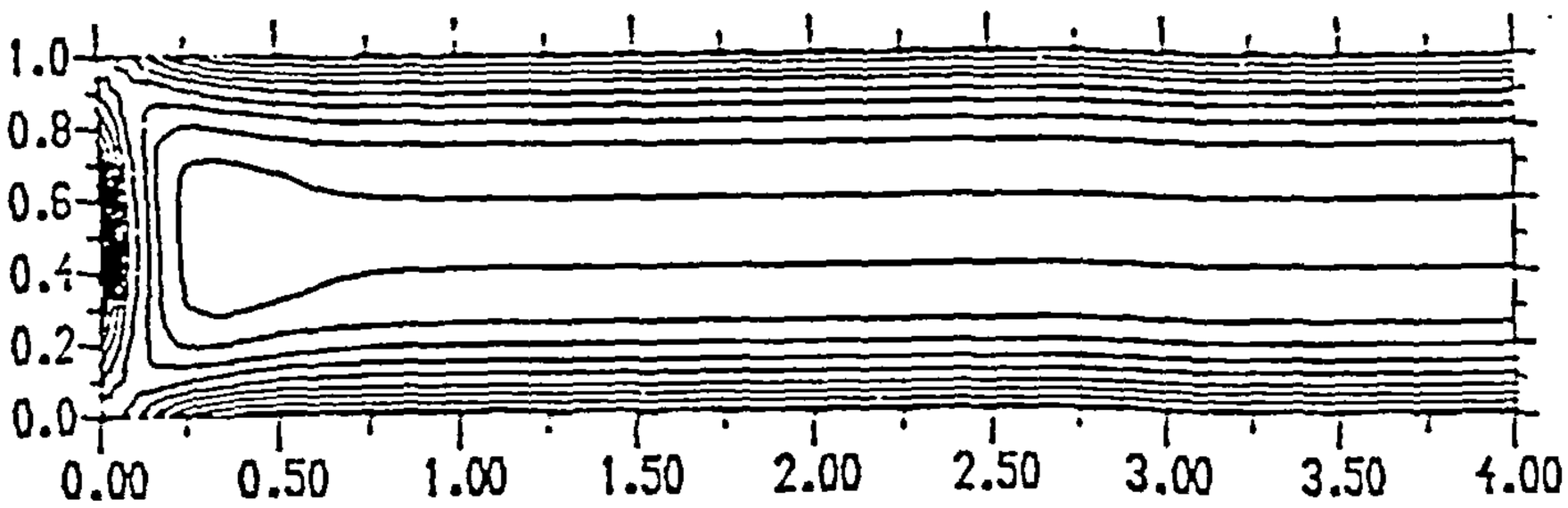

(b) Contour Step 0.01

(a) Contour Step 0.05

Figure 7.7: Contours at $t = 0.02$ of (a) stream function , (b) vorticity, (c) temperature, for $\sigma = 0.733$, $R_1 = 500$, using a 750×12 computational grid with $x_\infty = 60$ and the initial condition $T = x + 0.5, u = w = 0$ at $t = 0$ for the insulating case.

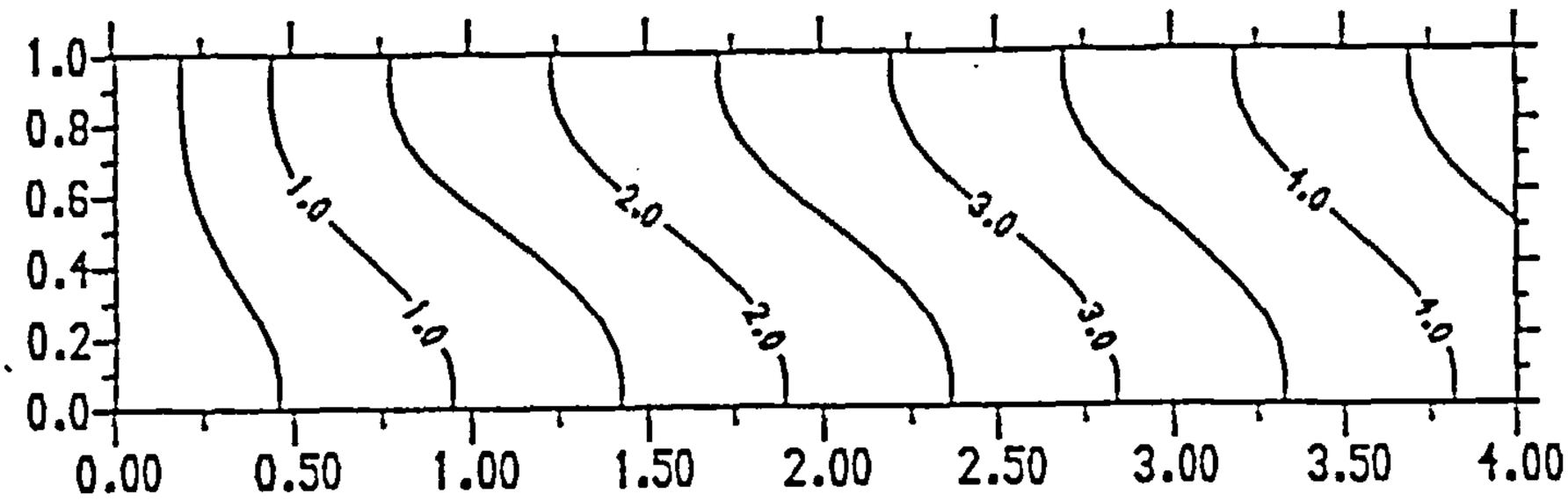

(c) Contour Step 0.50

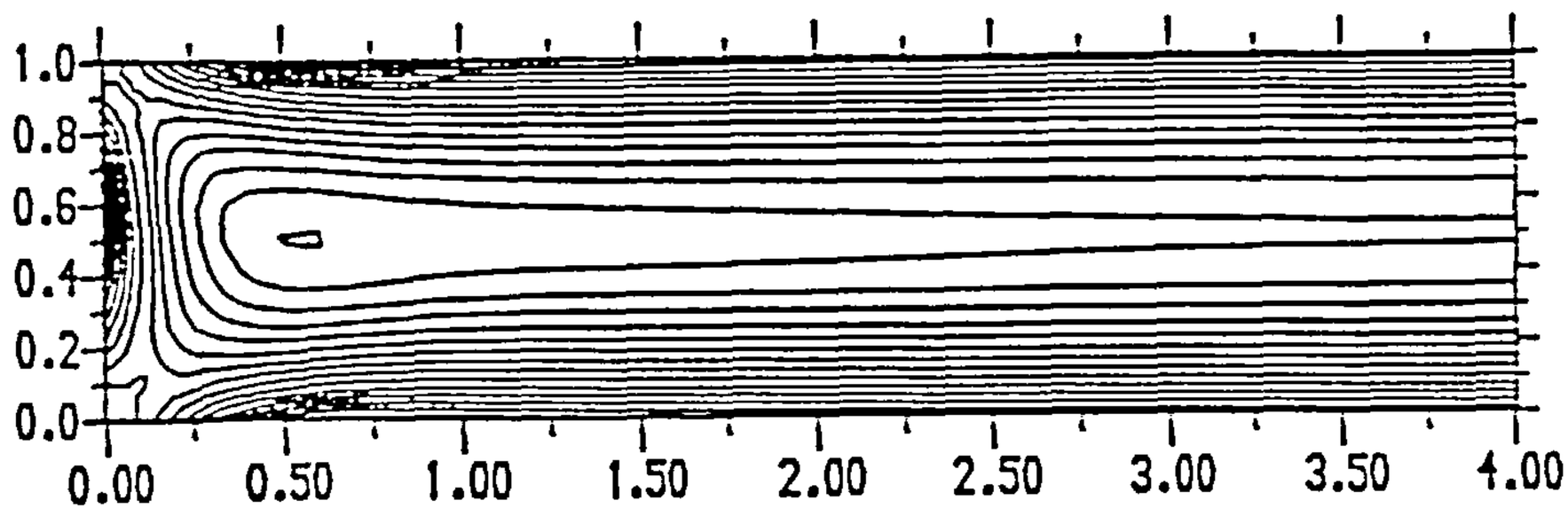

(b) Contour Step 0.01

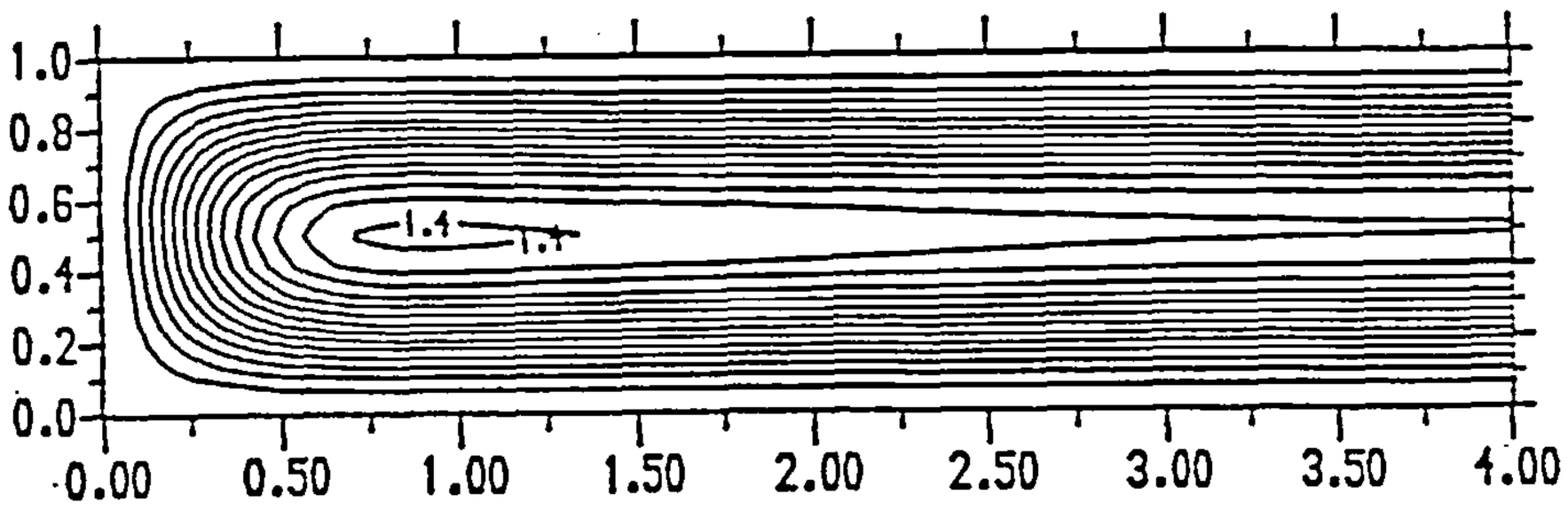

(a) Contour Step 0.10

Figure 7.8: Contours at $t = 0.5$ of (a) stream function , (b) vorticity, (c) temperature, for $\sigma = 0.733$, $R_1 = 500$, using a 750×12 computational grid with $x_\infty = 60$ and the initial condition $T = x + 0.5, u = w = 0$ at $t = 0$ for the insulating case.

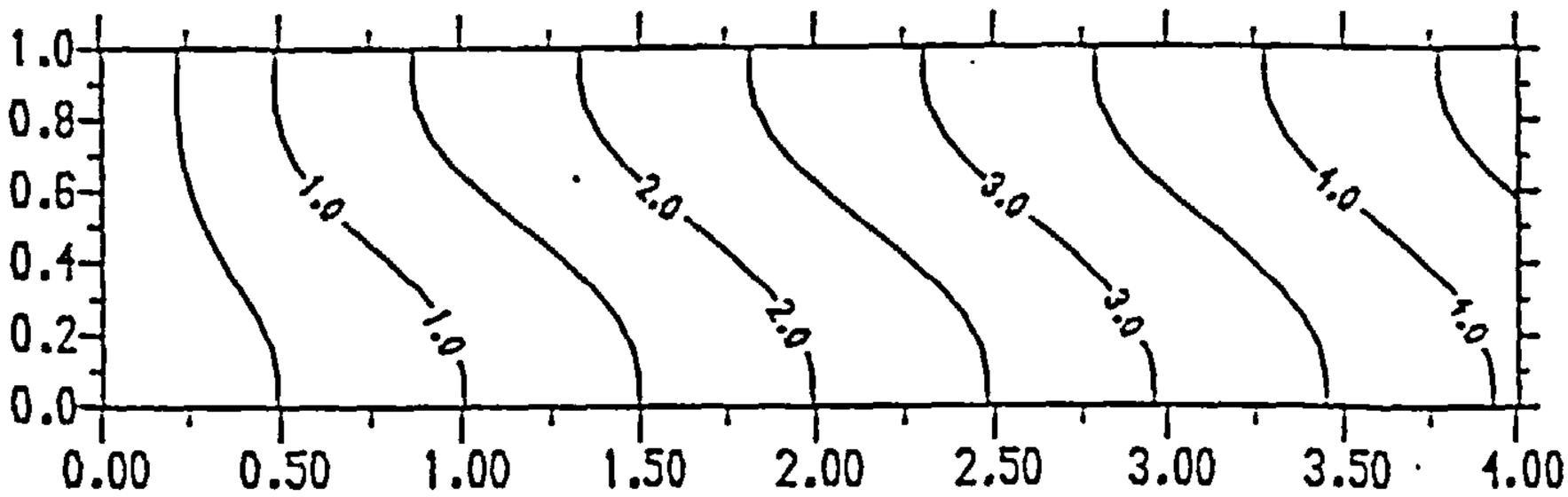

(c) Contour Step 0.50

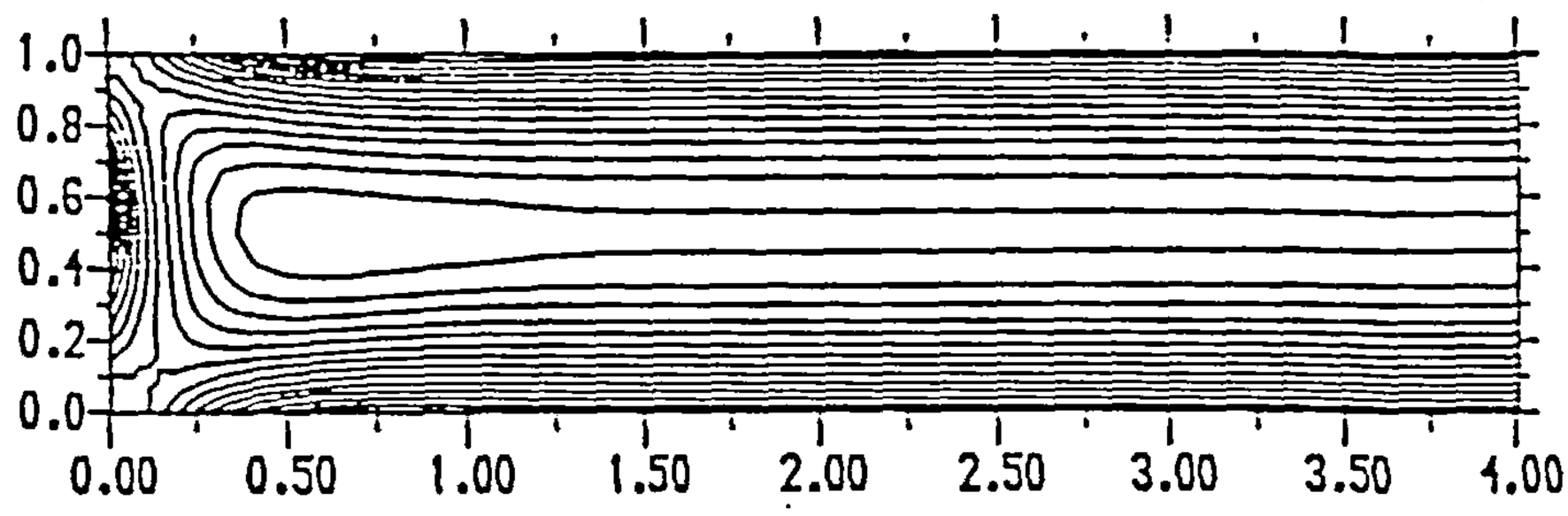

(b) Contour Step 0.01

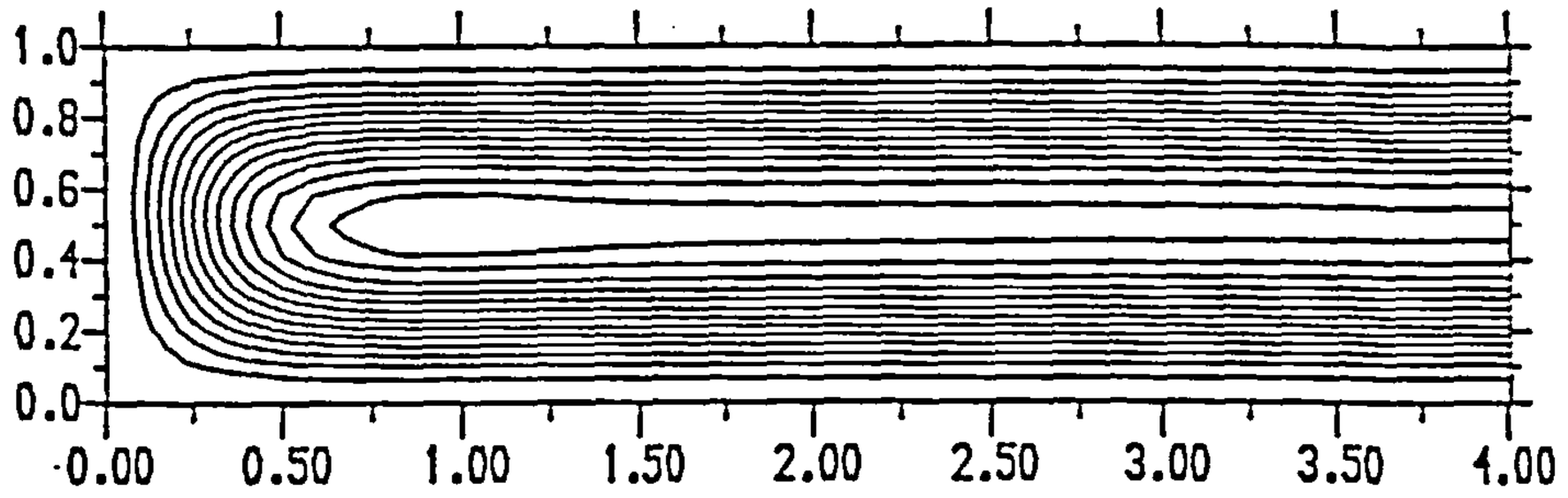

(a) Contour Step 0.10

Figure 7.9: Contours at $t = 5$ of (a) stream function , (b) vorticity, (c) temperature, for $\sigma = 0.733$, $R_1 = 500$, using a 750×12 computational grid with $x_\infty = 60$ and the initial condition $T = x + 0.5, u = w = 0$ at $t = 0$ for the insulating case.

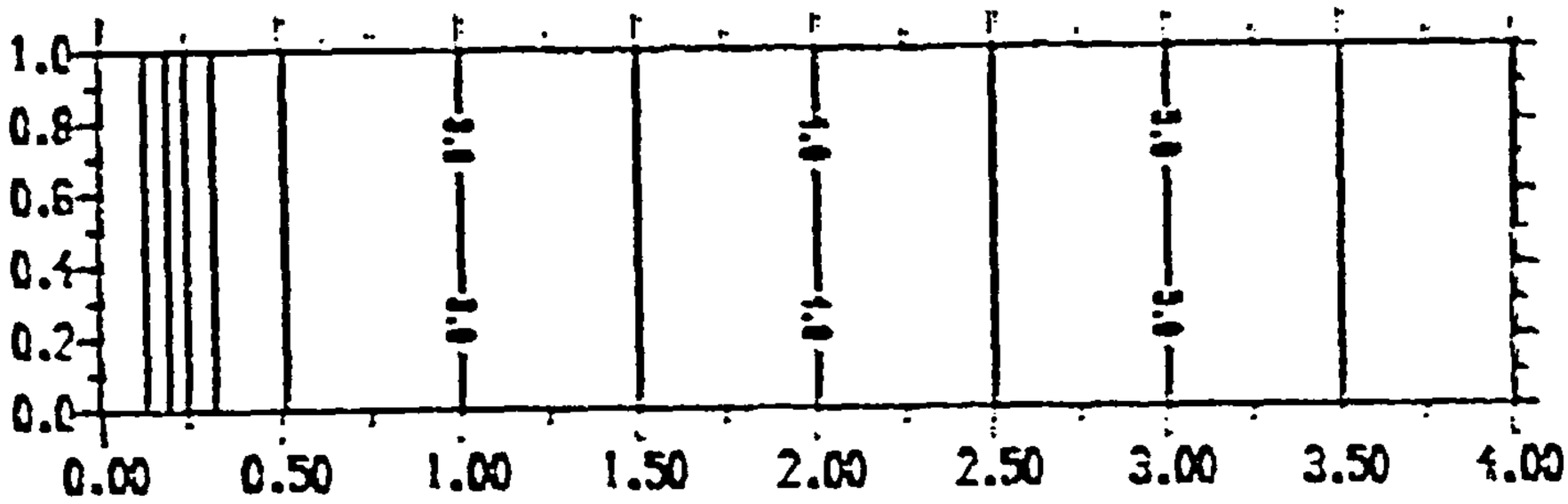

(c) Contour Step 0.50

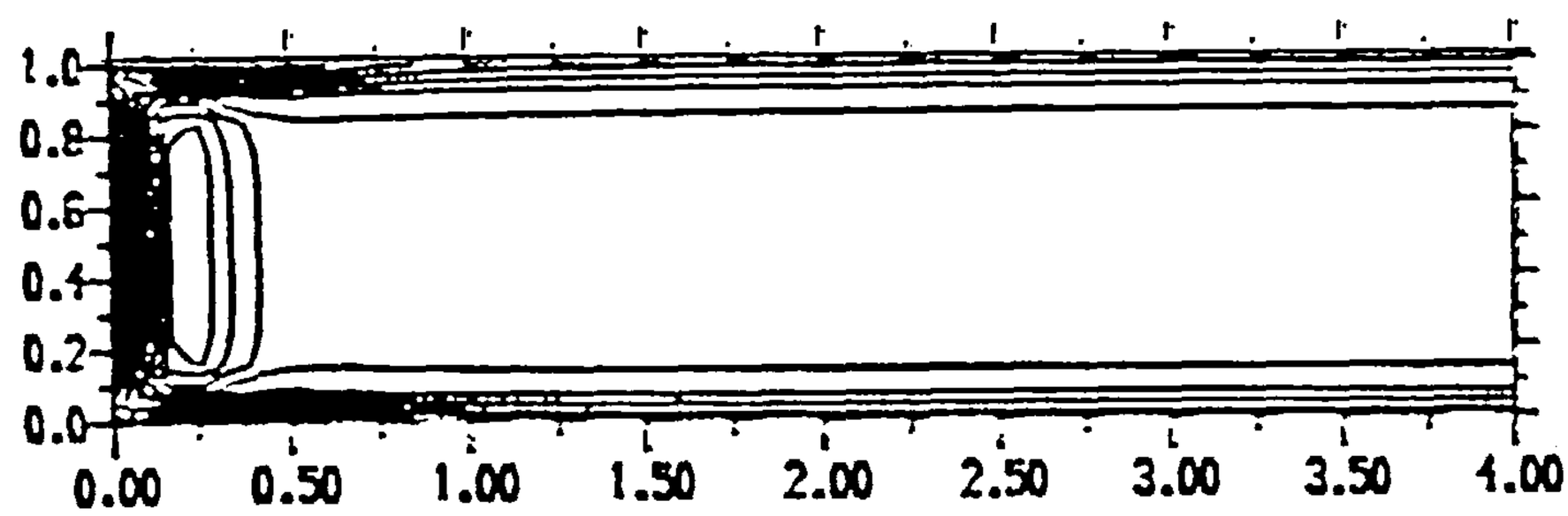

(b) Contour Step 0.01

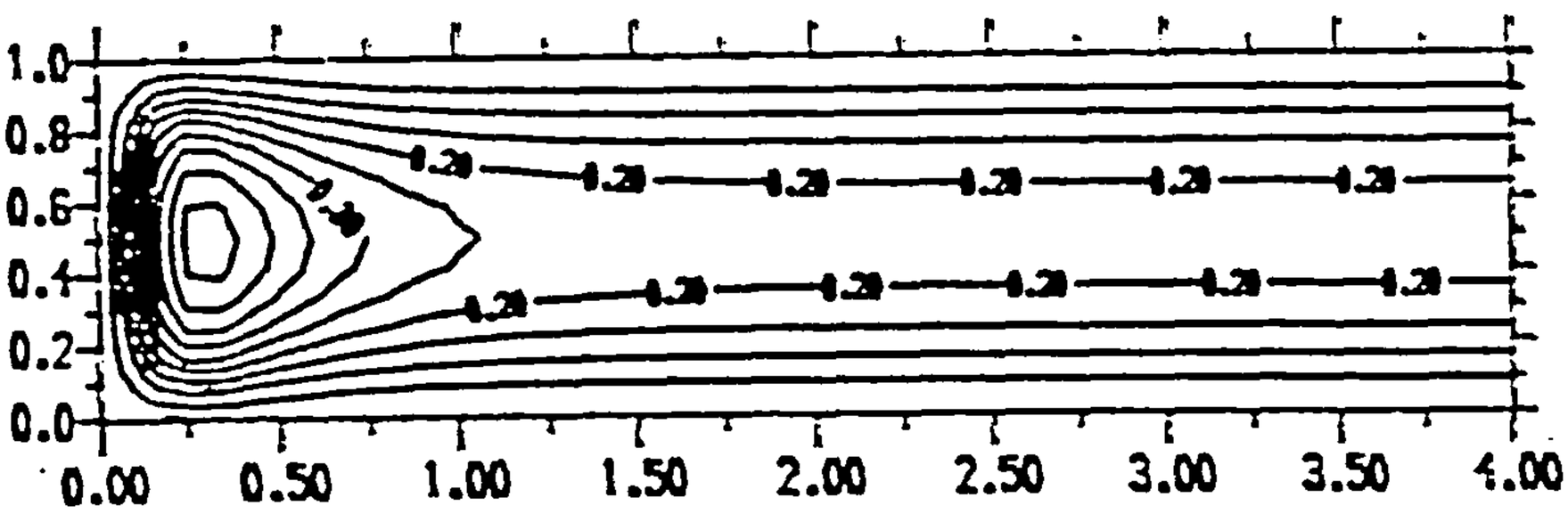

(a) Contour Step 0.05

Figure 7.10: Contours at $t = 0.005$ of (a) stream function , (b) vorticity, (c) temperature, for $\sigma = 0.733$, $R_1 = 500$, using a 750×12 computational grid with $x_\infty = 60$ and the initial condition $T = x + 2, u = w = 0$ at $t = 0$ for the insulating case.

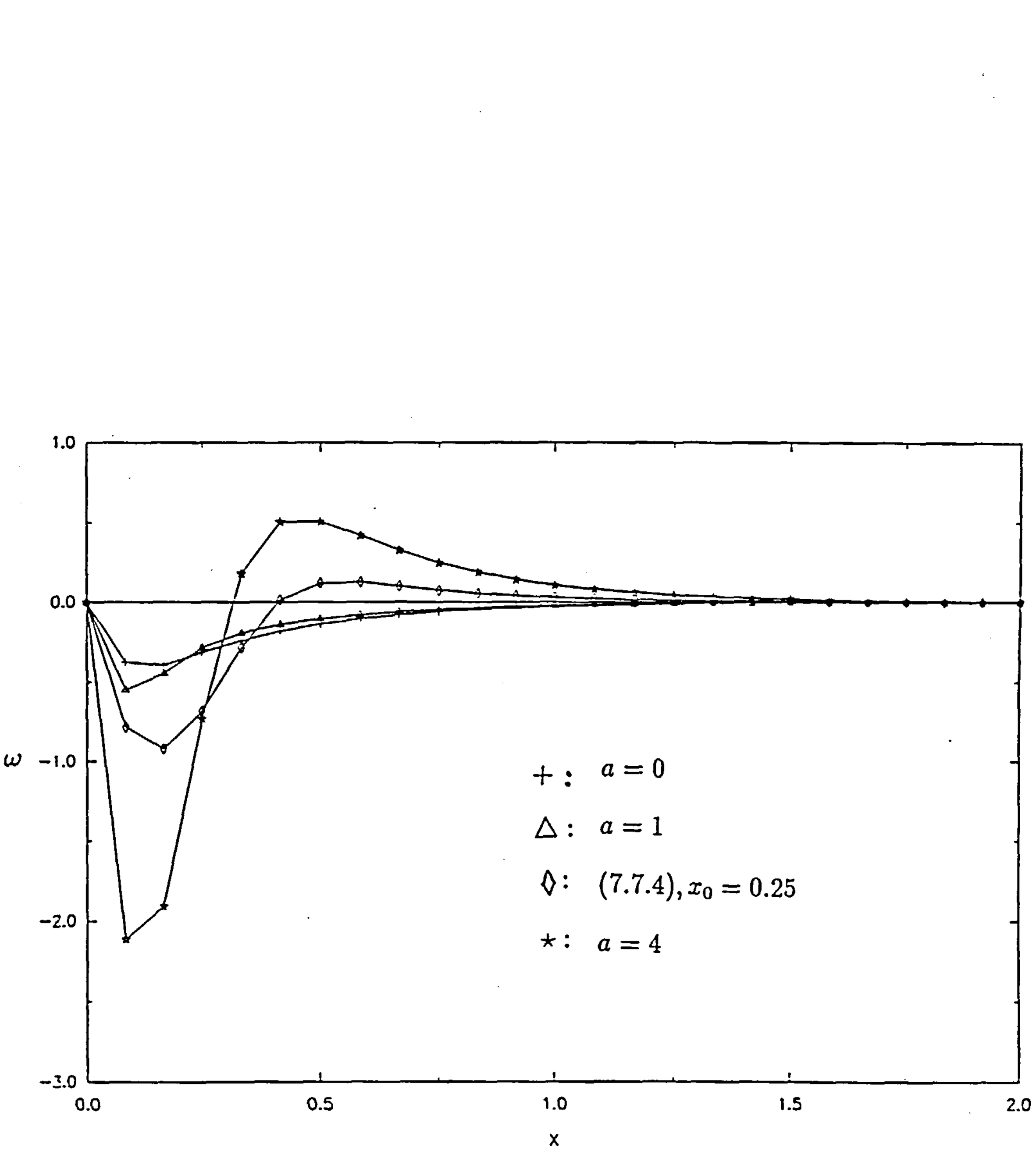

Figure 7.11: The vertical velocity at $t = 0.005$ on $z = 0.3$ with $\sigma = 0.733$ and $R_1 = 500$ for different initial conditions in the insulating case.

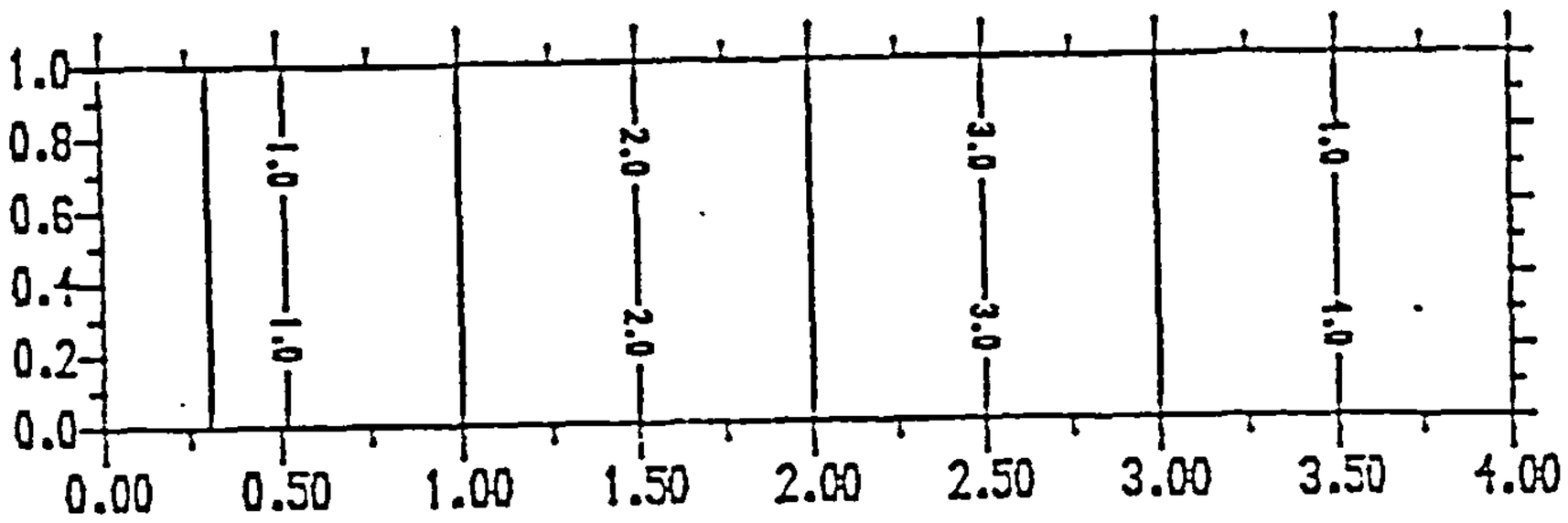

(c) Contour Step 0.50

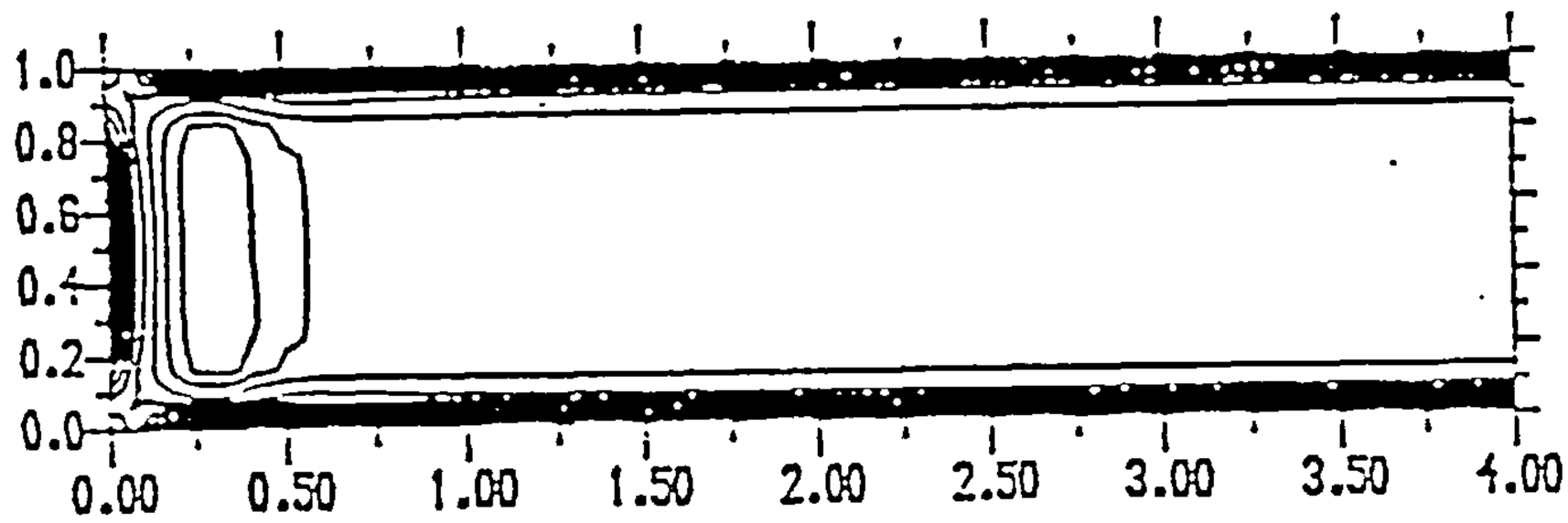

(b) Contour Step 0.00

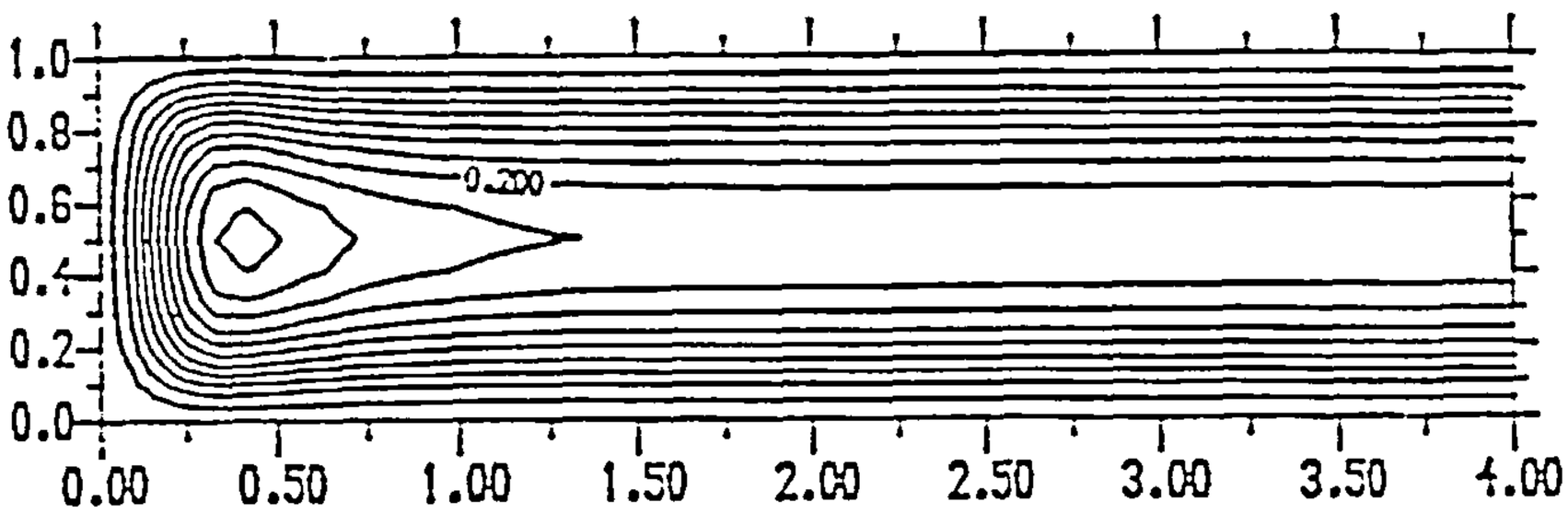

(a)

Contour Step 0.03

Figure 7.12: Contours at $t = 0.05$ of (a) stream function , (b) vorticity, (c) temperature, for $\sigma = 0.733$, $R_1 = 500$, using a 750×12 computational grid with $x_\infty = 60$ and the initial condition $T = x + 0.5, \quad x > 0.25, \quad T = 0, \quad x < 0.25, \quad u = w = 0$ at $t = 0$ at $t = 0$ $x < 0.25$ for the insulating case.

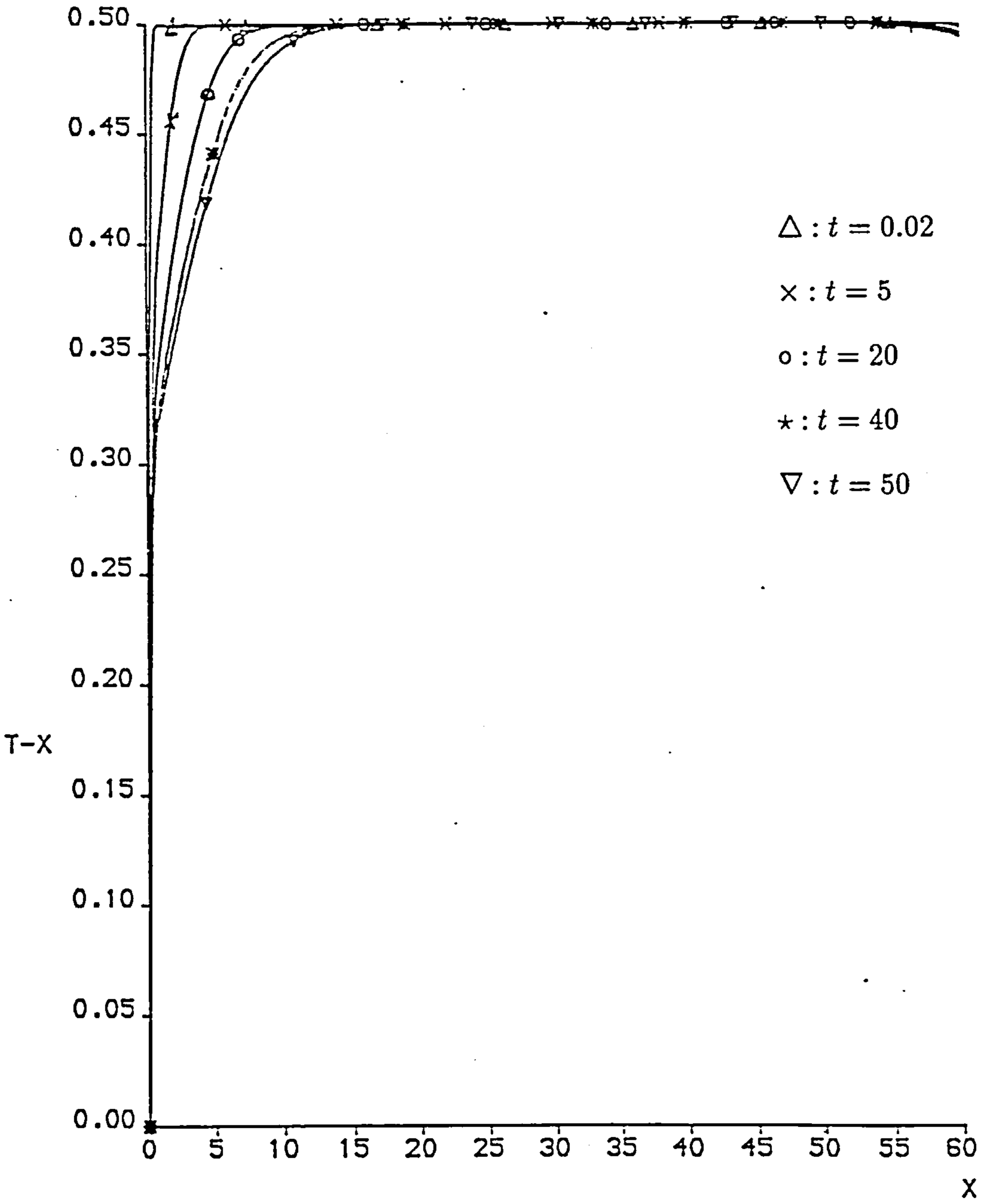

Figure 7.13: The function $T - x$ on $z = 1/2$ for $\sigma = 0.733$, $R_1 = 500$ at different time steps for the initial condition $T = x + 0.5, u = w = 0$ at $t = 0$ for the insulating case.

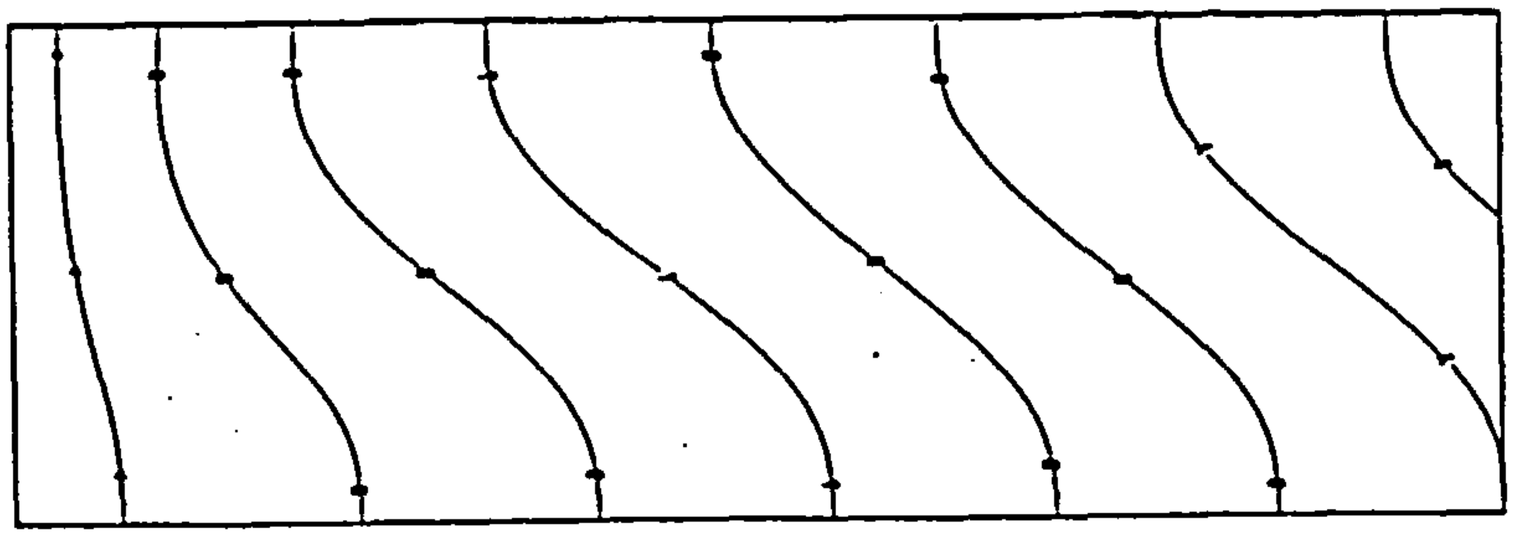

CONTOUR KEY	
1	0.2265789
2	0.6797367
3	1.1328945
4	1.5860523
5	2.0392100
6	2.4923678
7	2.9455256
8	3.3986834

(c)

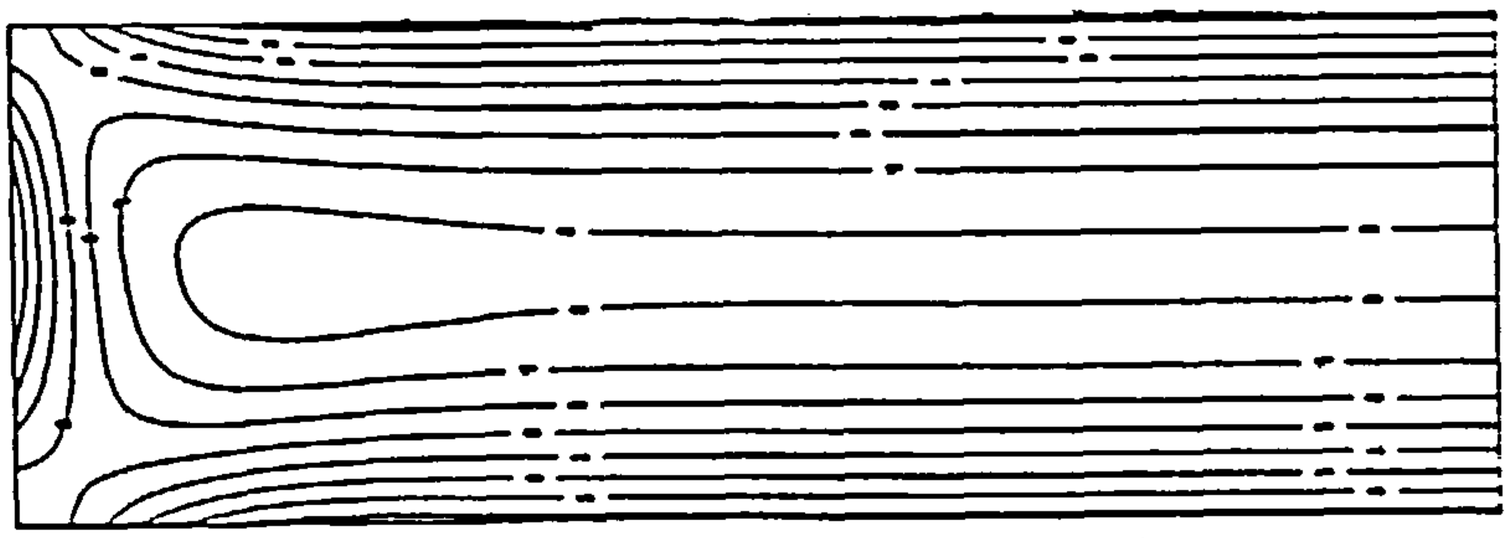

CONTOUR KEY	
1	-39.3413102
2	-30.9313097
3	-22.5213093
4	-14.1113088
5	-5.7013084
6	2.7086921
7	11.1186925
8	19.5286930

(b)

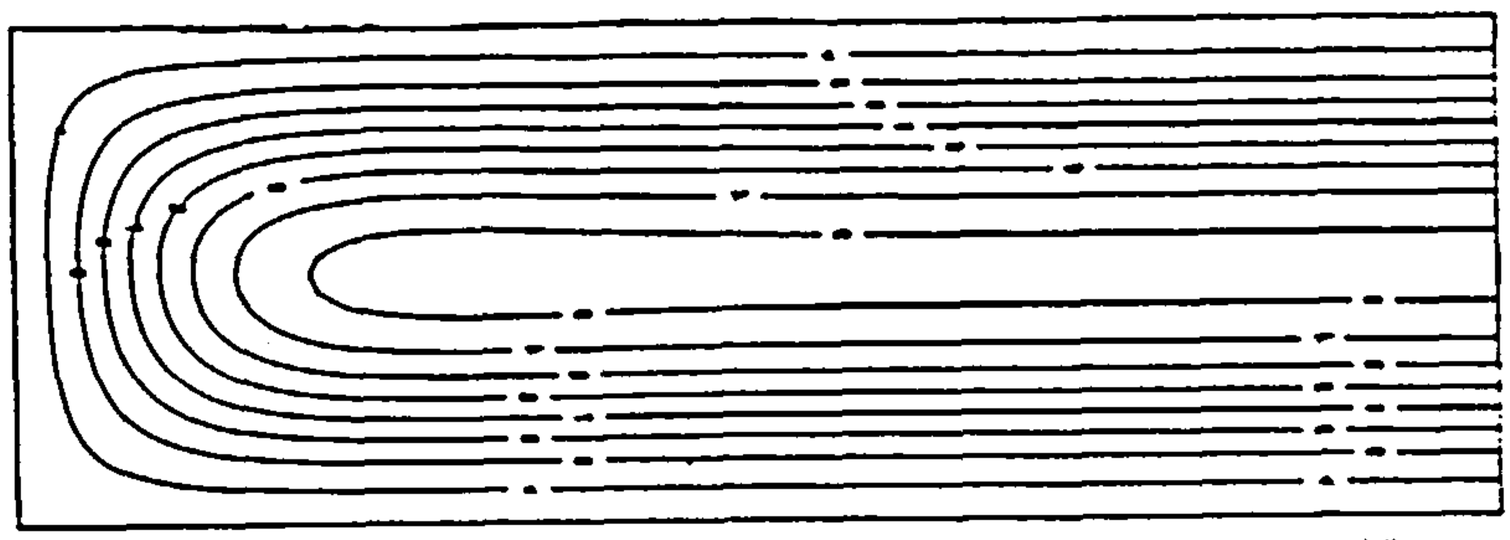

CONTOUR KEY	
1	0.0833490
2	0.2500470
3	0.4167449
4	0.5834429
5	0.7501409
6	0.9168389
7	1.0835368
8	1.2502348

(a)

Figure 7.14: Contours of the steady-state solution for (a) stream function , (b) vorticity, (c) temperature, for $\sigma = 0.733$ and $R_1 = 500$, using a 90×30 computational grid with $x_\infty = 3$.

Bibliography

[1] W.F Ames. *Numerical Methods for Partial Differential Equations.* Academic Press ; New York, 1977.

[2] A. Arakawa. Computational design for long-term numerical integration of the equations of fluid motion: Two dimensional incompressible flow, part 1. *J.Comp. Phys.*, 1:119–143, 1966.

[3] S.W. Armfield. Direct simulation of unsteady natural convection in a cavity. In *3rd Int. Symp. on Computational Fluid Dynamics*, pages 305–310, North-Holland, 1989.

[4] G.K. Batchelor. Heat transfer by free convection across a closed cavity between vertical boundaries at different temperatures. *Q.J.Appl.Math.*, 12:209–233, 1954.

[5] A. Bejan and C. L. Tien. Laminar natural convection heat transfer in a horizontal cavity with different end temperatures. *Trans. A.S.M.E. : J. Heat Trans*, 100:641–647, 1978.

[6] R. F. Bergholz. Instability of steady natural convection in a vertical slot. *J.Fluid Mech.*, 84:743–768, 1978.

[7] R.V. Birikh, G.Z. Gershuni, E.M. Zhukovitskii, and R.N. Rudakov. On oscillatory instability of plane parallel convection motion in a vertical channel. *Prikl.Mat.Mekh.*, 36:745–748, 1972.

[8] P.A. Blythe, P.G.Daniels, and P.G. Simpkins. Thermal convection in a cavity: the core structure near the horizontal boundaries. *Proc. Roy. Soc. A*, 387:367–388, 1983.

[9] P. Bradshaw, T. Cebeci, and J.H. Whitelaw. *Engineering Calculation Methods of Turbulent Flow.* Academic Press , New York, 1981.

[10] A. Brandt. Multi-level adaptive solutions to boundary-value problems. *Math. Comp.*, 31:333–390, 1977.

[11] C.-Y. Chow. *An Introduction to Computational Fluid Dynamics.* Wiley, New York, 1979.

[12] T.J. Chung. *Finite Element Analysis in Fluid Dynamics.* McGraw-Hill, New York, 1978.

[13] D.E. Cormack, L.G.Leal, and J. Imberger. Natural convection in a shallow cavity with differentially heated end walls. Part 1. Asymptotic theory. *J.Fluid Mech.*, 65:209–229, 1974.

[14] D.E. Cormack, L.G.Leal, and J.H.Seinfeld. Natural convection in a shallow cavity with differentially heated end walls. Part 2. Numerical solutions. *J.Fluid Mech.*, 65:231–246, 1974.

[15] R. Courant, K.Friedrichs, and H. Lewy. Uber die partiellen differenzgleichungen der mathematischen physik. *Mathematische Annalen*, 100:32–74, 1928.

[16] J. Crank and P. Nicholson. A practical method for numerical evaluation of solutions of partial differential equations of the heat- conduction type. *Proc. Camb. Phil. Soc.*, 43:50–67, 1947.

[17] G. Dahlquist, A. Bjorck, and N. Anderson. *Numerical Methods.* Prentice-Hall, Englewood Cliffs, N.J., 1974.

[18] P. G. Daniels. Transition to the convective regime in a vertical slot. *Int. J. Heat Mass Transfer*, 126:2071–2077, 1985.

[19] P. G. Daniels. Convection in a vertical slot. *J.Fluid Mech.*, 176:419–441, 1987.

[20] P. G. Daniels. The horizontal boundary-layer structure for the convective regime in a laterally heated vertical slot. *Q.J. Mech. Appl. Math.*, 40:257–277, 1987 a.

[21] P. G. Daniels. Minimum heat transfer by laminar natural convection across a laterally heated vertical slot. *Int. J. Heat Mass Transfer*, 11:371–375, 1990.

[22] P. G. Daniels and R.J. Gargaro. Buoyancy effects in stably-stratified horizontal boundary-layer flow. *J.Fluid Mech. (to appear).*, 1992 b.

[23] P. G. Daniels and R.J. Gargaro. Numerical and asymptotic solutions for the thermal wall jet. *J.Eng.Math. (to appear).*, 1992 a.

[24] P.G. Daniels, P.A.Blythe, and P.G. Simpkins. High Rayleigh number thermal convection in a shallow laterally heated cavity. *AT & T Bell Laboratories TM.*, $11523 - 871019 - 61$. 1987*a*.

[25] P.G. Daniels, P.A.Blythe, and P.G. Simpkins. Onset of multicellular convection in a shallow laterally heated cavity. *Proc. Roy. Soc. A*, 411:327–350, 1987.

[26] G. de Vahl Davis and I. P. Jones. Natural convection in a square cavity: a comparison exercise. *Int. J. Numer. Methods in Fluids*, 3:227–248, 1983.

[27] G. de Vahl Davis. Laminar natural convection in an enclosed rectangular cavity. *Int. J. Heat Mass Transfer*, 11:1675–1693, 1968.

[28] G. de Vahl Davis and G. D. Mallinson. A note on natural convection in a vertical slot. *J. Fluid Mech.*, 72:87–93, 1975.

[29] J.E. Drummond. *A Numerical Study of Natural Convection in Shallow Cavities.* Ph.D Dissertation, Ohio State University, 1981.

[30] J.E. Drummond and S.A. Korpela. Natural convection in a shallow cavity. *J.Fluid Mech.*, 182:543–564, 1987.

[31] J.W. Elder. Laminar free convection in a vertical slot. *J.Fluid Mech.*, 23:77–98, 1965.

[32] J.W. Elder. Numerical experiments with free convection in a vertical slot. *J. Fluid Mech.*, 24:823–843, 1966.

[33] S.M. ElSherbiny, G.D. Raithby, and K.G.T. Hollands. Heat transfer by natural convection across vertical and inclined air layers. *Trans. A.S.M.E : J. Heat Transfer*, 104:96–102, 1982.

[34] C.-E. Froberg. *Introduction to Numerical Analysis.* Addison-Wesley, 1969.

[35] C.-E. Froberg. *Numerical Mathematics.* Benjamin / Cummings Publishing Company, 1985.

[36] R.H. Gallagher, J.T. Oden, C. Taylor, and O. C. Zienkiewicz. *Finite elements in fluids.* Wiley, New York, 1975.

[37] R.J. Gargaro. *Thermally-Driven Shallow Cavity Flows.* Ph.D Dissertation, City University, 1991.

[38] P.H. Gaskell and N.G. Wright. A multigrid algorithm for the investigation of thermal recirculating fluid flow problems. In *5th Int. Conf. on Num. Meth. for Thermal Problems*, Montreal-Canada, 1987.

[39] A. E. Gill. The boundary-layer regime for convection in a rectangular cavity. *J.Fluid Mech.*, 26:515–536, 1966.

[40] A. E. Gill and C. C. Kirkham. A note on stability of convection in a vertical slot. *J.Fluid Mech.*, 42:125–127, 1970.

[41] S. Goldstein. *Modern developments in fluid dynamics*, volume 2. Oxford Univ. Press, 1938.

[42] A.D Gosman, W.M.Pun, A.K. Runchal, D.B. Spalding, and M. Wolfshtein. *Heat and Mass Transfer in Recirculating Flows.* Academic Press , New York, 1969.

[43] G. Hadley. Concerning the cause of the general trade winds. *Phil. Trans. Roy. Soc. Lond.*, 39:58–62, 1735.

[44] P. Haldenwang and G. Labrosse. 2-d and 3-d spectral Chebyshev solutions for free convection at high Rayleigh number. In *6th Int. Symp. on Finite Element Methods in Flow Problems*, Antibes, France, 1986.

[45] J. E. Hart. Stability of the flow in a differentially heated inclined box. *J. Fluid Mech.*, 47:547–576, 1971.

[46] J. E. Hart. Stability of thin non-rotating Hadley circulations. *J. Atmos. Sci.*, 29:687–697, 1972.

[47] J. E. Hart. Low Prandtl number convection between differentially heated end walls. *Int. J. Heat Mass Transfer*, 26:1069–1074, 1983.

[48] J. E. Hart. A note on stability of low Prandtl number Hadley circulations. *J. Fluid Mech.*, 132:271–281, 1983 a.

[49] J. Imberger. Natural convection in a shallow cavity with differentially heated end walls. Part 3. Experimental results. *J.Fluid Mech.*, 65:247–260, 1974.

[50] G. N. Ivey. Experiments on transient natural convection in a cavity. *J.Fluid Mech.*, 144:389–401, 1984.

[51] I.P. Jones. A numerical study of natural convection in an air-filled cavity: comparison with experiment. *Num. Heat Trans.*, 2:687–697, 1976.

[52] H.B. Keller. *in Numerical Solution of Partial Differential Equations.* Academic Press , New York, 1970.

[53] S. A. Korpela. A study on the effect of Prandtl number on the stability of the conduction regime of natural convection in an inclined slot. *Int. J. Heat Mass Transfer*, 17:215–222, 1974.

[54] S.A. Korpela, D. Gozum, and C.B. Baxi. On the stability of the conductive regime of natural convection in a vertical slot. *Int. J. Heat Mass Transfer*, 16:1683–1690, 1973.

[55] K. Kublbeck, G. P. Merker, and J. Straub. Advanced numerical computation of two-dimensional time-dependent free convection in cavities. *Int. J. Heat Mass Transfer*, 23:203–217, 1980.

[56] Y. Lee. *Numerical Study of Multicellular Natural Convection in Vertical Cavities.* Ph.D Dissertation,Ohio State University, 1981.

[57] Y. Lee and S.A.Korpela. Multicellular natural convection in a vertical slot. *J. Fluid Mech.*, 126:91–121, 1983.

[58] M. E. McIntyre. The axisymmetric convective regime for a rigidly bounded rotating annulus. *J. Fluid Mech.*, 32:625–655, 1968.

[59] J. Mizushima and K. Gotoh. Nonlinear evolution of the disturbance in a natural convection induced in a vertical fluid layer. *J.Phys.Soc.Japan*, 52:1206–1214, 1983.

[60] K.W. Morton and M.J. Baines. *Numerical Methods for Fluid Dynamics.* Academic Press , London, 1982.

[61] S. Ostrach. An analysis of laminar free convection flow and heat transfer about a flat plate parallel to the direction of the generating body force. *N.A.C.A. Rep.*, 1111, 1952.

[62] S. Ostrach. Natural convection in enclosures. *Advances in Heat Transfer*, 8:161–224, 1972.

[63] S.V. Patankar. *Numerical Heat Transfer and Fluid Flow.* Hemisphere/McGraw-Hill, New York, 1980.

[64] S.V. Patankar and D.B. Spalding. *Heat and Mass Transfer in Boundary Layers.* Intertext-Books, London, 1970.

[65] J. C. Patterson. On the existence of an oscillatory approach to steady natural convection in a cavity. *Trans. A.S.M.E : J. Heat Transfer*, 106:104–108, 1984.

[66] J. C. Patterson. Experiments in unsteady natural convection. In *Proc. Fourth Australasian Conference on Heat and Mass Transfer*, pages 299–306, Christchurch, 1989.

[67] J. C. Patterson and S. W. Armfield. Transient features of natural convection in a cavity. *J.Fluid Mech.*, 219:469–497, 1990.

[68] J. C. Patterson and J. Imberger. Unsteady natural convection in a rectangular cavity. *J.Fluid Mech.*, 100:65–86, 1980.

[69] D.W. Peaceman and H.H. Rachford. The numerical solution of parabolic and elliptic differential equations. *J. Sco. Indust. Applied Maths.*, 3:28–41, 1955.

[70] C. Quon. High Rayleigh number convection in an enclosure- a numerical study. *Phys. of Fluids*, 15:12–19, 1972.

[71] G. D. Raithby and H. H. Wong. Heat transfer by natural convection across vertical air layers. *Numer. Heat Transfer*, 4:447–457, 1981.

[72] L. F. Richardson and J.A. Gaunt. The deferred approach to the limit. *Phil.Trans. Roy. Soc. Lond. A*, 226:300, 1927.

[73] P.J. Roache. *Computational Fluid Dynamics.* Hermosa, Alberquerque, N.Mex., 1976.

[74] H.T. Rossby. On thermal convection driven by non-uniform heating from below. *Deep Sea Res.*, 12:9–16, 1965.

[75] S.G. Schladow, J.C. Patterson, and R.L.Street. Transient flow in a side-heated cavity at high Rayleigh number: a numerical study. *J.Fluid Mech.*, 200:121–148, 1989.

[76] N. Seki, S.Fukusako, and H.Inaba. Visual observation of natural convective flow in a narrow vertical cavity. *J. Fluid Mech.*, 84:695–704, 1978.

[77] G. Shiralkar, A. Gadgil, and C.L. Tien. High Rayleigh number convection in a shallow enclosure with different end temperatures. *Int. J. Heat Mass Transfer*, 24:1621–1629, 1981.

[78] P.G. Simpkins and K.S. Chen. Convection in horizontal cavities. *J.Fluid Mech.*, 166:21–39, 1986.

[79] F. T. Smith and P. W. Duck. Separation of jets or thermal boundary layers from a wall. *Quart. J. Mech. Appl. Math.*, 30:143–156, 1977.

[80] G.D. Smith. *Numerical Solution of Partial Differential Equations: Finite Difference Methods.* Oxford Univ. Press, Oxford, 1978.

[81] R.V. Southwell. *Relaxation methods in engineering science.* Oxford Univ. Press, Fair Lawn, N.J., 1940.

[82] R.V. Southwell. *Relaxation methods in theoretical physics.* Oxford Univ. Press, Fair Lawn, N.J., 1956.

[83] D.B. Spalding. *GENMIX-A General Computer Program for Two-Dimensional Parabolic Phenomena.* Pergamon Press, Elmsford, N.Y., 1977.

[84] R.W. Thomas and G. de Vahl Davis. Natural convection in annular and rectangular cavities- a numerical study. In *Heat Transfer.* Elsevier Pub., 1970.

[85] C.D. Upson, P. M. Gresho, and R. L. Lee. *Finite-element simulation of thermally induced convection in an enclosed cavity.* Report UCID-18602, Lawrence Livermore Laboratory, California, U.S.A, 1981.

[86] C. M. Vest and V. S. Arpaci. Stability of natural convection in a vertical slot. *J.Fluid Mech.*, 36:1–15, 1969.

[87] J. von Neumann and R.D. Richtmyer. A method for numerical calculation of hydrodynamic shocks. *J. Appl. Phys*, 21:232–237, 1950.

[88] K.H. Winters. Predictions of laminal natural convection in heated cavities. In R.W.Lewis, K.Morgan, and B.A.Schrefler, editors, *Numerical Methods in Heat Transfer*. John Wiley & Sons, 1983.

[89] K.H. Winters. Laminal natural convection in a partially divided rectangular cavity at high Rayleigh number. *J. Numerical Methods in Fluids*, 8:247–281, 1988.

[90] R.A. Wirtz and L.H. Liu. Numerical experiments on the onset of layered convection in a narrow slot containing a stably stratified fluid. *Int. J. Heat Mass Transfer*, 18:1299–1305, 1975.